University of Bath

PHD

Finite element and boundary element modelling of a physiotherapy transducer and its near-field

Hughes, Martin

Award date:
2001

Awarding institution:
University of Bath

Link to publication

General rights
Copyright and moral rights for the publications made accessible in the public portal are retained by the authors and/or other copyright owners and it is a condition of accessing publications that users recognise and abide by the legal requirements associated with these rights.

- Users may download and print one copy of any publication from the public portal for the purpose of private study or research.
- You may not further distribute the material or use it for any profit-making activity or commercial gain
- You may freely distribute the URL identifying the publication in the public portal ?

Take down policy
If you believe that this document breaches copyright please contact us providing details, and we will remove access to the work immediately and investigate your claim.

Download date: 14. May. 2019

Finite Element and Boundary Element Modelling of a Physiotherapy Transducer and its Near-Field

Submitted by Martin Hughes
for the degree of PhD
of the University of Bath
2001

COPYRIGHT

Attention is drawn to the fact that copyright of this thesis rests with its author. This copy of the thesis has been supplied on condition that anyone who consults it is understood to recognise that its copyright rests with its author and that no quotation from the thesis and no information derived from it may be published without the prior written consent of the author. This thesis may be made available for consultation within the University Library and may be photocopied or lent to other libraries for the purposes of consultation.

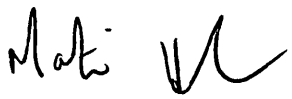

UMI Number: U145638

All rights reserved

INFORMATION TO ALL USERS
The quality of this reproduction is dependent upon the quality of the copy submitted.

In the unlikely event that the author did not send a complete manuscript
and there are missing pages, these will be noted. Also, if material had to be removed,
a note will indicate the deletion.

UMI U145638
Published by ProQuest LLC 2013. Copyright in the Dissertation held by the Author.
Microform Edition © ProQuest LLC.
All rights reserved. This work is protected against
unauthorized copying under Title 17, United States Code.

ProQuest LLC
789 East Eisenhower Parkway
P.O. Box 1346
Ann Arbor, MI 48106-1346

UNIVERSITY OF BATH
LIBRARY
45 27 MAY 2002
Ph.D

Abstract

The finite element and boundary element modelling of a medical ultrasound transducer and its resultant acoustic near-field are considered. The device is considered to be axi-symmetric and to radiate into an unbounded region of water.

A 1 MHz physiotherapy transducer with a *ka* value of 54 was designed and built in order to evaluate the model. The results of a series of experimental measurements are described and the device is shown to be a typical physiotherapy transducer. The near-field pressure region is seen to be highly variable close to the source and substantially different from that of an idealised plane piston.

The modelling of the structure and the surrounding fluid region are considered separately before a combined model is used to simulate the complete system. The device model requires the specification of a large number of parameters, in particular material properties, many of which are poorly defined despite a detailed knowledge of the transducer design. Three fluid modelling options are compared: two boundary element formulations (CHIEF and DAA2c), and the use of acoustic finite elements with 'infinite' wave envelope elements. An analysis of these options shows DAA2c to be practical and effective for realistic high *ka* systems. It is therefore used extensively here. The use of wave envelope elements is shown to be effective and reliable, but impractical for any substantial analysis of large systems. CHIEF is shown to become less accurate with increasing *ka*.

Despite the frequency dependence of the system and extreme pressure variations in the near-field, very good model-experimental agreement is observed for axial and cross-axial results, and for IEC standard parameters. The modelled structural vibrational behaviour is seen to be highly non-uniform. A sensitivity analysis of the system shows it to be very sensitive to the properties of the piezoelectric disc and the front matching layer.

Acknowledgements

I would like to thank my supervisor, Dr. Victor Humphrey, for his support and advice, as well as the other members of the Underwater Acoustics and Medical Ultrasonics group at Bath. In particular I thank Dr. Mark Cahill and Dr. Nic Jayasundere for their consistent assistance in the face of inconsistent questioning.

Thanks to my supervisor at the National Physical Laboratory, Dr. Trevor Esward, for his help and advice, and the members of the Mechanical and Acoustical Metrology section at NPL. In particular I would like to thank Mark Hodnett, with whom all experimental measurements were made, and Dr. Roy Preston and Pierre Gelat for their advice and input. I would also like to thank both NPL and the EPSRC for funding this work.

Thanks to Dr. Patrick Macey at SER for his continued help with PAFEC and his explanations of all things acoustic. I would also thank George Cattermole who built the physiotherapy transducer used here.

Finally I would like to thank my family and friends for their continual support during the course of this work. Without their encouragement I doubt I could have made it this far.

Contents

List of Key Symbols and abbreviations

The following is a list of the *key* symbols and abbreviations used in this thesis.

a	source radius
a_i	radial distance from the virtual source of a wave envelope element to the finite element – wave envelope element interface
A_{BCS}	beam cross-sectional area
A_{ER}	effective radiating area
$[B]$	strain-displacement matrix
BE	Boundary Element
BEM	Boundary Element Method
c	acoustic wave-speed
$[C]$	stress-strain matrix
CHIEF	Combined Helmholtz Integral Equation Formulation
d	displacement
$[\boldsymbol{D}]$	structural damping matrix
DAA	Doubly Asymptotic Approximation
DAA2c	second-order (curved) Doubly Asymptotic Approximation
d.o.f.	degrees of freedom
E	Young's modulus
$f(\omega)$	(frequency dependent) load vector
FE	Finite Element
FEM	Finite Element Method
g	Green's function
h	unknown variable
k	wave number, $k = 2\pi/\lambda$
$[\boldsymbol{K}]$	structural stiffness matrix
L	Lagrange polynomial
$[\boldsymbol{M}]$	structural mass matrix

m.s.d.	mean square difference
n	normal direction
$\underline{N}$	vector of shape functions
p	pressure
p'	trial function
q_i	unknown coefficients
Q	position vector
r, r'	distance between points
r	radial distance from the virtual source of a wave envelope element
R	residual
R_{BN}	beam non-uniformity ratio
r.m.s.	root mean square
S	surface
t	time
U_0	source velocity amplitude
v_n	normal surface velocity
V	volume
W_i	weighting functions
WEE	wave envelope element
Z	acoustic impedance
ζ , ξ	local co-ordinate components of displacement
ϑ	angle
λ	wavelength
μ	hysteretic damping factor
ρ	volume density
σ	Poisson's ratio
ϕ	electric potential
ω	angular frequency

1 Introduction

1.1 Ultrasound

The use of ultrasound in medicine has its origins in the early part of the 20th century when the interaction of ultrasonic waves with living organisms was first observed during work on the detection of underwater structures by ultrasound (Meire & Farrant, 1995). Work in the field of medical ultrasound has progressed significantly in the subsequent 80 years to the stage where its use is now routine in hospitals and medical facilities for a wide range of diagnostic and therapeutic applications. This introductory chapter briefly reviews these applications and then describes the ultrasonic transducers used and the fields that they generate. The possible approaches to modelling such systems are then described enabling the contents of this thesis to be placed in context. Finally, the aims of this project are introduced.

1.1.1 Diagnostic applications

The diagnostic use of ultrasound is essentially founded on the same principles that were developed earlier for underwater acoustic sonar echo-ranging. A transducer directs a pulsed wave into the area under investigation and the same or additional devices measure reflected waveforms. Information can be derived from these reflections based on the characteristics of the radiated waves and propagating medium. Progress in electronics, transducers and processing techniques have led to significant advances in medical ultrasound devices and their applications. The 1950s saw the introduction of the first pulse-echo ultrasonic imagining equipment for medical applications in the form of A-mode and B-mode scanners. A-mode scanners record the amplitude of detected echoes as a function of delay time, whilst for B-mode scanners echoes are displayed as dots with a brightness proportional to the echo amplitude. Subsequent B-mode 'compound' scanning of the patient from a number of directions enabled the generation of two-dimensional images. From such 'static' systems, real-time scanners evolved utilising either arrays of transducers to generate a

large number of scan lines or mechanical systems with the transducer(s) mounted in such a way that they could be swept over the area of interest automatically. The introduction of improved transducers and further developments in electronics have significantly improved the image quality and the rate at which frames can be displayed. Such imaging techniques are now widely used, most notably in the area of obstetric examination.

The development of the use of the Doppler principle to detect blood flow occurred at around the same time as the development of ultrasonic imaging systems. The Doppler effect is the apparent change in the observed frequency of sound produced by the relative motion between a source of sound and a receiver. This 'Doppler shift' - the difference between the transmitted and observed frequencies - can be exploited to measure flow. Early scanners simply used transducers to transmit continuous waves into blood vessels with Doppler shifted echoes measured by a separate device. Such devices do not provide range information but pulsed devices were subsequently developed enabling flow measurements to be made at a known depth. A variation on this type of device is a colour-flow imaging system where the standard 'grey-scale' images are replaced by colour images with different Doppler signals represented by different colours. Pulsed devices were later linked to real-time imaging systems, forming a 'duplex' system, with the blood flow data superimposed (in colour) on to grey-scale images of vessels. Again such systems are now commonly used for various imaging applications such as monitoring of the heart and analysis of blood vessels and tissue (Meire & Farrant, 1995; Hill, 1986; Ensminger, 1988; Hedrick et. al., 1995).

1.1.2 Therapeutic applications

From the earliest stages of the use of ultrasound for medical purposes the potential effect of ultrasonic waves on living tissue and its uses were considered. Rather than the echo-detecting techniques employed in imaging, therapeutic applications are based on the mechanical and thermal effects of a wave on the medium through which

it travels. Such effects are a direct result of the displacements of the medium resulting from the waveform propagation. Early attempts at using ultrasound as a tool for destroying diseased tissue were ineffective as they caused the destruction of a significant amount of normal tissue, but again much progress has been made in terms of the understanding and use of ultrasound, and the technology surrounding it. Today a number of therapeutic treatments are employed, such as physiotherapy, lithotripsy and ultrasound surgery (Meire and Farrant, 1995; Hill, 1986; Ensminger, 1988; Hedrick et. al., 1995; Duck et. al., 1998).

The processes by which physiotherapy ultrasonic treatment works are not well understood. However it is thought that temperature rises generated in the tissue are the most likely beneficial mechanism. Ultrasonic physiotherapy is now used for a variety of treatments such as soft tissue injuries, back and shoulder pain and the treatment of scar tissue. Lithotripsy involves the mechanical break-up of kidney and gallstones through the use of high amplitude shock waves, whilst techniques such as focused-ultrasound surgery exploit the thermal effects resulting from ultrasonic attenuation to ablate tissue.

One significant feature of some medical ultrasound applications is that the propagation of the wave through the media is non-linear (Duck et. al., 1998). In fact the equations defining propagation are inherently non-linear but in many cases the simplified linear wave equation is used. This linearised approximation has been used effectively in many cases for low-amplitude propagating waveforms and will be employed here. For the case of finite amplitude waves, however, the simplified linear wave equation is not sufficient. Nonlinear propagation results in the generation of harmonics of the fundamental wave and may therefore lead to the generation of extremely high frequency components. A comprehensive consideration of non-linear acoustics can be found in texts such as Hamilton and Blackstock (1998).

1.2 Ultrasonic transducers

Although there are many different applications for which ultrasonic devices can be used the basic principle of any medical ultrasound transducer is the same. The device is required to have a vibrating surface that can be coupled to the area of the patient being examined/treated. Figure 1.1 shows a front-to-back section of a typical circular transducer with an active element, matching and backing layers, and inner and outer casings. For a piezoelectric transducer the active element in Figure 1.1 is a piezoelectric disc. The action of such a disc is based on the piezoelectric effect whereby there is a coupling between the mechanical and electrical properties of the material. When the element is deformed a charge is generated on its surfaces. This *direct piezoelectric effect* can be used to create a receiver. Conversely, when a field is applied across the disc it deforms. This *indirect piezoelectric effect* can be exploited to make a radiating device, as considered here.

Piezoelectric ceramics are given a principal piezoelectric axis by a poling treatment that involves applying electrodes to the surfaces of the component and applying a high voltage between them. Consequently applying a voltage to these electrodes results in a deformation in the same direction. In Figure 1.1 the piezoelectric disc would have electrodes on its planar surfaces. For a transducer operating at a given frequency a disc thickness of $\lambda/2$ will theoretically induce optimum performance, where λ is the wavelength in the disc, with the disc deforming primarily in the thickness dimension (Hedrick et. al., 1995; Preston, 1991). This is based on the assumption that the vibrational behaviour of the disc is uniform, with a constant phase and amplitude of displacement across its face. For a real piezoelectric disc, however, this is not the case and in fact real elements have been shown to exhibit extremely non-uniform behaviour (Ikegami et. al., 1974; Guo et. al., 1992). Figure 1.2 shows an example of the potential vibrational behaviour of a piezoelectric disc deforming fundamentally in the thickness dimension. This is based on the work of Guo et. al. (1992), and shows the deformation of a radial section of a *modelled* PZT4 disc operating at its main resonant frequency. Such irregular response is clearly very

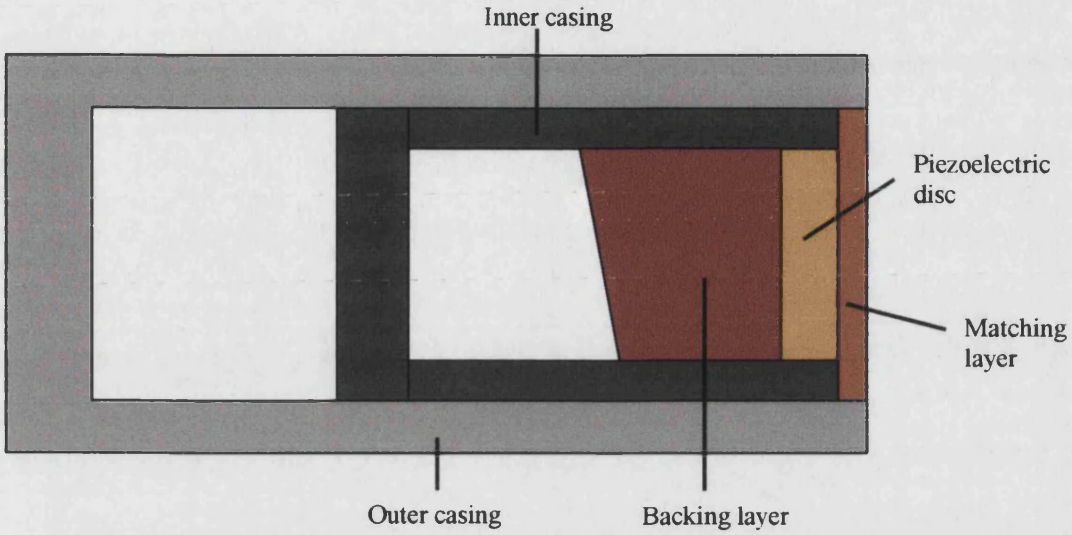

Figure 1.1 Cross-section of a general circular transducer design.

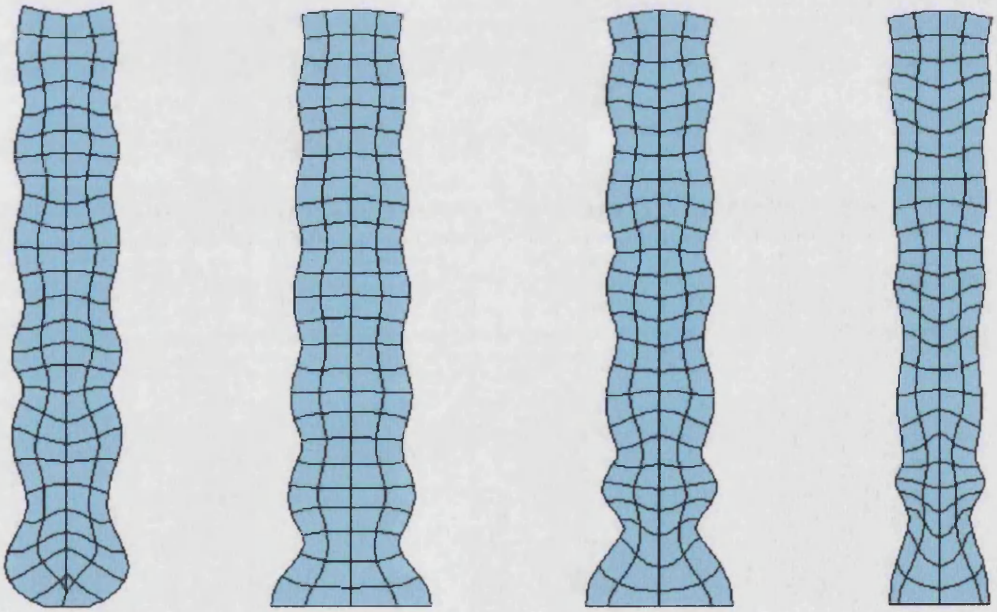

Figure 1.2 Vibrational behaviour of a PZT4 piezoelectric disc modelled using the finite element method and based on Guo & Cawley (1992). The disc deformation is exaggerated to emphasise the irregularity of the vibrational behaviour. The thickness of the disc is approximately 2mm whilst the magnitude of the deformation in the thickness dimension is of the order of 10e-6mm.

different from the uniform phase and amplitude model and is a major reason why modelling techniques other than idealised approaches are needed.

The matching layer in Figure 1.1 is designed to provide optimum impedance matching between the piezoelectric element and the media into which the device operates so that energy is transferred as efficiently as possible. Theoretically this requires that the impedance of the matching layer is given by the following optimal, plane wave, normal incidence impedance relationship (Zagzebski, 1996)

$$Z_{ml} = \sqrt{Z_p . Z_w} \ . \qquad (1.1)$$

Here Z is impedance and sub-scripts *ml*, *p* and *w* refer to the matching layer, piezoelectric element and water into which the device is operating, respectively. The optimum thickness is $\lambda/4$, again based on the idealised case (Hedrick et. al., 1995; Preston, 1991). Alternatively some devices use composite piezoelectric elements which inherently incorporate a matching layer, whilst others employ a number of matching layers for better impedance matching. If the transducer is to be used to produce short pulses a backing layer is included and designed to have similar impedance to the piezoelectric element so that energy will be transferred into it easily. It is also designed to be highly attenuating so that no reflections occur from the back of the layer. In continuous wave operation these features are unnecessary so the disc is air-backed.

The components mentioned so far are essential to the generation of ultrasound, however there are also practical considerations that influence the design. Specifically these relate to how the active element is mounted and how the device is housed. A real device is therefore likely to have a number of features not included in Figure 1.1 such as glue layers, wiring and connectors. Furthermore as ultrasonic transducers are used for a variety of medical applications, design criteria and operating requirements will vary considerably. Criteria which can vary between devices and applications

include the size and number of active elements; the mode of vibration in which the active element is designed to deform; operating frequencies and drive levels; operation in continuous wave or pulsed mode; pulse duration; and the use of focusing. Essentially, though, the principles of operation are the same as those described here.

1.3 The generated field

When a piezoelectric transducer is driven electrically by an alternating voltage applied across the electrodes, the piezoelectric coupling effect results in a mechanical vibration. The motion of the surface of the device in contact with the propagating medium causes an acoustic field to be radiated, with ultrasound waves propagating through the media as areas of alternately increasing and decreasing pressure. The equation describing sound propagation in a medium is obtained by combining the equations of continuity, motion and state. The equation of continuity expresses the principle of the conservation of mass, the equation of motion describes the conservation of momentum, and the equation of state relates the response of a medium to thermal and mechanical stress. By combining these equations a relationship is established between the pressure, density and local particle velocity in the medium during the passage of an acoustic disturbance. If the disturbance produces only small changes in the pressure, density and particle velocity, relative to their equilibrium values, then the equations of propagation can be simplified by considering only first order approximations (Kinsler et. al., 1982; Van Randeraat & Setterington, 1974; Verma, 1995). This linearised wave equation for pressure, p, can be expressed as

$$\nabla^2 p = \frac{1}{c^2}\frac{\partial^2 p}{\partial t^2} \qquad (1.2)$$

where c is the infinitesimal wave velocity. For the steady-state case, where the system is assumed to operate with simple harmonic motion, the pressure is a harmonic

function of time $p.\exp(-i\omega t)$. Suppressing the time factor results in the steady-state Helmholtz wave equation (Schenck, 1968; Francis, 1993):

$$\nabla^2 p + k^2 p = 0 \qquad (1.3)$$

where k is the acoustic wave number, $2\pi/\lambda$. When the effect of fluid loading is significant, the solution of this equation for a radiating structure is a substantial problem. A common approach is to express the pressure field as the integrated effect of point sources over the structure. The *linear* acoustic beam due to any radiating structure is frequently described as composing of two regions, the near-field and the far-field. The near-field is characterised by rapid variations in pressure and is generally limited to a region close to the source. The far-field is much less complex with the beam typically spreading with a gradual drop-off in pressure amplitude (Kinsler et. al., 1982; Zemanek, 1970). The solution to Equation 1.3, for the case where the radiating structure is a plane circular piston with the source vibrating with uniform amplitude $U_0 e^{i\omega t}$, can be obtained by considering the geometry shown in Figure 1.3. It can be shown (Kinsler et. al., 1982) that the pressure is given by an integral over the surfaces of the transducer:

$$p(r,\vartheta) = i\frac{\rho_0 c U_0 k}{2\pi}\int_S \frac{e^{-ikr'}}{r'} dS \ . \qquad (1.4)$$

The pressure p, at any point in the field (r,ϑ) is expressed in terms of the velocity amplitude of the source, U_0, and an integral of contributions over the source. An exact solution to Equation 1.4 is not generally available, although there is one for the pressure on-axis:

$$p(r,0) = 2\rho_0 c U_0 \left| \sin\left(\frac{1}{2} kr \left[\sqrt{1+\left(\frac{a}{r}\right)^2} - 1 \right] \right) \right| \qquad (1.5)$$

where a is the radius of the piston. For the case of the circular plane piston a numerical solution to Equation 1.4 can be achieved using a double numerical integration. In this way the normalised near-field for an idealised circular source of radius 12.55mm and operating at a frequency of 1.030MHz (equivalent to a ka of approximately 54) was calculated, and is shown in Figure 1.4. This shows how the normalised pressure amplitude $\left|p/2\rho_0 cU_0\right|$ varies as a function of normalised axial range $\left(z/\left(a^2/\lambda\right)\right)$ and normalised radial distance (x/a). The choice of operating conditions here is the same as those of a real device introduced in Chapter 3. Figure 1.4 highlights the complexity of the near-field region, particularly close to the source where extreme pressure fluctuations are clearly visible. It should be emphasised that the numerical integration used here was only possible due to the simplicity of the radiating source. For example, if the source vibrates with non-uniform speed this must be included inside the integral. For more arbitrarily shaped structures expressing the solution as an integral over the surface of the source is likely to be much more complex than for the case of the circular source in Equation 1.4.

1.4 Modelling

It should be clear that in the interests of treatment safety, efficiency and efficacy, there is a very definite need for the modelling of real medical ultrasound devices and their fields. With the increasing use of ultrasound in medicine and its expanding applications the need for adequate models is growing. The passage of ultrasound through the human body inherently involves mechanical and thermal effects. Although there is little direct evidence of present techniques causing unwanted biological effects it is recognised that many applications have the potential to do so (Hekkenberg et al., 1994; Hekkenberg, 1998). In terms of treatment efficiency and efficacy it is important that the application of ultrasound is carried out effectively and that patients are receiving the diagnoses or treatment that they require, and indeed that they are believed to be receiving. Modelling real devices enables detailed

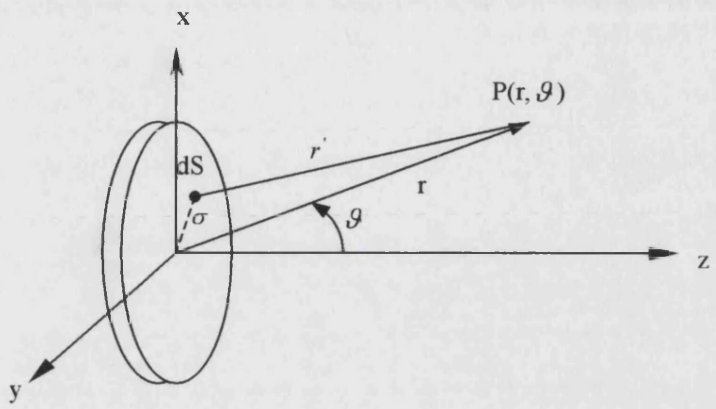

Figure 1.3 Geometry for the radiation from a plane circular piston relating to Equations 1.4 and 1.5.

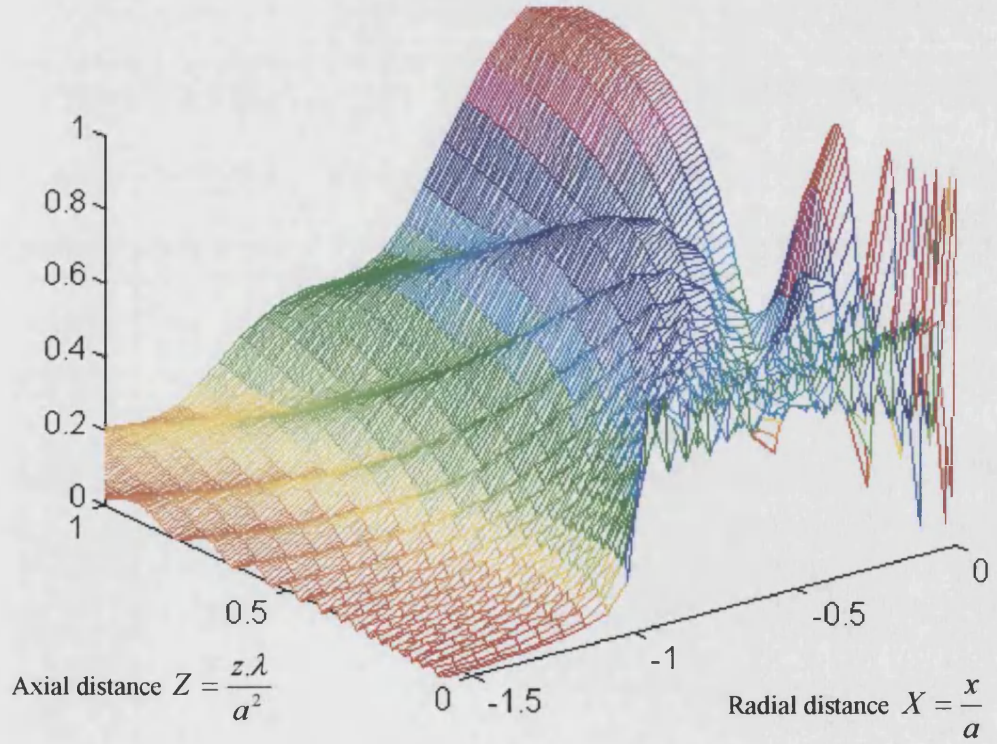

Figure 1.4 Near-field of an idealised plane piston source with *ka* of approximately 54. The pressure amplitude is normalised so that the maximum value is one.

consideration of how effectively they operate and also allows an investigation of realistic generated fields. Furthermore, a modelling technique that is capable of accurately predicting real field response is an ideal tool for use in studies aiming to establish and define internationally agreed standards on safety and performance. In addition to the implications for patient treatment, the simulation of realistic device behaviour should enable the investigation of device design to establish the significance of components and their effect on the generated field. This should lead to more effective and efficient devices as well as opening the way to novel designs and applications. Only a technique that is capable of modelling realistic behaviour can provide all of these potential benefits.

1.4.1 Modelling considerations

The simulation of a realistic medical ultrasound transducer and the field that it generates in a surrounding fluid media is a complex problem. The dynamical behaviour of the device, the fluid-structural interaction, and the effect on the surrounding fluid region must all be accounted for. Realistic medical devices generally operate at high frequencies and will have relatively large source-to-wavelength ratios, or *ka* values. If the near-field of the device is of specific interest then the simulation must be capable of accounting for the rapid pressure variations that occur close to the source. For a device with large *ka* this will mean accounting for variations on a very small scale. The complexity of the near-field for an idealised plane piston device was shown in Figure 1.4, and the difficulty of finding a direct solution to the Helmholtz equation even for simple sources has already been mentioned. Describing the field due to a realistic device with highly non-uniform source deformation is a much more difficult problem. The following are specific issues that are important when considering modelling such systems.

Firstly, a model of an ultrasound transducer will have a large number of independent parameters. The circular backed device in Figure 1.1 has over twenty-five material properties (densities, moduli, Poisson's ratios and damping factors) in addition to

dimensional and geometric parameters. Even if the components in the device and their dimensions are known, which in practice is not always the case, details of some material properties may be limited. Some properties may be difficult to measure and quoted tolerances are often large. In some cases no information will be available on specific properties of specific materials. Furthermore, property values can be dependent on the dimensional/geometrical nature of the sample being measured. Inaccurate values may therefore be applied as a result of differences between measured samples and components used in the device.

Of all the components in an ultrasound transducer the piezoelectric element is likely to have the most significant effect on the overall behaviour of the device and subsequent field. Furthermore any highly non-uniform behaviour of realistic piezoelectric components is likely to lead to complex interactions amongst other components. The active element is also likely to be the most difficult feature of the system to model accurately as it is an anisotropic material. The piezoelectric disc in Figure 1.2 has 12 distinct elastic and piezoelectric material properties, many of which are difficult to measure and quoted within tolerances of the order of $\pm 20\%$ (Vernitron, 1976). In light of the non-uniform vibration of such elements and the difficulty of accurately measuring piezoelectric properties, the sensitivity of the final device to the properties of the piezoelectric component is of particular interest. This is likely to be more significant for air-backed devices where the vibration is not damped by a backing layer.

Secondly, when modelling a real system some consideration must be given to the generation of experimental results against which models can be compared and evaluated. For simplified systems the model may be compared with analytical solutions, but when field results are significantly different to an idealised case there is a need for experimental measurements on the real device. Consideration must then be given to what can be measured in practice, what the significant features of the system are for model comparisons, and under what range of operating conditions these will be obtained. Furthermore the comparison must be made with knowledge of how

accurate and repeatable they are. Another concern for experimental measurements relates to how much direct, as opposed to indirect, evidence they provide. Consider electrical response measurements. Both model and real electrical measurements can be used to provide data on the position of resonances. For a piezoelectric disc, electrical data will indicate the resonance frequency and a consideration of the dimensions and properties of the disc may enable the *type* of modal behaviour to be determined at a given resonance. It does not, however, give the actual vibrational behaviour of the disc at that frequency.

So far modelling difficulties have been discussed in terms of the complexity of real device behaviour and field response, and the practical issues of accurately specifying parameter values or results for model-experimental comparison. One thing that has not been considered is the difficulty of establishing effective modelling techniques to accurately simulate specific features of the system. Within this category is the necessity to simulate an unbounded fluid region. In reality medical ultrasound devices will operate into bounded domains, whether it be a patient or a tank of water. However a common feature of some experimental measurements is the simulation of radiation into an unbounded fluid region, to avoid the effects of reflections. Experimentally this can be achieved by time-gating, the use of absorbent materials, or by making measurements in large but finite regions. To generate comparative modelling conditions there is a requirement to model an unbounded fluid region – not a physical reality but a mathematical simulation. Ironically, modelling such a region is itself likely to introduce a number of difficulties that would not arise for simulation in a bounded region.

To summarise, the simulation of a real medical ultrasound transducer operating into an unbounded fluid region, and the generation of near-field pressure data is a substantial problem. Any model needs to accommodate realistic piezoelectric behaviour, complex structural interaction, fluid-structural interaction and the simulation of an unbounded surrounding fluid media. The model may well have a large number of ill-defined parameters. Simulations will need to account for highly

irregular source behaviour and substantial field variations occurring on a small scale. The modelled systems source and field behaviour is likely to be sensitive to device parameters. For practical reasons only a limited amount of experimental measurements can be generated for model evaluation so the features that most comprehensively describe the field must be established in advance. Some account must be taken of the accuracy and repeatability of these experimental measurements. It must also be recognised that different types of source behaviour may produce similar indirect results, such as electrical response data. In practical terms the model must run relatively quickly, both to determine the electrical response of the system and so that a large number of models can be run for an analysis of model parameters.

1.4.2 Modelling options

Currently, device design often uses prototyping based on 1-D simulations such as equivalent electric circuit models. Such models use equivalent mechanical/electrical relationships to simulate the interaction between device components and the exterior media. They are restricted to 1-D behaviour only. As such they cannot account for the response of real piezoelectric elements or the complex behaviour due to the finite extent of components in the transverse direction. Such models can predict only axial field results and cannot therefore generate a comprehensive picture of the real near-field. They are, however, simple, cheap and quick to use. They can accommodate both the electrical and mechanical behaviour of the device in one model and accurately predict the position in the frequency domain of the main resonance of a device. In the case where the device operates in a manner close to the 'ideal' case they can generate reasonably accurate output. Such techniques have previously been successfully applied to the simulation of medical ultrasound devices, for example in Capineri et. al. (1993), and Wu & Chen (1999). Furthermore, some work has been approached on the issue of improving realistic device designs, eg. Lamberti et. al. (1997) and Turo et. al. (1999). From such work it can be seen that simplified 1-D models can be used effectively to direct *some* design features of *some* devices, however they have serious limitations.

A second modelling technique that has been used successfully in some problems of radiating structures is the finite difference method (FDM). The FDM can be a very effective and efficient technique for the propagation of acoustic fields, particularly when the system is time-dependent. FDM only requires a limited amount of earlier-time information to propagate a waveform, as compared to say, the finite element method (FEM) where the entire solution domain is solved at each time step. Unfortunately at this time there does not appear to be any effective FDM option for modelling complex structural behaviour such as that of realistic piezoelectric components. As a technique in itself the FDM is not appropriate for the type of system considered here, however the combined use of an alternative technique for modelling the structure and the FDM for modelling the propagating field is an option.

1.4.3 The finite element method

A modelling approach that has been adopted for some acoustic simulations and which can accommodate a number of features that 1-D modelling cannot, is the finite element method. Using FEM a continuous system is approximated by a segmented one containing a finite number of points. Appropriate loads and conditions are then applied to the segmented system and the response calculated. The response at the discretised points is then taken as the approximate response of the real system. FEM has its origins in the area of structural analysis by engineers. Semi-discrete systems such as frameworks were ideally suited to a segmented approximation by a finite number of points. From this came the approximation of more obviously continuous systems such as plates and 3-D structures. The use of FEM has grown and expanded considerably over the last forty years. The solution of large systems of simultaneous equations, which is essentially what FEM involves, is ideally suited to solution by computer and so the method has been aided by rapid improvements in computing capabilities. The technique is now applied to a wide range of systems and complex engineering problems (Cook, 1995; Desai, 1979).

FEM, along with the boundary element method (BEM), can accommodate all the features of the system under consideration here and outlined in section 1.4.2. Firstly FEM is well established for modelling complex structural behaviour. Secondly, the effective simulation of real piezoelectric components can be incorporated into a FEM package relatively easily. This is illustrated by the disc model response shown in Figure 1.2 which was generated by FEM. Thirdly, some packages have the capability of simulating acoustic regions and fluid-structural interactions. And fourthly, there are a number of options available in FEM and BEM for the simulation of unbounded fluid regions. In addition there are practical considerations such as the fact that many FEM packages can run on standard PCs and are relatively affordable. Furthermore, improving computing capabilities are likely to allow larger and more complex simulations to be approached. For these reasons FEM has been chosen as the modelling technique to be employed here.

Finally, some mention must be made to the specific FEM package used here. PAFEC, manufactured by SER Ltd., incorporates piezoelectric elements, acoustic elements, fluid-structural interaction, and several "infinite" fluid region options. In addition, the developers of PAFEC were willing to work in conjunction with both the Department of Physics at Bath and the Centre for Mechanical and Acoustical Metrology at the National Physical Laboratory (NPL) to improve and adapt software where required. PAFEC has been used for the simulation of radiating systems before, for example Macey (1996), Macey (1996) and Morgan et al (1999). However, to the author's knowledge, it had not been applied to realistic medical ultrasound devices and fields.

1.4.4 Restrictions of the modelling presented here

The work considered here is concerned with the steady-state harmonic response of a system excited at a single frequency. The system(s) to be considered will assume circular symmetry and all applied forces will be axi-symmetric. The structure is assumed to behave in a linear elastic manner. All materials, with the exception of the piezoelectric element, are assumed to be isotropic. Furthermore, all material

properties are assumed to be constant with frequency. The fluid is assumed to be homogeneous, isotropic and perfectly elastic. No dissipative effects are accounted for. Only acoustic waves of relatively small amplitude are considered so that linear propagation is assumed. All of these assumptions simplify the modelling requirements and are of practical significance in terms of making simulations and analyses feasible. The modelling techniques and conclusions drawn here are still, however, applicable to a large range of realistic ultrasound systems. Furthermore, the fact that the system under consideration here is assumed to be axi-symmetric does not mean that the techniques used cannot be applied to non-symmetric systems.

1.5 Aims

The main aim of this work is to assess the effectiveness of FEM for modelling the behaviour of realistic ultrasound devices of a type used in medical applications, and the subsequently generated near-field acoustic region. The issues raised in section 1.4.3 suggest that FEM has the capability for the successful simulation of such a system, however to date relatively little work has been carried out in this area. At least part of the reason for this are the modelling considerations outlined in section 1.4.2. The simulation of such a system requires consideration of a number of complex modelling problems and modelling techniques to be applied *simultaneously.* Furthermore a number of practical issues, in particular long run times, are likely to complicate any analysis. The work presented here will investigate the main issues related to modelling such a system. Consideration will be given to which modelling techniques are appropriate, the difficulties of modelling such a system and what approaches can be adopted for a successful, practicable simulation. The features of such a system that are likely to require detailed analysis, and those that are likely to be of little significance to model output will also be considered. The intention here is to establish appropriate techniques to generate an effective model and to outline how such a task should be approached.

1.6 Thesis layout

This chapter has introduced the basics of ultrasound transducers used in medicine and the nature of the field due to such devices. Consideration has been given to the need for modelling ultrasonic transducers and the difficulties in doing so. A number of modelling options have been described and reasons for choosing FEM given. The basics of FEM have been outlined and the aims of this work described.

Chapter 2 will consider FEM in more detail and seek to establish that the technique does indeed have the capability of modelling real, high frequency devices and fields. An overview of each of the steps in the technique will be given. In conjunction with detailed FEM examples in Appendix 1, simple acoustic examples will be used to show how analyses progress. Some consideration will be given to how FEM accommodates dynamic structural behaviour, realistic piezoelectric components, fluid-structural interaction, finite acoustic regions, and the simulation of unbounded fluid regions. Examples of FEM and BEM simulations of systems similar to those considered here will be discussed.

Having established that the necessary modelling techniques are available, consideration will move on to the specific modelling approach adopted here. Chapter 3 will consider a number of problems that were encountered when an initial attempt was made to model such a system. To overcome some of these issues a physiotherapy transducer was designed and built. Details of this and the corresponding device model are presented here. The experimental measurements made on the device are also reported. These includes those made in accordance with IEC standards on physiotherapy devices and additional measurements aimed at generating a more comprehensive picture of the near-field of the device for comparison with models. The difference between the measured data and idealised 1-D predictions is emphasised.

It will be discussed in Chapter 3 that before model-experimental comparisons could be made, some detailed consideration had to be given to the effective modelling of an unbounded fluid region. This is considered in Chapter 4. Here model results for idealised sources are compared against analytical results. Firstly an analysis of the use of "infinite" wave envelope elements (WEEs) is presented. The large number of parameters involved in a WEE analysis and the lack of references in the literature to similar work on large *ka* sources make a detailed explanation of these elements necessary. The intention is to establish the significance of the parameters in such a model with a view to establishing how they can be used most effectively. It will be seen that simulation run times and memory requirements are high for WEE models. Alternative "infinite" fluid region modelling options are therefore sought and two BEM options, CHIEF and DAA2c considered. Some description of these methods is given here. Comparison is then made for all three fluid-modelling options against analytical results for three idealised sources operating at three frequencies. Conclusions are drawn with respect to the modelling of unbounded regions, options and practical considerations.

Chapter 5 follows by combining the structural model with the fluid model to generate a combined model of the physiotherapy transducer operating into an unbounded fluid region. Firstly a model-to-model comparison is made for the device operating into each of the fluid options. Similar conclusions are drawn to those in Chapter 4. Model-experimental comparison follows for the near-field measurements given in Chapter 3. In general good agreement is observed however where comparability is poor the potential reasons for this are discussed.

Chapter 6 seeks to extend the model-experimental comparisons made in Chapter 5 by analysing the parameters in the model – and therefore the real device. There are two reasons for this. Firstly to improve upon model-experimental comparison by investigating two potential sources of discrepancies – differences between the components in the model and in the real device, and differences in the modelled and realistic parameters. Secondly is the desire to investigate the significant parameters in

the model and their impact on the generated field. It will be seen that a comprehensive analysis of model parameters is beyond the scope of this work. This is mainly due to the practical limitations of running a substantial number of models with varying parameters but is also due to some extent to the difficulty of making conclusive model-experimental comparisons for some measurements. However some consideration of how sensitive the behaviour of the device and field are to the model parameters is made. The potential for improved model-experimental comparability is also discussed.

Finally Chapter 7 summarises the conclusions that may be drawn from this work. There is a comprehensive discussion of the modelling approaches that have been adopted, the techniques that have been investigated, the measurements used for model evaluation and the results of the analyses that have been performed. This is followed by a brief summary of the specific conclusions that can be drawn here. In addition a number of areas are considered where the work outlined here might be extended and other areas that might benefit from the application of the techniques employed here.

1.7 Summary

This chapter is intended as an introduction to the subjects of medical ultrasound devices and their fields. The features of such systems and the difficulties of modelling them effectively have been discussed. Having proposed FEM as having the potential for modelling a real device and field, Chapter 2 will consider FEM in more detail. The governing equations and formulations that can describe a realistic medical ultrasound piezoelectric device radiating into an unbounded fluid region will be considered. Reference will also be made to previous works where the simulation of related systems has been considered before. The modelling approach adopted here for simulating a real system be outlined in Chapter 3 and models of the device and surrounding fluid region will follow.

Chapter 2

2.1 Introduction

The work presented in this thesis looks at the use of FEM and BEM for modelling medical ultrasound transducers and their fields. The first chapter considered the design of transducers and the nature of the near-field due to such devices, as well as the issues relating to modelling such a system. In particular it was considered why FEM is appropriate here. This chapter will attempt to give a comprehensive but concise overview of FEM and BEM and the issues and techniques involved in formulating and solving a finite element (FE) analysis. Some discussion of how these techniques have been applied elsewhere to the types of system considered here will also be presented. Subsequent chapters will consider the use of FEM and BEM in the simulation of a real medical ultrasonic device and the simulation of unbounded acoustic regions. In conjunction with the examples given in this chapter the same examples are progressed in Appendix 1 but include substantially more detail at each stage of the solution process.

2.2 The finite element method

When a direct solution to a problem is not feasible, some approximate numerical technique is employed. Here the problem is the response of a fluid-structure system to some forcing conditions, and the approximate technique to be considered is FEM. FEM approaches a solution by breaking the system down into a number of smaller segments (elements), each of which is represented by a finite number of points (nodes). The original system containing an infinite number of points is therefore approximated by a segmented system containing a finite number of points. Any individual parameter that may vary at a given node is known as a degree of freedom (d.o.f.). A node where a structure can displace in only the x and y directions, say, would therefore have 2 d.o.f.s at each node. Appropriate causes and conditions are

then applied to this segmented system. The response calculated at nodal points is taken as the approximate response of the real system.

What follows is a fairly rigorous outline of the processes involved in a FE analysis. There are numerous texts available on this subject (Zienkiewicz & Taylor, 1989; Desai, 1979; Cook, 1995). Ihlenburg (1998) further gives a very good overview of many features of FEM and BEM for dynamic systems with a surrounding fluid region. Still some detailed explanation should prove useful here. It will be seen that a number of mathematical techniques may be employed in any individual FE analysis. Variational calculus or weighted residual techniques are used in the formulation of the equations that define an element and its potential response to applied forcing. Gauss quadrature techniques are used for numerical integration on terms appearing in element formulations. A number of matrix manipulation techniques may be used. These include re-numbering of nodal d.o.f.s to reduce the size of non-zero diagonals in global matrices, 'banded storage formulations' so that non-zero terms do not have to be retained, and re-adjustment of matrix components to reinstate symmetry - again to reduce storage and calculation requirements. Also Gaussian elimination and other such techniques are employed for the solution of the large systems of simultaneous equations that describe the modelled system. Any detailed exploration of such methods is beyond the scope of the work presented here. Further details are available from a number of references such as Zienkiewicz (1971), Desai (1979), or Cook (1995). The explanations given here and in Appendix 1 should clarify how some of these techniques are employed in FEM.

2.2.1 Approach to a finite element analysis

The first consideration in FEM is how to discretise the system into smaller, more manageable elements. The questions of how many elements, the geometric shape of those elements and the number of nodes in an element are partly problem dependent and partly a question of balancing solution accuracy with the complexity and solution time of the approximation. When approaching a problem for the first time it is

advisable to follow any guidelines relating to similar problems whilst being aware that the discretisation process is likely to require regular reassessment. Consider, for example, Figure 2.1 due to Cook (1995). This shows a plate segmented into several elements, with a restraint enforced along A-E and a point force at C. Various element geometries and mesh intensities are used throughout the solution domain of the plate. It should be pointed out that this is by no means either a typical discretisation or an optimal approach. However this example shows that certain features, such as the geometry of the solution domain and areas where the response of the system is likely to be most or least extreme must be considered *in advance* to direct the discretisation process initially.

One point to be emphasised with FEM is that the solution of the modelled system is solved in its entirety by consideration of all features of the system *simultaneously*. For example, a structure radiating into a fluid might involve the dynamic behaviour of the structure in response to a forcing function, the interaction with/loading due to the fluid, acoustic radiation into the fluid, and boundary conditions such as structural restraints. The system is solved for all of these conditions simultaneously, so that although consideration may be given here to individual elements the simulation will only be effective once all features have been included.

2.2.2 Interpolating polynomial

Having made an initial discretisation of the system, consideration is given to how the *system* is expected to respond to applied conditions. This is another fundamentally important point in FEM. An educated choice must be made *in advance* of how the system is expected to respond. It follows from this that the modeller must possess some knowledge of the system under consideration, as well as a certain degree of insight into the expected results of the analysis. The response of the system can be considered in terms of how a particular sub-domain of the system, or element, is likely to respond. Another feature of FEM is that the solution is generated initially only at nodal points – although post-processing may involve interpolation to generate

values elsewhere within an element. In accordance with this, the analyst seeks to express the variation of the unknown, $h(Q)$, at a point Q in the solution domain of the element, *in terms of the unknown only at nodal points*. For the two-dimensional element shown in Figure 2.2a this can be expressed as (Ellis, 1994)

$$h(x,y) = \underline{N}(x,y)\underline{h} \ . \qquad (2.1)$$

Here $\underline{h}$ is a 4-term column vector containing the values of the unknown h at the 4 nodes. $\underline{N}$ is a 4-term row vector termed the vector of shapes functions or *basis* vector relating the values of the unknown anywhere in the solution domain of the element, $h(x,y)$, to the value of the nodal unknowns. $\underline{N}$ can be expressed as $\underline{N}(x,y) = [N_1, N_2, N_3, N_4]$.

A common approach to establishing such a relationship is to seek the unique polynomial that fits the nodes of an individual element. Lagrange interpolation techniques are frequently used to find a unique n^{th} order polynomial that passes through a set of data points (x_i, h_i), i=0, 1, 2,..., n. In two dimensions this polynomial takes the form

$$h = \sum_{i=0}^{N} L_j(x).L_k(y)h_i \qquad (2.2)$$

where j=0, 1, 2,..., n, k=0, 1, 2,..., m and N=nm. Also n is the number of points in the x direction and m the number of points in the y direction. Comparing Equations 2.1 and 2.2 it can be seen that $N_i(x,y) = L_j(x).L_k(y)$. So the vector of shape functions, $\underline{N}$, is dependent on both the geometry of the element under consideration and the number of nodes defining that element. The same principles applied here can be used to generate the shape functions for any FE.

2.2.3 Local co-ordinates

A relationship between the unknowns within the element and the unknowns at the nodal points has now been established, however this particular formulation for $\underline{N}$ is dependent on the position of the element. It is desirable to have a formulation for $\underline{N}$ that is not position dependent, in this example one that is appropriate for a generic linear 4-node quadrilateral element. Such a basis vector can be generated through the use of a local co-ordinate system. One such co-ordinate system uses a parent element defined in local co-ordinates ζ and ξ over the domains [-1,1] and [-1,1], as shown in Figure 2.2b. It will be seen that the integration of functions of the basis vector is a common part of FE analysis. Not only does the local co-ordinate system allow for the determination of a generic element basis vector, but the numerical integration of such functions is also made simpler by the definition of an element over the domains [-1,1] and [-1,1].

A *linear* transformation in both co-ordinate directions for Figure 2.2 can be expressed as

$$\zeta = \frac{2}{\alpha}(x - x_{mid}) \qquad (2.3a)$$

$$\text{and} \quad \xi = \frac{2}{\beta}(y - y_{mid}) \quad . \qquad (2.3b)$$

Using the same Lagrange interpolation technique as outlined in section 2.2.2, a basis vector expressed in local co-ordinates, $\underline{N^L}$, can then be generated giving a relationship

$$h(\zeta,\xi) = \begin{pmatrix} N^L{}_1 & N^L{}_2 & N^L{}_3 & N^L{}_4 \end{pmatrix} \begin{pmatrix} h_1 \\ h_2 \\ h_3 \\ h_4 \end{pmatrix} \quad . \qquad (2.4)$$

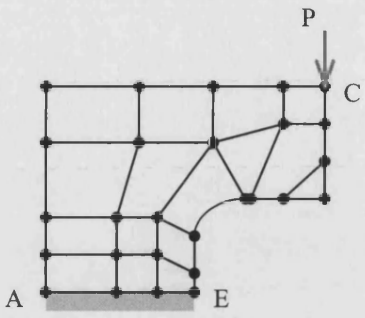

Figure 2.1 Example of the discretisation of a system due to Cook (1995).

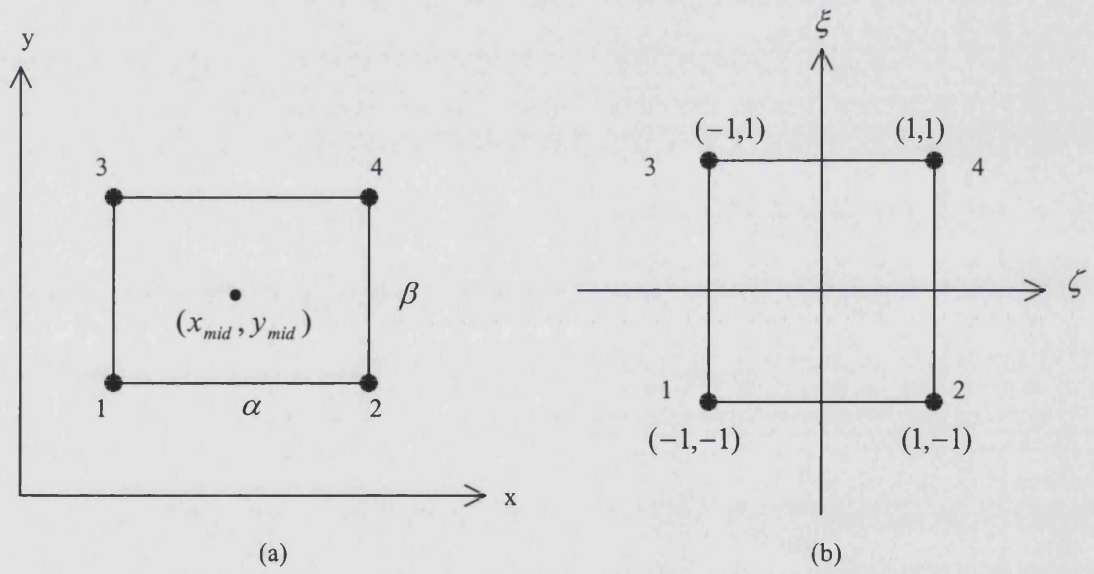

Figure 2.2 Geometry of (a) a 2-D quadrilateral element, and (b) the mapping of this 2-D quadrilateral element from global to local co-ordinates.

Any integration over the domain of the element can therefore be performed in local co-ordinates. It will be seen in section 2.2.5 how the transformation from global to local co-ordinates is applied in practice.

2.2.4 Governing equations

The response of the unknown within an element with respect to the unknown nodal values has been considered. Now the fundamental equations that actually govern the behaviour of the element must be determined. Clearly the types of element that are used is problem dependent and numerous types of element have been developed to simulate the behaviour of various systems. Examples include 2-D 'plate' elements allowing in-plane x and y direction displacement as well as xy shear displacement, and acoustic elements with a single pressure d.o.f. per node.

Fundamental relationships defining the behaviour of the system over a given domain are employed to generate the equations governing the behaviour of an element. Consider the problem of generating an acoustic element. The Helmholtz wave equation governing acoustic propagation in 3-D space for the steady-state case where the system responds harmonically, was introduced in chapter 1, Equation 1.3:

$$\nabla^2 p + k^2 p = 0 \ . \quad (1.3)$$

Generally the 'fundamental' equations are arranged in such a way as to be expressed in terms of the primary unknown in the analysis. Here this is already the case as the primary unknown is pressure.

2.2.5 Element equations

Having established the equation(s) that define the behaviour of a specific part of the system under analysis, there are primarily two techniques that are used to generate the equations that govern the response of an element. These are variational methods and

residual methods. As previously mentioned the detailed consideration of such techniques is beyond the scope of this work. However, continuing with the example of the generation of an acoustic element, the Galerkin weighted residual method will be employed here to indicate how element equations can be formulated.

Equation 1.3 defines the response of the primary unknown, pressure, within an acoustic element, for which an approximate solution is required. The residual technique now proceeds as follows:

- A trial function, p', is proposed as an approximation to the exact solution p.
- Expressions for the differences between the equations defining the behaviour of the pressure in the exact and trial cases are generated. This difference is the residual. Here this is simply the difference between equations in p and p' for the single Equation 1.3.
- Residuals are now minimised. This minimisation process "forces" the residual to be zero thus making the trial solution p' equal to the exact solution p. It is this minimisation process that generates the equations defining the behaviour of an element which are subsequently solved for the primary unknown(s).

It will now be reiterated that when solving a problem by FEM the whole system is solved simultaneously. The response of the single acoustic element considered here is governed only by the Helmholtz wave equation. When this element is part of a system there will be other equations governing the behaviour of other elements, as well as a number of boundary conditions. Boundary conditions both restrict the response of the system to specific conditions and also express 'natural' conditions across elements. All such features combined govern the response of the system leading to a series of equations for which the residual method would be applied. The minimisation of all of these equations simultaneously generates a system of equations that can be solved to approximate the response of the entire system. Here the residual technique will be applied only to a single element governed by Equation 1.3.

Of primary importance for the residual technique is the choice of trial function p'. In the Galerkin method it is proposed to be of the form

$$p' = \sum_{i=1}^{n} q_i N_i \quad . \qquad (2.5)$$

Here N_i are the *known* functions, q_i are *unknown* coefficients and i=0, 1, 2,..., n. Comparing Equations 2.5 with 2.1 it can be seen that taking the N_i as elements of the known basis vector $\underline{N}$, the values of the n nodal unknowns are given by q_i.

The expression for the residual R for Equation 1.3 is

$$R = \nabla^2 p' + k^2 p' \quad . \qquad (2.6)$$

Minimisation can be expressed as (Desai, 1979)

$$\int_D R(\psi).W_i(\psi)dD = 0 \qquad (2.7)$$

where D is the domain of the system under consideration and the W_i are weighting functions, i=0, 1, 2,..., n. For a 3-D problem this gives a system of n equations defined over the domain of the element, V:

$$\iiint_V \left(\nabla^2 p' + k^2 p'\right) W_i dV = 0 \qquad i=0, 1, 2,..., n. \qquad (2.8)$$

Applying the divergence theorem to the first term in the integral to reduce the system to first order and re-writing, (Eaton & Regan, 1996; Astley et. al., 1998):

$$\iiint_V (\nabla p' \cdot \nabla W_i) dV - k^2 \iiint_V p' W_i dV = \iint_S W_i \left(\frac{\partial p'}{\partial n} \right) dS \quad . \qquad (2.9)$$

The term on the right-hand side of Equation 2.9 is a surface integral representing the boundary conditions over the surface of the system, in this case the surface of the element with domain V. Here n is a normal co-ordinate. The element equations can be written

$$[\Delta \boldsymbol{K} - \omega^2 \Delta \boldsymbol{M}] q = \Delta f(\omega) \qquad (2.10)$$

where $\Delta \boldsymbol{K}$ and $\Delta \boldsymbol{M}$ can be described as (frequency independent) *element* matrices, and q is a vector of the primary unknowns at the elemental nodal points – in this case pressure. $\Delta f(\omega)$ is the (frequency dependent) element load vector, and is used to apply a forcing function (boundary condition) to the element. Typically this might involve the stipulation of the outward normal velocity, v_n at specific nodes. The relationship relating normal pressure to normal velocity can be described as (Cremers et. al., 1994; Astley et. al., 1998),

$$\frac{\partial p}{\partial n} = -i\omega\rho v_n \quad . \qquad (2.11)$$

It is standard practice with the Galerkin technique to make the weighting functions, W_i, equal to the basis functions N_i. The terms in Equation 2.10 are then given by

$$\Delta \boldsymbol{K}_{ij} = \iiint_V (\nabla N_i \cdot \nabla N_j) dV \quad , \qquad (2.12a)$$

$$\Delta \boldsymbol{M}_{ij} = (1/c^2) \iiint_V N_i N_j dV \qquad (2.12b)$$

$$\text{and } \Delta f_i = -i\omega \iint_S \rho N_i v_n dS \quad . \qquad (2.12c)$$

2.2.6 Formulation of element matrices

To outline how such a system of equations would be formulated and solved in practice, consider now a simple example based on the use of 2-D, 4-noded quadrilateral elements as shown in Figures 2.2a and 2.2b. In local co-ordinates the element matrices $\Delta \boldsymbol{K}$ and $\Delta \boldsymbol{M}$ are of the form

$$\Delta \boldsymbol{K}_{ij} = \int_{-1}^{1}\int_{-1}^{1} \left[\left(\frac{4}{\alpha^2}\right)\frac{\partial N^L{}_i}{\partial \zeta}\frac{\partial N^L{}_j}{\partial \zeta} + \left(\frac{4}{\beta^2}\right)\frac{\partial N^L{}_i}{\partial \xi}\frac{\partial N^L{}_j}{\partial \xi}\right]\left(\frac{\partial(x,y)}{\partial(\zeta,\xi)}\right) d\zeta d\xi \qquad (2.13a)$$

$$\text{and } \Delta \boldsymbol{M}_{ij} = \left(\frac{1}{c^2}\right)\int_{-1}^{1}\int_{-1}^{1} N^L{}_i N^L{}_j \left(\frac{\partial(x,y)}{\partial(\zeta,\xi)}\right) d\zeta d\xi \qquad (2.13b)$$

where $\left(\frac{\partial(x,y)}{\partial(\zeta,\xi)}\right)$ is the Jacobian of the transformation from global to local co-ordinates. This enables the integrals to be calculated over the domain of the local co-ordinates. Here $\left(\frac{\partial(x,y)}{\partial(\zeta,\xi)}\right) = \frac{\alpha\beta}{4}$. These terms are expressed in a manner ideal for numerical integration by a technique such as Gaussian Quadrature. In 2-D this takes the form (Ellis, 1994):

$$\int_{-1}^{1}\int_{-1}^{1} f(\zeta,\xi)\,d\zeta d\xi = \sum_{i=1}^{n}\sum_{j=1}^{n} w_k w_l f(t_k, t_l) \qquad (2.14)$$

where w_k are weighting factors in the range 0 to 1, and t_k are quadrature points in the range –1 to 1. For four point quadrature, as here, n=2 and these values are given as

$$t_k = \pm\frac{1}{\sqrt{3}} \quad \text{and} \quad w_k = 1$$

In fact this four-point scheme in 2-D agrees with the exact integral as it integrates up to the third power of the independent variable in each co-ordinate direction (Ellis, 1994). Either directly, or by quadrature as above, the element stiffness and mass matrices can then be calculated.

2.2.7 Formulation and solution of system matrices

Consider now Figure 2.3 showing a 2-D system of four such linear quadrilateral elements of unit side length joined together. *Element* stiffness and mass matrices can be calculated from Equations 2.13a and 2.13b and an equivalent *system* equation

$$[\boldsymbol{K}-\omega^2 \boldsymbol{M}]\, q = f(\omega) \qquad (2.15)$$

assembled element by element. This now expresses the *potential* of the system. How the system responds to given conditions is dependent on the boundary conditions applied to it, such as the forcing functions at particular nodes or the specification of pressure values at specific nodes. For example a force applied at the central node 5 only is equivalent to an infinitesimally small, infinitely long cylindrical source at the centre of the system and is the 2-D equivalent of a 3-D point source problem. For the case where the wave number, k=1, and $[f(\omega)]^T = (0,0,0,0,4,0,0,0,0)$, assembly of all of the terms in Equation 2.15 gives:

$$\left(\frac{1}{6}\right)\begin{bmatrix} 4 & -1 & 0 & -1 & -2 & 0 & 0 & 0 & 0 \\ -1 & 8 & -1 & -2 & -2 & -2 & 0 & 0 & 0 \\ 0 & -1 & 4 & 0 & -2 & -1 & 0 & 0 & 0 \\ -1 & -2 & 0 & 8 & -2 & 0 & -1 & -2 & 0 \\ -2 & -2 & -2 & -2 & 16 & -2 & -2 & -2 & -2 \\ 0 & -2 & -1 & 0 & -2 & 8 & 0 & -2 & -1 \\ 0 & 0 & 0 & -1 & -2 & 0 & 4 & -1 & 0 \\ 0 & 0 & 0 & -2 & -2 & -2 & -1 & 8 & -1 \\ 0 & 0 & 0 & 0 & -2 & -1 & 0 & -1 & 4 \end{bmatrix}\begin{bmatrix} q_1 \\ q_2 \\ q_3 \\ q_4 \\ q_5 \\ q_6 \\ q_7 \\ q_8 \\ q_9 \end{bmatrix} -$$

$$\omega^2\left(\frac{1}{c^2}\right)\left(\frac{1}{36}\right)\begin{bmatrix} 4 & 2 & 0 & 2 & 1 & 0 & 0 & 0 & 0 \\ 2 & 8 & 2 & 1 & 4 & 1 & 0 & 0 & 0 \\ 0 & 2 & 4 & 0 & 1 & 2 & 0 & 0 & 0 \\ 2 & 1 & 0 & 8 & 4 & 0 & 2 & 1 & 0 \\ 1 & 4 & 1 & 4 & 16 & 4 & 1 & 4 & 1 \\ 0 & 1 & 2 & 0 & 4 & 8 & 0 & 1 & 2 \\ 0 & 0 & 0 & 2 & 1 & 0 & 4 & 2 & 0 \\ 0 & 0 & 0 & 1 & 4 & 1 & 2 & 8 & 2 \\ 0 & 0 & 0 & 0 & 1 & 2 & 0 & 2 & 4 \end{bmatrix}\begin{bmatrix} q_1 \\ q_2 \\ q_3 \\ q_4 \\ q_5 \\ q_6 \\ q_7 \\ q_8 \\ q_9 \end{bmatrix} = \begin{bmatrix} 0 \\ 0 \\ 0 \\ 0 \\ 4 \\ 0 \\ 0 \\ 0 \\ 0 \end{bmatrix} \qquad (2.16)$$

Equation 2.16 can be easily solved by some Gaussian elimination technique to generate results for the pressure values at the 9 nodes.

A few points about the above system of equations are worth some mention. Firstly, the *system* matrices are themselves symmetric. This is clearly to be expected as the interaction between, say, nodes 2 and 6 is obviously the same as that between nodes 6 and 2. Secondly, there are entries in the system matrices only at positions where the row/column reference relates an interaction between nodes. If there is no direct relationship between the nodes, i.e. they do not have a common element, then there is a zero in the corresponding position. Thirdly, a number of the entries in the matrices are zero, a feature common to FE problems. Finally, the matrices are banded; that is, non-zero entries appear along the main diagonals with upper and lower 'triangles' containing zero entries only. These last two features are generally exploited for the purposes of reduction in matrix storage requirements. It is worth pointing out that the numbering of the nodes in the four-element problem of Figure 2.3 is optimal for the purposes of matrix storage requirements. Most FE packages employ optimal node-numbering routines as standard to best exploit banded matrices.

2.2.8 The use of symmetry

A final consideration here is the use of symmetry. Clearly the system shown in Figure 2.3 is symmetric about both the x and y (or ζ and ξ) axes. The requirement for symmetry along a specific line or plane is zero gradient, in this case $\frac{\partial p}{\partial n} = 0$. This is, in fact, the natural boundary condition for acoustic elements, so that no additional boundary conditions need to be included. Instead the problem can revert back to the format of Figures 2.2 with a forcing function term included at any node. Take, for example, $\Delta f_1 = 1$. This is the equivalent problem to the four-element case discussed in section 2.2.7. Note that in that case $\Delta f_5 = 4$, which in fact could be considered to be a result of unit contributions from each element. The resultant system of equations corresponding to Equation (2.16) is then

$$\left(\frac{1}{6}\right)\begin{bmatrix} 4 & -1 & -1 & -2 \\ -1 & 4 & -2 & -1 \\ -1 & -2 & 4 & -1 \\ -2 & -1 & -1 & 4 \end{bmatrix}\begin{bmatrix} q_1 \\ q_2 \\ q_3 \\ q_4 \end{bmatrix} - \omega^2 \left(\frac{1}{c^2}\right)\left(\frac{1}{36}\right)\begin{bmatrix} 4 & 2 & 2 & 1 \\ 2 & 4 & 1 & 2 \\ 2 & 1 & 4 & 2 \\ 1 & 2 & 2 & 4 \end{bmatrix}\begin{bmatrix} q_1 \\ q_2 \\ q_3 \\ q_4 \end{bmatrix} = \begin{bmatrix} 1 \\ 0 \\ 0 \\ 0 \end{bmatrix}. \qquad (2.17)$$

This gives the same nodal pressure values for nodes in similar positions to the 9-node example, with pressure values outside the 4-node system deduced from symmetry.

This completes the summary of FEM. This section has sought to explain how each part of the FE process works through the use of simple examples, and to consider how these individual parts combine for the solution of a modelled system. Clearly a system for which FEM is required will be considerably more complex than the problems considered here, nevertheless the solution of such a problem is based on the same principles.

In this section some detailed consideration has been given to acoustic elements. For the problem of an ultrasound transducer radiating into an infinite fluid medium a

number of other elements are required to approximate the real system. Some consideration will now be given to these elements.

2.3 Other types of element

Section 2.2 outlined the formulation and solution of a simple FE problem but the same techniques can be applied to larger systems, such as those considered here. The aim is to formulate and solve element and system equations of the form of Equations 2.10. On an element level, the difference between modelled systems is in the generation of the systems of simultaneous equations. This is determined firstly by the fundamental equations that describe the behaviour of the system, i.e. element equations for different types of element, and secondly by the technique used to express these equations into a form suitable for solution – essentially variational or residual methods. In section 2.2 acoustic elements, described by the steady-state Helmholtz equation, were generated and the Galerkin weighted residual technique used to formulate an element relating the behaviour within an element to the behaviour at elemental nodes. For the systems considered here other types of element will be used.

The system to be modelled is that of a circularly symmetric ultrasound transducer radiating into an unbounded fluid media. Simulating this requires structural elements to model the transducer, piezoelectric elements for the active element and acoustic elements to model the fluid region close to the device. Specific elements for the simulation of an unbounded fluid region will be considered in section 2.4. The system modelled here is also understood to have circular symmetry, thus significantly reducing the size of the problem. The specific use of axi-symmetry in the system will therefore be considered. Specific details of element formulation for each of these types, including fundamental equations describing the element and the formulation of a set of simultaneous equations relating elemental response to elemental nodal response, can again be found elsewhere (Zienkiewicz & Taylor, 1989; Desai, 1979;

Cook, 1995; Allik & Hughes; 1970). Here an overview of these elements and system equations will be given.

2.3.1 Structural elements

FEM has its origins in structural analysis and modelling. The terminology of 'stiffness' and 'mass' matrices used for the element and system Equations 2.10, is in fact based on similar structural equations. Such equations describe the dynamic response of structures to applied forces, rather than the acoustic region considered in section 2.2. In section 2.2.4, the Helmholtz equation was used as the fundamental equation governing the response of a (steady-state) acoustic element. For a structural element the governing equations relate strain and displacement and stress and strain, so that the displacement of the elemental nodes - displacement here being taken as the primary unknown - can be derived for applied forces and conditions. For linear, elastic, isotropic materials the stress-strain relationship for an element can be expressed as:

$$\{\sigma\} = [C]\{\varepsilon\} \quad . \quad (2.18)$$

Here, $\{\sigma\}$ is a vector of elemental stresses, $\{\varepsilon\}$ a vector of elemental strains, and $[C]$ an appropriate stress-strain matrix containing material properties Young's modulus and Poisson's ratio. The nature of $\{\sigma\}$, $\{\varepsilon\}$ and $[C]$ is dependent on the type of element (dimensions, geometry, number of nodes) and assumptions made about the response of the element. The strain-displacement relationship can be expressed as:

$$\{\varepsilon\} = [B]\{d\} \quad (2.19)$$

where $[B]$ is the appropriate strain-displacement matrix and $\{d\}$ a vector of nodal displacements. Similarly the nature of $[B]$ and $\{d\}$ is dependent on the nature of the element and restrictions on the response of the element. As in Equation 2.1, the

unknowns within an element (here displacements *d(x,y)* in 2-D) are related to nodal displacements through the (structural) vector of shape functions $[N_S]$:

$$d(x,y) = [N_S]\{d\} \quad . \qquad (2.20)$$

2.3.2 Dynamic harmonic response

For a structure approximated by FEM, driven by a load vector $\{R\}$, and with stiffness, damping and mass matrices [*K*], [*D*] and [*M*] respectively, the governing equation of structural dynamics is given by (Cook, 1995; Kinsler et. al., 1982)

$$[K]\{d\} + [D]\{\dot{d}\} + [M]\{\ddot{d}\} = \{R\} \quad . \qquad (2.21)$$

Here $\{R\}$ is time-dependent. For the steady-state harmonic case, as considered here, Equation 2.21 becomes

$$[K + i\omega D - \omega^2 M]\{d\} = \{f(\omega)\} \quad . \qquad (2.22)$$

Note the similarity with Equation 2.15 except for the additional damping in the system here. It is necessary to include damping so that the response of the system does not become infinite when ω corresponds to a natural frequency of the system (PAFEC, 1984). In PAFEC damping can be incorporated in structural models in the form of "hysteretic" damping terms. This is a mathematical technique that makes material moduli complex, eg. for Young's modulus, *E* (PAFEC, 1984)

$$\overline{E} = E(1 + \bar{i}\mu) \quad . \qquad (2.23)$$

The over-bar is taken to represent complex terms. The system stiffness matrix $[K]$ includes material moduli terms so the hysteretic damping term can be incorporated in the form of a complex stiffness matrix. Equation 2.22 can then be given as

$$[\overline{K}' - \omega^2 M]\{d\} = \{\bar{f}(\omega)\} \qquad (2.24)$$

where $\overline{K}'$ represents the complex stiffness matrix incorporating hysteretic damping.

2.3.3 Axi-symmetry

Axi-symmetry can easily be incorporated into the formulation of planar FEs, for a solid of revolution where the loading is also axi-symmetric. For a structural analysis the displacements in an axi-symmetric problem are still within the plane and can therefore still be accounted for by two components of displacement. The difference occurs in the stress and strain vectors, $\{\sigma\}$ and $\{\varepsilon\}$ respectively in Equations 2.18 and 2.19, and appropriate stress-strain and strain-displacement matrices $[C]$ and $[B]$ respectively. For plane strain and plane stress problems the vectors contain three terms each, x, y, and xy shear stresses/strains. For the axi-symmetric case the stress and strain vectors each contain an additional term, "hoop" stress/strain. Accordingly matrices $[C]$ and $[B]$ incorporate the appropriate additional material relationships (PAFEC, 1984; Cook, 1995).

2.3.4 Fluid-structure coupling/interaction

For the case where fluid-structural interaction is significant in the system under consideration, as here, the forcing vector $\{f(\omega)\}$ in Equation 2.22 represents both fluid-structure interaction and all other external forces (Ergin, 1997; Matthews, 1986). Hence

$$[K + i\omega D - \omega^2 M]\{d\} = f^{(k)} + f^{(p)} \qquad (2.25)$$

where $f^{(k)}$ is a load vector of applied forces and $f^{(p)}$ is a load vector representing the fluid pressure at the fluid-structure interface. Combining Equation 2.25 with Equations 2.15 and 2.12c, describing the acoustic system matrices and nodal forcing

vector on the surface of an acoustic element (and extending this to the surface of the acoustic system) respectively, it can be shown that (Macey, 1987; Morand & Ohayon, 1995):

$$\begin{bmatrix} [K] & [\Omega]^T \\ [0] & [K_a] \end{bmatrix} \begin{Bmatrix} \{d\} \\ \{p\} \end{Bmatrix} + \begin{bmatrix} [M] & [0] \\ -[\Omega] & [M_a] \end{bmatrix} \begin{Bmatrix} \{\ddot{d}\} \\ \{\ddot{p}\} \end{Bmatrix} = \begin{Bmatrix} \{f\} \\ \{0\} \end{Bmatrix} \quad . \qquad (2.26)$$

Here $[K]$ and $[M]$ are the *structural* stiffness and mass matrices respectively, and $[K_a]$ and $[M_a]$ are the *acoustic* stiffness and mass matrices respectively. $[\Omega]$ represents the connection between the structural and acoustic systems and is given by

$$[\Omega] = \int_S [N]^T \underline{n}^T [N_S] dS \quad . \qquad (2.27)$$

Here $\underline{n}$ is the normal at a point and $[N_S]$ represents the structural shape-functions.

2.3.5 Piezoelectric elements

As introduced in the Chapter 1, piezoelectricity is a property of certain materials where there is a coupling between the mechanical and electrical properties of the material. The electro-mechanical relationship for linear piezoelectric materials can be expressed in the matrix form (Van Randeraat & Setterington, 1974; Allik & Hughes, 1970; Guo et al., 1992)

$$\{T\} = [c^E]\{S\} - [e]\{E\} \qquad (2.28)$$

$$\{D\} = [e]^T\{S\} + [\varepsilon^S]\{E\} \quad . \qquad (2.29)$$

Here $\{T\}$ is the stress vector, $\{S\}$ the strain vector, $\{D\}$ the vector of dielectric displacement, $\{E\}$ the vector of field strength, $[c^E]$ the elastic constant matrix for constant electric field, $[e]$ the piezoelectric stress coefficient matrix, and $[\varepsilon^S]$ the

matrix of permittivity of the medium at constant strain. Piezoelectric materials are anisotropic, therefore more complex expressions are necessary to describe the material properties of such elements. For example, the elastic constant matrix $[c^E]$, for an axi-symmetric linear piezoelectric element is of the form (Kagawa & Yamabuchi, 1976)

$$\begin{bmatrix} c_{33}^E & c_{13}^E & c_{13}^E & 0 \\ c_{13}^E & c_{11}^E & c_{12}^E & 0 \\ c_{13}^E & c_{12}^E & c_{11}^E & 0 \\ 0 & 0 & 0 & c_{44}^E \end{bmatrix}.$$

Here the first subscript refers to the direction of the strain and the second gives the direction of stress (Van Randeraat & Setterington, 1974). For the FE formulation of piezoelectric materials the electrical potential, ϕ, is simply incorporated as an additional degree of freedom in the vector of displacement unknowns at each node. This leads to a system of equations similar to Equation 2.24 of the form

$$\begin{bmatrix} [M_{dd}] & [0] \\ [0] & [0] \end{bmatrix} \begin{Bmatrix} \{\ddot{d}\} \\ \{\ddot{\phi}\} \end{Bmatrix} + \begin{bmatrix} [K_{dd}] & [K_{d\phi}] \\ [K_{d\phi}^T] & [K_{\phi\phi}] \end{bmatrix} \begin{Bmatrix} \{d\} \\ \{\phi\} \end{Bmatrix} = \begin{Bmatrix} \{f\} \\ \{Q\} \end{Bmatrix} \qquad (2.30)$$

where the subscripts refer to the displacement and/or electrical potential d.o.f. which a given matrix is related to. A number of papers have been published including details of the terms in Equation 2.30 and/or containing FEM-experimental comparisons of the *electrical response* of (modelled) piezoelectric elements with real components. These include Guo et. al., (1992), Allik & Hughes (1970), Ostergaard & Pawlak (1986), and Locke et. al. (1987). Furthermore a number of publications on the simulation of realistic piezoelectric transducers have also been published, incorporating piezoelectric FEs and showing good model-experimental agreement. Examples of this are given in section 2.5.

2.4 Modelling unbounded fluid regions

In reality no physical domain will extend to infinity, however it is sometimes useful to develop mathematical models where it is assumed that they do. One such case occurs here when making model comparisons with experimental measurements on a physiotherapy device in accordance with the IEC standard. In this case the tank in which most of the measurements are made is lined with acoustically absorbent material to avoid reflections. The region of the tank is then approximated as an unbounded region in the corresponding model.

A simple way of accounting for such an unbounded fluid region in FEM is to model up to some large distance where the influence of the radiating source is expected to be minimal. Alternatively some appropriate boundary condition can be applied at a boundary to reduce reflections from this surface (Wood, 1976; Astley, 1983; Astley & Eversman, 1983). These approaches suffer from two drawbacks. Firstly there is the difficulty of establishing what constitutes a sufficient distance at which some condition can be applied. Secondly there is the fact that in some cases boundary conditions would need to be applied at such a large distance from the source that the modelling of the fluid region would prove computationally expensive, if not prohibitive. A second approach is the use of BEM whereby the surface of the structure is meshed with elements that incorporate some fluid-structural relationship. The system is solved initially for the fluid-structural interaction, generating pressure and normal velocity results at the surface of the structure. The exterior problem can then be solved for individual points in the field by summing the contributions over the surface of the structure. This method will be considered in the section 2.4.2. A third commonly used technique is to employ some sort of "infinite" element that is used in conjunction with standard acoustic elements. This type of element incorporates both an exponential term and a decay term to approximate the features of outward travelling waves that decay with distance, thus simulating an unbounded fluid region.

2.4.1 Wave envelope elements

The type of "infinite" element used in PAFEC is the wave envelope element. To use these elements the region immediately surrounding the radiating structure is modelled with acoustic elements out to some position in the near-field. A single layer of WEEs is then applied at this boundary. The geometry of this is shown in Figure 2.4. The WEE incorporates an appropriate asymptotic decay term as well as wave-like variation to account for both zero pressure at large distances *and* the existence of exclusively outward-travelling waves, as indicated in Figure 2.5. The inclusion of an exponential term in the basis function of the element, of the form e^{-ikr}, provides the wave-like variation, whilst a polynomial in $1/r$ provides the decay term. The order of the polynomial in $1/r$ is dependent on the number of radial nodes included in the element, and will be seen to be very significant in terms of the effectiveness of the simulation. A mapping of the finite WEE onto an infinite region allows the pressure at the last radial node in the element to be defined as zero. This prevents reflections from the outer edge of the element thus ensuring that the wave within the element is outward travelling only. These are essentially the gross features of a WEE. A large number of parameters must be defined in a system using WEEs and there are a number of practical difficulties in using these elements for systems of the type considered here. For these reasons WEEs are considered in some detail in Chapter 4. This includes a detailed account of the formulation of the elements, which have undergone a number of changes from their origins as "infinite" elements.

The WEE has its origins in the work of Bettess (1977) and Bettess and Zienkiewicz (1977) who sought to accommodate unbounded solution domains within FE analysis. Their approach was to model the region close to the radiating source with standard acoustic elements and beyond this to introduce "infinite" elements at some boundary. At this time the emphasis was placed on generating elements that coincided with standard elements at their inner surface but radiate the wave-front outward and away from the source – like a non-reflecting boundary condition – so that an accurate solution could be obtained close to the source. It was not the intention to model the

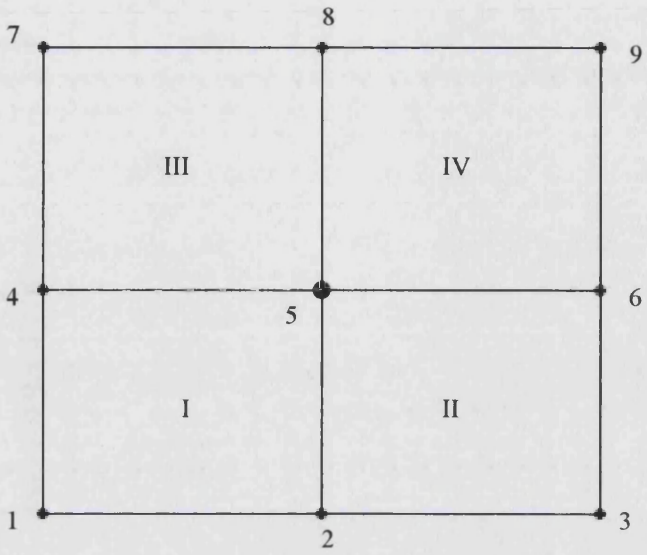

Figure 2.3 Four 2-D linear quadrilateral elements with a unit force applied at the central node, 5. Equivalent to an infinitesimally small, infinitely long cylinder.

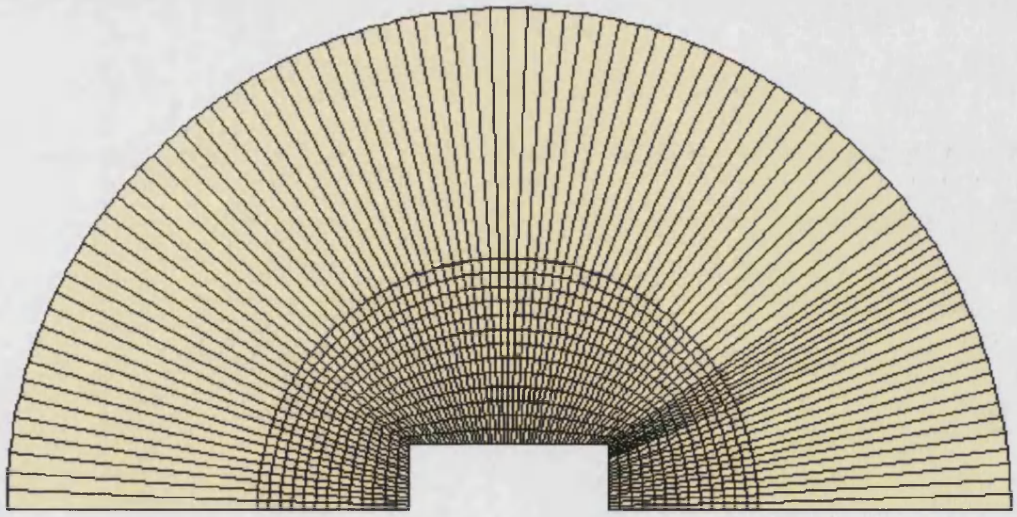

Figure 2.4 Typical geometry of a fluid-structural model incorporating WEEs. The structure (left blank here) is surrounded by acoustic finite elements up to some finite boundary. These elements are themselves then surrounded by WEEs incorporating outward-travelling, wave-like, decaying variation in pressure.

exact solution within the "infinite" elements (Burnett, 1994). Much subsequent work on infinite and WEEs has been based on adapting and improving on these early formulations.

Bettess (1977) suggested a shape function for an element based on standard Lagrange polynomials but incorporating an exponential decay term, with the element effectively extending to infinity. Problems arising from having to integrate over elements that contain nodes at infinity were avoided by making such terms relatively very large, but Gauss Laugerre numerical integration techniques were required to deal with the exponential term in the integral. Bettess and Zienkiewicz (1977) extended this to a shape function incorporating two exponential terms, one representing the wave shape and the other the decay of the wave with increasing distance, and used a specially designed approximate numerical integration technique to accommodate the exponential terms. Bettess (1980) reviewed this work and also considered a reciprocal as opposed to exponential decay term in the 'infinite' element shape function. In this case Gauss-Legendre numerical integration could be used although this required the definition of a new variable so that integration over the region $[-1,\infty]$ could be represented in terms of integration over [-1,1] as required by the numerical integration technique.

Astley and Eversman (1983) applied an alternative type of "infinite" element, the wave envelope element, to the problem of acoustic radiation. This had previously been used in other problems involving unbounded regions (Astley & Eversman, 1981). The WEE is used in a similar manner to the 'infinite' element in that it is compatibly matched to a region meshed by conventional FEs surrounding the radiating structure. There are however some differences in the element formulation and solution. Firstly, an amplitude decay of $1/r$ was used in conjunction with the standard wave-like variation, e^{-ikr}, where r was the distance from the source to the WEE/acoustic element interface. This meant that for large r the correct asymptotic behaviour of the pressure field was represented. Secondly, the weighting functions used in the integral generated for the minimisation of the residual in the Galerkin

formulation (see section 2.2.5), were selected to be the complex conjugates of the shape functions. This was in contrast to the standard choice of the basis function as the weighting function, which had been used in "infinite" element formulations up to that point. This choice eliminated the exponential terms in the integral so that standard Gauss-Legendre numerical integration could be used. Here the WEE shape function was defined in a finite region. Also in this work some comparison between the use of 'infinite' elements and WEE elements was made against theoretical results for an axi-symmetric plane piston source with $a = \lambda$, where a is source radius. Good agreement between theory and models was observed.

Zienkiewicz et al. (1983) improved on their "infinite" element by incorporating a new global-local mapping for the element domain. This mapped the global infinite domain onto a local finite one defined over the region [-1,1], making it ideally suited to solution by Gauss-Legendre techniques. Furthermore the mapping was such that the variation in the radial direction of the element, as usual described by a polynomial expression, became a series in powers of $1/r$. This allowed for a much better approximation of the real behaviour of the field variable actually within the "infinite" element, so that the use of higher orders of shape function for these elements would allow the finite/infinite element interface to be moved closer to the source. Bettess (1987) subsequently introduced this mapping into the WEE formulation of Astley (1983).

Astley et al. (1994) fully incorporated this mapping into the WEE formulation and made a change to the weighting terms in the residual formulation. Both of these measures taken together enabled the outer boundary of the element to be moved to infinity whilst maintaining bounded terms (i.e. those not involving calculations for a term explicitly expressed as being at infinity) in resulting system matrix formulations. It is this formulation that is used for WEEs in PAFEC and here, and is considered further in Chapter 4 with specific relevance to the type of systems modelled here.

2.4.2 The Boundary element method

The boundary element method is essentially a hybrid of the use of boundary integral equations and FEM. BEM involves expressing the equations that govern the behaviour of the system under consideration in terms of an integral over the surface of the system. Having done this, the surface of the system can be discretised, in the same way that the entire system might be discretised in a FE problem, and an approximate numerical solution sought to the integral problem. The technique is particularly useful in cases where an "infinite" region is to be modelled, as here. Only the surface of the radiating system needs to be considered initially with field values being calculated after the solution of the fluid-structural interaction problem at the boundary element (BE) surface. In practical terms this can make a significant difference to the number of d.o.f. in the modelled system, particularly for large systems. The combination of a structure modelled by FEM and a surrounding region modelled by BEM can easily be incorporated into the solution equations. The discretised pressure-velocity relationship of a boundary integral can be combined with similarly discretised force-displacement equations in a FE analysis. This system of equations can then be solved simultaneously (Ciskowski & Brebbia, 1991; Brebbia & Dominguez, 1989).

2.4.3 Classical formulation of the radiation problem

Interest in expressing the problem of a vibrating body of arbitrary geometry, radiating sound into an unbounded fluid medium as an integral formulation that could be solved numerically grew in the 1960s with the increased use of digital computers. The typical geometry of the problem as expressed by Schenck (1968) can be seen in Figure 2.6. Here an arbitrarily shaped object with total surface area S is immersed in an infinite fluid region R_0. The region interior to S is R_i. A point in the exterior region is designated by a lower-case Latin letter (e.g. x), one on the surface by a Greek letter (e.g. ψ), and one in the interior by an upper-case Latin letter (e.g. X).

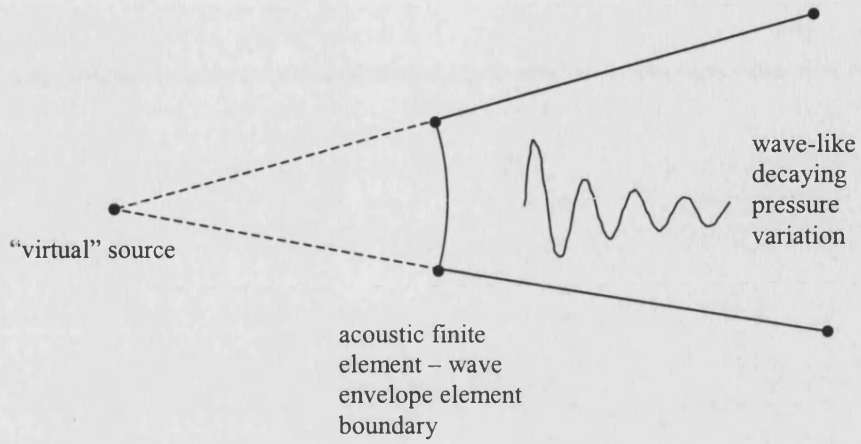

Figure 2.5 Geometry of an individual 2-D wave envelope element.

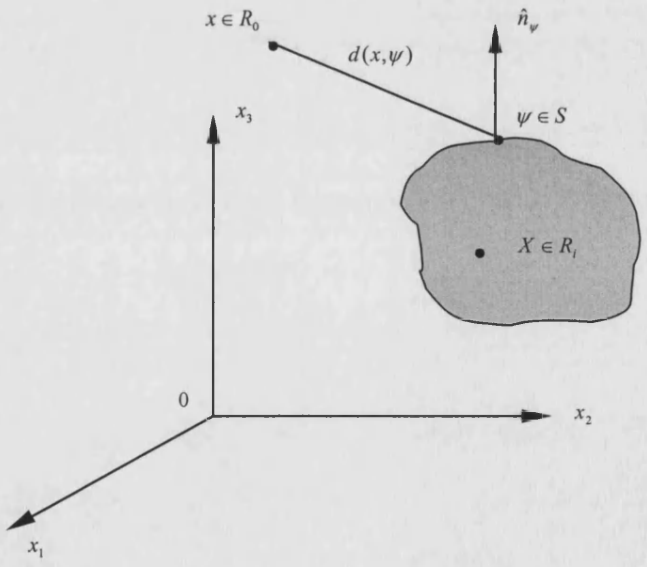

Figure 2.6 Geometry of the problem of an arbitrary structure vibrating in a fluid medium due to Schenck (1968).

The classical formulation of the radiation problem is based on the equation governing pressure variation in the acoustic region for the steady-state case, the Helmholtz wave Equation 1.3

$$\nabla^2 p + k^2 p = 0 \ .$$

Also from the "constituent" equation, introduced above in Equation 2.11, relating pressure on the surface of the structure to outward normal velocity, $v(\psi)$, at a surface point ψ, by

$$\frac{\partial p}{\partial n} = -i\omega\rho v(\psi), \quad \psi \in S \ . \qquad (2.31)$$

Furthermore, a "radiation condition" can be introduced

$$r^{\alpha}\left(\frac{\partial p}{\partial r} + ikp\right) \to 0 \text{ as } \quad r \to \infty \ . \quad (2.32)$$

This expresses that waves are radiated outwards and the pressure variation will diminish to zero at some large distance from the radiating source. In Equation 2.32, r is radial distance from the origin of co-ordinates and S_R is a sphere of radius R centred at the origin, and surrounding x and S, and α=1/2 or 1, depending upon whether the problem is 2-D or 3-D.

Equation 2.32 can be replaced by a radiation condition imposed at some far field boundary, S_2

$$\nabla p \cdot n_2 + ikp = 0 \ \text{ on } \ S_2 \ . \qquad (2.33)$$

The formulation and solution of the classical problem has been approached by a number of authors. Chen and Schweikert (1963) approached the problem by

describing field values in terms of an integral over a distribution of surface sources of unknown strength, at the structure/fluid interface. The integral was formulated to satisfy both the wave equation and the radiation condition for an arbitrary function describing source strength, so that the function could be determined by forcing the integral to satisfy Equation 2.31 also. The problem was then solved by discretising the surface into a finite number of 'elements', each element having constant phase and amplitude, and solving the problem numerically to calculate the unknown source strengths. From this, field values were easily computed.

An alternative "direct" approach has been followed by a number of authors (Baker & Copson, 1950; Ciskowski & Brebbia, 1991). This involves generating an expression relating surface velocity, surface pressure and pressure in the exterior acoustic region, from Equations 1.3, 2.31 and 2.32 by the use of a Green's function that satisfies these equations. Consider the Green's identity, (Baker & Copson, 1950):

$$\iiint_V (u\nabla^2 w - w\nabla^2 u)dxdydz = \iint_S \left(u\frac{\partial w}{\partial n} - w\frac{\partial u}{\partial n}\right)dS \quad . \qquad (2.34)$$

This expresses an integral over a volume in terms of a surface integral. Here $\partial/\partial n$ denotes differentiation along the outward normal to S. If u and w satisfy the wave Equation 1.3, it can be shown that $u\nabla^2 w - w\nabla^2 u = 0$, so that Equation 2.34 becomes

$$\iint_S \left(u\frac{\partial w}{\partial n} - w\frac{\partial u}{\partial n}\right)dS = 0 \quad . \qquad (2.35)$$

Recalling that what is required here is a relationship between surface velocity, surface pressure and pressure in the exterior region, it can be seen that by taking u in Equation 2.35 as surface pressure, an equation will be formed involving surface pressure $p(\psi)$ and the normal gradient of surface pressure $\partial p(\psi)/\partial n$. From Equation

2.31 it is seen that this is the same as having an expression in terms of surface pressure and normal surface velocity. What is required of the term w in Equation 2.35, therefore, is the introduction of an expression for exterior acoustic pressure. For such an expression consider the Green's function

$$g(x,\psi) = \frac{e^{ikr}}{4\pi r} \qquad (2.36)$$

where $r = |x - \psi|$, x is a position vector in the exterior region and ψ is a point on the surface. Replacing u and w in Equation 2.35 accordingly, and incorporating the radiation condition of Equation 2.32 to show that an integral over a sphere at infinity vanishes, the *exterior* Helmholtz integral takes the form

$$p(x) = \left(\frac{1}{4\pi}\right) \int_S \left\{ p(\varsigma) \frac{\partial}{\partial n_\varsigma} \left[\frac{e^{ikd(x,\varsigma)}}{d(x,\varsigma)} \right] - i\omega\rho v(\varsigma) \frac{e^{ikd(x,\varsigma)}}{d(x,\varsigma)} \right\} dS(\varsigma), \; x \in R_0, \; \varsigma \in S. \quad (2.37)$$

There are two other integral equations relating specifically to pressure *on* the surface of the structure and pressure *within* the volume enclosed by S, as opposed to the exterior pressure formulation of Equation 2.37. The first of these will be termed here the *surface* Helmholtz integral

$$p(\psi) = \left(\frac{1}{2\pi}\right) \int_S \left\{ p(\varsigma) \frac{\partial}{\partial n_\varsigma} \left[\frac{e^{ikd(\psi,\varsigma)}}{d(\psi,\varsigma)} \right] - i\omega\rho v(\varsigma) \frac{e^{ikd(\psi,\varsigma)}}{d(\psi,\varsigma)} \right\} dS(\varsigma), \; \psi, \; \varsigma \in S. \qquad (2.38)$$

Chertock (1964) used this for problems of radiating structures with reasonably simple geometry. He solved Equation 2.38 by approximating the radiating surface as a finite

number of points with *known* normal surface velocities, thus generating a system of equations that could be solved numerically for surface pressures. From this the exterior integral could also be solved numerically to generate field results.

The second integral equation will be termed here the *interior* Helmholtz integral:

$$\int_S \left\{ p(\varsigma) \frac{\partial}{\partial n_\varsigma} \left[\frac{e^{ikd(X,\varsigma)}}{d(X,\varsigma)} \right] - i\omega\rho v(\varsigma) \frac{e^{ikd(X,\varsigma)}}{d(X,\varsigma)} \right\} dS(\varsigma) = 0 \qquad X \in R_i,\ \varsigma \in S. \qquad (2.39)$$

This was solved numerically by Copley (1966) for the case of an axi-symmetric radiator, again by discretising the source and for *known* normal surface velocities. A problem encountered in this work, however, was one of uniqueness i.e. whether or not the true surface pressure was the *unique* solution to Equation 2.39 for known $v(\varsigma)$. Copley (1966) stated that for known $v(\varsigma)$, the true surface pressure was the unique function for which Equation 2.39 was satisfied at all points X in the volume V. For the cases considered by Copley, however, this condition was reduced to all interior points on the axis of symmetry, so that a numerical solution could be achieved.

In a second paper Copley (1967) established that both the 'simple-source' method as employed by Chen and Schweikert (1963), and the surface integral formulation used by Chertock (1964), failed at certain frequencies. The first due to non-existence and the second due to non-uniqueness, but both at the same frequencies – the characteristic frequencies of the interior of the radiating structure. Schenck (1968) reiterated the problem of failure at certain frequencies. He emphasised that problems arise not only *at* interior characteristic frequencies but also close to these frequencies.

2.4.4 CHIEF (Combined Helmholtz Integral Equation Formulation)

Schenck (1968) proposed an alternative technique for overcoming the problem of failure at, and close to, interior characteristic frequencies. This practical way of finding the unique surface pressure function that satisfies both the surface and interior Helmholtz integral equations is based on the fact that at any frequency there is only one solution that satisfies both of these equations. Additional "collocation" points are specified within the region surrounded by the BEs, to supplement the d.o.f. on the BE surface itself. The pressure function that satisfies both surface and interior integrals can then be established. From the surface results the exterior field values are then calculated by numerical solution of the exterior integral Equation, 2.37. More details of CHIEF are given in Chapter 4 where consideration is given to large *ka* systems. The method is also compared with the WEE option.

2.4.5 Doubly Asymptotic Approximations (DAAs)

An alternative approach to the exact solution of the discretised surface Helmholtz integral equation, Equation 2.38, for the calculation of surface pressure and normal velocities, is the use of an approximate relationship. As in the exact method, once the structural-fluid problem has been solved field values can then be calculated by the use of Equation 2.37. Doubly asymptotic approximations are a set of BE techniques used to supplement structural equations with an approximate fluid loading so that the system under consideration can be solved for the case of fluid-structure interaction. The theory behind these techniques is based in the solution of transient problems, with the name "doubly asymptotic" being a reference to the fact that the approximations used make the method applicable only at early or late times. They are, therefore, a combination of early time approximations (ETAs) and late time approximations (LTAs). The corresponding approximations in the frequency domain mean that the techniques are only effective at high frequencies or low frequencies, respectively. There are a number of DAAs employing different structural-fluid interaction approximations. In the most basic case the "plane wave" approximation,

$z = \rho c$, is used for the ETA. As for CHIEF, this technique will be given more consideration in Chapter 4 where it will be applied to the modelling of unbounded fluid regions for large *ka* systems. The three methods WEE, CHIEF and DAA2c (the approximation available in PAFEC) will be evaluated and compared for a series of models.

2.5 Applications of FEM and BEM to realistic ultrasound systems

It is clear that the FEM and BEM offer the possibility of effectively simulating realistic ultrasound systems such as the one to be considered here. Indeed the techniques have previously been applied to acoustic systems on a number of occasions. In 1973 Smith et. al. considered the problem of a sonar transducer operating in an unbounded fluid media. This incorporated many of the modelling features outlined in this chapter - a piezoelectric structure modelled by FEM with the surrounding media modelled by BEM, with comparisons made against experimental results. Indeed this work also highlighted the problem of establishing accurate piezoelectric material parameters, a feature that will be shown to be quite significant in later chapters here. The system was, however, limited with the structure consisting of a small number (~20) of piezoelectric elements only and operating at a maximum frequency of 70 kHz. Also comparisons were mainly made for the electrical response of the system although some low frequency beam patterns were compared. The model and experimental results were in good agreement. In 1974 Hunt et. al. considered a similarly simple low frequency system (≤ 10 kHz) and also showed good near-field agreement of model and experiment.

More recently Hansen (1997) has applied FEM to the problem of optimising the performance of a simple piezoelectric transducer operating at 20 kHz in air. Piranda et. al. (1998) have made a comparison of different BEMs that can be used to simulate a semi-infinite fluid region in conjunction with a FEM of a 2-D piezoelectric transducer. Again, however the structural model is a simple system incorporating at most 20 FEs. Gallaher et. al. (1999) have applied FEM and BEM to the problem of

optimising the performance of arrays of ring transducers operating in a surrounding fluid region at frequencies up to 15 kHz. Whilst Morgan et. al. (1999) used FEM and BEM to analyse the response of systems of ring transducers in water as operating conditions and the system alignment varied. Comparisons were made for electrical results with the system operating at frequencies up to 10 kHz.

1-D modelling techniques have been used for the consideration of optimising the performance of device front and back layers, as in Kocbach et. al. (2000) where 3-D FEM and1-D model comparisons for a piezoelectric disc and matching layer system operating in air close to 2 MHz have been made. Little work has considered components other than those in the primary direction of propagation. Han and Roh (1998) applied FEM to the problem of the effects of side layers on a 3-D shear wave piezoelectric transducer operating at 1 MHz, using the model to analyse the effect of varying side-layer parameters with the intention of improving device design. However some simplifying assumptions on the performance of the active element were applied, and a 1-D response of the front and backing layers was assumed. They reported limited model-experimental waveform comparisons, showing good agreement.

This brief outline of some FEM and BEM applications to acoustic systems emphasises that the techniques outlined here have the *potential* for modelling complex ultrasound systems. However to date many of the problems considered have been for systems operating at relatively low frequencies and incorporating relatively small numbers of FEs and BEs. Where systems operating at higher frequencies have been approached they have generally been substantially simplified with only limited model-experimental comparisons reported. Kocbach et. al. (2000) have presented work on the modelling of a piezoelectric disc operating into an unbounded fluid media modelled using WEEs. Exact details of this work are not available, however the abstract describes a piezoelectric disc/matching layer/fluid system of maximum *ka* value 30. Near-field comparisons are reported although the abstract gives little indication of the nature of these results. As far as the author is aware FEM and BEM

have not been applied to systems where realistic 2-D/3-D piezoelectric behaviour and 2-D/3-D component interaction, including those at the edge of the active element, have been considered. In addition, the operation of such a device in an unbounded fluid region has not been tackled and nor have extensive near-field model-experimental pressure comparisons been approached. It will be seen in the next chapter that the system considered here has ka ~54, and again to the author's knowledge no previous consideration of a realistic system of this size and its associated modelling problems has been reported.

2.6 Summary

This chapter has outlined FEM in some detail using simple examples to show how simulated systems are generated and solved. These examples are outlined in more detail in Appendix 1. Outlines of specific FEs that will be applied in this work has been given and the theoretical basis of element formulations discussed. BEM has also been considered, with specific reference to the solution of the 'classical' problem of a structure radiating into an infinite fluid region. Three alternative techniques for modelling unbounded regions have been introduced - the use of WEEs, CHIEF and DAA. These techniques will be considered in more detail in Chapter 4. Next, Chapter 3 will look at the modelling approach adopted here to establish the effectiveness of FEM for modelling realistic medical ultrasound systems. The design, construction and modelling of a real medical ultrasonic device will be outlined and the corresponding device model generated. A detailed summary of the experimental measurements made on the device will also be given.

Chapter 3

3.1 Introduction

Chapters 1 and 2 introduced the essential design of a physiotherapy transducer and looked at the FEM approach to modelling such a device including some of the features of a realistic model. The simulation of the surrounding fluid region was also considered. This chapter will start to consider the effectiveness of the FEM approach adopted here for modelling realistic medical ultrasound devices and their near-fields. The modelling is considered in two parts, with the investigation of the simulation of the surrounding unbounded acoustic region deferred to Chapter 4. This chapter will concentrate on the design and construction of a specific transducer and the experimental measurements made on it. The corresponding FEM model of the device will also be outlined. The building of a real device automatically meant that a large number of model parameters were known to some degree of accuracy, and made modelling the device significantly easier. Experimental measurements made on the real device were then used for testing and evaluating the model. Two sets of measurements are reported here. First, those made in accordance with IEC 61689:1996, the standard on physiotherapy devices (hereafter referred to as the IEC standard). Second, additional measurements made to generate a more comprehensive picture of the near-field are reported. The intention of these measurements is to consider the robustness of both the experimental procedure and the model. Details of the measurement set-up, procedure and rationale are also included.

3.1.1 Modelling approach

Initially FEM models of "general" circularly symmetric transducers radiating into an unbounded acoustic region were considered, using acoustic FEs and WEEs for the fluid region. These devices essentially contained the components described in Chapter 1 and shown in Figure 1.1. Operation at relatively high frequencies resulted in these initial models having a moderate *ka* value. Unfortunately a number of

problems were encountered. Firstly, the choice of model parameters and component parameters was made fairly arbitrarily based on limited references to realistic devices in the literature such as in Hill (1986) and Meire & Farrant (1995). Secondly, the model clearly indicated that the device vibration was non-uniform, and it was further obvious that the predicted field was significantly different from that generated by a corresponding plane piston model. This made comparison with idealised results inappropriate. Thirdly, there were significant concerns over the modelling of the acoustic region, specifically relating to the parameters for the WEEs and the meshing of this region. Inconsistencies could clearly be observed at the acoustic FE -WEE interface so that at least some of the irregular field response could be attributed to inaccuracies in the modelling of the fluid region. Finally, modelling was severely constrained by simulation run times. At this stage the use of a 90 MHz PC meant that models frequently required overnight runs to generate results for a single frequency. Later a 500 MHz PC would somewhat speed this up. The large run times were basically determined by the modelling of the acoustic region so it was clear that alternative modelling techniques for the surrounding unbounded fluid region would need to be considered.

To overcome these problems it was decided to initially consider the effectiveness of the modelling of the fluid separately from the modelling of the device. The use of structural models with idealised vibration enabled much of the uncertainty associated with a realistic device to be removed so that field comparisons could be made against easily generated analytical results. The WEE models for these ideal structures could also be compared with BEM options for the simulation of the fluid region. Although such techniques have been widely used for the simulation of infinite fluid regions outside of radiating structures, little work has been carried out for modelling the near-field of structures with *ka* values of the magnitude considered here. Chapter 4 will therefore consider idealised structures using WEEs, CHIEF and DAA2c for the unbounded fluid region. The effectiveness of these techniques will be evaluated and compared. Subsequent chapters will combine the fluid region models from Chapter 4 with the structural model from this chapter to generate models of the full system.

This chapter will concentrate on the design, construction, modelling and measurement of a real medical ultrasound transducer. The original criteria for the device was that it should be circularly symmetric, operate at a moderately high frequency with a relatively high *ka* value, and preferably that it should be designed to operate in continuous wave mode. A circular device would allow the investigation of the important features of many real devices whilst exploiting symmetry to reduce the computational requirements. A device operating around 1 MHz, although probably only classed as a 'moderate' frequency device, allows for the generation of a model that is practical to run in terms of run time and memory requirements. 1 MHz equates to an acoustic wavelength of approximately 1.5 mm in water and the 'rule of thumb' for meshing in FEM is generally taken to be that there should be at least 7 nodes per wavelength. A relatively large structure operating around 1 MHz therefore presents a significant but approachable challenge. The benefit of modelling a transducer operating in continuous wave mode is that the generation of field results is only required at one frequency, although some electrical response pre-analysis is required to determine the resonant behaviour of the device.

3.2 Physiotherapy transducer

A common design for a physiotherapy transducer is an air-backed, circularly symmetric device operating with a fundamental frequency around 1 MHz in continuous wave mode, meeting the modelling criteria here. Consequently a physiotherapy transducer was designed and the details passed to George Cattermole of S.I. Transducers for construction. It should be noted that a recent reassessment of the internationally agreed standards for the requirements of physiotherapy devices and associated fields also meant that there was a comprehensive and up-to-date set of guidelines around which the experimental measurements could be based.

Figure 3.1 shows the design of the device considered. A thickness poled Ferroperm Pz26 disc designed to have a thickness extensional resonant mode close to 1 MHz was mounted in a cylindrical ABS plastic inner casing. The disc was secured into a

groove, cut into the front end of the inner casing, with epoxy so that the front face of the disc was flush with the edge of the casing. The diameter of the disc was slightly smaller than the diameter of the groove so there was a small gap here of the order of 0.3 mm. A piece of flattened copper wire was passed across the front of the disc and held in place by a small amount of solder at opposite edges of the disc. On the back of the disc two leads of copper wire were attached at opposite edges using small amounts of solder. The back end of the inner casing had an ABS end cap with a hole drilled in the middle into which a Harwin pin was secured, by which electrical connections were made. The inner casing was housed within an outer casing made from a stainless steel tube with an inner diameter slightly larger than the outer diameter of the ABS casing. The inside surface of the outer casing was coated with epoxy and the ABS casing slid into it and secured. The face of the disc was not flush with the outer casing but secured at a depth equal to the thickness of the required quarter-wavelength matching-layer. The final part of the transducer construction was to pour the Araldite matching-layer into this recess and allow it to 'cure' for approximately a week before machining it down so as to be flush with the outer casing. The remaining component was an UHF connector mounted in the stainless steel end-cap. The wire from the front of the disc was passed between the inner and outer casings and connected to the case at the stainless steel end-cap. The wires from the back of the disc passed through the Harwin pin and into the UHF connector.

3.2.1 Physiotherapy transducer *model*

Figure 3.2 shows the initial model of the transducer that gave successful results. The Pz26 disc, inner casing, matching layer and glue layer are all included, along with dimensions measured during construction. The recess on which the disc rests in the real device, and the end-caps were not included in this model as it was designed to be a simple as possible whilst incorporating the features that were expected to be of most significance. Wiring and soldering were not included because of the use of symmetry. Although this could have some minor effect on the generated field it was not expected to be significant. An earlier model had included a full-size stainless-steel

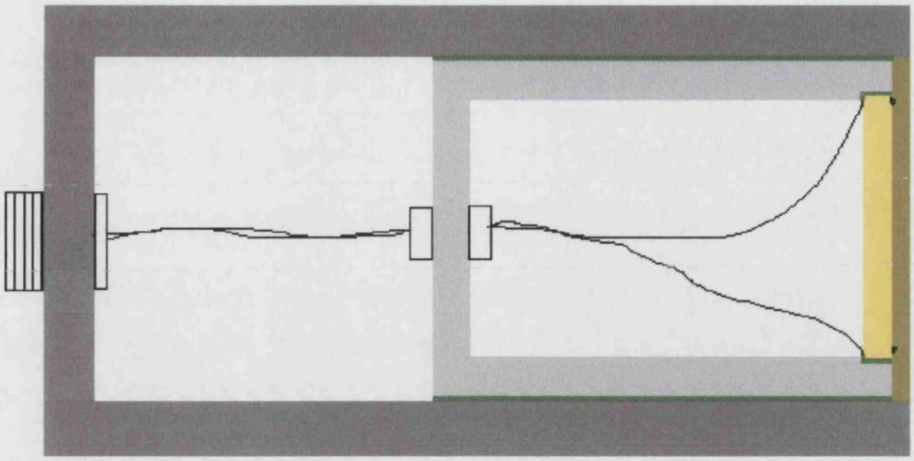

Figure 3.1 Physiotherapy transducer, back-to-front slice. Piezoelectric disc (yellow), matching layer (mustard), glue layers (green), inner casing (light grey), outer casing (dark grey), wires & solder (black), and end-caps.

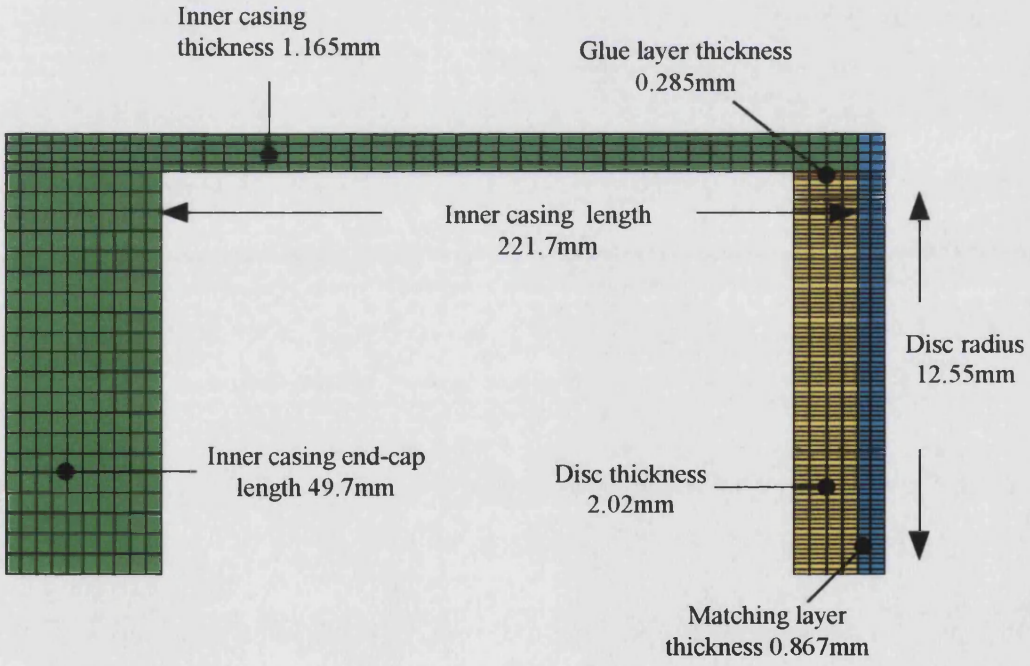

Figure 3.2 Physiotherapy transducer *model*. Back-to-front slice showing piezoelectric disc (yellow), matching layer (blue), glue layer (orange) and inner casing (green).

outer casing, however, because of its length this caused a significant increase in the number of d.o.f. in the model and subsequently the run time. Before the outer casing was dispensed with a sequence of models was used to investigate its effect. It was established that removing the outer casing and applying a fixed boundary condition to the outside of the inner casing (corresponding to a rigid outer casing) had no significant effect on model output. This was not unexpected, as a thick stainless steel casing with high impedance would be expected to behave similarly to a rigid structural boundary condition. Acoustic FEs still surrounded the outside surface of the outer casing location, as a zero pressure-gradient here enforces the rigid restraint. Chapter 6 will consider the components not included here in more detail.

Table 3.1 lists the material parameters that must be defined to generate this structural model along with values and the source of these values. Stainless steel is included for completeness. At this stage in the modelling process a number of piezoelectric properties were not directly available from Ferroperm, the disc manufacturers. At a later date, however, all properties were specified. For the modelling results here the initial values outlined in Table 3.1 were used. The significance of the piezoelectric properties and the newly defined Ferroperm values will be investigated in Chapter 6 when an analysis of all model parameters is considered. One final point should be made. A mistake occurred when calculating the required thickness of the matching layer due to the use of an incorrect velocity, so that the dimension shown is not for the material used. This should not effect the model however as the *measured* value is used.

3.3 Experimental measurements

Two sets of measurements were made for comparison with the model. Those specifically required by the IEC standard will be outlined in this section, while additional measurements intended to examine the repeatability of the experimental process and investigate the robustness of the model, will be presented in Section 3.4.

PARAMETER	*UNITS*	*VALUE*	*SOURCE*
Piezoelectric			
S_{11}^{E} (sxx) (syy)	10^{-12} m^2/N	13	Ferroperm (1995)
S_{33}^{E} (szz)	10^{-12} m^2/N	20	Ferroperm (1995)
S_{12}^{E} (sxy)	10^{-12} m^2/N	-4.23823	Madrid* (1999)
S_{13}^{E} (syz) (szx)	10^{-12} m^2/N	-7.0485	Madrid* (1999)
S_{66} (shxy)	10^{-12} m^2/N	34.47646	$S_{66} = 2*(S_{11}^{E} - S_{12}^{E})$
S_{44}^{E} (shyz) (shzx)	10^{-12} m^2/N	34.85	**estimate** Vernitron (1976)
ε_{33}^{S} (epzz type 2)	10^{-9} farads/m	6.34975	**estimate** Vernitron (1976)
ε_{11}^{S} (epxx type 2)	10^{-9} farads/m	7.35	**estimate** Vernitron (1976)
d_{31} (ezx type 2)	10^{-12} C/N	-130	Ferroperm (1995)
d_{33} (ezz type 2)	10^{-12} C/N	330	Ferroperm (1995)
d_{15} (exxz type 2)	10^{-12} C/N	494	**estimate** Vernitron (1976)
ρ	10^{3} Kg/m^3	7.70	Ferroperm (1995)
μ	-	0.001	**estimate** Vernitron (1976)
Eccobond* 24			
E	10^{9} N/m^2	2.70	Emerson & Cuming
ρ	10^{3} Kg/m^3	1.10	Emerson & Cuming
σ	-	0.25	**estimate** PAFEC (1995)
μ	-	0.01	**estimate** PAFEC (1995)
Araldite			
E	10^{9} N/m^2	3.315058	calculation
ρ	10^{3} Kg/m^3	1.14	CIBA-GEIGY (1982)
σ	-	0.41	**estimate** PAFEC (1995)
μ	-	0.03	**estimate** PAFEC (1995)
ABS			
E	10^{9} N/m^2	2.10	RS Components (1999)
ρ	10^{3} Kg/m^3	1.03	RS Components (1999)
σ	-	0.4	**estimate** PAFEC (1995)
μ	-	0.07	**estimate** PAFEC (1995)
Stainless steel			
E	10^{9} N/m^2	195	PAFEC (1995)
ρ	10^{3} Kg/m^3	7.70	PAFEC (1995)
σ	-	0.3	PAFEC (1995)
μ	-	0.005	PAFEC (1995)

Table 3.1 Material properties of original physiotherapy transducer model. Sources of property values are given in the references section.

All measurements were taken in the near-field of the device. It is in this region that the variation is most extreme and the maximum pressure values occur.

3.3.1 IEC standard measurements

The IEC standard is concerned with the characterisation of output performance, the requirements for safety due to the generated ultrasonic field, acceptance criteria for aspects of performance and the techniques for measuring all of these features. The parameters of significance here are acoustic working frequency, output power, effective radiating area A_{ER}, beam type, and beam non-uniformity ratio R_{BN} (Hekkenberg et al., 1994; Hekkenberg, 1998).

3.3.2 Acoustic working frequency

Here the acoustic working frequency is taken as the fundamental resonance frequency of the device. This is the primary operating frequency of the device and it is at this frequency that the majority of measurements were made. To determine the resonant frequency of the transducer its electrical response was measured at Bath using a Hewlett Packard 4192A impedance analyser controlled by a PC. The face of the transducer was immersed in water and the device driven in continuous-wave mode at a range of frequencies around 1 MHz. Figure 3.3 shows a plot of conductance versus frequency. The measurement was repeated a number of times over the course of this work, each time producing a similar curve. The exact position of the resonance has been seen to vary by a few kHz, although the final working frequency was determined to be 1.027 MHz. Some consideration will be given to the effect of frequency on the generated field later in this chapter. Figure 3.3 suggests that the response of the transducer may vary significantly with frequency close to resonance.

3.3.3 Output power

The output power was measured using a radiation force balance at NPL. The experimental set-up is shown in Figure 3.4. A Hewlett Packard (HP) 3336C synthesiser/level generator was connected to the transducer via an ENI 240L RF power amplifier (50 dB) and a HP 3403C true rms voltmeter. The transducer was held by a retort stand, boss and clamp and its face was submerged just below the surface of a beaker of de-gassed, de-ionised water (temperature approximately $20\,^{o}C$) which rested on an EMS precision ultrasound radiation force balance. The device was centred over an air-backed conical nickel target of diameter 60 mm and any air bubbles were brushed away from the transducer face. There was an acoustic absorber around the inner curved surface of the beaker that is not shown in diagram. The acoustic power output was directly related to the force exerted on the target. The drive level was increased up to a value that was not expected to damage the transducer and decreased in the same way to establish the consistency of the response of the device. A series of such measurements were made at frequencies around 1.027 MHz and a maximum power output of 14.10 W was measured for an rms drive voltage of 26.4 V. This value will be used later to establish generated intensity levels.

3.3.4 Scanning tank measurements made at NPL

Unless otherwise stated all acoustic field measurements were made using the scanning tank equipment shown in Figure 3.5 in accordance with the IEC standard. The transducer was driven in continuous wave mode with a voltage that did not cause intensity levels to exceed 0.5 W/cm^2 in order to avoid the possibility of cavitation in the water. The drive set-up was as for the radiation force-balance measurements with a HP true rms voltmeter connected across the amplifier. The transducer was held in a clamp that allowed it to be tilted and rotated, and was directed towards the Dapco 0.6 mm needle hydrophone held in a second clamp. The movement of both transducer and hydrophone were controlled by a Mclennan stepper-motor PM 170 series control-unit that allowed movement in the three orthogonal directions parallel to the sides of

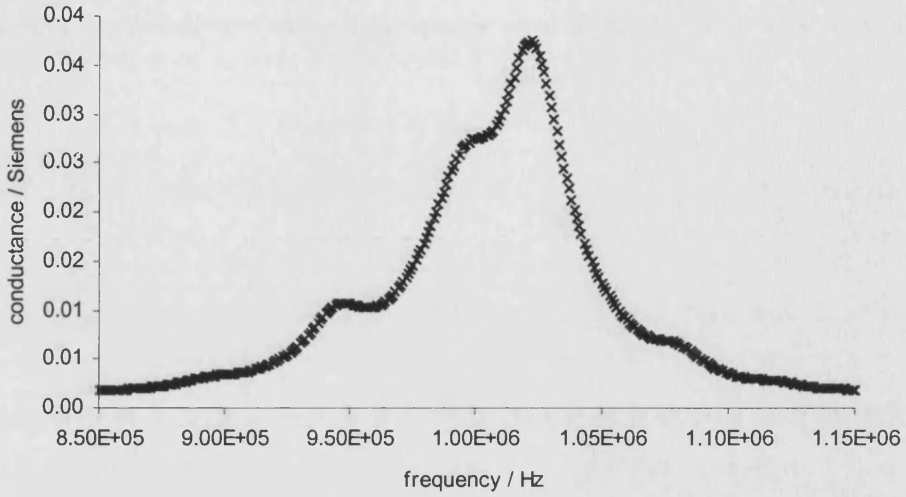

Figure 3.3 Conductance of the physiotherapy transducer versus frequency. Based on several measurements of the conductance of the device an acoustic working frequency of 1.027 MHz was established for the purposes of making all *IEC standard* measurements.

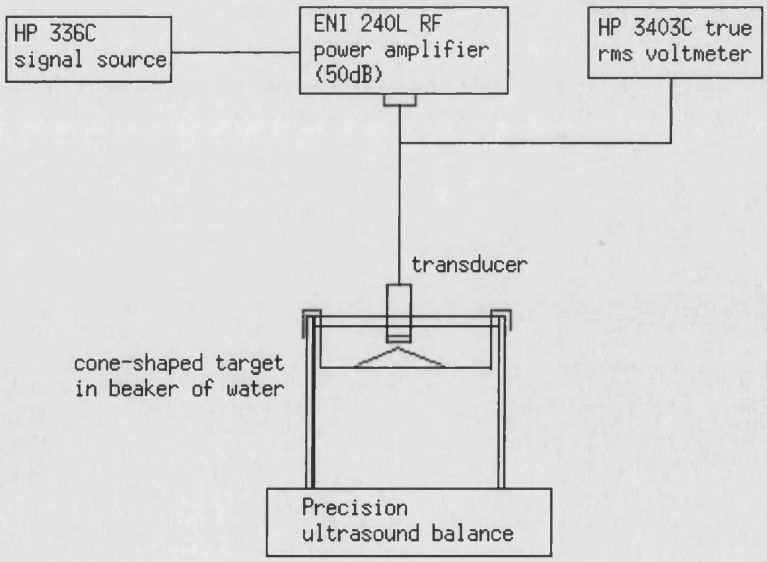

Figure 3.4 Radiation force-balance set-up.

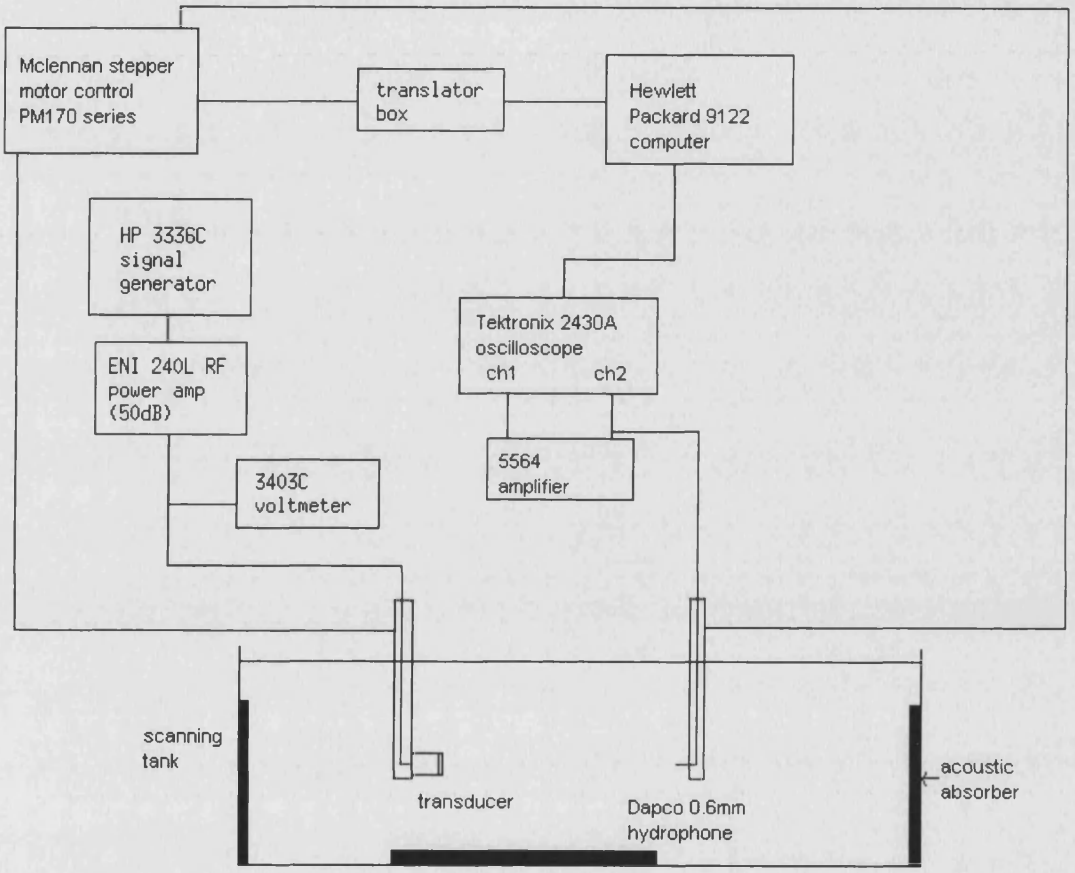

Figure 3.5 Scanning tank set-up.

the tank. A HP 9122 computer controlled the stepper-motor unit via a translator box. The same PC controlled the storage of data from the hydrophone that was recorded by a Tektronix 2430A oscilloscope. A 5564 amplifier amplified the signal from the hydrophone. Five pieces of acoustically absorbing material were placed in the tank to minimise reflections – one at each end, one at the base and one at each side (not shown in Figure 3.5). The tank was filled with de-gassed, de-ionised water, at around $20^{o}C$.

All of the field measurements were made using a Dapco 0.6 mm needle hydrophone, although in order to calibrate this device (to give absolute pressures) a few measurements were made with a reference membrane hydrophone. The use of a Dapco 0.6 mm hydrophone has been validated as providing field measurements of acceptable accuracy for devices with differing beam profiles (Hekkenberg et al. 1994; Hekkenberg, 1998). Furthermore the use of this type of hydrophone is generally recommended for a physiotherapy device operating in continuous wave mode (Preston, 1991). Of course there are limitations to the accuracy of such a device due to its finite size, and the measured signal will be proportional to pressure averaged over the receiver (Verma, 1995). Here the hydrophone element is less that half a wavelength in diameter for the source operating around 1 MHz. In areas where the pressure variation is most extreme, which is likely to be close to the source, the finite size of the hydrophone will make absolute results less accurate due to averaging. Hekkenberg et. al. (1994) covers the significance of spatial averaging and the directionality of the receiver on the IEC standard measurements, concluding that the standards are robust enough to account for such effects. For the additional near-field measurements it is expected that the absolute pressure values close to the source may be somewhat inaccurate but that the main features of the field will be represented accurately. Comparisons in the region close to the source are further complicated by the need to consider the variation with frequency (close to resonance) and in identifying the exact position of the hydrophone relative to the transducer.

3.3.5 Beam alignment axis

In order to make the measurements outlined here it was first necessary to establish the beam alignment (or acoustic) axis of the transducer. This procedure needed to be repeated between measurements to ensure that the device was aligned correctly and also to take into account the fact that the acoustic axis may be somewhat frequency dependent. The procedure specified for the IEC standard (Hekkenberg et al. 1994; Hekkenberg, 1998), was used to establish the beam alignment axis for *all* of the measurements made here. The procedure was as follows:

Firstly the hydrophone was positioned touching the face of the transducer approximately at its centre. The hydrophone was moved out to a near-field position at a range a^2/λ where a is the radius of the element and λ is the wavelength. Here the oscilloscope signal was maximised by adjusting the horizontal and vertical positions of the hydrophone. Next the hydrophone was moved to a far-field position at $2a^2/\lambda$ and again the signal was maximised, this time by adjusting the tilt and rotation of the transducer. The hydrophone was then moved back to a range a^2/λ and the whole process repeated. This sequence was repeated several times until an alignment was reached such that no further increase in the signal could be achieved. The axis so established was taken as the beam alignment axis. This process could be supplemented by an 'automatic' optimisation if required. Here the software moved the hydrophone in increments of the order of 0.01 mm and measured the voltage output until it decreased by ~ 1 dB. It did this in the +/- horizontal and vertical directions around the initial axial position, establishing the peak as the axial position.

3.3.6 Calibration of needle hydrophone

Absolute pressure values were not required for establishing the values of any IEC standards parameters, as the voltage response of the hydrophone was adequate. However for absolute model-experimental field comparisons actual pressure values were required. The calibration of the needle hydrophone is described now so that IEC

measurements of the acoustic field can be presented in terms of absolute pressure values.

The calibration process took a voltage measurement in the field using a *calibrated* membrane hydrophone and converted the voltage to a pressure value. The membrane was then replaced with the Dapco needle hydrophone and a voltage measurement taken at the same point in the field so a Dapco voltage-to-pressure conversion factor could be calculated. The membrane hydrophone used was a GEC Marconi PVDF bilaminar shielded model with a 0.5 mm element and was a direct replacement for the needle hydrophone in the experimental set-up. Comparative measurements were made at similar frequencies and for the same pre-amplified drive level of –27.0 dBm. The actual drive voltages were read from the rms voltmeter. Table 3.2 shows the needle hydrophone receive sensitivities for several frequencies around 1.027 MHz.

Frequency (MHz)	Receive sensitivity M (μV/Pa)
1.019	1.50654
1.023	1.62323
1.027	1.90125
1.031	2.09816
1.035	2.03642

Table 3.2 Dapco hydrophone sensitivity.

Here M is the output voltage equivalent to 1 Pascal.

3.3.7 Effective radiating area A_{ER}

Physiotherapy transducers are capable of generating relatively high intensity levels with the potential for causing adverse biological effects, (Hekkenberg et al., 1994; Hekkenberg, 1998). It is therefore important to know power and intensity levels being

delivered to a patient. Intensity is calculated by dividing acoustic output power by a characteristic area through which the majority of the ultrasound power passes. The IEC standard classifies this characteristic area as the effective radiating area A_{ER}.

The new IEC definition of A_{ER} was intended to make the parameter less sensitive to local variations in the acoustic field whilst relating it to the characteristics of both the source and the field. To achieve this an additional parameter, the beam cross-sectional area A_{BCS}, is used in the derivation of A_{ER} such that:

$$A_{ER} = F_{AC} * A_{BCS}(0) \quad . \quad (3.1)$$

Here $A_{BCS}(0)$ is the beam cross-sectional area at the transducer face that is derived from a linear regression applied to four A_{BCS} measurements made at different distances from the source and extrapolated back to the face. The use of four different planes of measurement has been shown to make A_{ER} less sensitive to field inhomogeneities (Hekkenberg et. al., 1994; Hekkenberg, 1998). A_{BCS} is the minimum area in a specified plane perpendicular to the beam alignment axis which contains 75% of the spatial integral of the total mean square acoustic pressure (pms_t) where

$$pms_t = \sum_{i=1}^{N} p_i^2 = \frac{1}{M_L^2} \sum_{i=1}^{N} U_i^2 \quad (3.2)$$

and N is the number of points in the scan, U_i is the hydrophone voltage (either peak or rms.) at the i^{th} point in the scan, p_i is the acoustic pressure at the i^{th} point in the scan, and M_L is the end of cable loaded sensitivity of the hydrophone.

F_{AC} in Equation 3.1 is a conversion factor used to compensate for the fact that A_{BCS} is determined from an area representing only 75% of the total mean square acoustic

pressure. Although this should mean that $F_{AC} = 1.333$, its value has been shown to be dependent on the distances chosen for the raster scan measurement planes (Hekkenberg et al. 1994; Hekkenberg, 1998). The standard gives the value to be used as $F_{AC} = 1.354$.

The measurement of A_{BCS} and subsequently A_{ER} proceeded as follows. The beam axis was found by alignment and the hydrophone moved along this axis to the point at which the planar raster scan was to be made. The peak signal in the plane $p(\max)_{rms}$, was established - which should be close to the axis - by moving the hydrophone horizontally and vertically in small increments or using the 'automatic optimisation process'. Having established the peak the hydrophone was moved in one of the four orthogonal horizontal and vertical positions until the –28 dB limit of $p(\max)_{rms}$, equivalent to 4%, was reached. Care had to be taken to ensure that a global, as opposed to local, minimum was achieved. The hydrophone was then returned to $p(\max)_{rms}$ and moved similar distances in the other three orthogonal directions, establishing the –28 dB position in each direction. The maximum of these four distances was doubled to give the dimensions of the square plane to be scanned about $p(\max)_{rms}$, using a constant step size. In practice a square grid of 51 points by 51 is scanned and the step size calculated accordingly.

The A_{BCS} value in a plane was calculated by sorting the U_i scan values into descending order and summing them to calculate the value of n that satisfies:

$$\frac{1}{M_L^2}\sum_{j=1}^{n} U_i^2 \le 0.75 pms_t < \frac{1}{M_L^2}\sum_{j=1}^{n+1} U_i^2 . \qquad (3.3)$$

Then $A_{BCS} = n\Delta s^2\ cm^2$, where Δs is the scan step size in cm. It should be noted that in practice M_L, the voltage-to-pressure conversion factor, does not need to be calculated due to the definition of pms_t in Equation 3.2.

The IEC standard has designated 10 mm, 20 mm, 40 mm and 80 mm as the distances from the source at which raster scans should be made for calculation of $A_{BCS}(0)$. Figure 3.6 shows part of the contour plot for the scan at 40 mm. The full scan measured an area covering +/- 51.25 mm off-axis in both horizontal and vertical directions, with a step-size of 2.05 mm. The scan data not included here all lies within the lowest voltage contour range shown. It can be seen that although the overall nature of the field is symmetric about the acoustic axis there are definitely signs of asymmetry. This may be significant in terms of establishing the beam alignment axis and generating axial scans. It may also be of particular importance when making model-experimental comparisons. However the planar raster scan is clearly comprehensive in its assessment of the field in a plane and as such is ideal for establishing the nature of the generated acoustic field. Figure 3.7 shows the four A_{BCS} field values and the extrapolation that establishes $A_{BCS}(0)$ as 2.24 cm^2. Equation 3.1 then gives a value for A_{ER} as approximately 3.03 cm^2.

3.3.8 Intensity levels and beam type

It was shown in Section 3.3.3 that the physiotherapy transducer has the capability of generating power in excess of 14 W. Dividing this by the value of A_{ER} gives an idea of the effective intensity levels that can be generated by the device, which in this case is approximately 4.66 W/cm^2. The "absolute maximum effective intensity" value defined in the IEC standard is 3 W/cm^2. This value is of little significance when making model-experimental comparisons, as increasing the model drive level will just linearly increase field pressure values. However it does highlight the potential for physiotherapy devices to generate high intensity levels with implications for adverse biological and heating effects. In practice, of course, the device would not be operated at the high drive level used to generate output power of the order of 14 W.

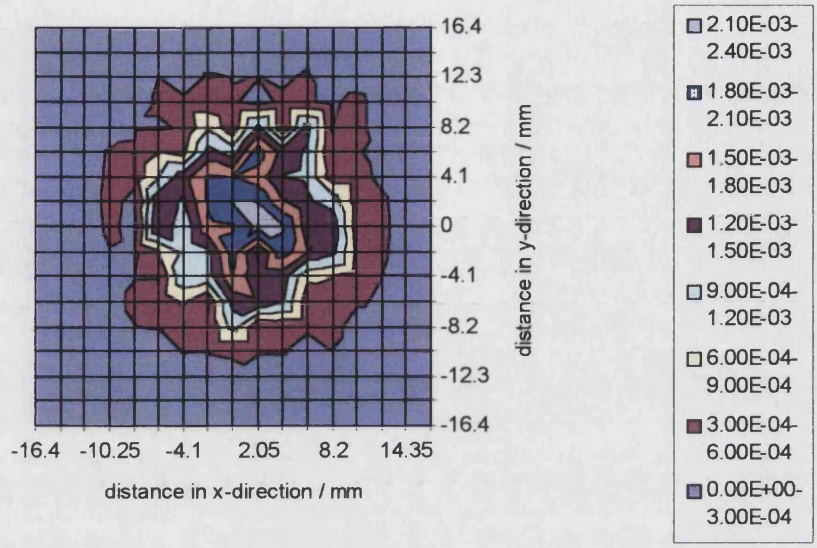

Figure 3.6 Contour plot of raster-scan data at 40 mm from the source. Plotted values are rms voltages, in volts, and measurements are centred about the beam-alignment axis.

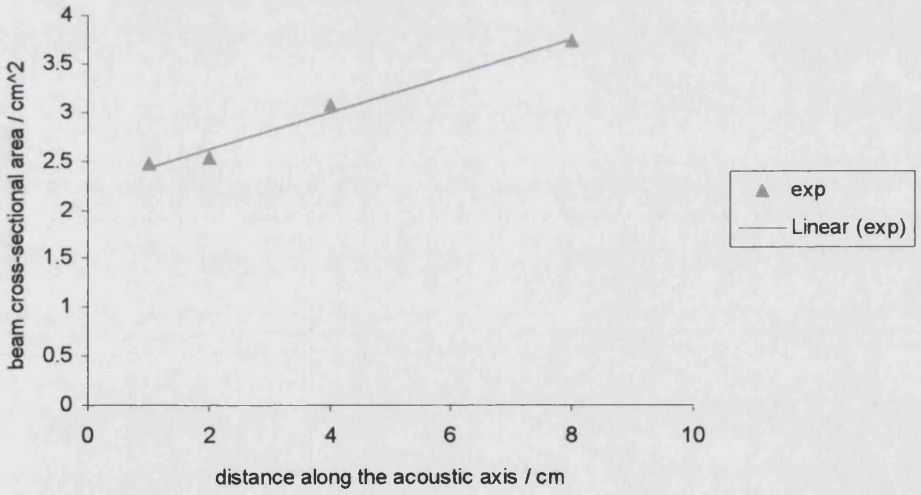

Figure 3.7 A_{BCS} values at the four planes specified by the IEC standard – 10, 20, 40 and 80 mm. Extrapolation back to the y-axis gives a value of A_{BCS} (0) as 2.24 cm^2 leading to a value of 3.03 cm^2 for the A_{ER}.

An additional parameter that can be determined from the A_{BCS} measurements is the categorisation of the beam type. This is based on the gradient (m) of the linear regression shown in Figure 3.7. The following 3 beam types are defined:

$$\begin{aligned} m > 1 \quad & \text{divergent} \\ -0.5 \le m \le 1 \quad & \text{collimated} \\ m < -0.5 \quad & \text{convergent} \end{aligned}$$

The value of m for the physiotherapy transducer used here is approximately 0.19 giving a *collimated* beam type.

3.3.9 Beam non-uniformity ratio R_{BN}

Physiotherapy devices can produce highly inhomogeneous ultrasonic fields with the potential for very high local acoustic pressures or 'hot spots' (Hekkenberg et al. 1994; Hekkenberg, 1998). Such hot spots may result in excessive heating in regions of the area being treated giving rise to potentially harmful effects. The evaluation of the non-uniformity of the generated field is therefore of considerable importance and to this end the beam non-uniformity ratio R_{BN} is specified in the IEC standard as

$$R_{BN} = \frac{I_{SPTA}}{I_{SATA}} \qquad (3.4)$$

where I_{SPTA} is the spatial peak temporal average intensity, and I_{SATA} is the spatial average temporal average intensity. Also

$$I_{SPTA} = \frac{p_{SP}^2}{2\rho c} = \frac{U_{SP}^2}{2M_L^2 \rho c} \qquad (3.5)$$

and $$I_{SATA} = \frac{power}{A_{ER}} = \frac{s^2 \sum_{i=1}^{N} \frac{p_i^2}{2\rho c}}{A_{ER}} = \frac{s^2 \sum_{i=1}^{N} \frac{U_i^2}{2M_L^2 \rho c}}{A_{ER}} \quad . \qquad (3.6)$$

Here p_{SP} is the acoustic pressure corresponding to U_{SP} (the maximum in-field voltage), ρ is the density of sound in water, c is the speed of sound in water, and s^2 is the area per raster scan measurement. For constant ρ, c and M_L during the measurements this leads to

$$R_{BN} = \frac{U_{SP}^2 A_{ER}}{\sum_{i=1}^{N} U_i^2 s^2} \qquad (3.7)$$

where the $\sum U_i^2 s^2$ term is averaged over the four A_{BCS} measurement planes for improved accuracy.

From Equation 3.4 R_{BN} is seen to essentially measure the ratio of the highest intensity in the field to the average intensity. The value of R_{BN} therefore literally specifies the relative level of the hottest hot spot. The calculated value for R_{BN} here is 4.77, which is well within the IEC maximum value of 8. The IEC maximum is twice the value of the R_{BN} calculated for a field due to an ideal plane piston source, and is used to allow some deviation from the ideal case (Hekkenberg et al. 1994; Hekkenberg, 1998).

This concludes the measurements made in accordance with the IEC standard. Consideration will now be given to additional measurements made on the transducer.

3.4 Additional measurements

Additional near-field measurements provided further insight into the performance of the transducer and the nature of the generated near-field. They also offered the opportunity for a more comprehensive model-experimental comparison and some consideration of the robustness of the experimental measurement process as well as the robustness of model-experimental comparability. What follows is an outline of the additional measurements made, an explanation of why this was considered necessary and what additional information they gave.

3.4.1 Frequency variation

It was mentioned in Section 3.3.2 that the conductance response for the physiotherapy transducer suggested that the device was sensitive to drive frequency. Some consideration of the effect of varying the frequency around the main resonance was therefore useful in terms of establishing how close to resonance such devices must be driven for their behaviour to remain consistent. In addition the operating frequency might be significant from a modelling point of view if the resonant frequency of the model was different from that of the real device. In more general terms a consideration of the operation of the *real* device off-resonance could be used for comparison with the model to test the robustness of the simulated system when operating off resonance.

With this in mind, a series of axial measurements were made at various frequencies close to the resonance of 1.027 MHz. In addition some cross-axial scans were made at 1.027 MHz and 1.031 MHz. Cross-axial scans were used here as an alternative to detailed raster scans in order to save time. These scans show off-axial data at orthogonal +/- horizontal and vertical directions about the axis. Figure 3.8 shows axial output at three frequencies: 1.023 MHz, 1.027 MHz and 1.031 MHz. Although there is some variation in the amplitudes of the various maxima and minima the features essentially remain consistent. Figure 3.9, on the other hand, showing axial

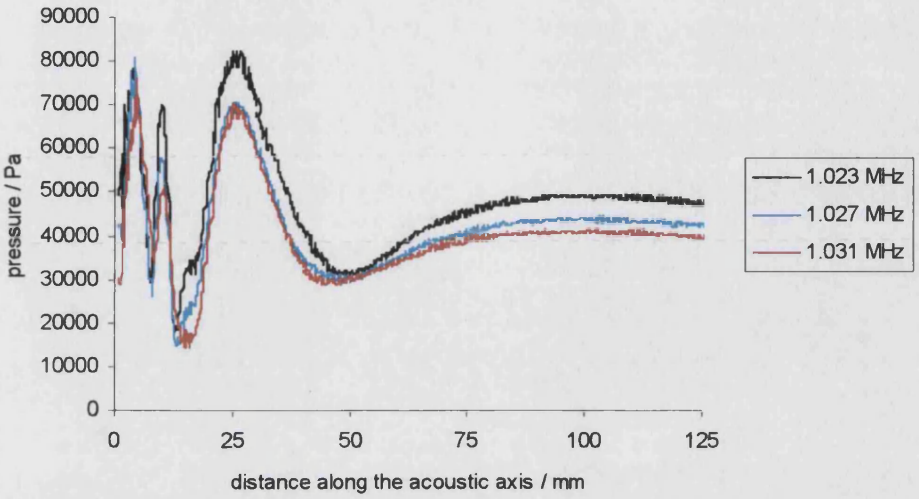

Figure 3.8 Measured axial response of the device at 3 frequencies centred about the resonant frequency of 1.027 MHz. The pressure values shown here have been calculated using the hydrophone sensitivities shown in Table 3.2.

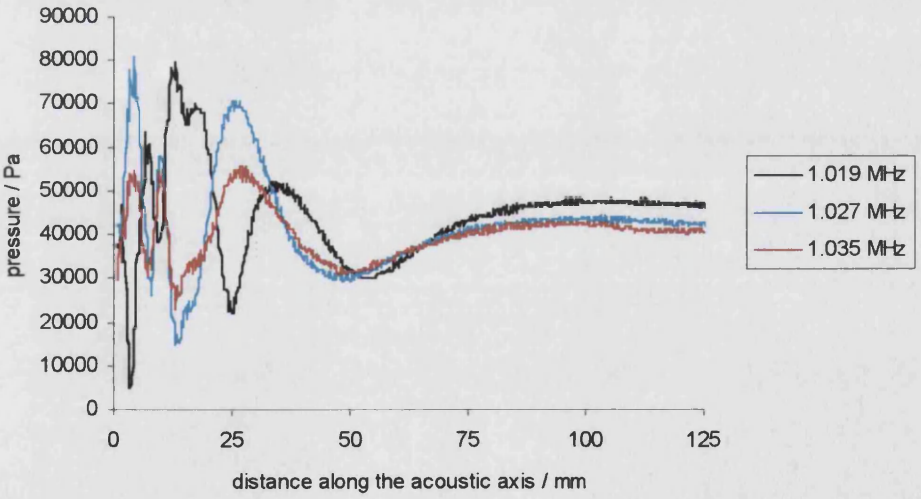

Figure 3.9 Measured axial response of the device at 3 frequencies centred about the resonant frequency of 1.027 MHz. There are clear differences in the features of the plots, particularly at 1.019MHz.

plots at 1.019 MHz and 1.035 MHz in addition to 1.027 MHz, shows some clear variations in the characteristics of the field. Figure 3.10 shows horizontal cross-axial output at 1.027 MHz and 1.031 MHz, and again although the general shape of the plot is consistent there are some obvious differences. These plots highlight the sensitivity of the device to operating frequency and suggest that the operating frequency may be significant for making accurate model-experimental near-field comparisons.

3.4.2 Repeat axial measurements

It has already been mentioned that the IEC standard was designed not to be overly sensitive to source and field inhomogeneities. In the case of model-experimental comparison however, a direct comparison between specific sections of the acoustic field would provide a good indication of the accuracy of the simulation. It must therefore be established how robust the *experimental* measurements are in critical areas of the field, so that an effective comparison can be made. Despite the efforts of the IEC standards derivation some parameters do rely on fairly specific measurements. For example the beam-alignment axis must be determined and along with it the peak pressure value in the field. It was therefore reasonable to consider how repeatable the beam-alignment process was. Repeat axial measurements were therefore made at the same frequency after realignment of the transducer to establish the repeatability of the experimental process. Figure 3.11 shows comparisons of three axial scans at 1.027 MHz made at various times when the scanning tank equipment had been re-adjusted. It can be seen that there is the potential for significant differences in the definition of the axis, particularly close to the source. Although two of the scans are in good agreement the third is somewhat different. It is likely that some error was made in finding the acoustic axis in this case, something that will be considered more closely when looking at model results in Chapter 5. These plots would suggest that although the IEC standard procedure for establishing the acoustic axis may be acceptable for characterisation of the generated field, care must be taken when making direct model-experimental axial comparisons. The output shown here

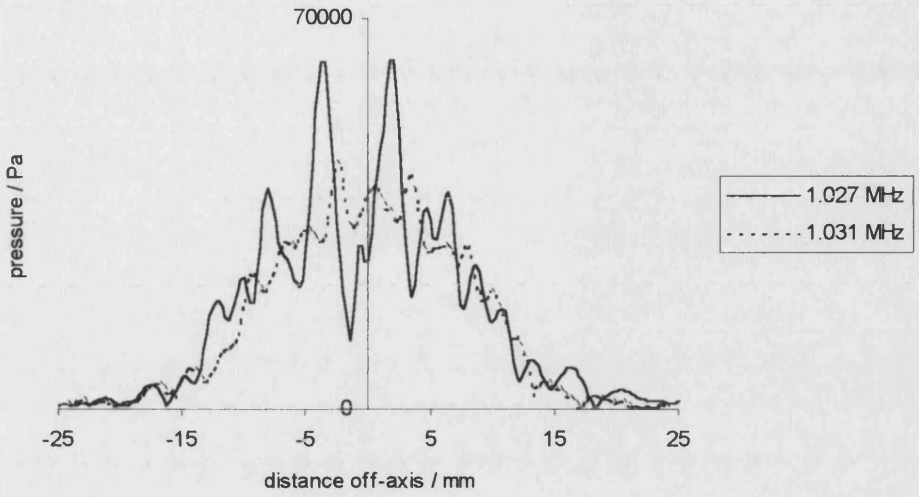

Figure 3.10 Horizontal cross-axial response at 10 mm from the source at 1.027 MHz and 1.031 MHz. The data has been re-centred for the purposes of comparison. Here the beam intensity is evenly distributed about the acoustic axis.

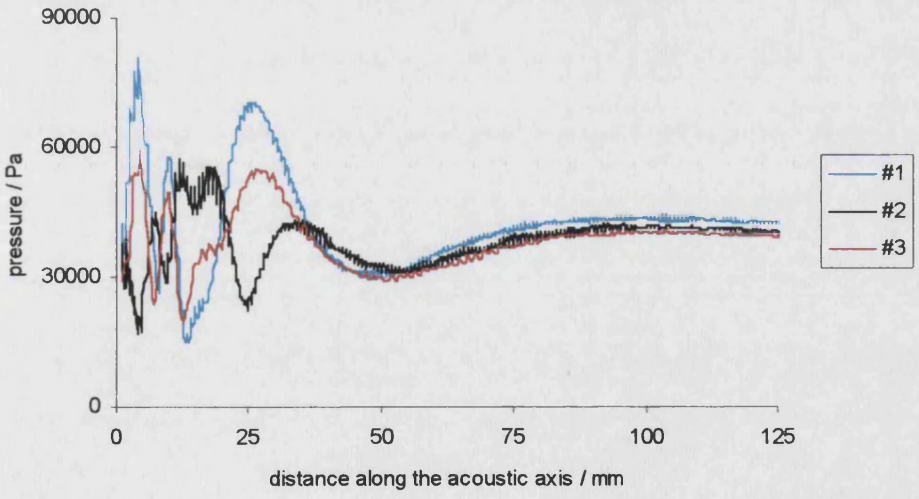

Figure 3.11 Repeat axial scans at 1.027 MHz made at different stages during the experimental process.

suggests that the position and amplitudes of the last on-axis minima and maxima are a feature that can be measured repeatedly with some success. However the position and amplitude of other maxima and minima close to the device are clearly less reliable. Axial comparison with model output in Chapters 5 and 6 will be made with this in mind.

There are two further points to note here. Firstly it will be seen that both real axial and cross-axial/planar scans shown here are significantly different from analytical output for an idealised plane piston source. This emphasises the need for a comprehensive assessment of the field due to a real device, as opposed to relying on idealised predictions, for the evaluation of models. Secondly, when the physiotherapy device was constructed there was some concern that it might not behave similarly to a "mass-produced" physiotherapy device used for medical purposes. In fact there are a number of reasons to believe that the device used here was behaving in a similar manner to 'typical' physiotherapy devices. Firstly the measured IEC parameters have conformed to standard physiotherapy transducer values. Secondly, comparisons of field measurements made here with those reported by Hekkenberg et. al. (1994) and Hekkenberg (1998) suggest that the main characteristics of field are consistent. Thirdly, these results were obtained at NPL, where such measurements are made on a regular basis; the field characteristics observed here are typical of those seen for other physiotherapy devices (private communication).

3.4.3 Repeat cross-axial scans

The potential for variation between successive raster scans raises different issues from the repeatability of axial scans. Clearly if a plane is scanned the overall characteristics of the field will be retained in the measurement even if the central point, about which the measurement is made, varies. What is significant here, however, is the accurate positioning of the hydrophone at a given distance away from the source where the planar scan is to be made. As the initial positioning of the hydrophone at the face of the transducer was made by hand, before it was moved a

specific distance away, inaccuracies might be expected here. In addition the axial and cross-axial scans in Figures 3.8-3.11 suggest that the exact position of field features such as maxima and minima are highly sensitive to the operating frequency, particularly close to the source. All of this could again prove significant in terms of making model-experimental planar comparisons at specific distances away from the device. In order to investigate this a series of cross-axial scans were made at 4.0, 4.5, 5.0, 5.5, and 6.0 mm from the source as well as at 9.0, 10.0, and 11.0 mm. Whilst rapid variations on a small scale might not significantly effect the IEC parameters measured they could clearly be significant if the response of the model is somewhat different to that of the real device. Furthermore such scans provide considerable insight into the variation of the field close to the source. Figure 3.12 shows the horizontal scans at 4.0-6.0 mm, and Figure 3.13 shows the scans at 9.0-11.0 mm, for the transducer operating at 1.027 MHz in both cases. It can be seen in both cases that although the overall nature of the field is reasonably consistent there is some variation. In particular there are some noticeable pressure changes moving away from the source between 4.0 mm and 6.0 mm. Some account will need to be taken of this type of extreme variation close to the source when model-experimental comparisons are made.

3.4.4 Parallel axis measurements

The planar scan shown in Figure 3.6 clearly suggests that the generated field is not truly axi-symmetric. This is in contrast to the model where axi-symmetry is assumed. Some assessment of the potential significance of such asymmetry on the model-experimental comparison is therefore useful. A reasonably straightforward way of investigating this is to make a set of scans *parallel* to the axis to establish the effect of moving off-axis. Figure 3.14 shows the series of measurements that were made in succession, on the acoustic axis and at 0.5 mm, 1.0 mm and 2.0 mm parallel to the acoustic axis when the transducer was operating at 1.027 MHz. It should be noted that the axial scan used here is the one that is in very poor agreement with the other two in Figure 3.11. The 0.5 mm and 1.0 mm scans show good agreement with the

axial one, however there is clearly some variation when measuring further off-axis. These results, along with the repeat axial scans again suggest that care will need to be taken when comparing the axial scan of the *circularly symmetric* model with that of the real device.

3.5 Summary

This chapter has considered the design and construction of a physiotherapy transducer and its corresponding transducer model. The real device has been shown to be an effective physiotherapy device, meeting the requirements of the IEC standard for physiotherapy transducers, and having field characteristics consistent with physiotherapy devices in general. It has also been observed that the generated field is considerably different from that of an ideal piston transducer. Furthermore it has been seen that there are a number of experimental considerations such as the location of the acoustic axis, the operating frequency, and distance from the source where minor changes have the potential for making a significant difference to the measured results. Care will clearly be required when making model-experimental comparisons for the near-field close to the transducer. This will be considered further in Chapter 5.

The following chapter will complete the assessment of the modelling process by establishing the effectiveness of the various techniques for modelling an unbounded acoustic region. Once an effective model of the unbounded fluid region has been generated, a complete model of the transducer radiating into such a fluid region will be generated. The experimental measurements shown in this chapter can then be compared with model output in Chapter 5.

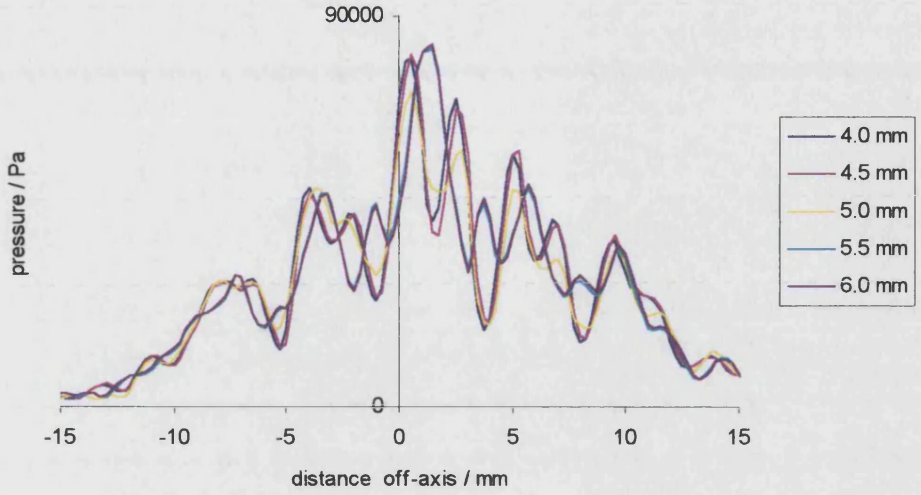

Figure 3.12 Cross-axial horizontal scans at 1.027 MHz. The output shown is made up of five cross-axial scans between 4.0 - 6.0 mm inclusive, in steps of 0.5 mm. The scans have NOT been re-aligned about the acoustic axis here.

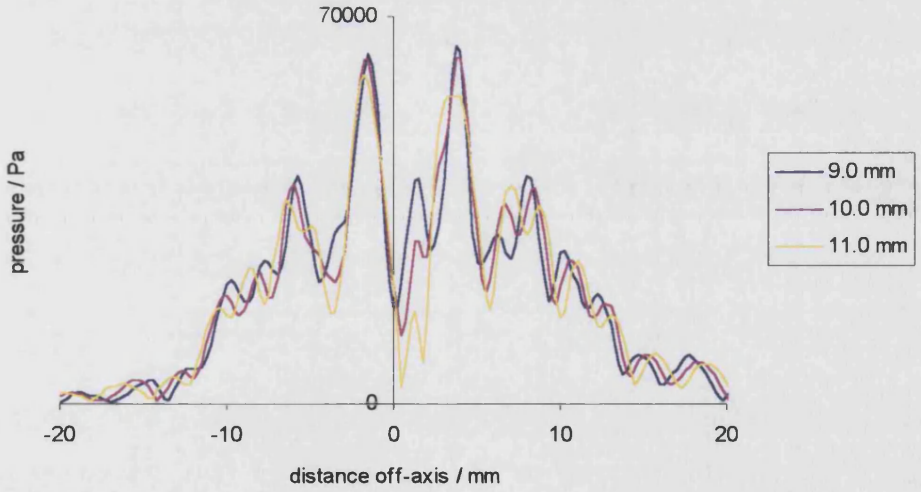

Figure 3.13 Cross-axial horizontal scans at 1.027 MHz. This output is made up of three cross-axial scans between 9.0 - 11.0 mm inclusive, in steps of 1.0 mm. Again the scans have NOT been re-aligned about the acoustic axis.

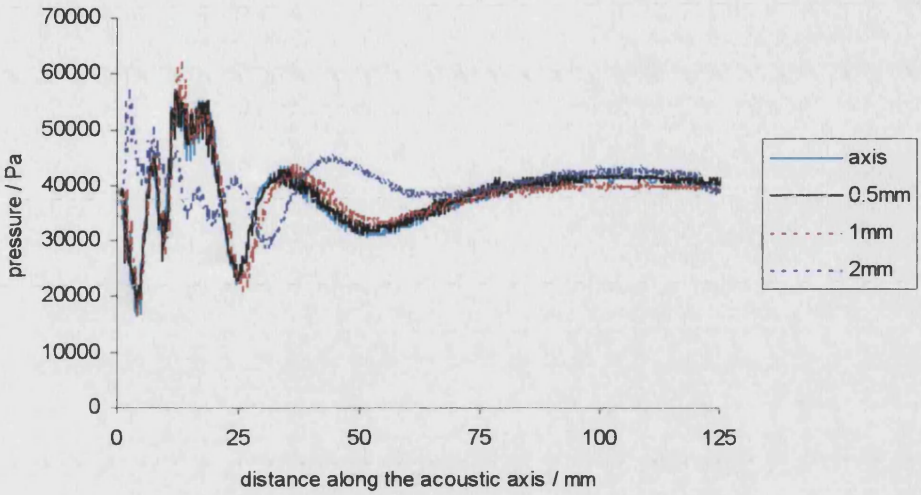

Figure 3.14 *Parallel* 'axial' scans on the acoustic axis and at 0.5 mm, 1.0 mm, and 2.0 mm parallel to this axis. There is reasonable consistency up to the 1.0 mm scan but clearly not at the 2.0 mm one.

Chapter 4

4.1 Introduction

A significant problem when considering solving the problem of a body radiating into an unbounded fluid region by FEM is that of how the unbounded region is to be modelled. As outlined in Chapter 2, one of three approaches is generally adopted. The first is to mesh with standard acoustic elements out to some (large) distance and apply an appropriate boundary condition. Often such an approach is computationally expensive, if not prohibitive, as is the case here. The second is to employ some sort of 'infinite' element that radiates pressure outwards, incorporating both wave-like variation and a decay term so that the pressure decreases towards zero at infinity. PAFEC employs wave envelope elements as their "infinite" elements. The third approach is to use boundary elements. Here only the fluid region on the surface of the radiating structure is discretised, and some fluid-structure relationship used in conjunction with the structural force-displacement equations so that the entire problem can be solved. When the fluid-structure interaction has been solved, exterior field values can easily be calculated.

Chapter 2 introduced the basic features of WEEs and two BEM options, CHIEF and DAA2c. Within the literature there is little discussion of which of these techniques are appropriate for the specific types of problem considered here. This chapter will now consider and compare these methods for modelling the near-field of high frequency, axi-symmetric, idealised sources radiating into unbounded fluid regions. Consideration will be given to the practical use of the models including computational requirements and simulation run times. Particular attention will be given to the WEE models for which it will be seen that a number of features must be addressed correctly for a successful simulation. The formulation of WEEs will be considered to establish how its features effect the accuracy of a fluid-structure system modelled in this way. Having established which fluid modelling techniques are appropriate for use here Chapter 5 will combine the structural model generated in

Chapter 3 with the fluid models used here to generate a model of the complete system.

4.2 Wave envelope elements

Possibly the most important features of the WEE, in terms of their practical use here, are the shape function and global-to-local mapping used to map an "infinite" element onto a finite one. These parts of the element formulation will therefore be considered in some detail. The formulations presented are based on the work of Astley et al. (1994), Astley (1996), Astley (1998), Astley et. al. (1998), Astley & Hamilton (2000), and Cremers et. al. (1994). In particular the work presented in Astley et. al. (1998) offers considerable insight into the practical issues associated with using WEEs.

4.2.1 WEE shape functions and global-to-local mapping

Figure 4.1a shows the geometry of an individual 2-D wave envelope element. As discussed in Chapter 2, shape functions must be generated that will relate the unknown in the element to the unknowns at element nodes only, as in

$$h(x,y) = \underline{N}(x,y)\underline{h} \ . \qquad (4.1)$$

Although the 2-D problem will be considered here the approach is applicable to the 3-D case. In the simple quadrilateral problem, considered in Chapter 2, the shape-function is generated by considering the Lagrange polynomial that passes through the nodal points. Here, however, several other points must be taken into consideration:

- The element must incorporate wave-like variation in the radial direction.
- It must also incorporate an appropriate decay term in the radial direction so that the field value decays to zero as the radial distance, r, tends to infinity.

- When using WEEs the approach is to use standard acoustic FEs between the source and the WEEs. Consequently at the acoustic FE-WEE interface the WEE must be compatible with standard acoustic FEs, in particular in the *angular* direction

As can be seen from Figure 4.1a the element is defined with two nodes on the acoustic-WEE interface, nodes 1 and 2 that are respectively distances a_1 and a_2 away from the "virtual sources" from which they originate. It is these *base* nodes at the interface that define the essential features of the element. Additional *mapping* nodes 3 and 4 at distances a_1 and a_2 away from nodes 1 and 2 in the radial direction respectively, are used for the global-to-local mapping of the element and to define the nature of the decay term. If quadratic acoustic FEs were used here, nodes 1-2 in the angular direction would include another node between them. There would also be another node in the radial direction between nodes 3 and 4.

The wave-like variation in the radial direction can be accommodated by the inclusion of an exponential term. The shape function for a node l can be defined as

$$\varphi_l(x,y) = P_l(x,y)e^{-ik(r-a_i)} \qquad (4.2)$$

where r is the distance along the radial edge measured from its "virtual source". At the acoustic-WEE interface where $r = a_i$, (i=0, 1, 2), the exponential term reduces to unity. $P_l(x,y)$ corresponds to the "conventional" basis function relating the variation in the element to the variation at the elemental nodes. The formulation of this term will be outlined shortly.

As in previous problems a global to local mapping will enable a generic element to be derived. In this case it is this mapping that enables the infinite region in Figure 4.1a to be mapped into a finite space. Consider Figure 4.1b, which shows the parent element used in Figure 2.2b. The mapping from the global to the parent element is as follows

Node	Global	Parent
1	(x_1, y_1)	(−1,−1)
2	(x_2, y_2)	(−1,1)
3	(x_3, y_3)	(0,−1)
4	(x_4, y_4)	(0,1)

This can be expressed as

$$x = \sum_{i=1}^{4} M_i(\zeta,\xi)x_i \quad \text{and} \quad y = \sum_{i=1}^{4} M_i(\zeta,\xi)y_i, \qquad (4.3)$$

where

$$M_1 = \frac{(1-\xi)\zeta}{(\zeta-1)},\ M_2 = \frac{-(1+\xi)\zeta}{(\zeta-1)},$$

$$M_3 = \frac{-(1-\xi)(1+\zeta)}{2(\zeta-1)} \text{ and } M_4 = \frac{-(1+\xi)(1+\zeta)}{2(\zeta-1)}. \qquad (4.4)$$

It can be seen that this enforces the following mapping along the radial edge of an element

$$\zeta = 1 - \frac{2a_i}{r} \qquad (4.5)$$

where i=0, 1,..., 4. For WEEs the decay term used in the 2-D case is a polynomial in $1/\sqrt{r}$, and for the 3-D case is a polynomial in $1/r$. From the mapping in Equation 4.5 it can be seen that this is the same as polynomials in $\sqrt{1-\zeta}$ and $(1-\zeta)$ respectively. Consider the 2-D case of $L_j^m(\sqrt{1-\zeta})$, a Lagrange polynomial in $\sqrt{1-\zeta}$, as defined in Chapter 2, where m represents the number of terms in the polynomial and j represents the node within that element. For the generic element in Figure 4.1b, the polynomial for the base node 1, say, would be

$$L_1(\sqrt{1-\zeta}) = \frac{(\sqrt{1-\zeta}-\sqrt{1})}{(\sqrt{2}-\sqrt{1})} = \sqrt{\frac{a_i}{r}} \quad . \qquad (4.6)$$

This is a first order polynomial in $1/\sqrt{r}$. Similar terms for base node 2 and mapping nodes 3 and 4 would also result. An extension to this formulation is to increase the order of the polynomial in $1/\sqrt{r}$. Consider now Figure 4.2 showing a generic WEE with 5 nodes along each radial edge, equally spaced between $\zeta = -1$ and $\zeta = 0$. Using this formulation the same node, base node 1, would now have a polynomial

$$L_1\left(\sqrt{1-\zeta}\right) = \frac{\left(\sqrt{1-\zeta}+\sqrt{1+\frac{3}{4}}\right)\left(\sqrt{1-\zeta}+\sqrt{1+\frac{1}{2}}\right)\left(\sqrt{1-\zeta}+\sqrt{1+\frac{1}{4}}\right)\left(\sqrt{1-\zeta}-\sqrt{1}\right)}{\left(\sqrt{2}+\sqrt{1+\frac{3}{4}}\right)\left(\sqrt{2}+\sqrt{1+\frac{1}{2}}\right)\left(\sqrt{2}+\sqrt{1+\frac{1}{4}}\right)\left(\sqrt{2}-\sqrt{1}\right)} \qquad (4.7)$$

which is now a fourth order polynomial in $1/\sqrt{r}$. The element shown in Figure 4.2 is classed as a WEE with *radial order* 5, referring to the number of nodes (base and mapping) in the radial direction. It will be seen that increasing the radial order of an element will, in some cases, allow the WEE-acoustic FE interface to be moved closer to the radiating source. A final point to note is that at a specific node j, $L_j(\sqrt{1-\zeta})$ is unity for ζ_j and zero at all other radial nodes.

So far consideration has been given to the wave-like term and the radial decay term in the WEE basis function. It was also mentioned above that the WEE and acoustic FE must be compatible at the WEE base nodes. Both the exponential term and polynomial decay term in $1/\sqrt{r}$ have been shown to be unity at the base nodes of the WEE. To complete the definition of the WEE shape function, some account must be taken of the WEE-FE compatibility in the *angular* direction, defined by the ξ co-ordinate in the generic formulation. An interpolated value of the "virtual source" is

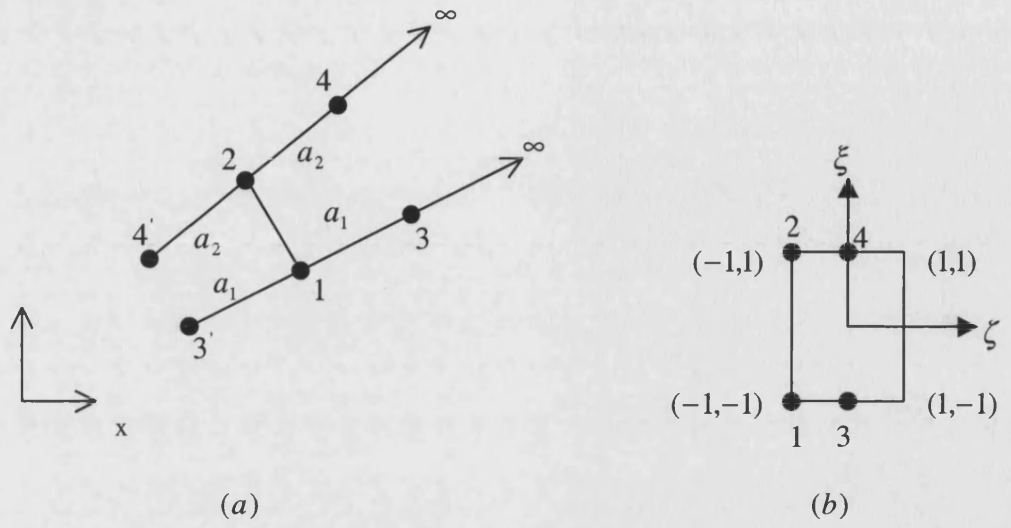

(*a*) (*b*)

Figure 4.1 Geometry of an individual wave envelope element. (a) The geometry of the problem in the global system, and (b) The mapping that allows the infinite domain to be mapped to the finite domain of [-1,1], [-1,1]. This is for the 2-D case.

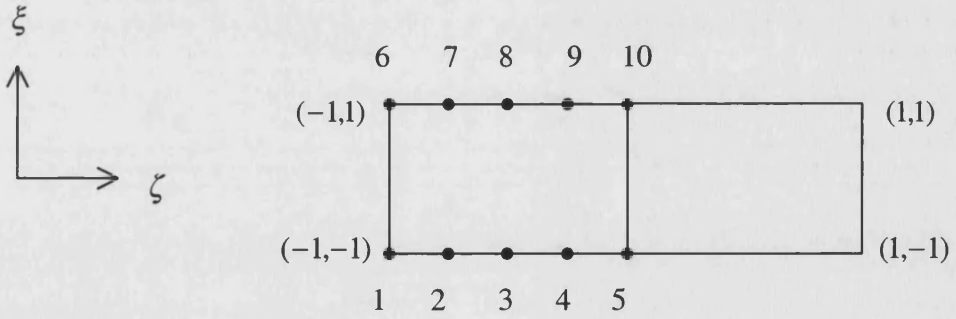

Figure 4.2 Geometry of a (generic) WEE of radial order 5. Here nodes 1 and 6 are *base* nodes and nodes 2-5 and 7-10 are *mapping* nodes used for the definition of the decay term.

therefore required. To this ends a continuous quantity $a(\xi)$ is defined over the base of the element

$$a(\xi) = \sum_{i=1,2} S_i(\xi) a_i \qquad (4.8)$$

where $S_i(\xi)$ are the shape functions defined over the base of the parent element. In this case, for *linear angular* shape functions, there are two terms for base nodes 1 and 2 in Figure 4.1b, or 1 and 6 in Figure 4.2. For Figure 4.1b, Equation 4.8 can be written as

$$a_i = a(\xi) = [(1-\xi)/2]a_1 + [(1+\xi)/2]a_2 \quad . \qquad (4.9)$$

For a quadratic element the *quadratic angular* shape functions $S_i(\xi)$ would be used. The "conventional" term $P_l(x, y)$, is now defined as a combination of the Lagrange polynomial term and the angular shape function

$$P_l(x, y) = \frac{1}{\sqrt{2}} . S_i(\xi) . \sqrt{1-\zeta} . L_j^m(\sqrt{1-\zeta}) \quad . \qquad (4.10a)$$

The additional term, $\sqrt{1-\zeta}$, is included so that there are no constants in this expression. This ensures that the shape function is of the form

$$\varphi_l \sim \left\{ \frac{\chi_1}{\sqrt{r}} + \frac{\chi_2}{\sqrt{r}^2} + ... + \frac{\chi_m}{\sqrt{r}^m} \right\} e^{-ik(r-a_i)} \quad . \qquad (4.11)$$

As multiplying by $\sqrt{1-\zeta}$ is equivalent to multiplying by $\sqrt{\frac{2a_i}{r}}$, from Equation 4.5. This ensures that $\varphi_l \to 0$ as $r \to \infty$, i.e. $\zeta \to 1$. The additional $1/\sqrt{2}$ in Equation

4.10a is then required so that $P_l(x,y)$ is unity at the *base* nodes (where $\zeta = -1$), as required. The "standard" formulation, ensuring that the shape function is equal to unity at a given node and zero at all others, is lost here for *mapped* nodes by the inclusion of these terms. This is not significant, however, as the purpose of these elements is to provide strategic points for the formulation of the decay term. Combining Equations 4.2, 4.5, 4.8 and 4.10a then gives a complete basis function in local co-ordinates

$$\varphi_l(x,y) = \frac{1}{\sqrt{2}}.S_i(\xi).\sqrt{1-\zeta}.L_j^m(\sqrt{1-\zeta}).e^{-ika(\xi).(1+\zeta)/(1-\zeta)} \quad . \qquad (4.12)$$

This formulation can be extended to three dimensions where the polynomial decay term would be in $1/r$ and the equivalent formulation for the "conventional" term would be

$$P_l(x,y) = \frac{1}{2}.S_i(\xi).(1-\zeta).L_j^m(1-\zeta) \quad . \qquad (4.10b)$$

One significant feature of a commonly used WEE formulation, and incorporated by PAFEC, is that the same virtual source and distance to the WEE interface, a_i, is used for all elements. This means that the quantity $a(\xi)$ in Equations 4.8, 4.9 and 4.12 can simply be replaced by the constant a_w.

This completes the formulation of the shape functions for a WEE. From Equations 4.2, 4.10 and 4.12 it can be seen that the formulation meets all necessary requirements. The exponential term accounts for the wave-like variation. The Lagrangian term accounts for the polynomial decay term with distance. The infinite-to-finite mapping accounts for a zero pressure condition at the outer edge of the element, making the wave-like variation exclusively outward travelling. And the final expression is formulated so that it is equal to unity at base elements, making it compatible with acoustic FEs.

4.2.2 Element formulation

Having defined the shape functions for a WEE relating the pressure variation within the element to pressure values at nodal points, the element formulations can now be considered. As in Chapter 2, the equations governing the variation of the primary unknown within the element, pressure, must first be defined. In fact these equations are exactly the same as those for the classical radiation problem considered in Chapter 2, section 2.4.3. They are repeated here and shown in Figure 4.3. Firstly, pressure in the acoustic region, p, must satisfy the Helmholtz wave equation

$$\nabla^2 p + k^2 p = 0 \quad . \qquad (4.13)$$

Secondly, in the "classical radiation" problem, pressure on the surface of the structure is related to outward normal velocity. Here the corresponding expression relates pressure on the base of the element to outward normal velocity

$$\partial p / \partial n_\xi = -i\omega\rho v_n(\xi) \qquad (4.14)$$

on the interface surface S_1. Thirdly the radiation condition at the outer edge of the element is

$$r^\alpha \left(\frac{\partial p}{\partial r} + ikp \right) \to 0 \text{ as } \quad r \to \infty . \quad (4.15)$$

As in Chapter 2 this can be replaced by a radiation condition imposed at some far field boundary, S_2,

$$\nabla p \cdot n_2 + ikp = 0 \text{ on } S_2 \quad . \qquad (4.16)$$

The formulation and solution of the system of equations describing the simulation now follows the procedure set out in Chapter 2, sections 2.25-2.27. Firstly, following the Galerkin residual process, a trial function $p^{'}$, is proposed in terms of known basis functions φ_l and unknown coefficients q_l

$$p^{'} = \sum_{l=1}^{\eta} q_l \varphi_l . \qquad (4.17)$$

Here η is the total number of nodes in the system. Next a residual is defined for each of the governing Equations, 4.13, 4.14 and 4.16 and these residuals are minimised thus forcing the trial solution to be equal to the real solution. It is this minimisation of *all* of the governing expressions for *all* elements and *all* nodes that generates a set of equations describing the behaviour of the system conforming to the governing equations. This produces a set of 3η equations in η unknowns, which are then combined to yield a system of η equations that can be described as

$$[\mathbf{K}+ik\,\mathbf{R}-k^2\mathbf{M}]\,q=\mathbf{F}, \qquad (4.18)$$

where

$$q = [q_1, q_2, ..., q_\eta]^T , \qquad (4.19a)$$

$$\mathbf{K}_{ij} = \int_V (\nabla W_i \cdot \nabla \varphi_j) dV , \qquad (4.19b)$$

$$\mathbf{R}_{ij} = \int_{S_2} (W_i . \varphi_j) dS , \qquad (4.19c)$$

$$\mathbf{M}_{ij} = \int_V W_i . \varphi_j dV , \qquad (4.19d)$$

and $$\mathbf{F}_i = \int_{S_1} ik\rho c\, W_i . v_n dS\,. \qquad (4.19e)$$

The significant difference now between the standard Galerkin formulation and the technique used here is in the choice of weighting functions, W_i. In a standard formulation, as in Chapter 2, the weighting functions are chosen to be the same as the basis functions giving symmetric coefficient matrices in the system such as in Equation 4.18. In the case of WEEs, however, the weighting functions are made up of a product of three terms:

$$\left(\frac{a_i}{r}\right)^2 P_i e^{ik(r-a_i)}. \qquad (4.20)$$

From Equation 4.2 it can be seen that the second and third terms here are similar to the basis function φ_i except that the exponential term, $e^{ik(r-a_i)}$ is the complex conjugate of the term in the basis function. This eliminates the exponential from all integrals making them easier to evaluate. The first term, $\left(\frac{a_i}{r}\right)^2$, is included to make the volume integrals in the "stiffness" and "mass" matrices in Equations 4.19b and 4.19d respectively, and the "damping" matrix in equation 4.19c, finite as $r \to \infty$ (Astley et. al., 1994).

The expansion of the system of Equations 4.18 follows. The WEE system equations are then easily combined with the standard acoustic FE formulation at coincident nodes. It should be emphasised that for the acoustic FEs the weighting functions remain the same as the basis functions, as described in Chapter 2. Again as in Chapter 2, this set of equations can be combined with structural equations to form a system simulating a source radiating into an unbounded fluid region modelled with acoustic FEs close to the source and a layer of WEEs outside this. Boundary conditions can

then be incorporated and the full set of equations solved by Gaussian elimination or some such technique.

This completes the outline of the theoretical basis of WEEs. Next consideration will be given to how these elements are used in practice and how the parameters described in the formulation of the WEE equations effect such simulations.

4.3 Radiating systems incorporating acoustic FEs and WEEs

To begin, consider Figures 4.4 and 4.5 showing WEE model predictions for the axial variation and radial variation at a range of 5 mm from an ideal source, respectively. These predictions are for a 12.55 mm radius, axi-symmetric, ideal, plane piston source operating in continuous wave mode. The cylindrical structure here is 31.77 mm long with a radius of 15.885 mm. The operating frequency is 1.030 MHz equating to an acoustic wavelength of less than 1.5 mm in water. These parameters were chosen to correspond to the equivalent physiotherapy device described in Chapter 3. An ideal source was generating by restraining the structural elements in the source to displace with uniform phase and amplitude in the direction of the acoustic axis only. A constant amplitude displacement of 1.0E-09 m was prescribed. This was an arbitrary choice but was of the order of the source displacement of a real device. All other structural elements were completely restrained. All model results were generated on a Viglen genie P3 500MHz PC. Here the model incorporates both acoustic FEs and WEEs. As discussed in Section 4.2.1, a number of parameters must be specified in order to generate the (unbounded) acoustic region of such a model. Figure 4.6 shows the features of the acoustic region that must be considered. Details of these features for the plane piston model considered here are:

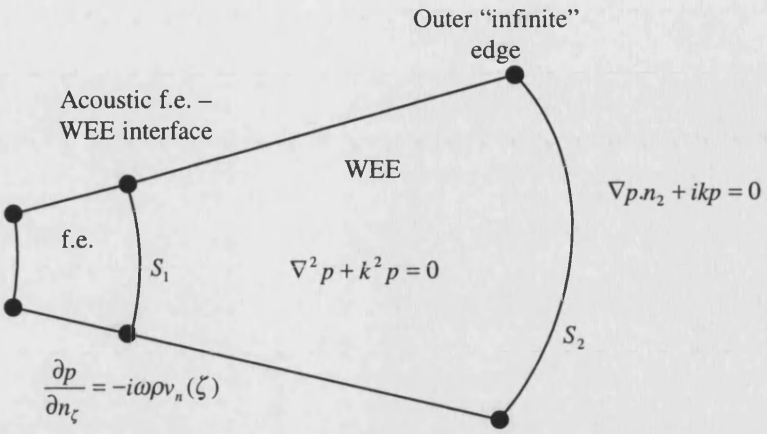

Figure 4.3 Governing equations for a wave-envelope element (WEE).

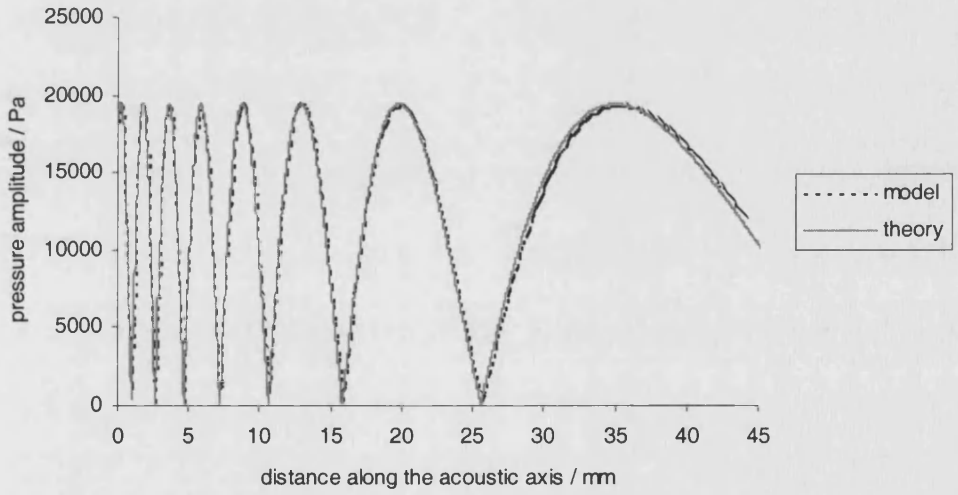

Figure 4.4 Model/theoretical axial response for a 12.55 mm radius, ideal plane piston source operating at 1.030 MHz.

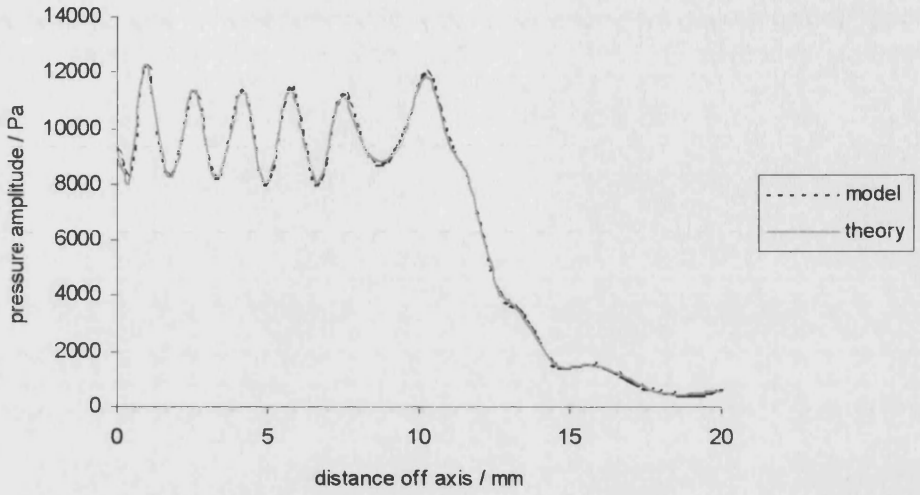

Figure 4.5 Model/theoretical radial response at 5 mm from the source for a 12.55 mm radius, ideal plane piston source operating at 1.030 MHz.

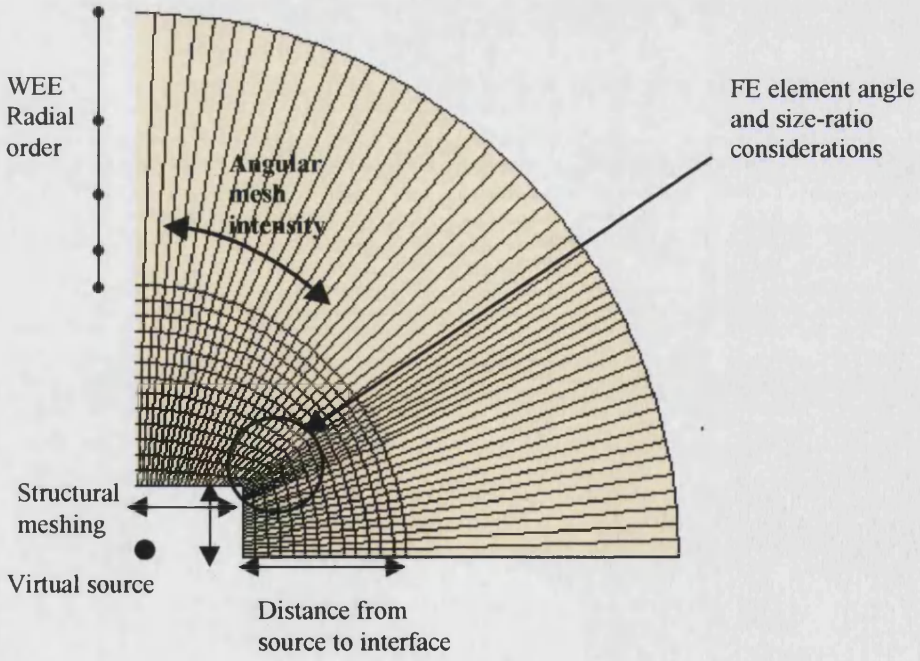

Figure 4.6 Modelling considerations for a cylindrical structure with "rectangular" cross-section radiating into an unbounded fluid region modelled with acoustic FEs and WEEs.

- The radial order of the WEEs is 9
- The *axial* distance from the source to the acoustic-WEE interface is 44.115 mm, and therefore the shortest distance from the structure to the WEE interface is 37.535 mm at the top corners of the structure.
- The "virtual source" of the WEEs is in the centre of the structure on axis – that is 15.885 mm behind the face of the piston radiator.
- The angular mesh intensity along the acoustic-WEE interface is 3 elements per wavelength throughout the whole of this boundary – this in turn determines the meshing on the structure which, by the nature of the geometry of the problem, is therefore significantly larger than 3 elements per wavelength (of the order of 6-10 elements per wavelength).
- The acoustic element meshing in the *radial* direction is over 6 elements per wavelength.
- The total number of nodes in the model is approximately 236,000. Here this is very close to the total number of d.o.f. as the majority of the model is made up of acoustic FEs with only one d.o.f. per node.
- The run time of the model (for one frequency) is approximately 5 hours.
- Whilst running the PC requires in excess of 2 GBytes of memory space.

In Figures 4.4 and 4.5 the model results are compared with analytical predictions obtained using a numerical integral solution to Equation 1.4. Very good model-theoretical agreement is observed, although there are some signs of reflections from the FE-WEE interface towards the edge of the axial output (for $z > 30$ mm). (It should also be noted that although axial data is only presented here up to the interface, propagating the source data using a simple routine can generate results further along the axis. This technique is used to generate output for the physiotherapy transducer WEE model in Chapter 5.) The accuracy of the model used here is due to the fact that all of the above mentioned parameters were specified effectively. It should be noted that inappropriate choices of these parameters can give rise to erroneous results and that in practice it took significant effort to obtain the agreement

shown. The effect of each of the model parameters on model output will now be considered in detail.

4.3.1 Radial order

It was observed earlier that the radial order refers to the order of the polynomial used for the decay term in the shape function of the WEE. Astley et. al. (1998) discussed how WEEs of radial order m are capable of exactly representing multi-pole fields of order $m-1$. It has previously been discussed (Zienkiewicz et. al., 1983; Cremers & Fyfe, 1995) how a combination of higher radial orders for the WEEs and a relatively large region of acoustic FEs, allow the WEEs to better approximate the behaviour of standard acoustic elements. This allows for a better approximation to the unbounded field of a given source and emphasises the dependence of the accuracy of the solution on both the order of the WEE and the modelled acoustic FE region.

In practice, however, for many of the models considered elsewhere (Cremers et. al., 1994; Astley et. al., 1998) radial orders up to orders 5 or 6 have been adequate for the successful simulation of the surrounding unbounded fluid region. Indeed there has been some discussion (Cremers & Fyfe, 1995; Astley et. al, 1998; Morgan et. al. 2000) of instability problems linked with models employing higher radial order WEEs. No such problems have been encountered here where models have been generated incorporating elements of radial order up to and including 10. In fact Figure 4.7, showing axial output for the same plane piston model considered above but this time with WEEs of radial order 6 and 8, shows a clear reduction in the accuracy as the radial order is decreased. The implication here is that *only* higher radial orders are capable of effectively simulating the surrounding unbounded fluid region for the system considered here. Although the reduction in radial order could be countered by an increase in the region of acoustic FEs, for this model increasing the extent of the FE region pushes both simulation run time and memory requirements towards the limits of the PC. It can be seen that some balance must be sought

between the position of the acoustic-WEE interface and the radial order of the WEE decay term.

4.3.2 Acoustic-WEE interface mesh intensity

Next, consider the angular mesh intensity requirement at the acoustic-WEE interface. The regularly quoted rule of thumb when using standard acoustic elements is that of at least 3 elements per wavelength, although significantly more intense meshing is also frequently advised. The original model, with radial order 9 restored, is now considered where the meshing is only one element per wavelength. The model axial output is compared with theory in Figure 4.8, where the accuracy of the agreement is again reduced. Having said that, considering the reduction in mesh intensity the corresponding reduction in accuracy is not overly concerning. However it must be emphasised that if the acoustic-WEE interface were to be brought closer to the structure the significance of the angular meshing would be more prominent. Astley et. al. (1998) highlights this, showing the intensity of the transverse (angular) resolution to be of particular importance at high frequencies for all multi-pole solutions.

Three further points should be made with respect to angular meshing requirements. Firstly, the meshing requirement must be retained throughout the whole of the acoustic-WEE interface, even where little variation in the field value is observed or expected. Secondly, increasing the mesh intensity here to some value significantly higher than 3 elements per wavelength shows little improvement compared with using a meshing of 3. Thirdly, the effect of the angular meshing on the mesh intensity throughout the rest of the model must be considered. The meshing at the interface has a direct effect on the meshing at the structure, and therefore on the acoustic FE region between the structure and the interface. A constant meshing requirement of 3 elements per wavelength at the interface is likely to mean a significantly more intense meshing requirement for both the acoustic FEs and the structure. This can lead to a significant increase in the number of d.o.f.s in the system, as here. Alternative meshing geometries on the structure are an option, however in practice this is

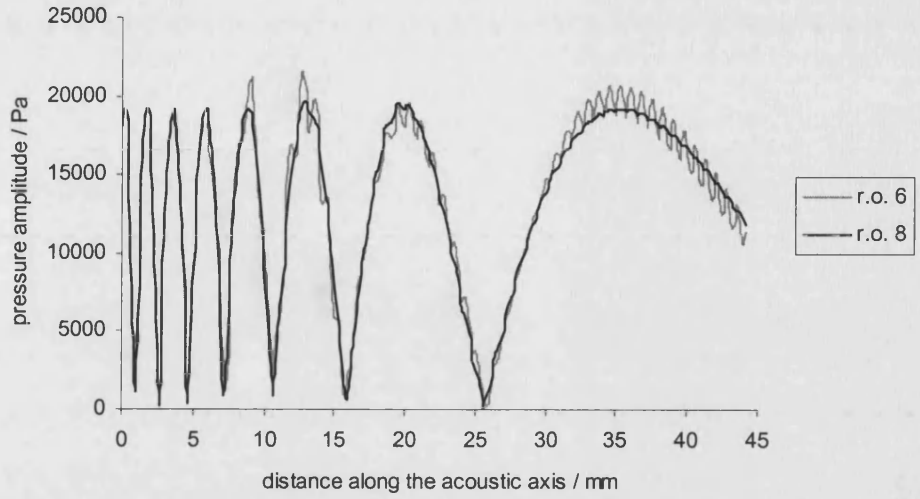

Figure 4.7 Model axial response for a 12.55 mm radius, ideal plane piston source operating at 1.030 MHz for models using WEEs with radial order 6 and 8.

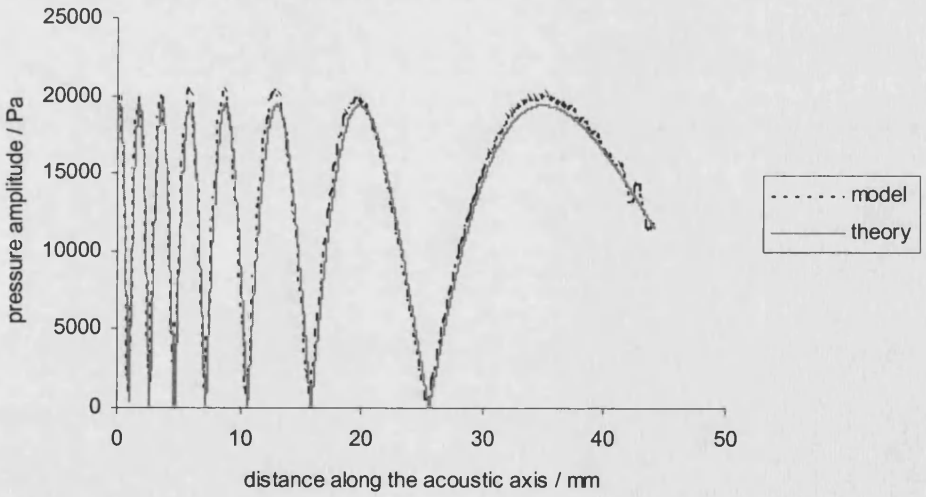

Figure 4.8 Model axial response for a 12.55 mm radius, ideal plane piston source operating at 1.030 MHz for a model where the meshing at the acoustic-WEE interface has been reduced from 3 elements per wavelength to one.

complicated by the fact that the meshing of separate sections on the structure must then correspond to meshing at the interface. This problem is magnified in the case of the real physiotherapy transducer model where there are a number of separate sections along the face of the device, corresponding to the disc, glue layer, inner and outer casing.

4.3.3 Meshing in the acoustic FE region

Now consider the meshing requirements in the acoustic FEs. The radial meshing used in the above model is approximately 6 elements per wavelength. Figure 4.9 shows how the axial output is changed when the meshing is reduced to 4 elements per wavelength. It can be seen that the model agreement is again less accurate. Two points are raised here. Firstly, a mesh intensity of at least 6 elements per wavelength would appear to be required *close to the source.* It can be shown that the mesh intensity around the structure meets this requirement in the angular direction due to the 3 elements per wavelength specification at the WEE interface. However further out, it has been observed that at the WEE interface a meshing of 3 is sufficient. So further away from the source it is possible that the radial meshing could also be reduced in line with angular meshing requirements. Secondly there are some practical considerations. There are restrictions on the ratio of the size of the sides of the quadrilateral acoustic FEs used, and indeed keeping the ratio of the sides as close to unity as possible is a reasonable requirement. It must be observed that, due to the semi-circular nature of the WEEs, at the top corners of the structure where the structure is closest to the WEE interface these size ratios are likely to be of even greater importance. Care must be taken that meshing requirements are simultaneously met in both directions without violating FE side restrictions.

4.3.4 (Relative) Distance from the source to the acoustic-WEE interface

Next consider the distance from the source to the WEE interface on axis. Figure 4.10 shows the results of a model where all parameters are kept the same as the standard

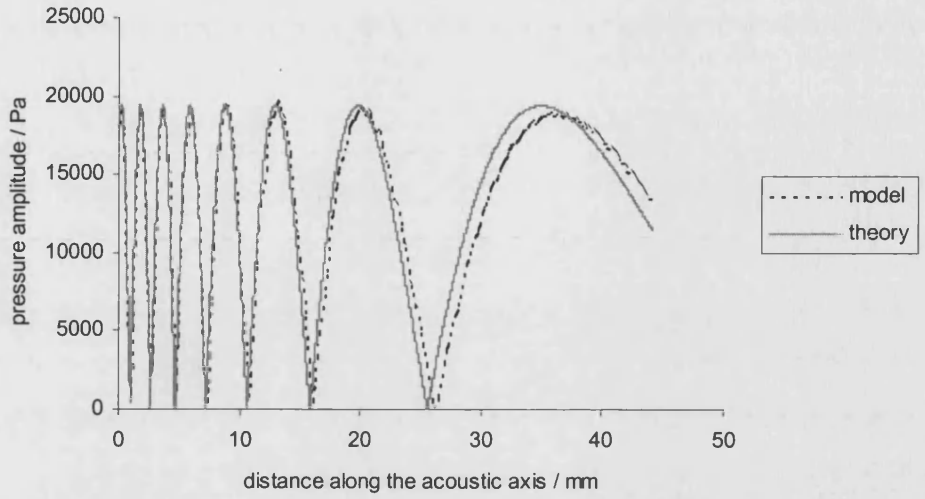

Figure 4.9 Model axial response for a 12.55 mm radius, ideal plane piston source operating at 1.030 MHz for a model where the meshing in the radial direction has been reduced from 6 elements per wavelength in the original to 4.

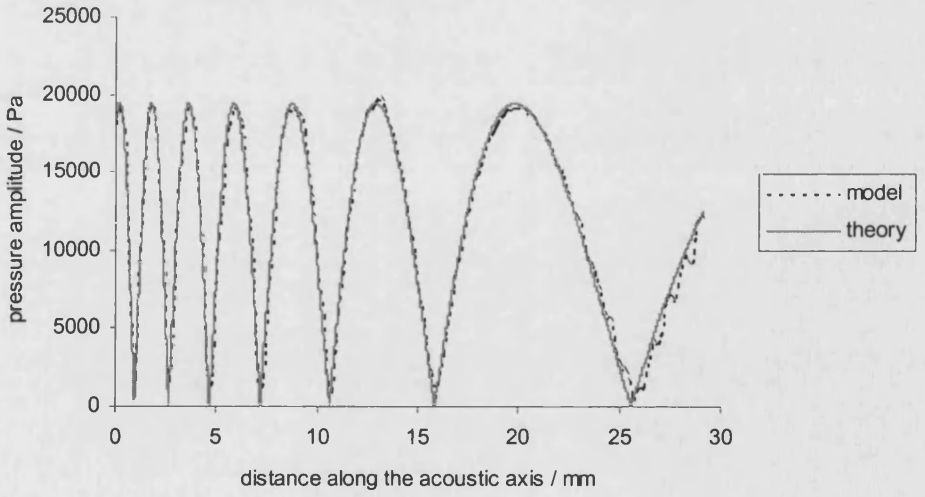

Figure 4.10 Model axial response for a 12.55 mm radius, ideal plane piston source operating at 1.030 MHz for a model where the distance from the source to the acoustic/WEE interface is reduced from 44.115 mm to 29.115 mm on axis.

case except that the distance from the source to the acoustic-WEE interface is reduced from 44.115 mm to 29.115 mm. This equates to a shortest distance of approximately 22.5 mm at the top corners of the structure. Again some reduction in the accuracy of the agreement is observed, and although it is not excessive it must be reiterated that this is for the case where all other WEE parameters remain unchanged.

4.3.5 Position of the WEE "virtual source"

Finally consider a model where the "virtual source", the central point about which the WEEs are defined, is moved closer to the active face of the source. Figure 4.11 shows the axial output, which would appear to be in better agreement than the original model. This is to be expected as moving the "virtual source" closer to the face of the structure means that the WEE interface is now the corresponding distance further away from the source on axis. This means that there is a much larger area of acoustic FEs in front of the source, and as discussed above this is likely to lead to an improvement in the approximation of the real field over the WEE interface. Considerations on the positioning of the WEE virtual source has been approached elsewhere (Cremers et. al., 1994). Frequently previous consideration has involved either point sources or spherical sources, where the geometry is ideally suited to the use of WEEs. Here Figure 4.12 shows the geometry of the model, emphasising that moving the position of the virtual source has a significant impact on the meshing considerations throughout the acoustic FE region. It should be noted that the number of elements in Figure 4.12 is substantially less than that in the idealised model for which axial and radial output have been presented.

There are three points to be considered here. First are the size ratios of the acoustic FEs. Because the "virtual source" has been moved closer to the source the acoustic FE region in front of the source is now larger, whilst the region behind the structure is now smaller. Increased meshing in the radial direction is required to accommodate the larger acoustic region in front of the source. However if the radial meshing is kept constant throughout the acoustic region this can lead to significant over-meshing in

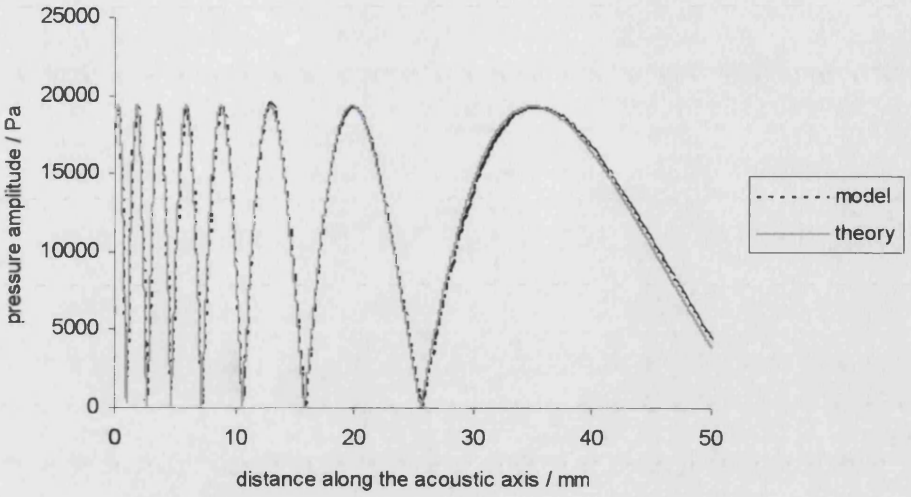

Figure 4.11 Model-theoretical axial response for a 12.55 mm radius, ideal plane piston source operating at 1.030 MHz where the "virtual source" of the model has been moved closer to the face of the piston.

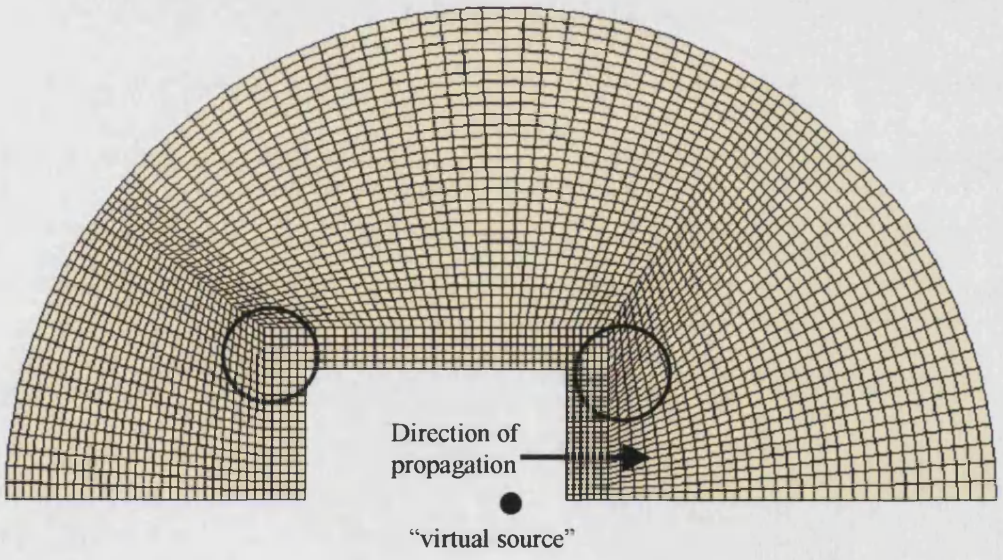

Figure 4.12 Geometry of the model of a 12.55 mm radius, ideal plane piston source operating at 1.030 MHz where the "virtual source" of the model has been moved closer to the face of the piston. Increased mesh intensity is required in some areas, and angles within the quadrilateral acoustic FEs are affected.

the radial direction at the back of the structure. The possibility of violating side-size ratio restrictions for the quadrilateral elements is therefore a distinct possibility. Although varying the mesh intensity in this region is an option it can be a complex task. Secondly there are the angles subtended in the elements at the face of the source. To define the WEEs the angles from their central point must be specified. These are dependent on the size of the structure and the distance to the interface. Again these angles must meet certain geometrical requirements for the variation in the quadrilateral element to be valid. In practice moving the position of the virtual source closer to the face of the structure, although beneficial in terms of solution accuracy, causes considerable increases in the angles here. Finally a mention must be made of the effect on mesh intensity on the structure. When the virtual source is moved closer to the face the angles generated in the FE region are larger and the distance to the interface in front of the source is greater, but the meshing requirement at the WEE interface remains 3 elements per wavelength. Therefore more elements will be required along the face of the source to accommodate these changes. This is not of great relevance here where only a face-plate is required for an ideal plane piston model. However when the physiotherapy model is considered, the structural meshing is much more significant and increasing the meshing here can significantly increase the number of d.o.f.s in the entire problem.

4.3.6 WEE parameters – summary and guidelines

To summarise, it has been shown that modelling an unbounded fluid region for a large *ka* system (here *ka*~54) can be achieved effectively using acoustic FEs and WEEs. The system considered here was an ideal plane piston model with similar size, geometry and operating conditions to the real physiotherapy device outlined in Chapter 3. However, in order to generate an effective model a number of parameters must be considered and chosen correctly in order to generate a successful model. The choice of these parameters is by no means obvious. In addition the choice is by no means straightforward, not least because the parameters are generally linked so that changing one has an impact on another. There are also a number of practical aspects

that must also be tackled and all modelling considerations are compounded by long simulation run times. Some general guidelines for the modelling of large *ka* systems using WEEs follows.

Firstly, as for the modelling of any system, it is advisable to have field data against which the model can be compared and evaluated. As is the case here, if there is a lack of field results for the specific system under consideration, it is beneficial to model an alternative, similar system for which theoretical or analytical results are readily available. For the case of a circularly symmetric transducer, the corresponding ideal plane piston source is an obvious initial choice. Secondly, the modeller needs to be aware of the theoretical formulations of the modelling techniques. Here this specifically refers to the shape functions of the WEEs, as outlined in section 4.2.1, and the governing equations that dictate the behaviour within an element, outlined in section 4.2.2. Combining this knowledge with practical considerations gained by attempting to model a relevant system will lead to a good understanding of the features that are of significance when attempting a simulation. Here the important features are

- *ka* size – structural dimensions, frequency and wavelength
- Radial order
- Distance to interface
- Angular mesh intensity at the interface
- Mesh intensity in the radial direction (for acoustic FEs)
- WEE virtual source position
- Element angle and size restrictions
- Number of d.o.f.
- Simulation run time and memory requirements

It should be appreciated that many of these features are linked, so that varying one will have an impact on others.

Finally, modelling of any system with a large number of d.o.f.s, will be adversely affected by long simulation run times. It is advisable to start by considering models with smaller *ka* values. This will enable many features of a modelling 'protocol' to be established without having to deal with excessive run times, particularly if errors are made in simulation specifications. Errors are always likely when such a large number of parameters are concerned and where the geometry and meshing requirements of the systems are complicated. This is even more applicable here as many of the relevant parameters are difficult to establish correctly before performing a simulation, and the accuracy of models must be balanced against run times and memory requirements.

4.4 Boundary element models

Due to the excessive run times and memory requirements of the WEE models, alternative "infinite" fluid modelling approaches were sought. Specifically, two BEMs, CHIEF and DAA2c will now be considered. An outline of the BEM was given in Chapter 2. The essential idea is to express the equations that govern the behaviour of the modelled system in terms of an integral over the surface of the system. Having done this, the surface of the system can be discretised and an approximate numerical solution sought to the integral problem. When modelling an unbounded fluid region only the surface of the radiating system needs to be considered initially, compared with the WEE technique where some extensive fluid region must be included directly. Once the fluid-structural interaction problem is solved at the BE surface, field values are calculated using some additional integral expression. In practical terms, for large *ka* systems, the use of BEM has the potential for significantly reducing the number of d.o.f.s in the modelled system. In Chapter 2 the full system of equations for a structure radiating into a fluid region was given in Equation 2.29 as

$$[K + \bar{i}\omega D - \omega^2 M]\{d\} = f^{(k)} + f^{(p)} \qquad (4.21)$$

where $f^{(p)}$ represents the fluid loading at the fluid-structure interface. For the BEM this term will be in the form of an integral over the surface of the structure involving surface pressure and normal (surface) velocity. Essentially, the system is solved by the simultaneous solution of the equation of motion of the structure and the integral equation at the fluid-structure interface (Huang & Wang, 1985).

The "classical" radiation problem was discussed in Chapter 2, and the equations governing the response of a system with a structure radiating into an infinite fluid region considered. The geometry of the problem is shown again in Figure 4.13. These governing Equations, 4.13-4.17 were repeated above in section 4.2.2 for the formulation of WEEs. In Chapter 2 the "direct" approach of generating an expression relating surface velocity, surface pressure and pressure in the exterior acoustic region from these equations, was considered. This led to three integral equations

$$p(x)=\left(\frac{1}{4\pi}\right)\int_S\left\{p(\varsigma)\frac{\partial}{\partial n_\varsigma}\left[\frac{e^{ikd(x,\varsigma)}}{d(x,\varsigma)}\right]-i\omega\rho v(\varsigma)\frac{e^{ikd(x,\varsigma)}}{d(x,\varsigma)}\right\}dS(\varsigma),\ x\in R_0,\ \varsigma\in S, \quad (4.22)$$

$$p(\psi)=\left(\frac{1}{2\pi}\right)\int_S\left\{p(\varsigma)\frac{\partial}{\partial n_\varsigma}\left[\frac{e^{ikd(\psi,\varsigma)}}{d(\psi,\varsigma)}\right]-i\omega\rho v(\varsigma)\frac{e^{ikd(\psi,\varsigma)}}{d(\psi,\varsigma)}\right\}dS(\varsigma),\ \psi,\ \varsigma\in S \quad (4.23)$$

and

$$\int_S\left\{p(\varsigma)\frac{\partial}{\partial n_\varsigma}\left[\frac{e^{ikd(X,\varsigma)}}{d(X,\varsigma)}\right]-i\omega\rho v(\varsigma)\frac{e^{ikd(X,\varsigma)}}{d(X,\varsigma)}\right\}dS(\varsigma)=0,\quad X\in R_i,\ \varsigma\in S. \quad (4.24)$$

These three equations are commonly referred to as the exterior Helmholtz integral, the surface Helmholtz integral, and the interior Helmholtz integral respectively. Here x is a point in the exterior region, X a point in the interior region, and ψ and ς are points on the surface. Ideally the surface integral, Equation 4.23, would be used as the

'fluid-loading' term in Equation 4.21 above, and solved simultaneously with the system of equations describing structural response. From the surface pressure and velocity results generated by this system, the exterior integral, Equation 4.22, could then be used to generate field values. The use of Equation 4.22 following the solution of the fluid-structure problem is the standard procedure for generating field results. Unfortunately solving Equation 4.23 is not so straightforward.

4.4.1 CHIEF (Combined Helmholtz Integral Equation Formulation)

A problem encountered in the solution of the *surface* Helmholtz integral, Equation 4.23, is one of uniqueness, i.e. whether or not the true surface pressure is the unique solution for known $v(\varsigma)$. The solution of Equation 4.23 is non-unique at an infinite number of values of k related to the corresponding *interior* Equation 4.24 (Seybert & Rengarajan, 1987; Matthews, 1986). This is a purely mathematical problem, and not a physical one. In order to overcome the problem, Schenck (1968) introduced the Combined Helmholtz Integral Equation Formulation (CHIEF) which sought to find the *unique* surface pressures that satisfied *both* the surface and interior Helmholtz integrals. This is achieved by firstly taking the standard N x N system of equations generated from the surface integral. Then an additional N_C equations, for the interior integral at C points, are generated resulting in an over-determined $(N+N_C)$ x N system. This system can then be solved. Ciskowski & Brebbia (1991) give a good account of the formulation of the "fluid loading" term, $f^{(p)}$, in Equation 4.21 above for the solution of a radiating problem where the surface is modelled using CHIEF.

The significant practical feature here is the specification of the additional C "collocation" points within the region interior to the BEs. Although when computing facilities are limited the specification of a large number of additional collocation points may be unwanted, here an excessive number of points is not a problem. Of interest is how many additional points are required to generate an effective model, and where they should be positioned. Schenck (1968) gave little indication of how to

position the additional points but did state that only a small number of "good" points were required to generate good results. Here "good" points are those that do not coincide with a nodal surface of the interior problem – i.e. points where the interior (homogeneous) problem gives zero pressure. Seybert & Rengarajan (1987) concluded that even if five interior points are located on a nodal surface but one is not, then an accurate solution could be expected. In both of these papers reference has been made to the fact that with increasing frequency the eigen-frequencies of the interior problem become more closely spaced, and are therefore more difficult to account for by the inclusion of a finite number of additional collocation points. Results in section 4.5 will be seen to support this.

4.4.2 Doubly Asymptotic Approximations (DAAs)

An alternative approach to the exact solution of the discretised surface Helmholtz integral, Equation 4.23, for the calculation of surface pressure and normal velocities, is the use of an approximate relationship. As in the exact method, once the structural-fluid problem has been solved field values can then be calculated by use of Equation 4.22. Doubly asymptotic approximations (DAAs) are a BEM option that are used to supplement structural equations with an approximate fluid loading so that the system under consideration can be solved for fluid-structure interaction. The advantage of DAA techniques is that the problem of non-uniqueness, as outlined in section 4.2.1 above, are avoided, and furthermore, that the fluid matrices generated in the solution are frequency independent (Geers & Felippa, 1983; Huang & Wang, 1985). This is of particular significance where consideration is to be given to a system over a range of frequencies, as here for the analysis of model parameters.

There are a number of alternative DAAs, their differences being due to the structural-fluid interaction approximations used. For the case of high frequencies, of interest here, the first order DAA formula, DAA1, uses the plane wave approximation (Felippa, 1980)

$$p = \rho c \dot{d} \qquad (4.25)$$

where $\dot{d}$ is surface velocity. In the solution of a radiating structure, Equation 4.25 is used in place of the *surface* Helmholtz integral and incorporated into the fluid-structure Equation 4.21 so that the full set of (approximate) fluid-structure equations can be solved simultaneously. In PAFEC the *curved* second-order approximation, DAA_2^c is used, which, for the high frequency case, uses the following approximation (Felippa, 1980; Felippa, 1980)

$$p - \kappa c p^* = \rho c \dot{d} \quad . \qquad (4.26)$$

Here κ is described as the "mean curvature" of the tangent to the plane at the point on the structural-fluid surface that the approximation is applied to, and the asterisk in p^* denotes temporal integration. It is clear that the plane wave approximation results if the "mean curvature" κ is set to zero. A comprehensive account of the formulation of the different DAA techniques in the frequency domain can be found in Nicolas-Vullierme (1991) or Ginsberg (2000).

4.5 Idealised model comparisons

There are relatively few references in the literature to comparisons of "infinite element" and BEM approaches to the modelling of unbounded fluid media for a radiating source. Seybert et. al. (2000) compares fluid modelling options for a specific structure operating at low frequencies, but certainly little comparison has been made in terms of large *ka* sources where the near-field of the radiating structure is of interest. Burnett (1994) gives a good overview of the options available, whilst Everstine (1997) presents a summary of the theoretical formulations for a number of approaches including a consideration of exact and DAA BEMs and a look at the "infinite" element approach. However no reference is made to comparative field results. Consideration will now be given to the generation of near-field data for three

idealised sources of varying *ka* for each of the methods outlined above – WEE, CHIEF and DAA2c. Comparison will be made for the accuracy of the solutions, run times and the practicality of using these methods here.

All models involve the same structure - the cylindrical, transducer-like, circularly symmetric structure used previously in this chapter and corresponding to the real physiotherapy device. Three different source variations will be considered, firstly the plane piston case, secondly the source amplitude will vary with radial distance as a cosine function between 0 and $\pi/2$, and thirdly the source amplitude will have a Gaussian variation with radial distance. Each of the source amplitude variations is shown in Figure 4.14. There is no phase variation at the source. The "cosine" and "Gaussian" source curves are considered because the real device will not include the sharp decrease to zero displacement occurring at the edge of the plane piston source. This is due to both the physical restraint of the real device at the edges of the disc and the non-uniform vibrational behaviour of the transducer face. These two sets of source data could be expected to be a compromise between the plane piston case and the real device and are therefore likely to give more insight into the effectiveness of each of the unbounded fluid modelling options. Finally, each of these models will be considered when operating at 300 kHz, 650 kHz, and 1.030 MHz. Models have been meshed according to *ka* size and models with alternative meshing intensities have been generated to establish that meshing plays no part in any model to model discrepancies observed here.

All of the WEE results were compared against analytical results. In each case the WEE model was in excellent agreement with predicted results, the worst agreement being for the plane piston case shown in Figures 4.4 and 4.5. Comparisons of different models will, therefore, be shown here as WEE results can be considered to be accurate. Only axial output up to the WEE interface will be included for the WEE models, however the accuracy of the DAA2c and CHIEF models should be clear from these comparisons. Only axial results are shown but radial results at 5 mm from

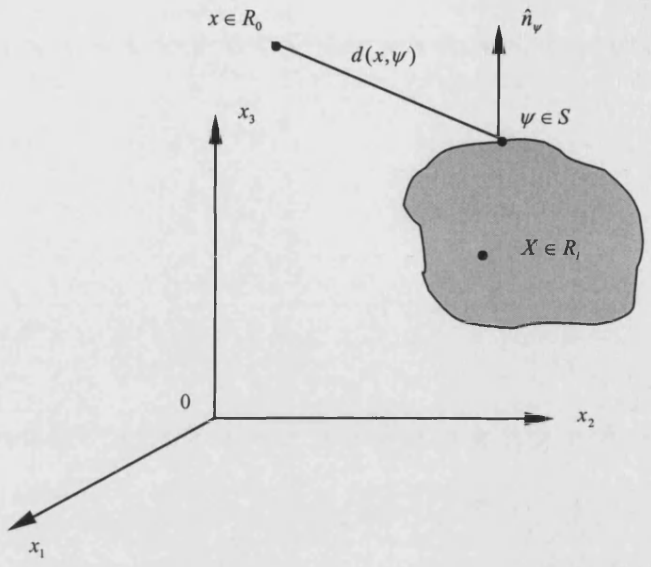

Figure 4.13 Geometry of the "classical" radiation problem of a structure vibrating in a fluid medium due to Schenck (1968).

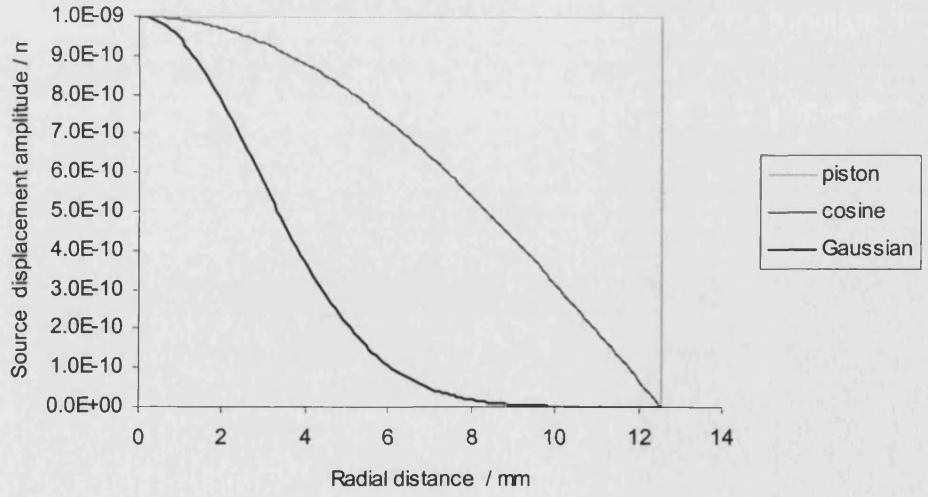

Figure 4.14 Amplitude variation for three ideal models – plane piston source, "cosine" distribution, and "Gaussian" distribution. The phase variation is constant for all models.

the source were also generated. The accuracy of all radial results was comparable to axial results.

For all of the CHIEF models an additional 840 collocation points were included, positioned in fairly randomly spaced lines throughout the interior of the structure, including very close to the surface. This is a large number of additional points, although as discussed before, compared to the WEE models the run times of the CHIEF models is very short. This number of collocation points was chosen based on a number of runs of the 1.030 MHz plane piston model including varying numbers of points. The inclusion of further points affected output but did not substantially improve it. However no substantial optimisation of either the number of points or their positioning has been performed here. For the models operating at 1.030 MHz the run time (for one frequency) was approximately 5 hours for the WEE model, less than half an hour for CHIEF and around 10-20 minutes for DAA2c. Run times for the models operating at lower frequencies was substantially reduced as the meshing was varied in accordance with frequency.

4.5.1 Idealised models operating at 300 kHz

Figures 4.15-4.17 show model results for the plane piston, "cosine" and "Gaussian" models respectively, all operating at 300 kHz. The corresponding *ka* value is ~ 16. It is clear that the CHIEF and WEE models are in excellent agreement for all three models. DAA2c agreement is also generally very good although there are some discrepancies close to the source for both the piston and "cosine" models. The "Gaussian" model is in excellent agreement. There is some evidence to suggest that the DAA2c output is improving from the piston model to the "cosine" model to the "Gaussian" model.

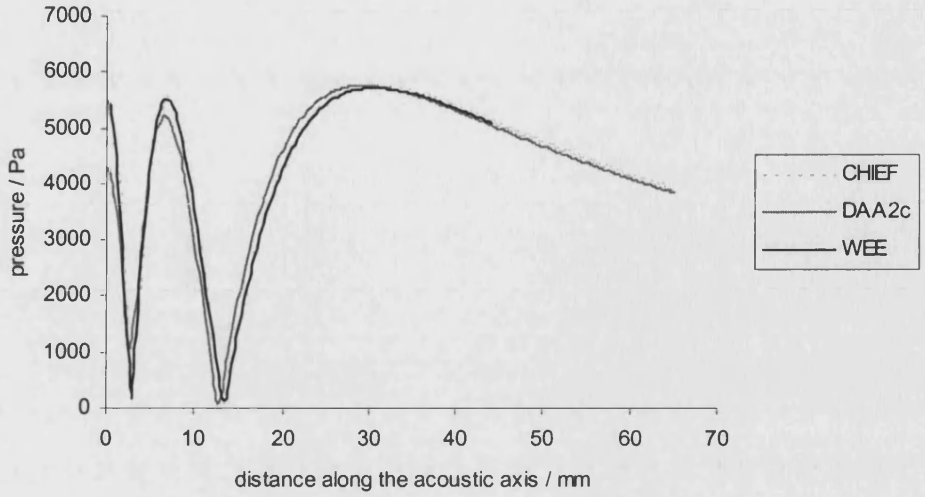

Figure 4.15 Model comparison for an ideal, circular plane piston source of radius 12.55 mm, operating at 300 kHz with a source displacement of 1.0E-9 mm as shown in Figure 4.14. Axial comparison of results for two BEMs, CHIEF and DAA2c, and a model incorporating acoustic FEs and WEEs is shown. CHIEF and WEE output is almost identical.

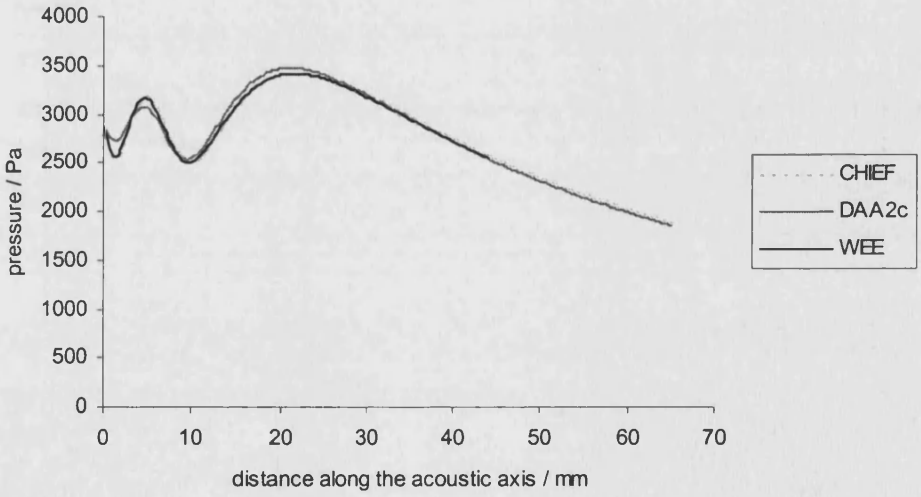

Figure 4.16 Model comparison for the same model as in Figure 4.15, source of radius 12.55 mm, operating at 300 kHz, but here with cosine variation of source displacement amplitude as shown in Figure 4.14. Again axial comparison is shown for two BEMs, CHIEF and DAA2c, as well as a model incorporating acoustic FEs and WEEs. Again CHIEF and WEE outputs are almost identical.

4.5.2 Idealised models operating at 650 kHz

Figures 4.18-4.20 show model results for the plane piston, "cosine" and "Gaussian" models respectively, now operating at 650 kHz. The corresponding *ka* value is ~ 34. Here similar, if not better, agreement is seen for the WEE and DAA2c models compared to the 300 kHz case. The plane piston model is in reasonable agreement, although there are some significant discrepancies close to the source for DAA2c. The "cosine" model is in good agreement and the "Gaussian" in excellent agreement. Any improvement over the 300 kHz model is likely to be due to the fact that the DAA2c technique is more accurate at higher frequencies. Although excellent agreement is still observed for all three models for the "Gaussian" case, there are clearly some problems with the CHIEF plane piston and "cosine" sources. The previously mentioned closer spacing of the solutions for the interior problem with frequency is the likely cause of this, as the same number of collocation points does not now account for the non-uniqueness of the problem entirely. As expected, therefore, some of the CHIEF results are getting worse with increasing frequency.

4.5.3 Idealised models operating at 1.030 MHz

Figures 4.21-4.24 show model results for the plane piston (Figures 4.21 and 4.22), "cosine" and "Gaussian" models respectively, now operating at 1.030 MHz. The corresponding *ka* value is ~ 54. The operating conditions of this model correspond to the real physiotherapy device operating at its fundamental resonance frequency. Essentially the same progression that has been observed for the two lower frequency cases has continued here. For the plane piston case the DAA2c model is still showing some significant differences close to the source. Moving away from the source, however, but still well within the near-field, the results are in good agreement. The WEE and DAA2c results for both the "cosine" and "Gaussian" sources are in excellent agreement. The CHIEF model is now only in reasonable agreement for the "Gaussian" source and shows significant inaccuracies for the plane piston and cosine cases.

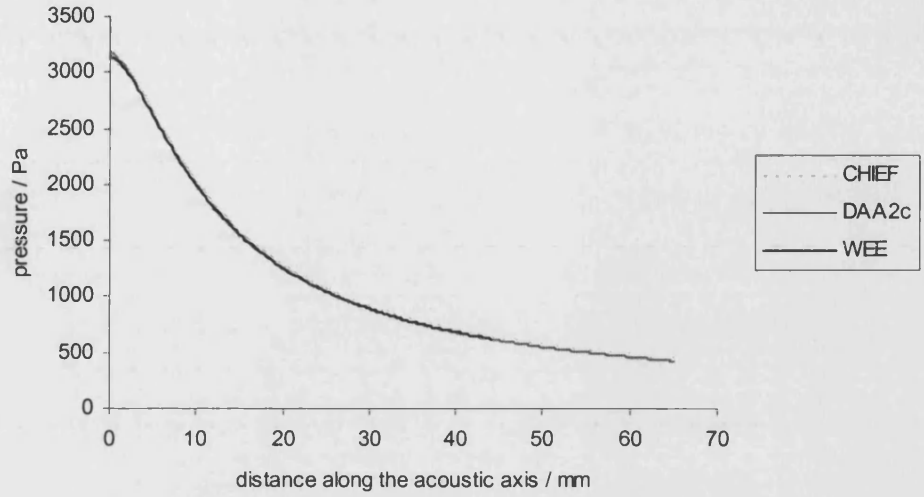

Figure 4.17 Model comparison for the same model as in Figure 4.15, source of radius 12.55 mm, operating at 300 kHz, but with a Gaussian source displacement amplitude as shown in Figure 4.14. Again axial comparison is shown for two BEMs, CHIEF and DAA2c, as well as a model incorporating acoustic FEs and WEEs.

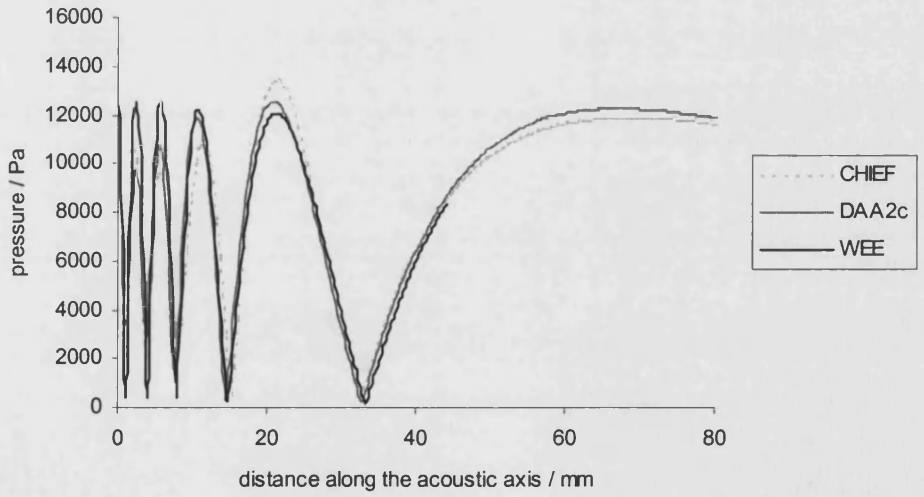

Figure 4.18 Model comparison for an ideal, circular plane piston source of radius 12.55 mm, operating at 650 kHz with a source displacement of 1.0E-9 mm as shown in Figure 4.14.

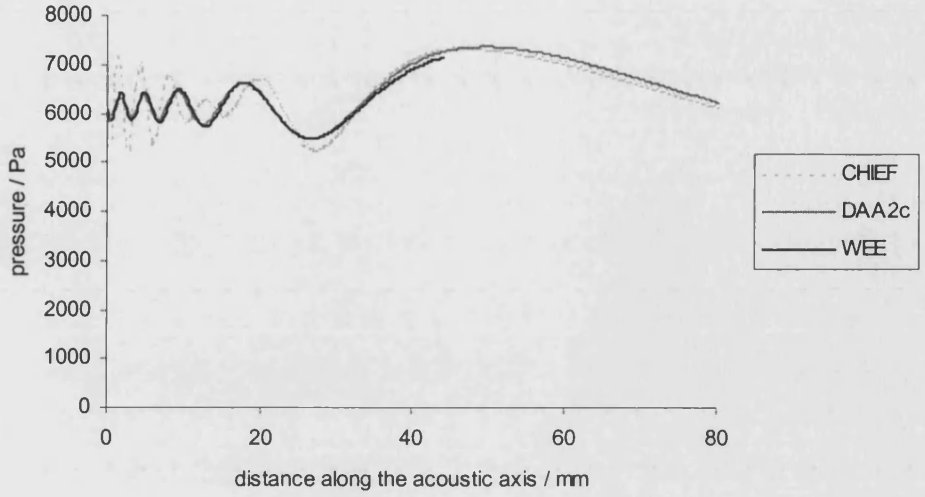

Figure 4.19 As Figure 4.18 but for a source with a cosine variation of source displacement amplitude, operating at 650 kHz.

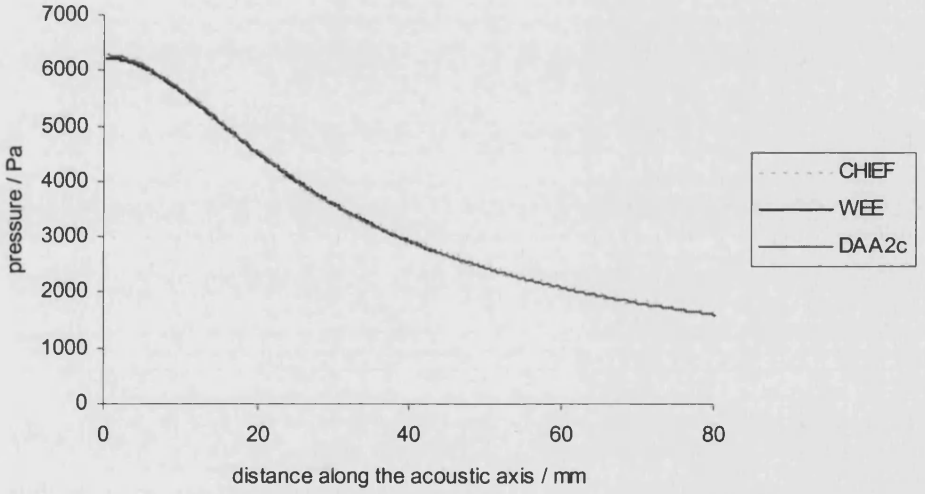

Figure 4.20 As Figures 4.18 and 4.19 but for a source with a Gaussian variation of source displacement amplitude, operating at 650 kHz.

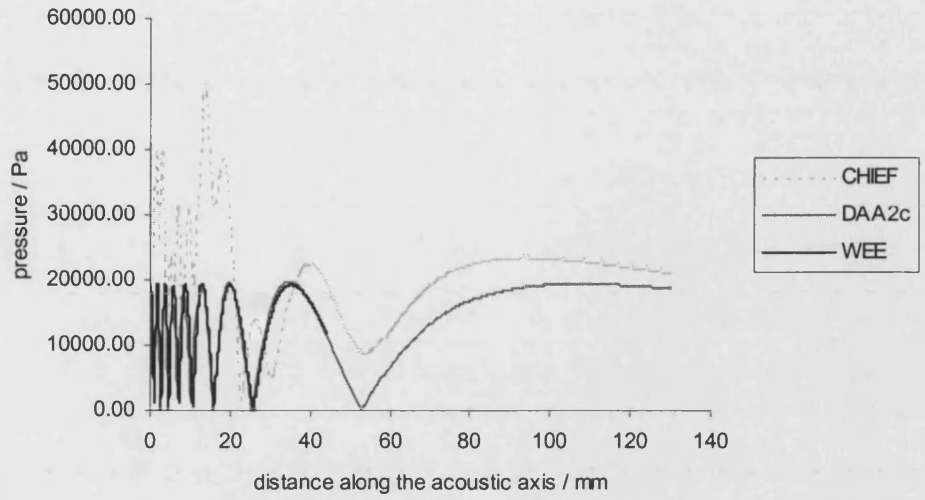

Figure 4.21 Model comparison for an ideal, circular plane piston source of radius 12.55 mm, operating at 1.030 MHz – these are the same features as the real physiotherapy device and equivalent to a *ka* value of ~ 54. Again source displacement is 1.0E-9 mm. Note the larger axial range.

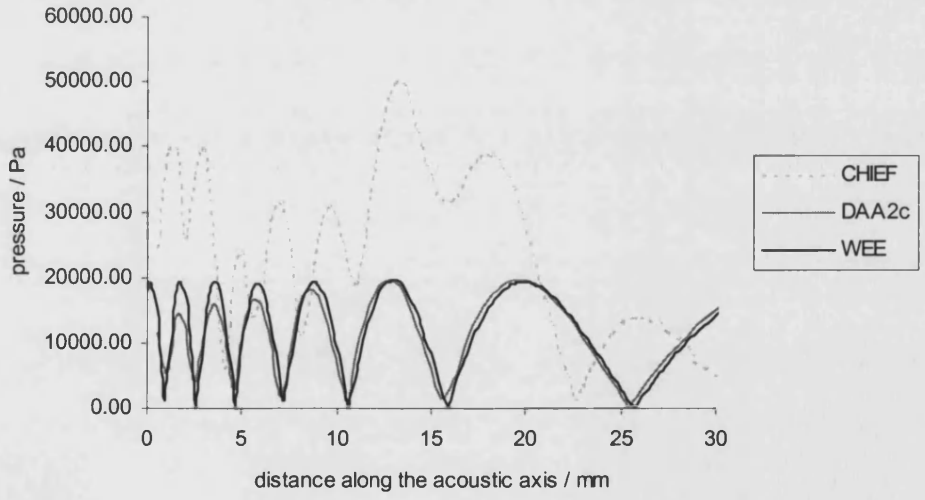

Figure 4.22 As for Figure 4.21 but now over a shorter axial range to emphasise the variation close to the source.

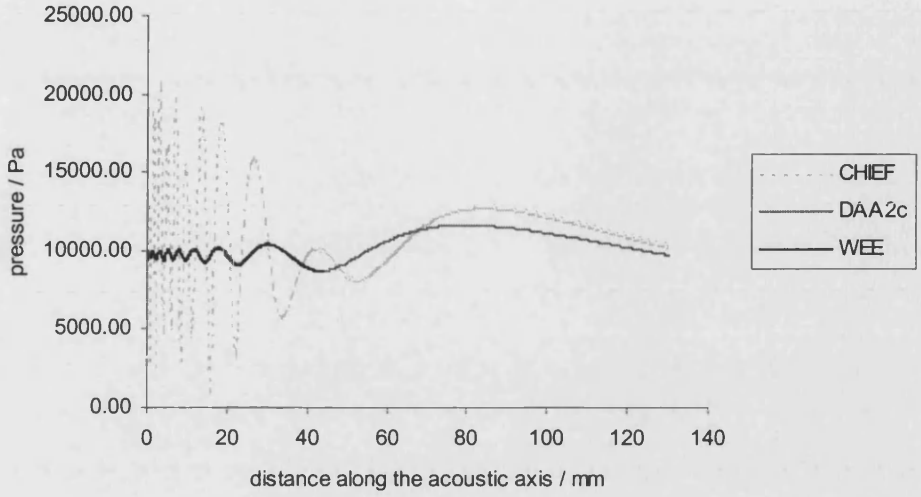

Figure 4.23 As Figure 4.21 but for a source with a cosine variation of source displacement amplitude, operating at 1.030 MHz.

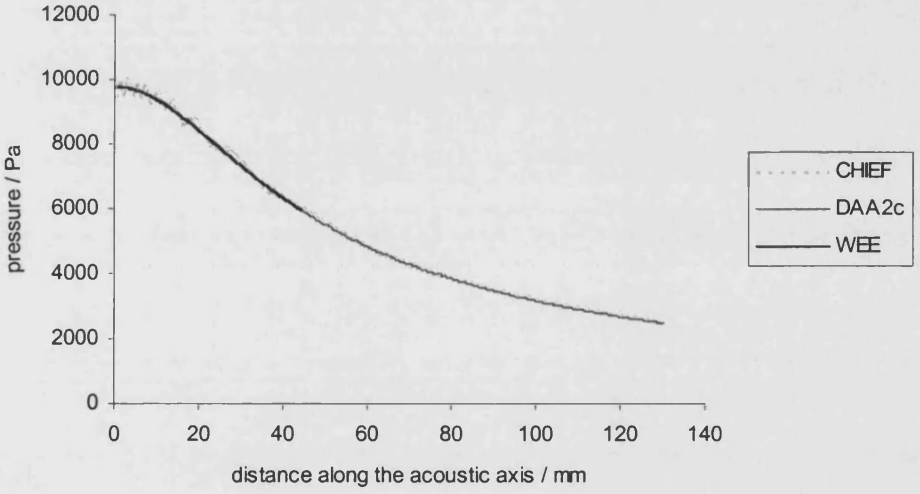

Figure 4.24 As Figures 4.21 and 4.23 but for a source with a Gaussian variation of source displacement amplitude, operating at 1.030 MHz

4.6 Summary

This chapter has considered three options for modelling an unbounded fluid region surrounding a radiating device, where the accurate simulation of the near-field is of particular interest. The techniques considered here are the use of acoustic FE and WEEs, the exact CHIEF BEM, and the approximate DAA2c BEM. A comprehensive assessment of the use of WEEs has been outlined, including a consideration of the element equations defining pressure variation within the element. Also some guidelines have been suggested for using these elements when modelling the near-field of a large *ka* device. Some consideration of the unwanted effects of specifying WEE parameters poorly has been reported. A theoretical outline of CHIEF and DAA2c has also been presented. The three options have been assessed on a comparison of idealised sources of similar dimensions and operating characteristics up to those of the real physiotherapy transducer introduced in Chapter 3.

It has been shown that the WEE approach is accurate for all models when all parameters are specified correctly. Unfortunately these simulations take a long time to run - of the order of several hours for a source with *ka*~54 and running at only one frequency. Also the parameter specification for the acoustic FEs and WEEs is fairly involved. CHIEF has been seen to be accurate for smaller *ka* devices but becomes highly inaccurate for larger systems. This is not unexpected due to the fact that the interior resonances of the structure become more densely spaced for increasing *ka*. CHIEF uses collocation points to overcome problems of uniqueness for the solution of the surface Helmholtz integral. The specification of these additional collocation points is somewhat arbitrary making the accuracy of the technique unpredictable, although it is significantly quicker than the WEE option taking only around 30 minutes to run a similar model with *ka*~54. Finally the DAA2c method has shown a general improvement with increasing *ka* value, and for the largest model is in excellent agreement with the analytical solution for both the 'Gaussian' and 'cosine' models. Observed discrepancies with the plane piston model only occur close to the source. It is likely that, due to the approximate nature of the DAA method, it is not

accurately accounting for the fluid-structure interaction at the edge of the plane piston source where the displacement abruptly falls from a maximum to zero. This type of discontinuity will not occur in a real device. The DAA2c takes only 10-20 minutes to run at one frequency and, because the matrices generated for the fluid are frequency independent, will run relatively very quickly over a range of frequencies. At this stage the proposed modelling strategy would be to use the DAA2c option for all models whilst continually assessing the accuracy of results against corresponding WEE models.

Some further assessment of the three modelling options will be made in the next chapter for the realistic physiotherapy transducer with the fluid models generated here being combined with the structural model generated in Chapter 3 in order to simulate the full system. It is expected that the WEE model will work effectively but extremely slowly, whilst the DAA model should be both fast and accurate. The CHIEF model of the real device should show some level of inaccuracy. Following this, model-experimental comparisons will be made based on the measurements outlined in Chapter 3.

Chapter 5

5.1 Introduction

The previous chapters have introduced a real physiotherapy transducer and measurements made on it as well as separate models of the device and a surrounding unbounded fluid region. This chapter describes the combination of this work to simulate a complete physiotherapy transducer-fluid system and the comparison of the field predictions with experimental measurements. Firstly, the transducer structural response and consequent field results will be compared for the three fluid-modelling options considered in the last chapter. Then, having established an effective and practical model of the real system, a comprehensive model-experimental comparison will be made for the near-field results. It is emphasised that these are initial comparisons. Chapter 6 will consider variations in the basic structural model considered here in an effort to improve the model-experiment agreement and to investigate the significance of parameters in the transducer design.

5.2 Comparing modelling options

Comparisons of the unbounded fluid modelling options for idealised structures in Chapter 4 established that both the WEE and DAA2c options were *likely* to provide an effective model for a real transducer-fluid system, whilst CHIEF was likely to be somewhat inaccurate. Further consideration is now given to these fluid-modelling options for the simulation of the real physiotherapy transducer system.

The BE models were generated with a mesh intensity, on the surface of the structure, of approximately 6 elements per acoustic wavelength. The DAA2c model generated then had a total of around 9000 d.o.f., with the CHIEF model having an additional 840 collocation points. The corresponding WEE model was meshed according to the three elements per wavelength requirement at the acoustic FE-WEE interface. This model, corresponding to the ideal model used in the previous chapter, had

approximately 250,000 d.o.f.. The simulation run time for the WEE model was longer than for the idealised case, taking in the region of 5-7 hours to run on a 500MHz PC. This was due to the inclusion of a large number of additional structural elements. The CHIEF model took only around 20 minutes to run at one frequency whilst the DAA2c model took less than 15 minutes. In all cases this is for the model operating at one frequency, but for the BEM models this was for the generation of structural results only. Additional field results increased the computation time for the BEM models although not substantially if only a small area of the field was predicted. The modelled *real* device operated in continuous wave mode with an arbitrary drive voltage of 1 volt.

5.2.1 Source deformation

For a model to model comparison the first parameter to establish was the acoustic working frequency. As in the experimental measurement the model was run over a range of frequencies and the electrical response measured. Here the DAA2c model was used as it had the shortest run time. Figure 5.1 shows comparative conductance plots over the frequency range 0.9 MHz-1.1 MHz for the model and the real device. These plots show somewhat different features although the main resonance is in a similar position in the frequency domain. The model resonance is at 1.029 MHz compared to 1.027 MHz for the real device. 1.029 MHz will be taken as the acoustic working frequency for the model. The resonance at 1.029 MHz was chosen over the resonance at 0.974 MHz due to both the nature of the corresponding disc vibration at this frequency and the fact that the resonance of the device would be expected to be higher than that of the disc. This is the case for the real device where fundamentally the disc is designed to be resonant close to 1.00 MHz. The most likely explanation for the discrepancies between electrical results here is differences between the modelled disc and the real one. This will be considered in the next chapter where an analysis of disc parameters and their effect on the modelled transducer will be investigated.

Comparisons could then be made between the predicted source deformations for models of the real device operating into each of the fluid options at resonance. For the WEE model contour plots of the pressure variation in the acoustic FE region and across the acoustic FE-WEE interface clearly showed up any reflections from the FE-WEE interface. Having generated a WEE model without such reflections it was therefore reasonable to accept it as accurately simulating radiation into an unbounded fluid region. The WEE option was therefore used as a benchmark against which the BEM models were compared. Figure 5.2 shows the structural displacement amplitude in the axial direction for WEE, DAA2c and CHIEF models operating at 1.029 MHz for a drive voltage of 1 volt. Overall all three models show good agreement although there are some discrepancies particularly close to the centre of the source. The source displacement is clearly highly non-uniform. The corresponding phase of the displacement is shown in Figure 5.3 and also shows good agreement for all models. Source displacement in the radial direction showed similarly good agreement.

5.3 Field results

It is useful to consider how the variation in source deformation shown in Figures 5.2 and 5.3 effects acoustic output. The WEE model only generated accurate field results within its acoustic FE region so a propagation program was used to generate more extensive results. The FORTRAN 77 program was a variation on the double numerical integration routine used earlier for the generation of field results due to an ideal plane piston source. Now the source velocity was included under the integral in Equation 1.4 so that complex (axial direction) velocity results could be extracted from the FE structural model and propagated. Comparisons between propagated results and those generated directly by FEM or BEM showed excellent agreement for all three fluid-modelling options. From now on WEE field results will be those generated by the propagation routine whereas BEM results were generated directly. Figure 5.4 shows an axial comparison for all three models against one of the experimental scans shown in Chapter 3. The experimental scan was made for an r.m.s. drive-voltage of 2.43 V so the model output has been linearly scaled up

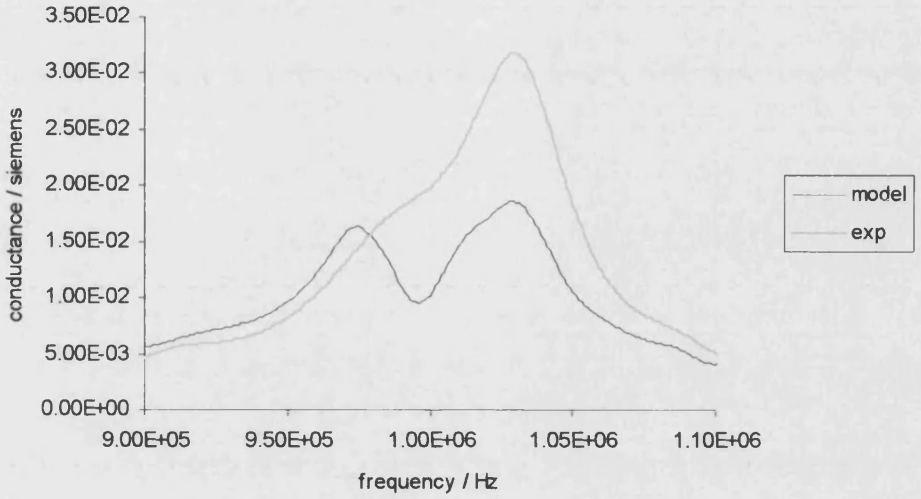

Figure 5.1 DAA2c-experimental electrical conductance data showing a *model* TE resonance at 1.029 MHz and *experimental* resonance close to 1.027 MHz. It should be emphasised that the *experimental* "acoustic working frequency" was established from a number of re-measurements of the electrical response of the device and 1.027 MHz chosen based on these results.

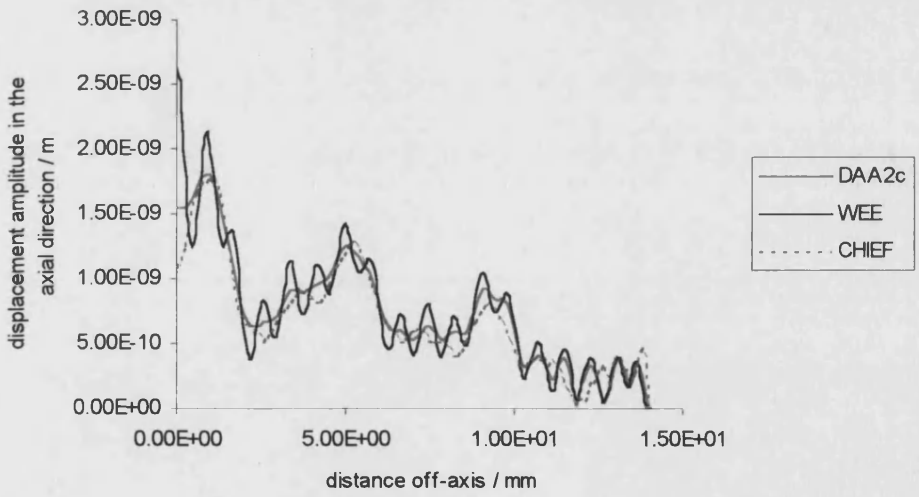

Figure 5.2 Comparison of source displacement amplitude, in the axial direction, for WEE and BEM models running at 1.029 MHz for a drive level of 1 volt.

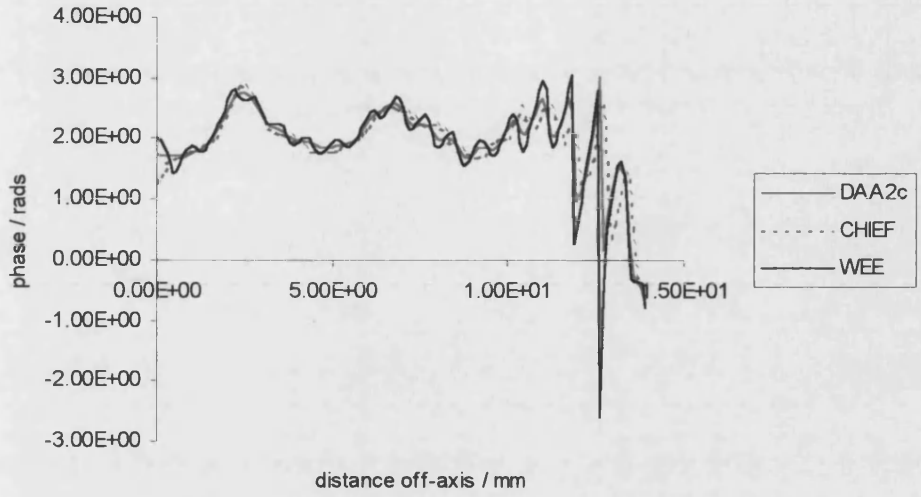

Figure 5.3 Comparison of source displacement phase, in the axial direction, for WEE and BEM models running at 1.029 MHz for a drive level of 1 volt.

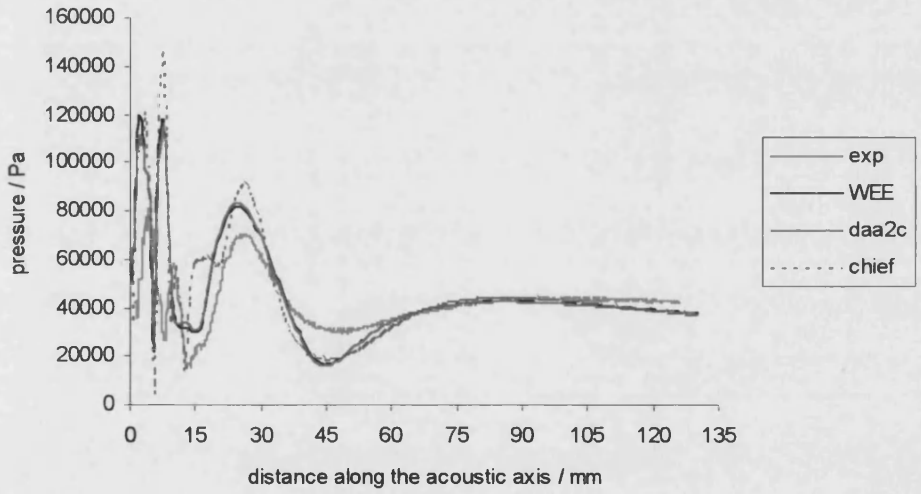

Figure 5.4 Axial comparison of model and experimental results at 1.029 MHz. The WEE output was generated by propagating the source data; whilst results for the two BE models were generated directly. Here the WEE and DAA2c outputs are very similar.

accordingly. This particular axial scan was chosen because it is one of the two shown in Chapter 3 that are in generally good agreement. Figures 5.5 and 5.6 compare the model results at 5 mm and 10 mm from the source with experimental data for the same r.m.s. drive voltage, 2.43 V. Model data is generated every 0.5 mm compared to experimental results generally in steps of 0.25 mm.

Overall good agreement is shown between the three models for all acoustic output shown in Figures 5.4-5.6. In particular it can be seen that the WEE and DAA2c models are in excellent agreement. There are some obvious differences for the CHIEF model. As far as the model-experimental comparison is concerned there is generally good qualitative and quantitative agreement for all three plots. Model axial plots show very similar features to two of the three experimental plots shown in Chapter 3. Similar maxima and minima are seen at reasonably similar axial positions, and the last axial maximum *absolute* pressure values are in very good agreement. It is the last axial maxima that are in good agreement for all the experimental measurements reported in Chapter 3. The most striking differences are in the magnitudes and locations of the minima and maxima close to the source. However, this is where most differences were reported experimentally. The axial results will be considered in more detail later in this chapter. There are also some differences in the spread of the radial data about the axis, as well as some differences in magnitudes. Overall, however, particularly for the 5 mm output, the model-experimental agreement is very good both qualitatively and quantitatively. It should be re-emphasised that there is a significant difference between these model-experimental measurements and corresponding *ideal, plane piston* field data shown in Chapter 4. Experimental radial data has been re-aligned to be centred about the acoustic axis.

These results show that WEE and BEM source displacement data are in good agreement. Likewise, the model field data is in reasonably good agreement, particularly for the WEE and DAA2c results. There are, however, some differences with CHIEF output. The acoustic field results are in reasonably good agreement with the experimental measurements made on the real device. All of these results

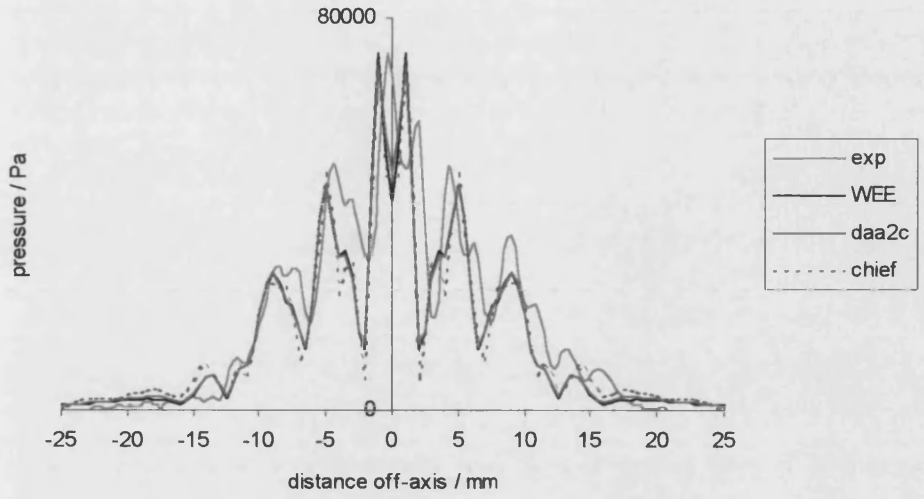

Figure 5.5 Comparison of model and experimental field data at 5 mm from the source. As in Figure 5.4, WEE output is generated from the propagation program whilst BE output is generated directly. Also the WEE and DAA2c output is again in very close agreement. The experimental result was aligned centrally about the acoustic axis.

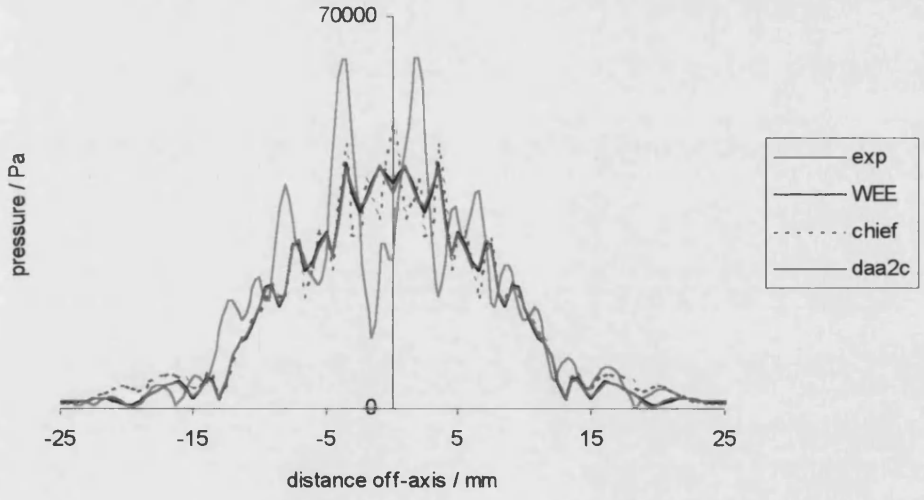

Figure 5.6 Comparison of model and experimental field data at 10 mm from the source. As in Figures 5.4 and 5.5, WEE output is generated from the propagation program whilst BE output is generated directly. The WEE and DAA2c output is again in very close agreement, and the experimental result was aligned centrally about the acoustic axis.

(including the fact that there are no signs of reflection at the FE-WEE interface in that model) would appear to suggest that the fluid-structural interaction is being modelled effectively by the WEE and DAA2c techniques and less effectively by CHIEF. This agrees with the results in the previous chapter. It is reasonable to conclude, therefore, that both DAA2c and WEE are available to us for accurate simulations and analysis of models. Although WEE output is in excellent agreement with DAA2c, large run times make it impractical to use for any extensive analysis. The modelling will therefore proceed using the DAA2c model with regular verification against the corresponding WEE model. Throughout the course of the modelling presented in this thesis the DAA2c-WEE comparability has been as good as that observed in Figures 5.4-5.6.

5.4 IEC standard experimental-model comparisons

This section describes model-experimental comparisons made for the IEC standards measurements outlined in Chapter 3. Clearly there is no need to establish a beam alignment axis for the circularly symmetric model. In addition there is no real need to consider model power output, as increasing the amplitude of the voltage in the model will simply produce a linear increase in acoustic pressure values. Consideration will, therefore, be given to comparative pressure measurements.

5.4.1 A_{BCS}, A_{ER} and beam type characterisation

Firstly consider the calculation of the beam cross-sectional area, A_{BCS}, at four planes. Each value can be calculated by generating pressure results out to some large radial distance in the appropriate plane and establishing where the field reduces to 4% of the in-plane maxima - taking care that it is a global maximum. Experimentally, once this distance is established, the distance is doubled and separated into 50 sections so a step size can be calculated. The A_{BCS} value in a plane is then calculated by sorting the U_i voltage values (or p_i pressure values) into descending order and summing them

to calculate the number of terms that include 75% of $\sum U_i^2$ (or $\sum p_i^2$). This number is then multiplied by the step-size *squared* to give a value for A_{BCS} in that plane. Once the four A_{BCS} values have been generated they can be plotted and extrapolated back to the source to calculate $A_{BCS}(0)$. From this a value of the A_{ER} and a definition of the beam type can be made.

To generate similar results for the model some additional steps have to be included. Once the position where the field reduces to 4% of the in-plane maxima had been established the model *radial* data was converted into *a square grid* of data as in the experimental case. This was done using simple linear interpolation to estimate the grid values between model radial values. Experimentally the meshing is generally restricted to 51 by 51 points because of practical limitations. For the model no such limitations exist and A_{BCS} values were calculated using a grid with approximately 90 by 90 points. The model A_{BCS} values were then calculated as in the experimental process.

A comparison of the model-experimental A_{BCS} values at the designated four planes is shown in Figure 5.7 along with the corresponding fitted lines. Table 5.1 shows the model-experimental extrapolated values for $A_{BCS}(0)$, along with the standard deviation in the intercept estimated from the linear regression. Also shown is the resulting A_{ER} values calculated as in Chapter 3.

The $A_{BCS}(0)$ values are in excellent agreement, certainly well within the standard error for both regression lines. Consequently the resulting A_{ER} results are also in excellent agreement. This is a very encouraging result. The nature of the calculation of the A_{ER} suggests that the overall beam pattern is consistent between the model and the experiment. This is further highlighted by a comparison of the "beam type" which is based on the gradient (m) of the regression line used in the calculation of A_{ER}.

Model and experimental results for m are also compared in Table 5.1 and they are also seen to be in good agreement. The beam type for both model and experimental is *collimated*, although it should be emphasised that the corresponding model-experimental values of m show a much closer agreement than is required for the beam types to be classified similarly from the definition in Chapter 3.

	experiment	model	extra models
$A_{BCS}(0)$ / cm^2	2.24	2.28	2.15
$A_{BCS}(0)$ standard error / cm^2	0.08	0.15	0.09
m (gradient)	0.19	0.20	0.24
m (gradient) standard error	0.02	0.03	0.02
A_{ER} / cm^2	3.03	3.09	2.91

Table 5.1 Model and experimental calculations for $A_{BCS}(0)$ and A_{ER} from the plots shown in Figures 5.7 and 5.8. The column labelled "extra models" is calculated using 17 planes of data as opposed to the IEC standard requirement of four. The experimental results and original model results are generated using planes of data at 10 mm, 20 mm, 40 mm and 80 mm.

At this stage the model offered the opportunity to consider the IEC standard definition of the $A_{BCS}(0)$, and therefore A_{ER} and beam type, in more detail. Specifically $A_{BCS}(0)$ is calculated based on the regression of four sets of planar data. The specific choice of the positions of the four planes is outlined in Hekkenberg et. al. (1994), and Hekkenberg (1998), and is designed to best represent the nature of the beam whilst taking into account the practical limitations of how many physical measurements can be made. For the model no such practical limitations apply and a much larger region of the field can be considered. Figure 5.8 shows the results for the calculation of A_{BCS} at seventeen planes, along with a fitted line. Table 5.1 shows, in the column headed "extra models", the resulting values of $A_{BCS}(0)$, m and A_{ER}. From Figure 5.8 the variation in A_{BCS} is obviously not linear, and provides a much better

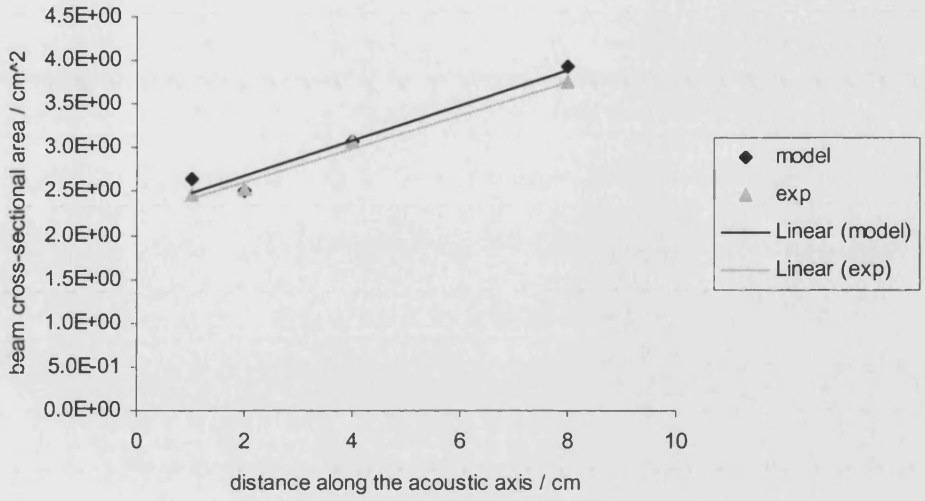

Figure 5.7 Model-experimental comparison of beam cross-sectional area A_{BCS}. A_{BCS} is calculated at four planes specified by the IEC standard – here at 10 mm, 20 mm, 40 mm and 80 mm so that the results can be extrapolated back to the source to calculate $A_{BCS}(0)$. From this the effective radiating area A_{ER} can be established.

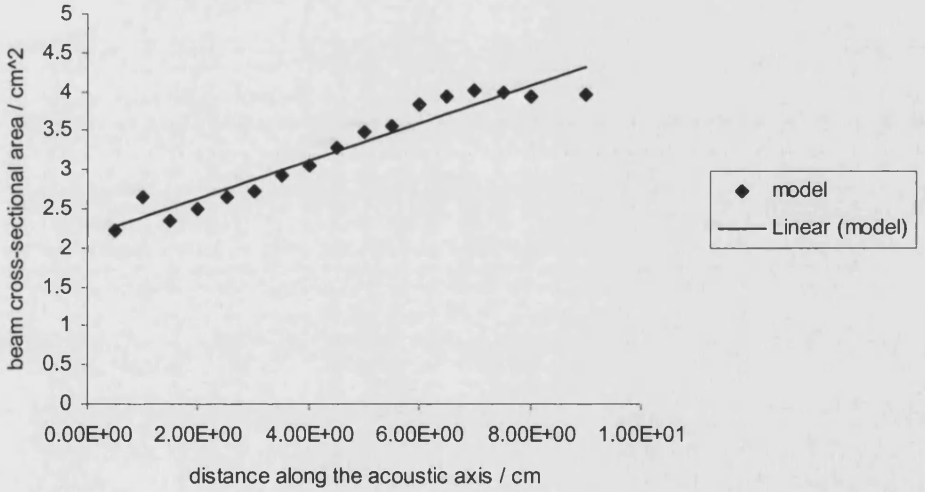

Figure 5.8 Model beam cross-sectional area A_{BCS} at seventeen planes so that the results can be extrapolated back to the source to calculate $A_{BCS}(0)$ and compared with the IEC calculation made using four sets of planar data.

indication of the overall variation in the beam than Figure 5.7. One set of planar data of particular interest is that at 10 mm which can clearly be seen to be significantly different from those at 5 mm, 15 mm and 20 mm. In practice only data at 10 mm and 20 mm is used for the calculation of A_{BCS}. From Table 5.1 it is clear that although there is some difference in the calculated values for $A_{BCS}(0)$, m and A_{ER}, they are essentially in very good agreement, both with model results based on the IEC standard and the corresponding experimental data. It is reasonable to conclude that the IEC definition of four planar measurements accurately accounts for the overall nature of the (modelled) beam in this case.

5.4.2 R_{BN}

Next the model beam non-uniformity ratio, R_{BN}, was calculated. The pressure equivalent version of Equation 3.7 was used

$$R_{BN} = \frac{p_{SP}^2 A_{ER}}{\sum_{i=1}^{N} p_i^2 s^2}. \quad (5.2)$$

Here p_{SP} is the maximum pressure value in the entire field, N is the total number of points in each scan plane, p_i are the individual pressure values and s^2 is the area of a square in the generated grid of pressure results. The denominator in Equation 5.2 is averaged over the four planes at 10 mm, 20 mm, 40 mm and 80 mm. The experimentally calculated value for R_{BN} is 4.77. From the model the value is 12.4! Clearly there is a significant difference, and what's more this value is much higher than the R_{BN} maximum allowable value of 8 specified by the IEC standard. From Figure 5.4 the axial maxima for the experimental measurement is seen to be close to 80 kPa compared with nearly 120 kPa for the model. Because Equation 5.2 involves p_{SP}^2 this would make the model R_{BN} value around 2.25 times greater than the

experimental result, and as the actual difference is a factor of 2.6 it can be seen that this is the major cause of the difference between model and real R_{BN} results.

There are several possible explanations for the lack of agreement between model and experimental R_{BN} values, including differences between the model and the real device. It is also possible, however that there is an experimental issue related to finding the maximum pressure value in the field. In the next section model-experimental axial comparisons and field results very close to the source will be considered. It will be seen that there are some features of the beam-alignment process used in the IEC standard that could lead to misalignment close to the device. It will also be seen that extreme pressure variations close to the source make locating the maxima in the field very difficult. Furthermore, in the near-field hydrophone averaging effects may reduce the maximum pressure measured.

This concludes model-experimental comparisons for IEC standard measurements. The overall nature of the modelled field is in very good qualitative agreement with experimental results. Good quantitative agreement has also been observed for much of the field, and IEC measurements for the A_{ER} and the beam type are in excellent agreement. The model value for R_{BN} is much higher than the measured value for the real device and exceeds IEC standards specifications. Some consideration of the reasons for this will be made in the next section where model-experimental comparisons will be made for other field measurements.

5.5 Non-IEC measurements

Additional measurements that were made to test the robustness of both the experimental process and of the model will now be considered.

5.5.1 Model field variation with frequency

The variation of the model behaviour with frequency is potentially significant due to the narrow bandwidth of the source; the variation with frequency observed for the real device and the poor agreement obtained for the electrical response confirm this. The experimental results in Chapter 3, Figures 3.8 and 3.9, suggested that the field generated by the device was reasonably consistent within 4 kHz of the resonance but showed some significant variations only 8 kHz off resonance. Similarly, model results at 4 kHz off resonance showed little variation from those generated at resonance. However model axial output shown in Figure 5.9, for 1.021 MHz and 1.037 MHz (either side of the model resonance at 1.029 MHz) still show relatively little variation with frequency. Similarly Figure 5.10 showing *radial* output at 5 mm from the transducer for frequencies at 8 kHz off resonance, again show little significant variation with frequency. Additional model runs, at frequencies further off resonance, showed similar features to the plots at and around resonance. Overall these results would appear to suggest that the model is not fully accounting for the field variation with frequency observed experimentally.

A further comparison should be mentioned. In Chapter 3, an experimental comparison for radial output at 10 mm from the source was shown for the device operating at resonance (1.027 MHz) and at 4 kHz above this. Here, Figure 5.6 showed some reasonable model-experimental comparison for a similar plot where both the real device and the model were operating at resonance. Figure 5.11 now compares model output at 10 mm from the transducer for a frequency of 1.029 MHz, with the corresponding experimental result at 1.031 MHz. Excellent agreement, both quantitatively and qualitatively, is observed.

Overall it is clear that variation with frequency close to resonance is capable of causing significant changes in specific areas of the real near-field close to the source, making exact model-experimental comparison here difficult. It appears that the more

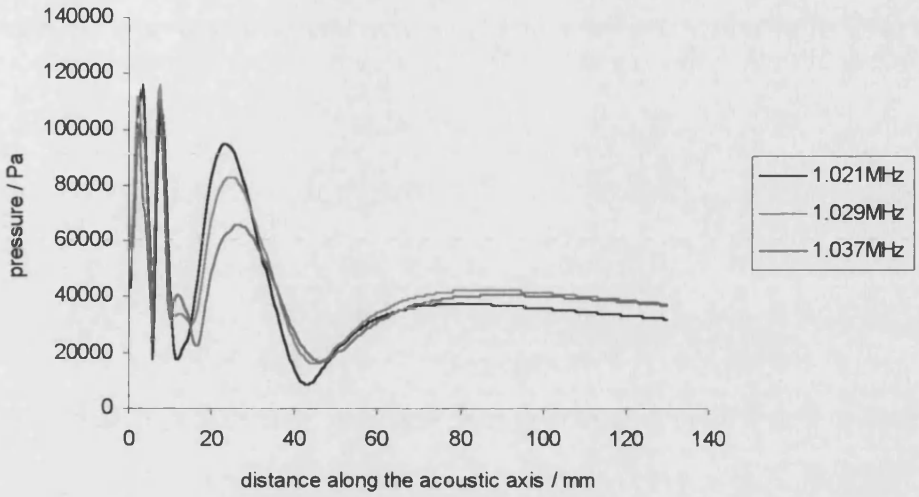

Figure 5.9 Model axial comparisons at different frequencies for DAA2c model.

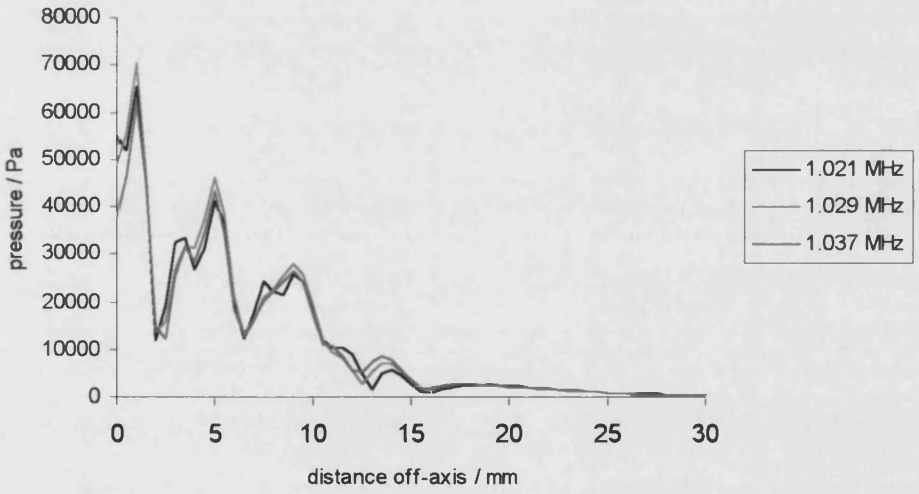

Figure 5.10 DAA2c model radial comparisons at 5 mm from the face of the device for different frequencies.

extreme experimental pressure variation with frequency is not fully accounted for by the model.

5.5.2 Model output on and close to the acoustic axis

It has been observed experimentally that generating repeatable axial field results is not straightforward. In addition the calculation of the model R_{BN} in section 5.4.2 has shown that there are significant differences between the maximum pressure value in the model and the corresponding value measured for the real device – both of which are taken as lying on or close to the axis. All considerations of axial variation are further complicated by the variation with frequency observed experimentally and discussed above. In order to examine the effect of mis-alignment experimentally, as well as to consider off-axis variation close to the axis, experimental measurements were made in lines parallel to the axis. In Chapter 3 the output for these runs was presented for 0.5 mm, 1.0 mm and 2.0 mm off-axis, and shown in Figure 3.14. Although the axial plot itself here showed significant disagreement with two further axial plots, the nature of the off-axis variation was fairly clear. At 0.5 mm and 1.0 mm off-axis little variation was observed, whilst at 2.0 mm the variation close to the source was significant but remained essentially unchanged around the last axial maxima. The corresponding model plots are shown in Figure 5.12, and generally show similar variations to the experimental case. Overall the results around the last axial maxima are consistent, and output up to 1.0 mm off-axis remains fairly constant although there are some clear reductions in amplitude close to the source. The 2.0 mm off-axis results are significantly different to that closer in.

It has already been discussed that the most significant factor for the model-experimental R_{BN} discrepancy is in the comparative axial maxima. An analysis of the plot at 0.5 mm off-axis in Figure 5.12 shows that even this close to the axis the maximum value has fallen to a level approaching the experimental value, and indeed at 1.0 mm off-axis the maximum value has dropped significantly lower. It was discussed in Chapter 3 that the beam-alignment process involved maximising the

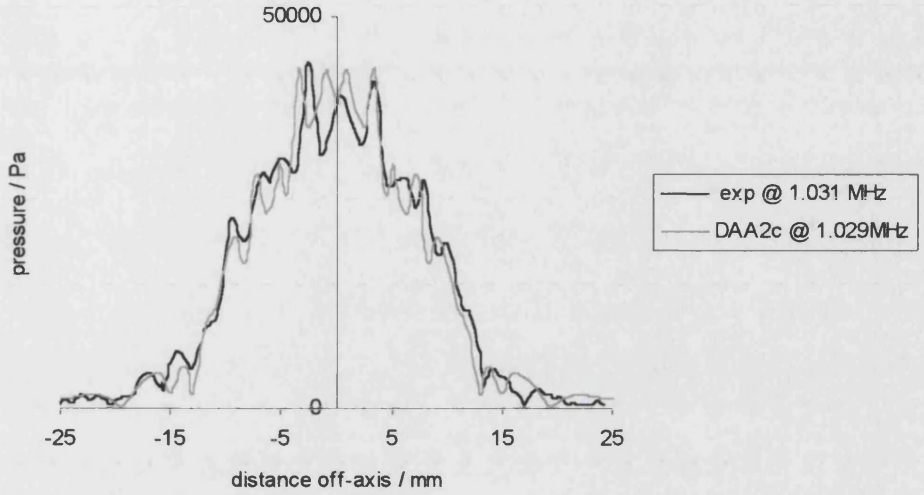

Figure 5.11 DAA2c model-experimental radial field data comparisons at 10 mm from the source. Here the model run is at 1.029 MHz (resonance) and the experimental output is for a run at 1.031 MHz, close to resonance.

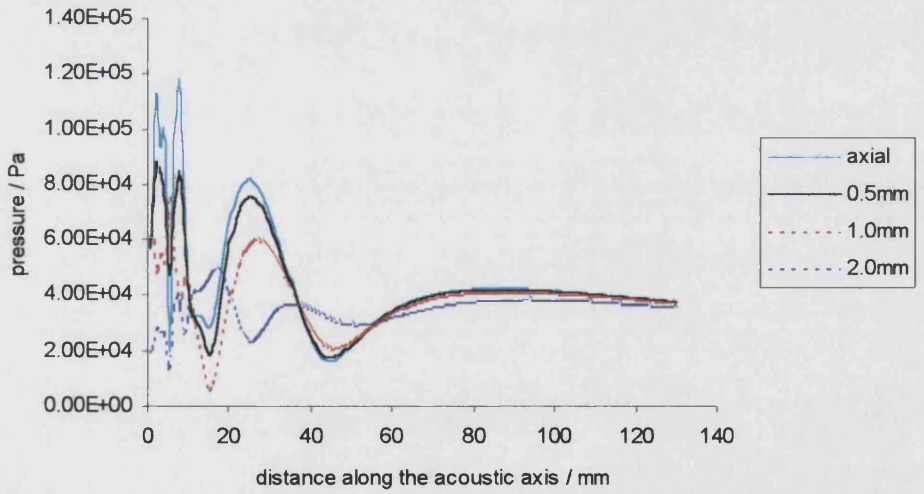

Figure 5.12 Model parallel axial scans at 0.5 mm, 1.0 mm and 2.0 mm. As in the experimental case the plots remain fairly consistent close up to 1.0 mm off-axis, however the 2.0 mm plot shows significant variations close to the source. Results around the last axial maxima are more consistent.

pressure around the theoretical position of the last axial maxima and at twice this distance. Whilst this may be accurate in terms of generating planar data for the generation of A_{BCS} results, there is clearly some possibility that close to the source there may be some mis-alignment. This is compounded by the extreme variation close to the source, which is clear for both the model and the real device. Also some variation with frequency close to resonance has been shown and the real device is not truly circularly symmetric. Furthermore there is fact that the main "hot spot" for the *model* appears to have dimensions of the order of less than a wavelength, undoubtedly making it difficult to locate in the experimental case, and measure accurately with a hydrophone of finite size (0.6 mm). Taking all of these points together it is reasonable to conclude that an alternative to inaccurate model parameters for the model-experimental difference in the R_{BN} may be the difficulty of establishing the experimental field maxima.

To further consider the possibility that, experimentally, the transducer might be mis-aligned close to the source, field output was generated for a line running from the device off-centred by 1 mm to the axis at 120 mm. A comparison of the axial plot from this model with the experimental axial results used previously is shown in Figure 5.13. Much better agreement is shown both qualitatively and quantitatively. In particular the position and amplitudes of the maxima close to the source for the model are now closer to experimental results. Using the maximum result from this plot as the maximum in the field generates a model R_{BN} value of 5.01; this is in comparison to 4.77 experimentally and 12.4 for the original model.

5.5.3 Planar and cross-axial results

In Chapter 3, Figures 3.12 and 3.13 showed cross-axial results at 4.0 - 6.0 mm away from the source, in steps of 0.5 mm, and at 9.0 -11.0 mm from the source, in steps of 1.0 mm. Similar results, generated for the model operating at resonance, are shown in Figures 5.14 and 5.15. Both model and experimental results only serve to highlight

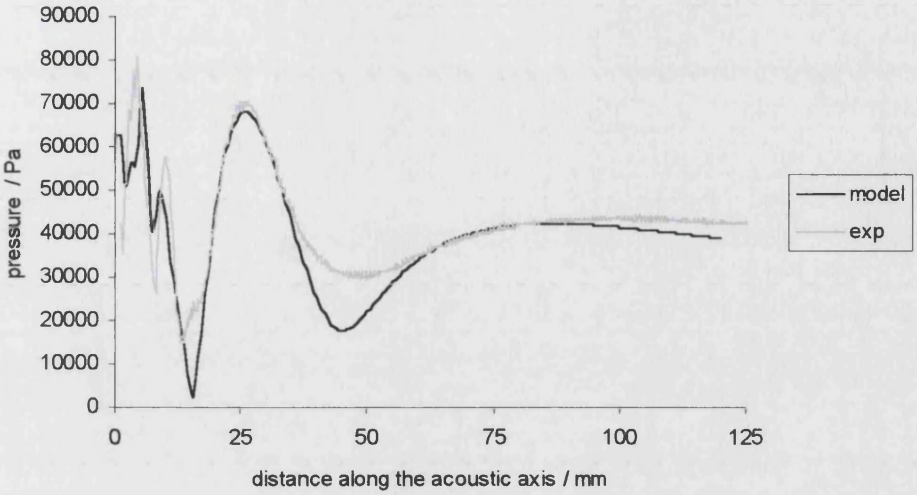

Figure 5.13 Model scan along a line from 1 mm off-centre at the transducer face to the axis at 120 mm. Comparison is made against an experimental *axial* result. The intention here is to consider the effect on the axial results close to the source due to a minor misalignment of the "acoustic axis".

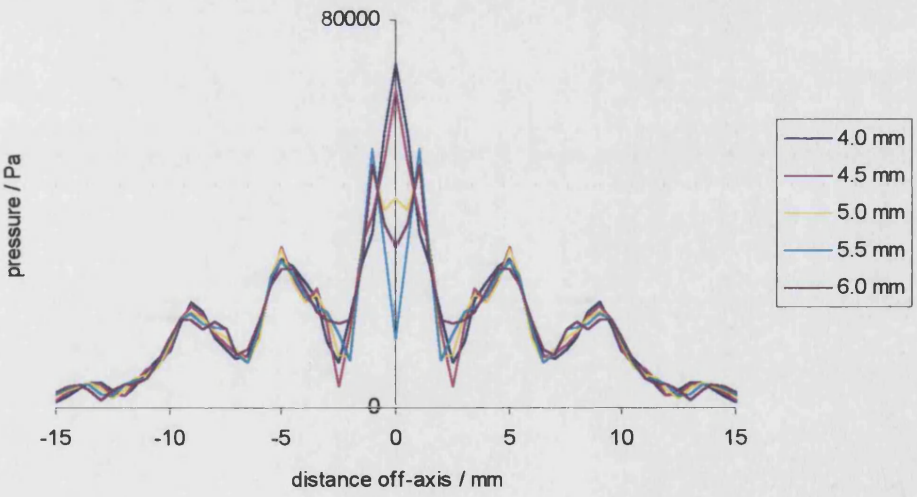

Figure 5.14 Model radial scans from 4.0 - 6.0 mm in steps of 0.5 mm for the device operating at 1.029 MHz.

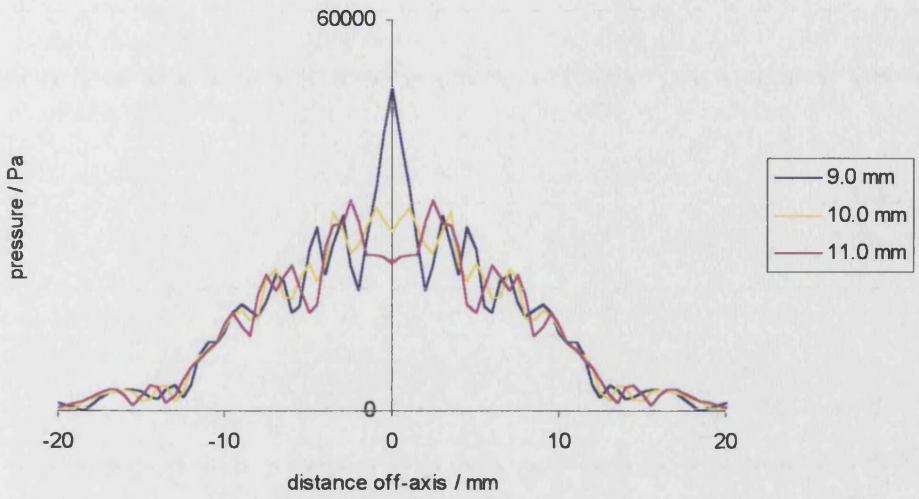

Figure 5.15 Model radial scans from 9.0 - 11.0 mm in steps of 1.0 mm, at 1.029 MHz.

the fact that the region very close to the source is complex and involves significant variations in pressure over distances shorter than a wavelength.

A final model-experimental comparison is shown for planar results at 40 mm from the source. Figure 5.16 shows the full planar data over an area of 41 mm x 41 mm. From these plots it is clear that both the dimensions of the beam and the amplitude over the scan are in good agreement for model and experiment. However there are some differences, not least because the real data can be seen to be less than perfectly symmetric. The step size for the experimental results of 2.05 mm, compared to around 0.7 mm for the model, may account for the fact that considerably more detail can be observed in the model plot.

5.6 Summary

Source and field data for models of the physiotherapy transducer model operating into infinite fluid regions using WEE, DAA2c and CHIEF techniques have been compared. Overall very good agreement has been observed for all three models although there are some discrepancies for the CHIEF model. This is in agreement with the idealised models considered in Chapter 4 and leaves the WEE and DAA2c models as viable options for generating a successful simulation of a large *ka* device operating into an unbounded fluid region. The effectiveness of the WEE method has been shown for all types of sources considered here, as long as the large number of parameters considered in Chapter 4 are specified effectively. The fact that any irregularities in the fluid region can be clearly observed as reflections in a contour pressure plot at the FE-WEE interface also make this a desirable technique to employ. However the simulation run time of the WEE model is considerable, even for one frequency and is therefore impractical in terms of making any comprehensive analysis of model parameters. It can, however, be used for comparative modelling purposes when required, on the basis that the WEE solution can be accepted as an accurate simulation.

(a)

(b)

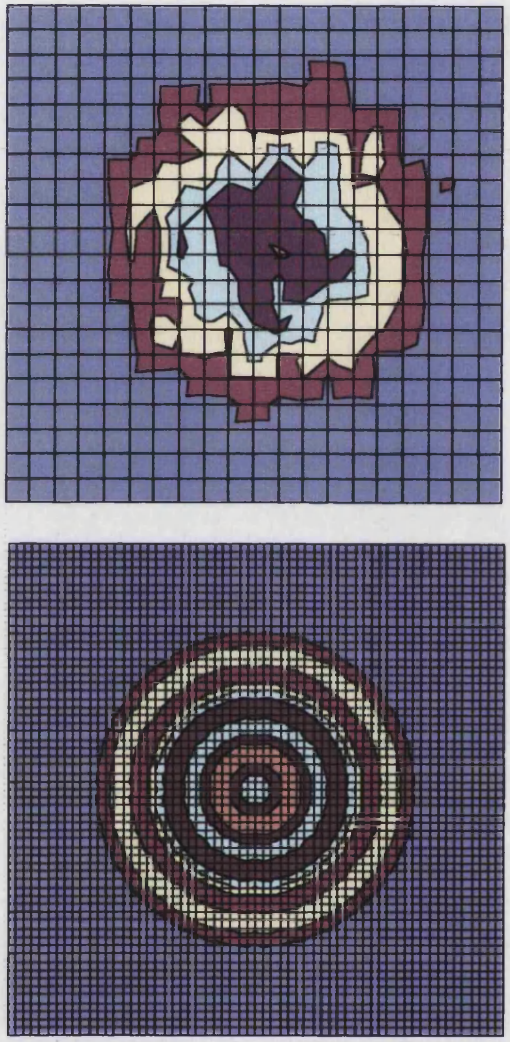

Figure 5.16 Model-experimental axial comparison of planar data at 40 mm from the source. The area covered in each case is 41 mm x 41 mm, and the contour limits used are the same for each plot and shown on the right. (a) The experimental output pressure equivalent to the voltage results shown in Chapter 3, Figure 3.6. (b) The corresponding model plot. The overall nature of the plots is in reasonable agreement qualitatively and quantitatively, although there are clearly more variations in the model output. This may in part be due to the relatively large step size (2.05 mm) used to generate the experimental results.

The DAA2c model has been shown to be effective for large *ka* systems, although some inaccuracies were observed close to the source for the plane piston case in the previous chapter. No such problems have been encountered for the realistic source data considered here. The DAA2c model runs significantly faster than the WEE model and a scan over a range of frequencies can be accomplished quickly due to the frequency *in*dependent fluid-loading matrices used in the technique. The generation of field results after the solution of the fluid-structural interaction problem is straightforward and fast. For these reasons all analysis shown here and in subsequent chapters use the DAA2c technique and have been regularly and successfully verified against WEE models.

Comparisons of model and experiment have been made for both the IEC standard and additional measurements shown in Chapter 3. The model has shown excellent agreement for IEC measurements of A_{ER}, A_{BCS}, and beam type. The use of a large number of planar scans to calculate the A_{ER} has been shown to give similar results to that calculated using only the four planes specified by the IEC standard. This confirms the effectiveness of the definition of the A_{ER} despite some non-linear variation in A_{BCS} model measurements. A series of near-field cross-axial scans have shown good qualitative and quantitative agreement with experiment. In particular, model-experimental comparison of radial data at 5 mm from the source for devices operating at resonance has shown very good agreement. Furthermore a model-experimental comparison of radial data at 10 mm from the source for the model operating at resonance and experimental result at 4 kHz off resonance have shown excellent agreement. The variation in axial and cross-axial scans with frequency close to resonance have shown some good agreement although further off-resonance the model is not accounting for the significant variations observed experimentally. Scans parallel to the acoustic axis have shown variation similar to that observed experimentally. Likewise planar scans at 40 mm from the source have shown reasonable model-experimental agreement overall. Cross-axial scans close to the source have shown evidence of extreme and rapid variations with distance away from

the source, both experimentally and for the model. Overall both experimental and model field results have shown very significant differences from the corresponding ideal plane piston case. In addition the vibrational behaviour at the face of the modelled transducer is highly non-uniform.

There are some model-experimental discrepancies. Firstly the electrical response shows some significant differences although the main resonances are very close. The most likely reason for this is the inaccuracy of the model piezoelectric parameters. This will be considered in the following chapter. Secondly, in areas close to the source, the magnitude and exact position of the minima and maxima of the axial scan is somewhat different between the model and experiment. This was seen to be an area where the repeatability of experimental measurements was poor. Model results are in good agreement further out in the near-field where good experimental comparability was observed. Thirdly there is a significant difference between the model and experimentally calculated R_{BN} values, mainly due to differences in the axial maxima value close to the source. In an attempt to investigate these last two points model output was generated for the case when the acoustic axis is mis-aligned by 1.0 mm at the source. The magnitudes, and to some extent, the positions of the maxima in the corresponding 'semi'-axial scan showed a marked improvement. The R_{BN} based on the maxima from this 'semi'-axial scan also showed a significant improvement in comparison to the experimental result.

There are a number of possible reasons for the model-experimental discrepancies seen here. The model is clearly an approximation of the real system and as such will involve some error. Secondly there will be some error in the experimental measurements. It is noticeable that the model and experiment are in good agreement for measurements of A_{BCS} and A_{ER}, where averaging is involved and absolute pressure values are not calculated, but show poor agreement when relative magnitude values are more significant, as for the R_{BN}. The likelihood of some mis-alignment of the device for the experimental case has been considered. It has been observed that

the alignment process used does not favour measurements made close to the device. In addition in this area pressure variations have been observed to be both extreme and rapid, occurring on a scale of less than a wavelength. This not only makes the location of maxima difficult experimentally but also makes it difficult to measure the values accurately with a finite size receiver. The fact that the real device is not truly circularly symmetric further complicates the issue. Further out in the field, but still within the near-field, model-experimental agreement is better both qualitatively and quantitatively.

A further likely source of errors is in the differences between the parameters in the real device and the model parameters. Firstly there is the fact that a number of features of the real device were not included in this initial model, such as the recess which the disc rests on and some glue layers. Secondly there is the fact that a number of material properties were known only approximately, if at all, particularly piezoelectric constants. Thirdly there may have been some discrepancies in the dimensions of the device. These are not likely to be significant as components were measured before the device was constructed; however, it is possible that minor variations in areas such as glue layer and matching layer thickness could have a significant effect.

Finally there are a number of areas of the structural model that have not been considered. Features such as wires and soldering were not included because of the use of symmetry in the model. Likewise irregularities in the transducer construction causing it not to be symmetric were not included. Also it is likely that some component material properties are affected by the dimensions of components within the device, or by the frequency at which the device operates. For example, it is reasonable to consider whether or not the Young's modulus of a very thin glue layer is the same as that quoted by manufacturers from measurements made on a larger sample that was cured under significantly different conditions.

Overall, then, there are a number of potential reasons for the differences observed here. It must be emphasised that very good qualitative and quantitative agreement has been observed for many measured field features, and that the consideration of the slight mis-alignment for the acoustic axis has led to a significant improvement in the results that previously showed most differences. Chapter 6 will consider the component, material and dimensional features outlined above as possible sources of discrepancy. This is with the intention of improving model-experimental comparative results and analysing the response of the device and field to variations in the basic design considered here.

Chapter 6

6.1 Introduction

Output from the full transducer-fluid system model was compared with corresponding experimental measurements made on the real physiotherapy device in the last chapter. Generally good agreement was observed, with the model accurately predicting both the characteristics of the real acoustic near-field and often absolute pressure values. The near-field was shown to be significantly different to idealised theoretical and analytical 1-D predictions. However some results were not in good agreement, specifically the magnitude of axial results close to the device and the electrical response with frequency. A number of possible reasons for these discrepancies were considered in Chapter 5 – experimental error, difficulties in accurately measuring some areas of the near-field, non-repeatability of specific measurements and modelling error. Further possibilities included differences between the real and modelled devices such as different components, the non-symmetry of the real device, and inaccurate model parameters. Some of these issues have been investigated and the results are described in this chapter.

This chapter will extend the modelling in Chapter 5 from its use for model-experimental comparisons to use as a tool for the analysis of model parameters. The analysis of the model will involve sensitivity analyses to examine the significance of the parameters in the model and their potential effect on the generated near-field. Investigating these differences between models will allow potential sources of the model-experimental differences to be identified. Such an analysis also has implications for device modelling and design in general. Differences between the original transducer model and the real device can be considered in several categories - components, component dimensions, geometry and material properties. The significance of the non-symmetry of the real device or non-symmetrical components will not be considered here due to the use of a symmetric model. This means that the wiring and solder will not be considered. All other components will be investigated.

6.1.1 Difficulties in analysing model parameters

Any analysis of model parameters is difficult for a number of reasons. Firstly, there are a number of other possible sources of differences between the model and experimental results that have already been mentioned. Secondly, many of the results used for comparison purposes are measured indirectly. There is no specific measurement of the vibrational behaviour of the real device, but 'secondary' measurements of the electrical response of the device or the generated acoustic field. Thirdly, the model has already shown that the behaviour of the device is significantly non-uniform and that there is complex interaction between components and some sensitivity to frequency. Fourthly there are a number of practical considerations – the simulation run times, the extraction of results and difficulty of extracting information. Add to this the large number of model parameters and the limited availability of some accurate material properties and it is clear that such an analysis is a difficult, if not unfeasible task. In order to approach the problem, therefore, a number of concessions will be made.

6.1.2 Analysis limitations

Out of the large number of parameters in the models considered here, it is likely that a number of them are of relatively little significance in terms of the behaviour of the device and their effect on the acoustic field. Establishing which features of the device are of *little* significance is important in its own right for design criteria, but it will also be used here to significantly reduce the size of the "parameter spaces" that need to be searched more thoroughly. Without such a reduction the analysis required here would be unfeasible. This can be emphasised by considering a model of a disc alone, operating in vacuuo. Such a model requires 14 independent parameters to describe it and takes approximately two minutes to run over 100 frequencies on a Viglen genie 500 MHz PC. A search of the entire parameter space for just two values per parameter would require 2^{14} models and take approximately 23 days to generate the results. Any analysis of the output would be in addition to this.

6.2 Differences between the model and the real device – components

There are a number of features of the real device that were not included in the original model for reasons other than symmetry. This was either because it was expected that certain components would have little effect on the generated acoustic field or because the inclusion of these components would significantly increase run times and memory requirements. These components were:

- the outer casing;
- the inner-outer casing glue layer;
- the (disc) recess;
- the disc-recess glue layer;
- the inner and outer casing connectors.

Taking the DAA2c model used to generate the output in Chapter 5 as a basis, each of these components were added to the model *individually* to determine the effect on the generated field. Within this series of "additional component" models some variation in material parameters was also included for a more comprehensive analysis. Comparisons involved calculating the mean square difference (m.s.d) of the axial pressure results from the original model over the range 0.5 mm to 120 mm in steps of 0.5 mm, the emphasis being on establishing the potential effect on the source and subsequent field.

Figure 6.1 shows the axial output for the two models with the largest m.s.d. from the original model, and the original model axial results. The results are given for the resonant frequency of the individual model – in this case all were resonant at 1.029 MHz. All three models are in good agreement close to the source and it is only further out (but still well within the near-field) that differences occur. In fact the model which includes an 0.2 mm thick recess, and an 0.1 mm thick glue layer between the disc and recess, is generally in good agreement with the original model result. For this particular model the Young's modulus of the glue has been *increased*

by 30% from the original model value. This value for Eccobond *24, quoted in Table 3.1, is based on information supplied by the manufacturers, but is not quoted directly on their data sheet (Emerson & Cuming, 1999). The model with the largest difference is that which includes both a stainless steel outer casing and a glue layer between the inner and outer casings. Here the glue layer is 0.2 mm thick and the outer casing is 1.685 mm thick. Furthermore the Young's modulus of the glue layers was *reduced* by 30% from the original model value. The source displacement amplitude data, in the axial direction, for both of these models together with that for the original, are shown in Figure 6.2. It is clear that the source deformation for the three models differs relatively little, with the only significant difference being towards the outer edge for the model with the outer casing. Figure 6.3 shows the corresponding radial field results at 5 mm from the source.

Two main differences between the experimental and model results were identified in Section 6.1 above. The main issue as far as the electrical response of the device is concerned is likely to be the piezoelectric component. The fact that the resonance frequency of all three models shown in Figures 6.1 - 6.3 is the same would suggest that none of the features here have any significant effect on the electrical response of the modelled device. The second issue is the axial pressure close to the source. It is clear from Figure 6.1 that the model variations here have had little significant effect in this area, certainly in terms of "optimising" results towards experimental axial data. The results shown are for the models with the largest m.s.d.. In order to check that differences around the last axial maxima were not masking differences closer to the source the m.s.d. was also calculated for the first 30 mm of the axial response. The same two models, shown in Figures 6.1 - 6.3, were identified as those with the largest m.s.d..

From these results, it would seem reasonable to conclude that none of the additional components considered are of significance in terms of improving model-experimental comparisons. Furthermore, the modelled device appeared to be fairly insensitive to variations in and/or the inclusion of these components. It is worth mentioning that the

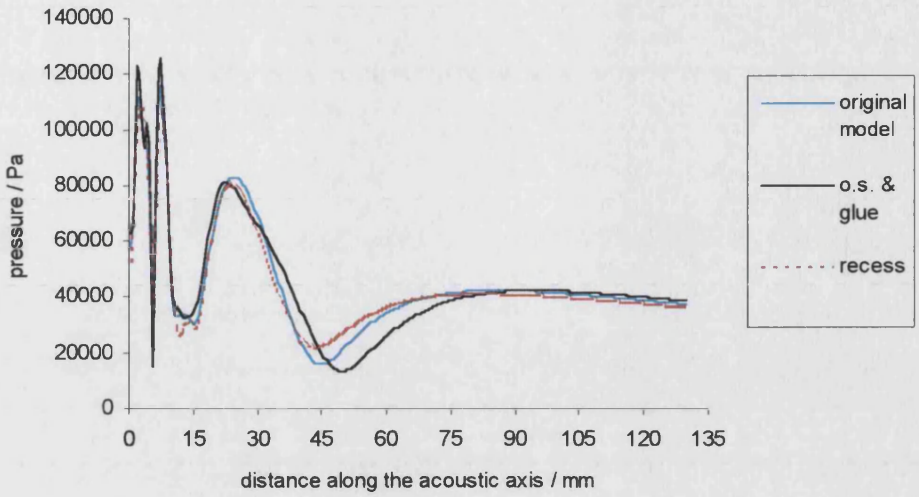

Figure 6.1 Axial output for models with additional components compared with the output for the original model used in Chapter 5. The "o.s. & glue" model includes both a 1.685 mm thick stainless steel outer casing and an 0.2 mm thick glue layer between the inner and outer casings. The "recess" model includes an 0.2 mm thick recess cut into the inner casing, on which the disc rests, and an 0.1 mm thick glue layer holding the disc here.

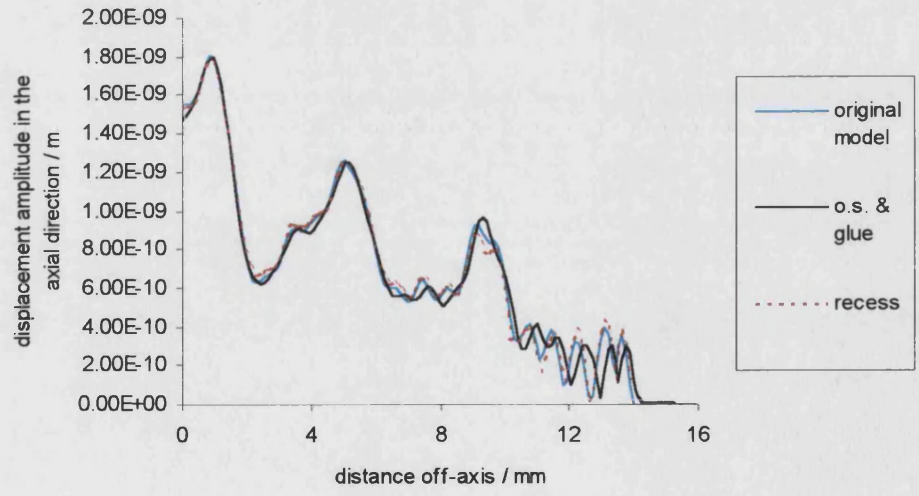

Figure 6.2 Source displacement amplitude in the axial direction, for models with additional components compared with the original model used in Chapter 5. The two additional models are as described for Figure 6.1. All results are for an operating frequency of 1.029 MHz and a drive level of 1 volt.

inclusion of 0.2 mm thick glue layers at the outer edge of the inner casing and at the recess on which the disc rests does appear to have some impact on field results. Specifically, results generated here for a glue layer with a Young's modulus ± 30% of the original value have produced some changes. This would indicate that the properties of such glue layers could be of some significance in device construction and modelling, however the effect is clearly limited.

6.3 Differences between the model and the real device – inaccurate properties

A second source of differences between the model and real device are component parameters – material properties, dimensions and geometry. The dimensions of all the components were measured before the construction of the device and the component geometry was known. Varying the dimensions and geometry was, therefore, unlikely to improve the model-experimental agreement; it was however considered in order to determine the significance in terms of device behaviour and field response more generally. However, the glue layer at the edge of the disc is relatively very small and its characteristics more difficult to ascertain accurately. In addition in the real device the disc may not be exactly centred leading to non-uniform glue thickness throughout the circumference of the disc. Such features can be considered here to some degree by investigating the significance of the thickness of this layer.

The most significant component parameters considered here are likely to be material properties. In has been emphasised that a number of material properties used in the model are either difficult to measure in practice or are quoted within large tolerances. The accuracy is likely to be further reduced due to variations between the samples on which measurements were made and those in the device. The material properties of the device make up the majority of the input parameters in the simulation – 24 in the model as outlined in Chapter 3.

6.3.1 Components at the edge of the disc – glue layer and inner casing

Components in the principle direction of propagation will be significant for the generated field. However, the model can also be used to investigate the behaviour of other components which cannot be accounted for by 1-D models. The deformation at the source has been seen to be highly non-uniform. This is essentially due to the irregular vibrational response of the piezoelectric element and restraints at the edge of the disc. The non-uniform behaviour of the device is compounded by subsequent interactions amongst the structural components. In this section the influence of the components at the edges of the active element, that is the inner casing and disc glue layer, will be investigated.

As in Section 6.2, the first task was to establish if varying the parameters, within a range indicated by the tolerances, had a significant effect on the generated field. The results were compared with the original model axial output and experimental data, using the m.s.d., for a series of models where each parameter was varied on an individual basis. Each component was described by four material properties – Young's modulus (*E*), Poisson's ratio (σ), density (ρ) and a hysteretic damping factor (μ) - as well as its dimensions. For both components E and ρ were quoted by the manufacturers (Emerson & Cuming, 1999; RS Components, 1999) whereas σ and μ were estimated (Kaye & Laby, 1992). The only glue layer dimension was its thickness, whilst the inner casing was defined by the thickness and length of the cylindrical section and the thickness of the end cap. The comparison with experimental results (shown originally in Chapter 3, Figures 3.8, 3.9 & 3.11, and used for model-experimental comparisons in Chapter 5) considered parameter variations over ranges relatively close to the original values. The more general sensitivity analysis was performed over larger ranges.

6.3.2 Variations in the supporting (disc) edge glue layer

Models with varying glue thickness and material properties were run over ranges of up to $\pm 40\%$ of the standard values, with parameters generally varied on an individual basis. As in Section 6.2, little variation was observed. Figure 6.4 shows the axial comparison for the two models with the largest m.s.d. compared to original model axial results. The model with the largest m.s.d. actually has the Eccobond material properties replaced by the matching layer material - Araldite. This was considered here as the curing process for the Araldite may have influenced the properties of the glue layer. The model with the second largest m.s.d. has NO glue layer. Once again the resonance of both models remains 1.029 MHz suggesting little impact on the electrical response of the modelled device. The nature of the axial variation again suggests that the changes considered here have little effect on either the axial variation close to the source or indeed the beam in general. A m.s.d. comparison of these results against the experimental axial output used in Chapter 5 showed little if any improvement. It seems reasonable to conclude that although the properties of the edge glue layer can have some effect on the device and field response, the model is relatively insensitive to the variation of these parameters.

6.3.3 Variations in the inner casing

Models were run with inner casing dimensions varied by up to $\pm 10\%$ of the measured values. Variations in E and ρ of up to $\pm 25\%$ of the quoted values were also considered, whilst σ was varied over the range 0.2 - 0.49 and μ over the range 0.001 - 0.3. The axial results are compared with the original model results in Figure 6.5 for the two models with the largest m.s.d. compared with the original model results. The experimental axial output used in Chapter 5 is also shown to highlight the nature of the last axial maxima for these plots. One model has a value for ρ 25% less than the quoted value and the second has E 25% more than the quoted value. There is little significant effect on the axial variation close to the source and a m.s.d. comparison against experimental measurements showed no improvement. Similar

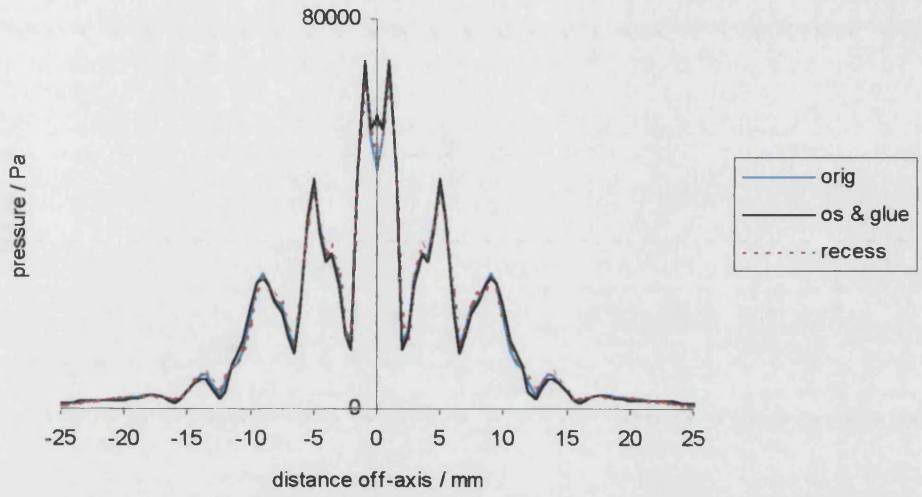

Figure 6.3 Radial output at 5mm from the source, for models with additional components as in Figures 6.1 and 6.2.

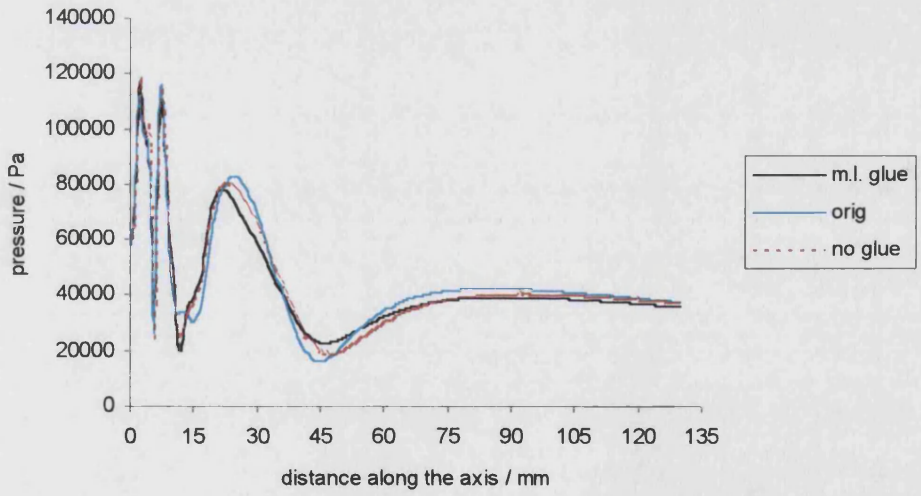

Figure 6.4 Axial output for a model with a glue layer at the edge of the disc having the same material properties as the matching layer (m.l. glue), and a model without a glue layer here (no glue). These are compared with the output for the original model used in Chapter 5. Again all models are operating at 1.029MHz.

results were again observed when the m.s.d. was considered for axial results up to 30 mm only. The resonance remained at 1.029 MHz for both models suggesting little impact on electrical response. Overall then it is reasonable to conclude that variations in this component were unlikely to improve model-experimental comparability.

A further analysis of inner sleeve parameters was considered without restricting variation to values close to the original ones. Models where either E or ρ were varied by significantly more than 25% were observed to generate results with larger m.s.d.s than shown in Figure 6.5. The variation in both σ and μ still had little impact. Instead of considering a whole range of results for varying values of E and ρ it seems more sensible to establish the effect of changing parameters to those of a material with significantly different properties. A model was generated where the inner casing has stainless steel properties, as for the outer casing. The axial plot for this is shown in Figure 6.6. Also shown is a model with a larger m.s.d. that has the thickness of the inner casing reduced by 25%. This is now resonant at 1.031 MHz whilst the model with stainless steel casing remains resonant at 1.029 MHz. Once again little variation is observed very close to the source for both models, however further out there are some clear differences. Overall, however, the characteristics of the plot remain fairly consistent. A calculation of A_{ER} and beam type was made for both of these models for a more comprehensive assessment of the effect on the overall field. The result of this is shown in Table 6.1 compared to the original model output.

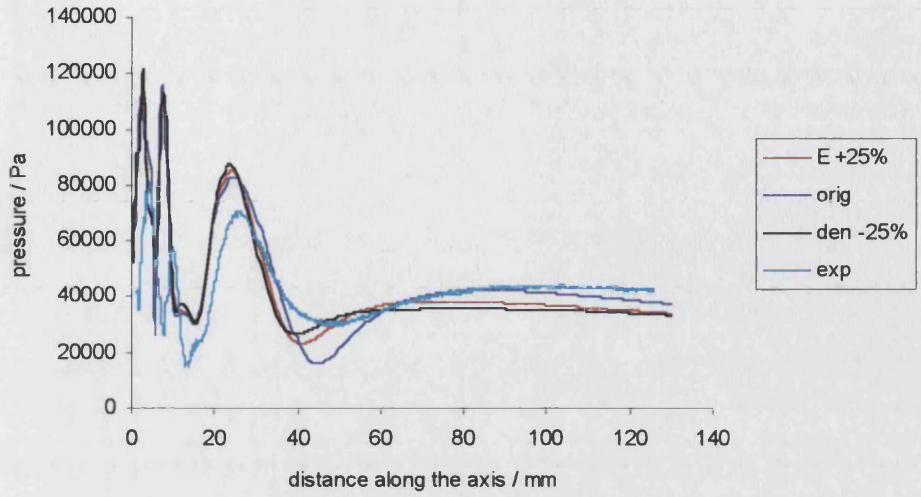

Figure 6.5 Axial output for models with varying material properties for the ABS inner casing. Comparison is made here against the original model (orig) and experimental results (exp). The model with the largest m.s.d. (den –25%) has a density value 25% lower than the original quoted on the RS data sheet. The second largest m.s.d. (E +25%) is for a Young's modulus 25% higher than the quoted value.

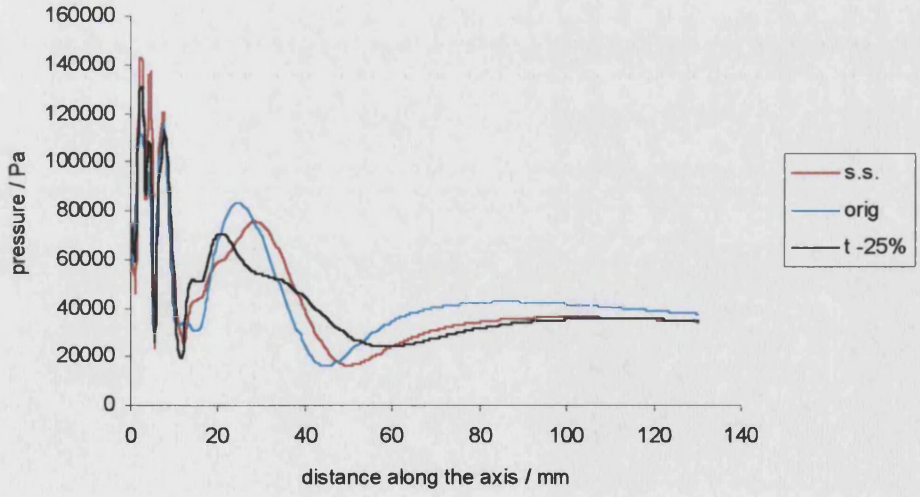

Figure 6.6 Axial output for models with significantly varying parameters for the ABS inner casing. The model with the largest m.s.d. (t –25%) has a thickness 25% lower than the measured value and is resonant at 1.031MHz. The second largest m.s.d. (s.s.) has had the ABS material properties replaced with those of stainless steel and remains resonant at 1.029MHz.

Model	Original	Inner casing thickness reduced by 25%	Inner casing stainless steel
m (gradient)	0.20	0.27	0.28
beam type	collimated	collimated	collimated
A_{ER} / cm^2	3.09	3.01	3.25

Table 6.1 Model-to-model comparison of A_{ER} and beam-type for additional models showing significant differences in axial output from the original model.

It is clear that despite some fairly significant differences on the axial plot, the overall effect of varying the inner casing in this manner has had little effect on the nature of the field and the magnitude of the pressure maxima and minima within it. The results here for the glue layer and inner casing are quite significant as, along with the comparison of additional components in section 6.2, they suggest that the precise way in which the disc is mounted is not significant for the overall vibration of the transducer. Of course this applies to the mountings considered here, but the ranges considered indicates that alternative "edge" mountings are not likely to be significant.

A final point arises with respect to the length of the inner casing. It has been confirmed that the exclusion of the outer casing has little effect on the behaviour of the model. The exclusion of this casing allows for a reduction in the size of the overall modelled transducer structure, which in turn reduces the modelling requirements of the unbounded fluid region. The length of the inner casing therefore essentially determines the length of the modelled structure. Here an analysis of this dimension has revealed that a large reduction in the length of the casing has no significant effect on model output. Figure 6.7 shows axial variation for a model with inner casing length reduced from 23.0 mm to just 5.0 mm. The comparison with the original model result shows little effect on the response of the device and the resonance remains at 1.029 MHz, however model run time is significantly reduced to less than 5 minutes for one frequency. Such a model could therefore be used for a

faster analysis of model parameters. The analysis of the matching layer in section 6.5, where some consideration will be given to a multi-dimensional parameter space for the full transducer-fluid system, will use this 'reduced' DAA2c model. Unless otherwise stated all other *device* model analyses will be based on the original full-size model generated in Chapter 3.

6.4 The piezoelectric disc

The piezoelectric element is likely to be very significant for the nature of the source deformation and subsequent field of any device. For an air-backed device where there is no backing layer to damp out some of the irregular vibrational behaviour in the disc the response of the disc is likely to be even more significant on source deformation. In addition, the piezoelectric component is difficult to model accurately for several reasons. Firstly there is the large number of parameters necessary to model the disc – 14 altogether. Secondly, many of the disc parameters are quoted in the manufacturers literature (Ferroperm, 1995; Vernitron, 1976) within relatively large tolerances. Due to the difficulty of measuring some properties and the possible differences between piezoelectric samples, conversations with manufacturers have led the author to believe that even the quoted tolerances may err on the optimistic side. Thirdly, in general the modelling of the piezoelectric element must be evaluated against *indirect* experimental results, whether this is electrical response or field data generated by the full device. This is certainly the case here, as no measurement of the deformation of either a piezoelectric disc or the source of the device has been made. However when the physiotherapy device was constructed, a disc was taken from the same batch as that used in the device so that electrical measurements could be made on it. There were, therefore, three indirect ways of investigating the modelled response of the piezoelectric component that were available here:

- comparison with the electrical response of the reference piezoelectric disc;
- comparison with the electrical response of the *transducer*;
- comparison with the experimental field of the transducer.

The problem with the electrical and field predictions for the transducer is that they are clearly affected by a number of other model parameters. Furthermore the much shorter run times associated with an analysis of the disc alone strongly suggested that a direct analysis of the effect of the piezoelectric properties on the disc behaviour was much more realistic than that of a full transducer-fluid system model. For these reasons the analysis of the effect of the disc parameters will be based around comparisons with the experimental electrical response of a disc on its own. Comparisons, of a secondary nature, will then be made for a full transducer model.

6.4.1 "Optimisation" of electrical response data

Patrick Macey from PAFEC supplied batch code for a series of models to run with varying parameters. Here models were generated automatically based on specification of the parameters to be varied, limits for parameters values and incremental sizes. It should be emphasised that the parameter values must therefore be pre-determined – this is *not* an optimisation routine incorporating analysis of model output. Admittance results were output for each model run over a pre-determined frequency range. On this basis a Fortran 77 program was written to analyse conductance data and make comparisons with chosen 'optimal' data files – either the standard disc *model* electrical response or experimental measurements on a real disc. The program was designed to identify results with conductance peaks close to the right frequencies and with similar amplitudes. This was achieved by analysing a data file of model electrical results, establishing the relative positions and magnitudes of peaks and comparing this against a similar analysis of the 'optimal' electrical response file. In addition an m.s.d. comparison of the model electrical response against the 'optimal' file was also made.

6.4.2 Initial model-experimental *disc* electrical response comparison

Figure 6.8 shows a comparison of the conductance of a disc model using data as for the standard model with the experimental measurements made on the real disc.

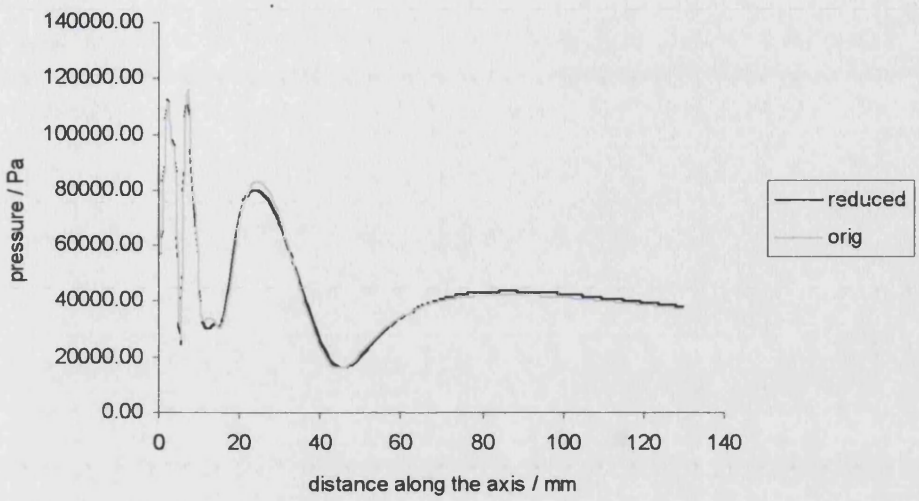

Figure 6.7 Axial output for model with significantly shorter inner casing (length 5.0 mm) compared to the original model output (length 23.0 mm). The output is similar enough to suggest that the reduced model could be used for the analysis of varying model parameters, and significantly reduce the time that this takes. Both models are resonant at 1.029MHz.

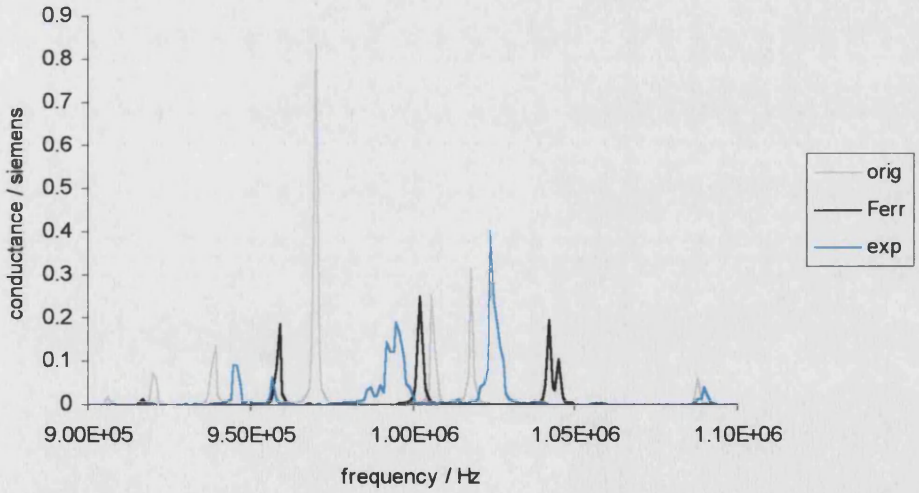

Figure 6.8 Model-experimental comparison of electrical response of Pz26 piezoelectric disc. The experimental measurements are made on a disc from the same batch as the one in the physiotherapy transducer. Comparison is made against model results for the disc properties used in the original transducer model (orig) and those later provided by the disc manufacturers, Ferroperm (Ferr).

Chapter 3 mentioned the fact that a number of property values not originally specified by Ferroperm were subsequently made available. The disc model with these property values is also included in Figure 6.8. The original and Ferroperm material property values are shown in Table 6.2. Experimental measurements were made with the same impedance analyser used for measuring the response of the transducer outlined in Chapter 3. The measurements have been repeated a number of times.

The obvious concern resulting from the plots shown in Figure 6.8 is the significant differences between the curves. The original disc model has a main resonance at 970 kHz and the thickness extensional mode at 1.018 MHz is the second largest. The resonance at 970 kHz is undoubtedly the reason for the secondary resonance apparent in the modelled *transducer*, considered in Chapter 5 and shown in Figure 5.1. The disc model based on Ferroperm data has two resonances at 1.042 MHz and 1.002 MHz, some distance either side of the experimental resonance at 1.024 MHz. Experimentally there is also a secondary resonance around 995 kHz. The inconsistency in these results is in contrast to the general accuracy of *transducer* model-experimental *field* comparisons. This would seem to suggest either considerable good fortune with respect to the piezoelectric parameters in the original model, or some robustness in the behaviour of the full system compared to the electrical response of the disc. These results suggest that there is considerable room for improvement in the modelling of the disc. Unfortunately the differences between the two models would also suggest that the disc (model) might be sensitive to a number of parameters. A substantial analysis of the piezoelectric properties will therefore follow.

6.4.3 Initial disc model "optimisation" towards real *(disc)* electrical response data

As outlined in Section 6.4.1 the starting point for the analysis of such a large number of parameters was to try and identify those that were of least significance. To achieve this a series of disc models were run over a range of frequencies for models with

parameters varying on an individual basis. The Ferroperm guide (1995) quotes the accuracy of measurement within limits of between ±2.5% and ±10%, whilst other guides (Vernitron, 1976) quotes limits of ±20%. The initial analysis involved parameters varying by up to 10% from the *Ferroperm* data. Models of all 14 parameters were run over five values each and comparisons made against the *Ferroperm model* output. Analysis by the program outlined in Section 6.4.1 suggested that the results were sensitive to *all* parameters but highlighted the five independent elastic compliance parameters, S_{11}^E, S_{33}^E, S_{12}^E, S_{13}^E and S_{44}^E, as being most significant. The extent of the variation in electrical response can be seen in Figure 6.9. Here the Ferroperm disc model electrical response is compared with a similar model where the S_{11}^E, S_{33}^E and S_{13}^E parameters are varied by –4%, -5% and +6% respectively. The fact that this analysis involved varying parameters by no more than 10% emphasises the difficulty of comprehensively analysing disc parameters.

Based upon these results it was decided to analyse the piezoelectric properties in more detail by initially varying the five elastic constants simultaneously. From the results of varying these five parameters, future runs would consider all of the material parameters at some stage. In this way some attempt to investigate a number of "multi-dimensional" parameters spaces of the disc model would be approached. No further analysis of the disc dimensions was considered as the disc on which experimental measurements were made was measured accurately.

6.4.4 Secondary disc model "optimisation"

A series of analyses were made using both the original piezoelectric properties and the Ferroperm values as starting points. Searches were made, over varying ranges, by initially altering the five elastic constants. Here the searches were over multi-dimensional spaces as opposed to the initial searches made by varying parameters on an individual basis. The data was analysed using the program described in section 6.4.1 with the experimental results as a reference. At subsequent stages, once an electrical response was achieved showing good agreement with the experimental

measurements, a small area around that set of parameters was chosen as the search space. During these searches the remaining material parameters were considered as additional variables or in place of one of the elastic constants. In all several thousand models were considered and all material parameters considered to some extent. After all of the simulations had been run the data was further analysed using a m.s.d. approach that allowed for some shifting in the frequency domain of the electrical results compared to experimental data. It should be pointed out that the earlier consideration of the search space for 14 parameters with 2 values per parameters would involve in excess of 16,000 models. So although some significant effort and computing power went into making this analysis, relatively small search spaces were analysed.

Figures 6.10 and 6.11 show the electrical response of four models compared with experimental measurements on the real disc. The models shown here are in best agreement with the experimental results. Overall the models generate similar features to the experimental electrical response. The material parameters for all of these models are given in Table 6.2. Figures 6.12 and 6.13 show the displacement amplitude variation (in the axial direction) along the "radial" face of the disc for all four models compared with similar results for the disc model used in the original transducer model. The deformation is for the resonant frequency closest to the experimental resonance at 1.024 MHz. Note that no experimental measurements have been made to generate real disc deformation data for comparison. Figure 6.14 shows the displacement *phase* variation (in the axial direction) along the same face of the disc for all four models. There are clearly some extreme differences between the model disc deformations, not least compared against the original disc used for the transducer model in Chapter 5. From Table 6.2 there are also clearly some significant differences between model parameter values.

Figures 6.15 and 6.16 show the electrical response for four modelled *transducers* operating into water and incorporating the disc model parameters shown in Table 6.2. They are compared with the experimental plot. Although agreement is not good no

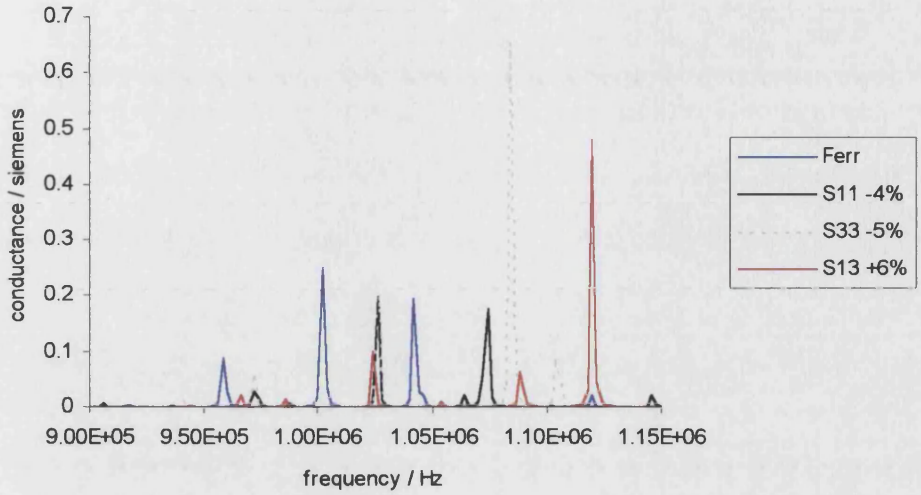

Figure 6.9 Model-model comparison of electrical response of disc in vaccuo. The starting point for all of these models was the quoted Ferroperm values. Additional models shown here are generated by varying the S_{11}^{E}, S_{33}^{E} and S_{13}^{E} parameters by –4%, -5% and +6% as shown. The results shown exhibit the largest variation from the original Ferroperm model.

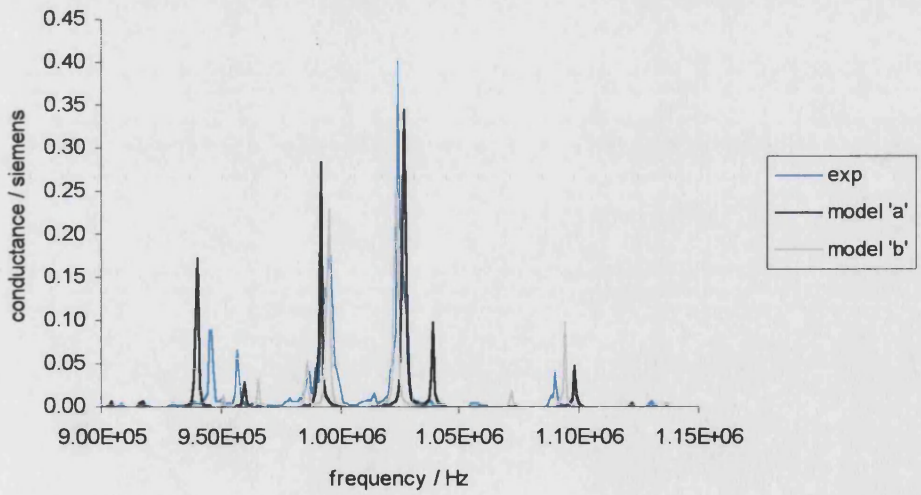

Figure 6.10 Model-experimental comparison of electrical response of disc in vaccuo-air. The models were generated from a large analysis of modelled disc parameters. The parameters for models 'a' and 'b' are shown in Table 6.2.

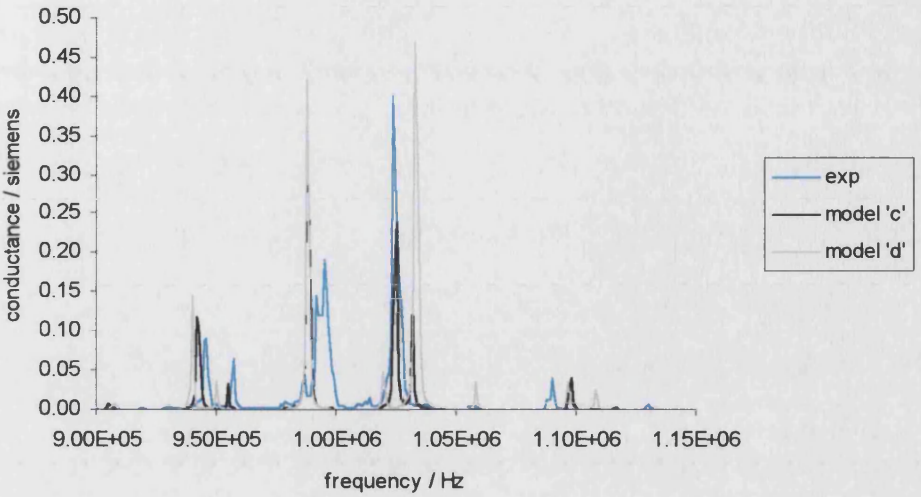

Figure 6.11 Model-experimental comparison of electrical response of disc in vaccuo-air. The models were generated from a large analysis of modelled disc parameters. The parameters for models 'c' and 'd' are shown in Table 6.2. The experimental results are shown in (exp).

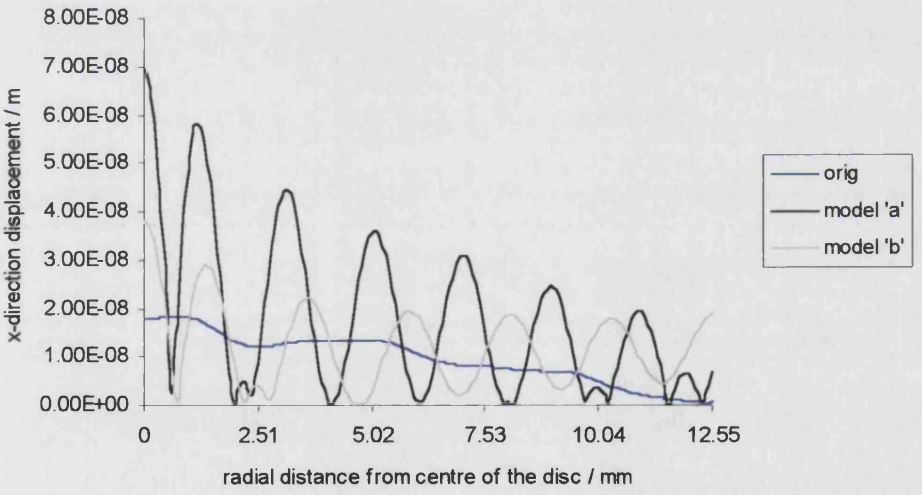

Figure 6.12 Model-model comparison of the displacement amplitude (in the axial direction) for the face of the disc in vaccuo. The comparison is made against the disc from the original transducer model (orig). The parameters for models 'a' and 'b' are shown in Table 6.2 and the electrical response of these models is shown in Figure 6.10.

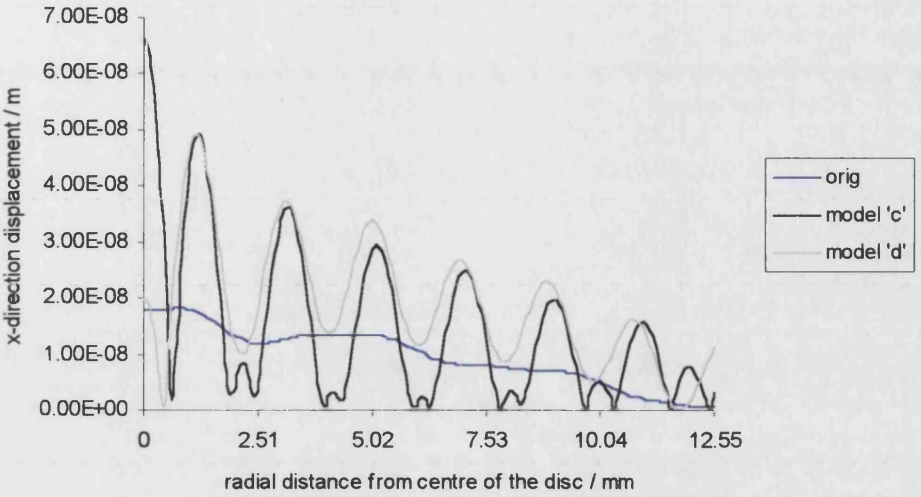

Figure 6.13 Model-model comparison of the displacement amplitude (in the axial direction) for the face of the disc in vaccuo. The comparison is made against the disc from the original transducer model (orig). The parameters for models 'c' and 'd' are shown in Table 6.2 and the electrical response of these models is shown in Figure 6.11.

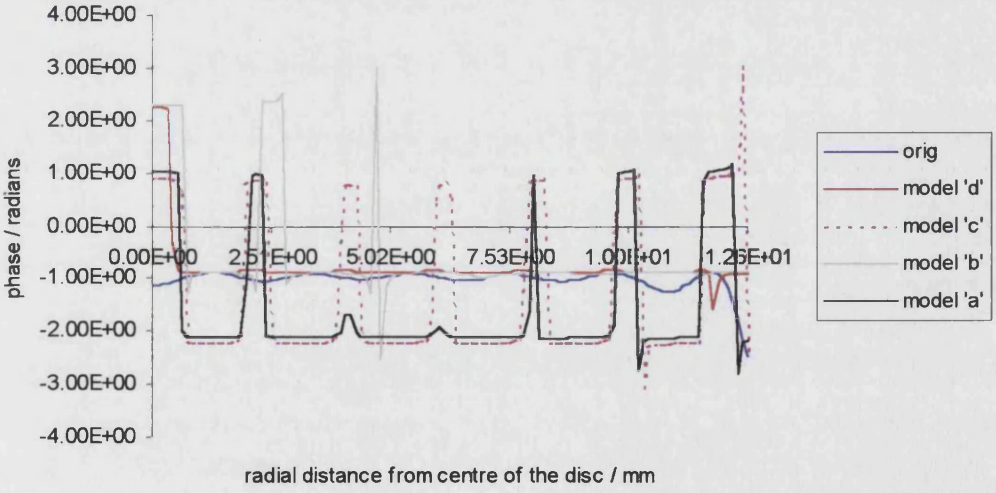

Figure 6.14 Model-model comparison of the displacement ***phase*** (in the axial direction) for the face of the disc in vaccuo. The comparison is made against the disc from the original transducer model (orig). The parameters for models 'a', 'b', 'c' and 'd' are shown in Table 6.2.

parameter	original	Ferroperm	Model 'a'	Model 'b'	Model 'c'	Model 'd'	units
S_{11}^{E}	13	13	12.6	12.5	13	13.4	10^{-12} m^2 / N
S_{33}^{E}	20	19.6	19.8	21.0	19.6	19.0	10^{-12} m^2 / N
S_{12}^{E}	-4.23823	-4.35	-4.45	-4.125	-4.45	-4.45	10^{-12} m^2 / N
S_{13}^{E}	-7.0485	-7.05	-6.90	-7.40	-6.95	-7.00	10^{-12} m^2 / N
S_{44}^{E}	34.85	33.2	35.7	27.5	34.5	34.7	10^{-12} m^2 / N
ε_{33}^{S}	6.34975	6.1950	6.195	6.1993	6.00	6.195	10^{-9} farads / m
ε_{11}^{S}	7.35	7.3278	7.20	7.165	7.20	7.20	10^{-9} farads / m
d_{31}	-130	-125	-115	-130	-115	-115	10^{-12} C / N
d_{33}	330	328	285	310	285	285	10^{-12} C / N
d_{15}	494	327	300	533.4	300	300	10^{-12} C / N
ρ	7.70	7.70	7.70	7.60	7.70	7.70	10^{3} kg / m^3
μ	0.001	0.001	0.001	0.001	0.001	0.001	-

Table 6.2 Comparison of model piezoelectric properties. The second column gives the values used in the original model. The third column lists the values later made available by the manufacturers, Ferroperm. The four subsequent columns give the values used to generate the electrical results shown in Figures 6.10 and 6.11 following the analysis of the piezoelectric parameters. Note that the omission of the S_{66} values is due to the fact that this parameter is automatically calculated from other parameters.

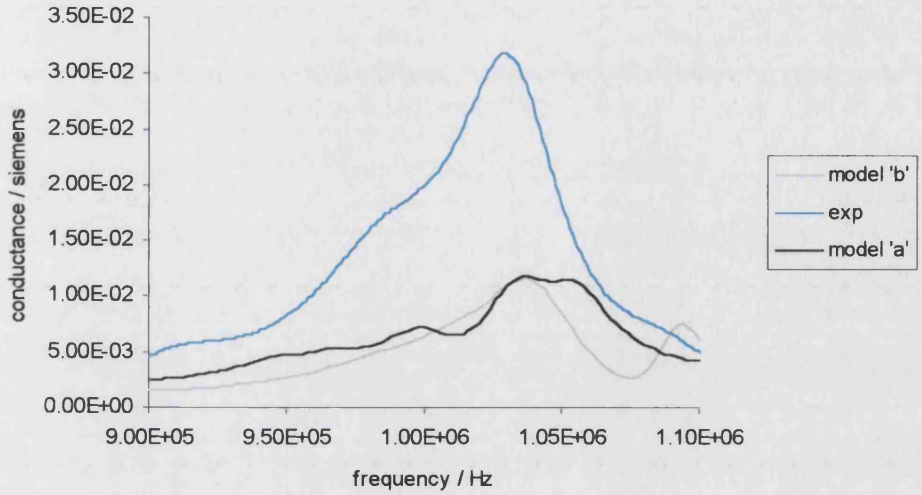

Figure 6.15 Model-experimental comparison of electrical response of ***transducer-fluid*** system. The transducer models are the same as the original one used in Chapter 5 except that here the piezoelectric material parameters for models 'a' and 'b' are as shown in Table 6.2. The experimental result (exp) was presented in Chapter 3, Figure 3.3.

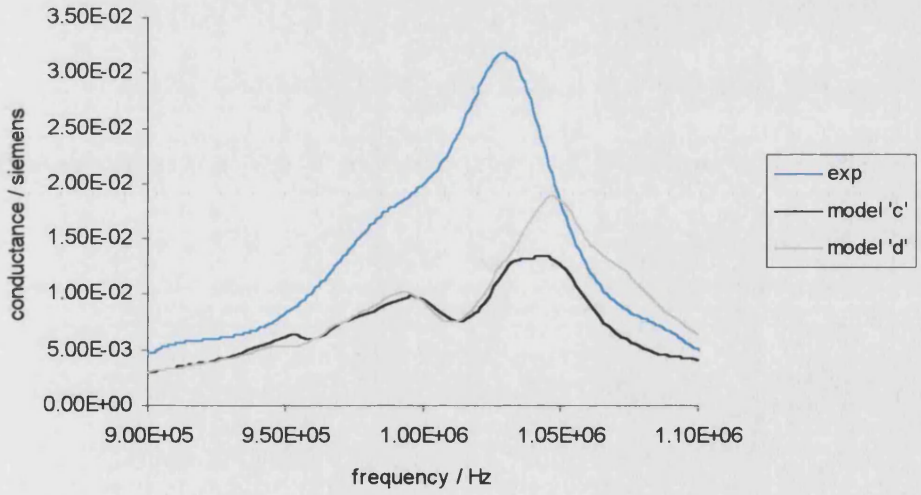

Figure 6.16 Model-experimental comparison of electrical response of ***transducer-fluid*** system. The transducer models are the same as the original one used in Chapter 5 except that here the piezoelectric material parameters for models 'c' and 'd' are as shown in Table 6.2. The experimental result (exp) was presented in Chapter 3, Figure 3.3.

further consideration has been given to improving the model-experimental comparability of the *electrical* results of the transducer-fluid system. This is because electrical data is primarily used here to establish the working frequency of the device – modelled or real – and the main area of interest is the near-field pressure results and how sensitive they are to model variations.

Figures 6.17 and 6.18 further show the axial pressure plots due to these four transducer-fluid models operating at the resonant frequencies established from Figures 6.15 and 6.16, and again compared with experimental data. It can clearly be seen that the piezoelectric properties alone have a significant effect on the generated field. It can also be seen that in the areas where model-experimental comparability was least accurate, the very near-field, there is the potential for varying piezoelectric properties to have a substantial effect. No model-experimental m.s.d. comparisons have been made here as the "optimisation" of the disc parameters was made for model-experimental *electrical* results. A model-experimental *near-field pressure* optimisation for the piezoelectric parameters would be a much larger problem.

6.4.5 Disc modelling – conclusions

The response of the piezoelectric disc model is very difficult to analyse comprehensively and effectively. A large number of parameters are required to define the disc model and a comprehensive analysis of such a parameter space is beyond the limitations of this work. The analysis of disc parameters is further complicated by the fact that manufacturers quote property values within wide tolerance limits, not least because of the difficulty of measuring many of these properties in practice. It has also been seen that the electrical response of the disc model is highly sensitive to all parameters. It is difficult to establish whether or not the "optimal" solutions achieved here are local as opposed to global optima even for the small parameter spaces investigated. This leads to a further point. The "optimal" solution is obviously dependent on the analysis of model-experimental electrical results. The analysis techniques used here are by no means definitive. Some compromise has to be

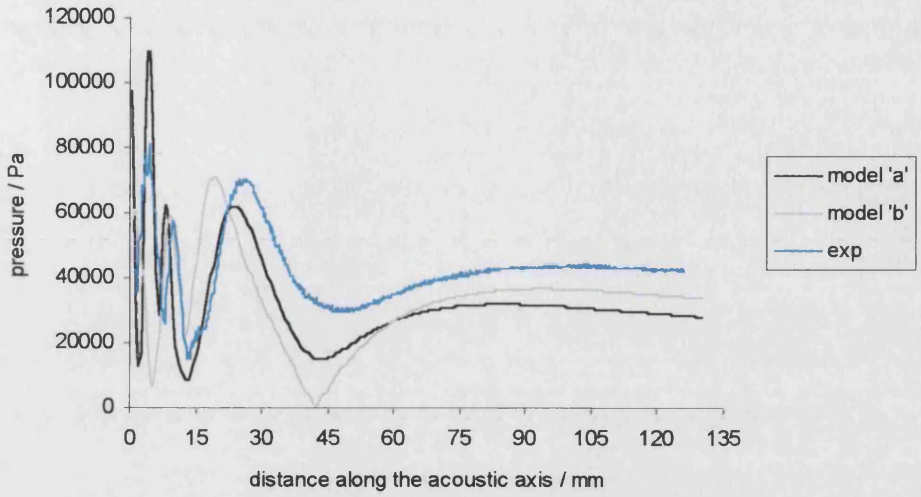

Figure 6.17 Model-experimental comparison of axial pressure amplitude. The transducer models are the same as the original one used in Chapter 5 except that here the piezoelectric material parameters for models 'a' and 'b' are as shown in Table 6.2. The experimental axial results (exp) are those that have been used extensively both here and in Chapter 5.

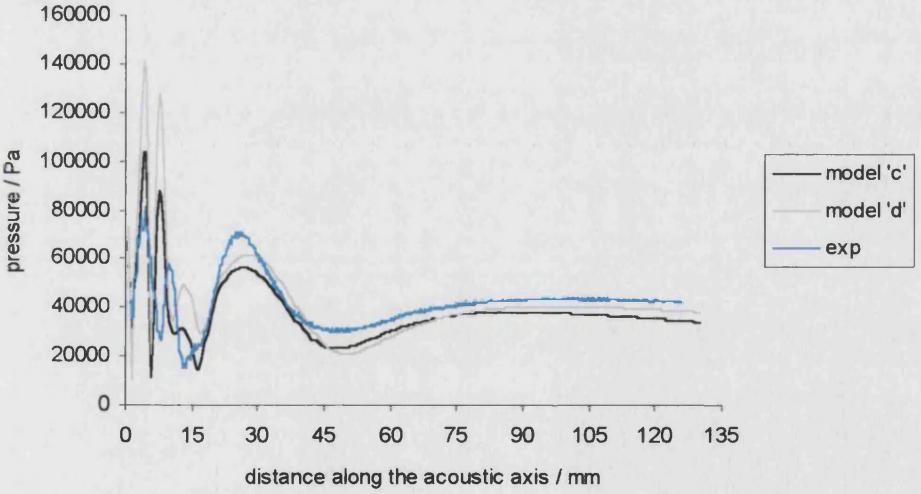

Figure 6.18 Model-experimental comparison of axial pressure amplitude. The transducer models are the same as the original one used in Chapter 5 except that here the piezoelectric material parameters for models 'c' and 'd' are as shown in Table 6.2. The experimental axial results (exp) are those that have been used extensively both here and in Chapter 5.

accepted between how comprehensive the analysis is and how accurate the model-experimental comparison can be, so some inaccuracy must be expected.

It has been observed that different combinations of parameter values can achieve similarly accurate electrical results whilst producing significantly different vibrational results. This implies that model agreement for the electrical response of the disc is no guarantee that the model and real disc agree in terms of vibrational response. Therefore a comparison of disc electrical response alone is not sufficient to optimise the model disc performance towards real disc behaviour. Although it may be possible to analyse the real disc vibrational behaviour experimentally this has not been approached here. For a more comprehensive assessment of the disc such experimental measurements are likely to significantly improve both the modelled disc and the modelled transducer-fluid system agreement with experiment.

The analysis here involved searching a number of small multi-dimensional parameter spaces to optimise the electrical output of a disc model to corresponding experimental results. A feature that is not considered is exactly what parameter values are realistic as compared to what can be considered by a mathematical model. One conclusion, however, is that the piezoelectric parameters do not need to be known extremely accurately for the vibrational behaviour of the main resonance to produce fairly accurate results in the corresponding transducer model. Although the *electrical response* of the modelled disc is highly sensitive to a number of parameters the corresponding transducer-fluid system is not so sensitive, as far as the gross vibrational behaviour is concerned. This means that to accurately simulate the general response of the device and field, the modelled piezoelectric disc must just respond with what is primarily a deformation in the thickness of the disc around the desired frequency. The detailed vibrational behaviour of the disc with deformations occurring on a scale relative to a wavelength is likely to account for at least some of the specific features of the transducer behaviour and field response. It is therefore to be expected that some of the piezoelectric parameters are responsible for such features.

This analysis of the disc should emphasise the complexity of modelling this component. An analysis of the disc parameters directly within a transducer model to try and improve model-experimental fields results would be significantly more complex and require an excessively large number of models and simulation run times. The more specific features of the field are likely to be more dependent on the piezoelectric properties but there are also a number of other factors likely to effect these features, including the matching layer parameters which will be considered next.

6.5 The matching layer

It is clear that the matching layer will have a significant effect on the nature of the generated field as its thickness and material properties are chosen with the intention of optimising the efficiency of the device. As before, the analysis will begin with a consideration of parameters on an individual basis to establish whether or not the transducer model is sensitive to these parameters.

6.5.1 Initial matching layer analysis

There are five matching layer parameters, the thickness and four material properties – E, ρ, σ and μ. In the original model the thickness of the layer is known fairly accurately from measurements made during construction. The manufacturer provided the value for ρ. E was based on a calculation made after a measurement of the velocity of sound on a sample of the material provided by George Cattermole. σ and μ were both estimates. The nature of the 'curing' process takes approximately a week once the Araldite is applied to the transducer face, and the material is actually a mixture of two materials as specified by CIBA-GEIGY (1982). The properties of the material may depend on the curing process, especially as the layer used in the device is small (< 1 mm) compared to the dimensions of the sample used for the calculation of E. For these reasons the accuracy of all of these material properties is uncertain.

On this basis a fairly wide range of values was considered for this initial analysis. The m.s.d. comparison for axial results against the original model output suggested that the system is sensitive to all of the five parameters. It was decided to proceed by analysing this five-dimensional parameter space in some detail. To reduce run times the reduced-size model mentioned in Section 6.3.3 was employed as the basis model. All other component parameters remain unchanged from the original model used in Chapter 5.

6.5.2 Analysis/"Optimisation" of matching layer properties

For the multi-dimensional analysis of the matching layer parameters, m.s.d. comparisons with both the original model axial pressure results and the experimental axial data were made. For the general analysis the emphasis was on the largest m.s.d. to determine the potential variation in field output due to relatively small parameter variations. In contrast, for the comparison with experimental results, the interest was in the smallest m.s.d. in order to try and improve on the experimental agreement. The m.s.d. calculation was made for both the full axial output (~130 mm) and just the first 30 mm of axial output. The results of these analyses are shown in Figures 6.19-6.21.

Figure 6.19 shows the axial pressure amplitude for models with the largest m.s.d. compared with the original model. They emphasise the potential field variation due to relatively minor parameter variations. The material properties for the two models shown, models #1 and #2, are given in Table 6.3. In particular these results highlight the potential effect on the very near-field of the device, and specifically the maximum (axial) field value which is of significance for the calculated value of the R_{BN}. Figures 6.20 and 6.21 show model-*experimental* comparison of axial pressure amplitude for models #3, #4 and #5 having amongst the smallest m.s.d. compared to experimental axial results. They emphasise the potential improvement in field results due to relatively minor parameter variations. Properties for these models are also shown in Table 6.3.

	Thickness	Young's modulus	Density	Poisson's ratio	Damping factor
original	0.867	3.315	1.140	0.41	0.03
#1	0.867	2.652	1.250	0.37	0.01
#2	0.911	2.983	1.140	0.39	0.01
#3	0.911	2.983	1.140	0.43	0.03
#4	0.867	3.978	1.030	0.43	0.01
#5	0.911	3.646	1.140	0.43	0.03
units	mm	10^9 N/m^2	10^3 kg/m^3	-	-

Table 6.3 Matching layer parameters for the five models shown in Figures 6.19 - 6.21 and the original model values for comparison.

In particular Figure 6.21 emphasises the fact that the axial variation close to the source can indeed be significantly reduced in magnitude to levels comparable to experimental results. These results re-emphasise the conclusion that matching layer parameters can have a significant effect on the generated field, including specific measurements such as R_{BN}.

6.6 Summary

Following the generation of an effective transducer-fluid system model in Chapter 5, this chapter has looked at the potential significance of the modelled device parameters on the behaviour of the device and the generated near-field. A substantial optimisation towards experimental results or indeed a comprehensive search of the multi-dimensional parameter space of the modelled device is beyond the scope of this work. Nevertheless some analysis of individual components and individual parameters has been approached and provided useful information on the effect of specific parameters on the overall system.

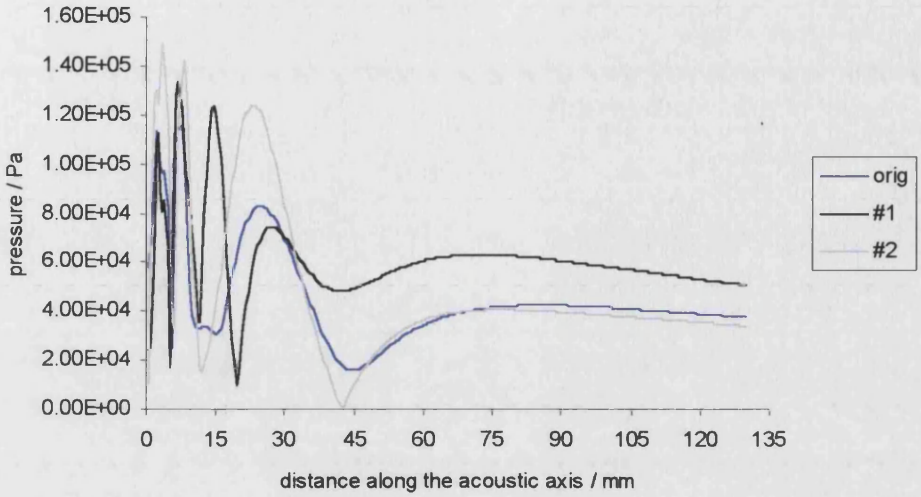

Figure 6.19 Model-model comparison of axial pressure amplitude for varying matching layer parameters. Models #1 and #2 properties are shown in Table 6.3 and they are compared against the original (reduced size) model output (orig). These models have amongst the largest m.s.d. from the original model results and emphasise the potential field variation due to relatively minor parameter variations.

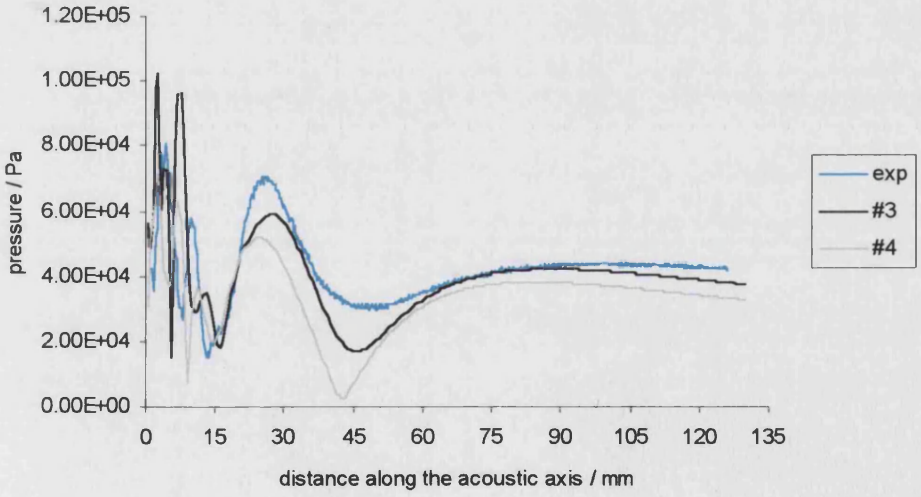

Figure 6.20 Model-experimental comparison of axial pressure amplitude for varying matching layer parameters. Models #3 and #4 properties are shown in Table 6.3. These models have amongst the smallest m.s.d. compared with experimental axial results (exp) and emphasise the potential improvement in field results due to relatively minor parameter variations.

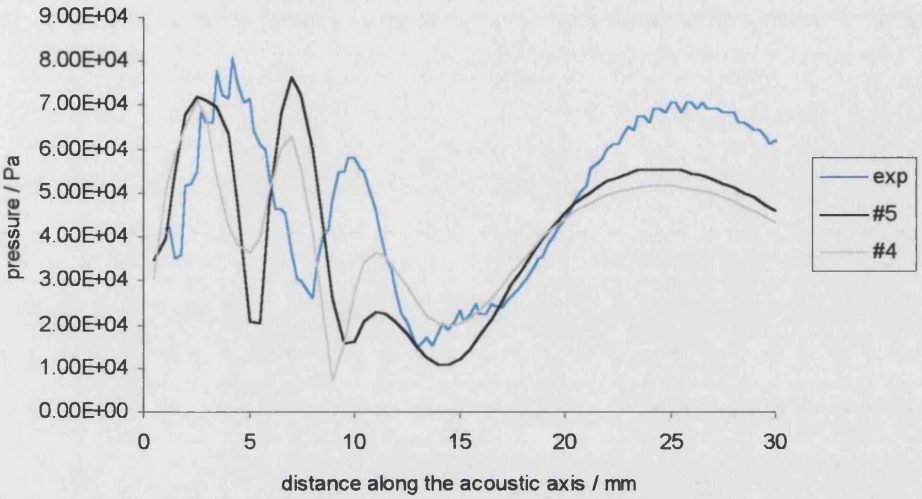

Figure 6.21 Model-experimental comparison of axial pressure amplitude up to the first 30 mm from the face for varying matching layer parameters. Models #4 and #5 properties are shown in Table 6.3. These models have amongst the smallest m.s.d. compared against experimental axial results (exp) for the first 30 mm of axial results.

The conclusions of these analyses are that the gross field characteristics of the device are due to the response of an air-backed device with an active element operating in essentially a thickness-extensional mode and somewhat restrained at its edges. Although there is some potential for components such as the disc glue layer, inner casing and inner-outer casing glue layers to have some impact on the behaviour of the device and field, in general the modelled system in fairly insensitive to variations in these component parameters. By contrast the system is highly sensitive to variations in all piezoelectric and matching layer parameters. Models generated here have shown the potential for effecting the very near-field of the device so that it is more consistent with experimental results considered in Chapters 3 and 5. In addition, some models have generated results significantly different from experimental results, including regions of the near-field where the original model is in good agreement with experiment.

The analyses of model parameters presented here is only really a starting point for the consideration of the significance of parameters and their effect on the behaviour of the modelled device and subsequent pressure field. With reduced model sizes and improving computing facilities a more comprehensive analysis should be possible, leading to the pro-active design of medical ultrasound devices and fields.

This concludes the work presented in this thesis. The final chapter will now bring together all of the work presented here and discuss the conclusions that can be drawn and how they have been arrived at. The important issues and difficulties that have arisen during the course of this work will also be considered. Finally there will be a look at some of the ways in which this work can be continued or extended and some problems to which it might be applied.

Chapter 7

7.1 Introduction

The preceding chapters have looked at the modelling of a real physiotherapy ultrasound transducer and its near-field using finite element and boundary element techniques. The design and construction of a specific transducer has provided considerable insight into the device components and allowed real measurements to be made for model comparison. However the techniques employed here and the issues encountered are likely to be applicable to the modelling of a range of real medical ultrasound systems. The modelled device contains a large number of parameters and radiates into an unbounded fluid region. Three fluid-modelling options have been compared for the simulation of the surrounding fluid medium. The near-field of the real device is seen to be complex with extreme pressure variations occurring on a small scale, however the transducer is both an effective physiotherapy device and fairly typical. The corresponding model has been shown to be generally capable of accounting for such non-uniform field results, even very close to the source, and some considerable analyses of the sensitivity of the system to device parameters has been approached. Where model-experimental discrepancies have been encountered a number of possible explanations have been considered.

What follows is a summary of the work presented in this thesis and the conclusions that can be drawn here. This will begin with a comprehensive discussion outlining the modelling processes and analyses that have been followed, establishing exactly how and why the work here has been progressed, and the implications for the future use of FEM and BEM for the simulation of real medical ultrasound systems. This is followed by a brief summary of the most significant conclusions that can be drawn from this work. Finally there will be a look at some of the areas that this work could be applied to and some of the considerations for further work.

7.2 Discussion

This work has encountered a number of problems relating to the successful simulation of realistic medical ultrasound devices and fields, the use of FEM and BEM for this purpose and the assessment of the modelling methods. These can be considered in several categories:

- Practical issues;
- Modelling of the transducer;
- Modelling a surrounding unbounded fluid media - with particular interest in the near-field region;
- The generation of accurate, repeatable experimental measurements against which model results can be comprehensively tested and assessed.

Summarising these issues here should offer considerable insight into the problems associated with the simulation of real medical ultrasound systems using FEM and BEM, and how they have been tackled.

7.2.1 Practical issues

There are a number of practical features of the work presented here that should not be underestimated and are likely to be at least one reason why this type of modelling approach has not previously been considered in detail. In addition, such issues are likely to remain somewhat of a restriction to future work in this area.

FEM and BEM were chosen here because they offered the potential for modelling realistic device behaviour - specifically the realistic response of piezoelectric components - and could accommodate the simulation of a surrounding fluid media. PAFEC was specifically chosen because it was one of only a few packages that offered these options and was affordable. Whilst using PAFEC, however, two significant practical difficulties were encountered.

Firstly there is the difficulty of actually using PAFEC. As with many such packages it is very difficult to learn how to use effectively. This issue should not be underestimated as it can lead to significant problems when generating a model of a system. Perhaps more significantly it can lead to problems in generating accurate and effective models. In addition to this a number of errors have been found in the package. This is undoubtedly not just an issue with PAFEC, and indeed the manufacturers have been extremely helpful when it came to such issues. Nevertheless it should be highlighted that when applying a piece of software such as this to problems not previously considered (and therefore problems for which the package has not been extensively tested), errors are very likely. This highlights the need for extensive testing and evaluation of models. An example of a specific bug that was encountered was one that generated a spreading wave from the front edge of the modelled device. The nature of the wave meant that it did not show up on axial near-field plots or radial plots within the radius of the device. In fact the problem only came to light during the calculation of the model A_{ER} where the analysis of large cross-axial planes is required. The bug turned out to be due to an inadequate number of points being used for the solution of the exterior Helmholtz integral in the generation of field results. This was a problem for the current work because of the relatively high frequency being used compared with previous studies. It should be noted that in this case the realistic nature of the additional wave made it difficult to be sure that this was an artefact. This highlighted the need for comparisons of different models.

A second issue is that of simulation run times and memory requirements. This has been of particular significance when considering models with large numbers of nodes. Here the biggest problem has been with the use of acoustic elements and WEEs for the simulation of the surrounding media. The run times for such models has been excessive – of the order of 5 hours for one frequency on a 500 MHz PC, and reduced from ~12 hours on a slower PC. In addition the memory requirements of such models have limited the extent of the acoustic region that could be modelled using acoustic elements and have therefore enforced the positioning of the acoustic-

WEE interface at specific points. The use of WEEs will be considered in more detail shortly, however the successful simulation of WEE systems with a *ka* value much larger than the one considered here, ~54, has not been possible for the PC used.

The alternative BEM options for modelling the fluid region have substantially reduced the size of the problem, so that corresponding models can now take as little as 15 minutes to run for one frequency. Furthermore the nature of the DAA2c technique means that many of the systems matrices only have to be solved once, making runs over a range of frequencies much more approachable. However several facts must be kept in mind. The systems modelled here exploit circular symmetry to reduce the size of the problem and the operating frequency is around 1 MHz, which would be considered moderate, if not low, in terms of many medical ultrasound devices. Also, for any comprehensive analysis of system parameters, including searching large multi-dimensional spaces, such run times would still be excessive if not prohibitive. On the plus side ever improving computing options, the reduction in the size of modelled systems through the omission of non-significant components and the possibility of linking parameters through mathematical relationships could help to overcome such difficulties.

7.2.2 Modelling the transducer

Here consideration will be given to the issues that have arisen specifically relating to the model of the *device*. These can be summarised as follows:

- The accuracy of quoted and estimated parameter values;
- The large number of parameters required to define the model of the device;
- The sensitivity of the model to specific device components and parameters;
- The indirect nature of experimental data for the assessment of the modelled device;
- The sensitivity of both the model and the real device to operating frequency;

- Differences between the real device and the model - manufacturing irregularities and components not modelled.

The modelled physiotherapy *device* requires around 30 independent parameters to define it completely. A major reason for designing and building a real medical ultrasound device was to gain a comprehensive knowledge of the components in the device, their dimensions and the materials used. Therefore many device model parameters are accurately known. A number of others are not, specifically material properties of various components. Many material properties, in particular those of the piezoelectric element, are either difficult to measure accurately in practice or measured on material samples different to the components used here, and are therefore less accurate. Tolerances for piezoelectric parameters are quoted between $\pm 2.5\%$ and $\pm 20\%$, (Ferroperm, 1995; Vernitron, 1976). In addition some manufacturers simply do not report some material properties. For these reasons alone model-experimental comparisons are bound to encounter difficulties and some analysis of parameters is required to improve comparability.

A comprehensive analysis of parameters and the sensitivity of the modelled system to parameter variations would require consideration of a dimensionally large parameter space. The number of parameters in the system here and the relatively long run times for simulations make such a comprehensive sensitivity analysis unfeasible. Instead the approach adopted has been to initially vary parameters on an individual basis over a fairly small range of values and compare the near-field axial pressure response against that of the original model and experimental data. In this way the potential sensitivity of the model to each parameter is assessed. Where the system has been found to be particularly sensitive to certain components a more comprehensive analysis of the multi-dimensional parameter space of that component has been approached. Whilst such methods are by no means ideal they are practical for the number of model parameters to be considered here and associated run times.

Analysis of parameters on an individual basis suggests that although all parameters can have an effect on the behaviour of the modelled system, most components are fairly insensitive to variation. The gross behaviour of the device would appear to be determined by the basic design features – an air-backed disc deforming fundamentally in its thickness dimension and restrained at its edges. It is of particular interest that the vibration of the disc is fairly insensitive to variations in the mounting. The components to which the vibration is highly sensitive are the piezoelectric element and matching layer. An analysis of the five matching layer parameters was made by scanning through the five-parameter space for a few values for each parameter. Model-model and model-experimental axial pressure comparisons were made. This established that the specific features of the vibrational response of the modelled device and subsequent near-field are highly sensitive to variations in all the matching layer parameters. Furthermore it established that variations in these parameters could account for specific model-experimental discrepancies observed close to the source.

For the analysis of disc parameters a modelled disc in vacuuo was used instead of the full transducer-fluid system. Comparisons were then made for the electrical response of the model against experimental results made on a real disc in air. This process significantly reduced model run times enabling the running of several thousand models including searches of multi-dimensional parameter spaces. From this analysis several conclusions were drawn. Firstly, both the electrical and vibrational response of the model is highly sensitive to all piezoelectric parameters. Secondly, good disc model-experimental *electrical* agreement could be achieved for a number of models with varying parameter values and exhibiting different vibrational behaviour. This suggests that any disc analysis/optimisation based solely on electrical results is likely to prove ineffective for considering the effect on the vibrational behaviour of the disc, the disc in a transducer and the subsequent field. Experimental measurements of the disc and transducer face vibrational behaviour would therefore prove very useful for model-experimental comparison. In fact this can now be identified as an essential element of future work. Thirdly, the use of different disc models within the

transducer-fluid model established that variations in piezoelectric parameters are capable of producing significant variations to the specific features of device response and generated near-field. Similarly to the case of the matching layer, results imply that inaccurately specified piezoelectric parameter values could account for observed model-experimental discrepancies.

The issue of the operating frequency for the model when making comparisons with experiment has arisen here. Comparisons have been made for models operating at *their* resonant frequencies against experimental results generally generated at 1.027 MHz – the 'working frequency' of the real device. In practice this has lead to a significant increase in run times as it has been necessary to first consider the electrical response of the system before the generation of field results. This approach was adopted partly because both the model and the real device are fairly sensitive to frequency variations due to their high Q nature. Also the sensitivity of the modelled system to parameter variations has meant that the position of the resonance can shift substantially between models - making model-model and model-experimental comparison at a pre-determined frequency ineffective here. For a comprehensive sensitivity analysis/optimisation of parameters the pre-specification of a frequency at which comparisons would be made could be used as an inherent part of the optimising function. For the limited analysis possible here this is not appropriate.

A final point concerns differences between the model and real device other than those relating to inaccurate dimensions or material properties. Firstly, the real device will not be truly circularly symmetric and therefore cannot be compared exactly to the model used here. Also a number of components in the real device such as wiring and soldering are not accounted for by the model due to the model's symmetry. There is also the fact that the model is a discretised approximation of the real system, and that the finite elements used can only approximate the behaviour of real systems that behave according to the somewhat idealised equations that define those elements. All of these issues make some model-experimental differences inevitable and may play a role in the poor agreement of some model-experimental field and electrical results.

7.2.3 Modelling an unbounded fluid region

During this work the simulation of the surrounding unbounded fluid region has been investigated in some detail and at some stages considered separately to the modelled device. This is primarily because the initial techniques used to model the fluid region did not perform accurately. Furthermore the practical limitations of the use of acoustic elements and WEEs required that some further options be considered if any substantial analysis of the modelling of real fields and devices was to be undertaken. For these reasons three fluid-modelling options, WEE, CHIEF and DAA2c were compared. Comparisons were made for three idealised source profiles with the same dimensions as the physiotherapy transducer – a plane piston source, a ½ cosine source and a Gaussian each operating at 300 kHz, 650 kHz and 1.030 MHz. Also the three options were compared for the realistic source behaviour of the modelled device operating around 1.030 MHz. The near-fields of the idealised sources were compared against analytical results and those for the real source against experimental field results.

The WEE model involves surrounding the structure with standard acoustic elements up to some boundary where WEEs are introduced. These elements are designed to simulate outward-travelling wave-like behaviour, so if they are matched to the acoustic elements correctly the surrounding fluid region effectively becomes infinite. A number of parameters must be defined accurately for this acoustic-WEE matching to be effective:

- the distance from the structure to the acoustic-WEE interface;
- the angular meshing along the interface;
- the meshing in the acoustic region;
- the radial order of the WEEs – this determines the decay term within the elements and therefore effects the compatibility at the acoustic-WEEs interface;
- the positioning of the 'virtual source' about which the WEEs are defined.

The approach adopted here for the use of these elements has been as follows. Initially the acoustic region in front of the radiating structure is made as large as possible so the WEEs are implemented at the furthest boundary possible – allowing for run time and memory requirements. Subsequent re-analysis can be concerned with reducing the size of this region. When all features are accounted for correctly an angular meshing of three elements per wavelength at the interface and three to six throughout the acoustic region has proved effective here. The position of the 'virtual source' about which the WEEs are defined would appear to be very much problem dependent. Here the source has been specified at the centre on the structure on-axis. Further comments on this will be made when considering geometrical issues when using WEEs.

There have been references in the literature to mathematical problems arising from defining a radial order as being too high for specific problems, (Cremers & Fyfe, 1995; Astley et. al, 1998; Morgan et. al. 2000). This is in addition to acoustic-WEE mismatches occurring due to defining the radial order as being too low. No such mathematical problems have arisen here. In fact in contrast to models generated elsewhere (Cremers & Fyfe, 1995; Astley et. al, 1998) where the optimum radial order necessary to generate accurate results has been orders 5 or 6, here the use of radial order 9 has been *essential* for generating accurate results. Reports of mathematical problems have been for systems with (much) smaller *ka* values than those considered here. For a realistic medical ultrasound system the use of high radial orders is likely to be a necessity rather than posing a potential problem.

When all of these features discussed here are accounted for, and parameters specified correctly, the acoustic-WEE option for all three idealised source types operating at all three frequencies was in excellent agreement with analytical predictions.

Unfortunately the practical use of the WEE option has been shown to be fairly restricted for the type of problem considered. Firstly the parameters considered above must be specified accurately for the simulation to work effectively. Also there is an

issue of geometrical differences between the definition of the WEEs and realistic devices leading to some potentially difficult balancing of meshing requirements with element size and angular restrictions. The positioning of the 'virtual source' also effects the geometry of the problem. It would be beneficial to have this source close to the radiating source, however this can lead to significant violations to the geometrical and size restrictions placed on acoustic elements for the structure considered here. It should be pointed out that some attempt to overcome such problems through the use of elliptically shaped WEEs has been approached (Astley & Hamilton, 2000)). Finally there is the issue of excessive run times and memory requirements of WEE models. Here memory requirements have almost been pushed to the limit for the modelling of the system on a 500 MHz PC and simulation run times are around 5 hours for one frequency, emphasising that the use of WEEs is severely restricted. The fact that the effectiveness of the WEE option can be easily established through the analysis of pressure variations across the acoustic-WEE interface, however, means that it can be used for the evaluation of other models. This is exactly how it has been used here.

The alternative to the use of some sort of 'infinite' element such as WEEs is the application of BEM, using an integral relationship at the structural surface relating normal pressure and normal velocity here. This type of approach has been considered many times before (Chen & Schweikert, 1963; Chertock, 1964; Copley, 1967; Schenck, 1968). Once the fluid-structure problem has been solved the generation of exterior field results is relatively trivial using an additional integral relationship. CHIEF and DAA2c considered here use the same exterior integral but different techniques for the fluid-structure relationship. The use of BEM requires that only the surface of the radiating structure is meshed, resulting in significantly reduced run times for larger models.

CHIEF uses the *exact* (Helmholtz) integral relationship for fluid-structure behaviour. There is a problem of non-uniqueness with this integral that CHIEF overcomes by the definition of additional *interior* points and the solution of an interior surface integral.

Non-uniqueness occurs for surface pressures that are a solution to this interior problem. Solving both surface and interior problems allows for the unique solution of the correct surface pressure results. There are two main problems with the use of this method. Firstly, although there are some guidelines with respect to the positioning of the additional interior nodes (Seybert & Rengarajan; 1987), essentially this is a fairly arbitrary procedure. Secondly, the non-uniqueness is related to the interior resonances of the boundary element so that for increasing structural size or frequency the problem becomes more extreme. It has been suggested (Schenck, 1968; Seybert & Rengarajan; 1987) that for increasing *ka* the CHIEF option would not be effective and indeed that is exactly what has been observed here. For smaller *ka* values CHIEF models showed excellent agreement with analytical results but for *ka* values appropriate for the physiotherapy system agreement was very poor. Overall then the conclusion on the use of CHIEF is that it is ineffective for large *ka* devices such as those found in many real medical ultrasound systems.

The DAA2c method uses a Doubly Asymptotic Approximation for the fluid-structure surface relationship, as opposed to the exact Helmholtz integral used in CHIEF. The exact integral takes into account all the interactions between coincident fluid and structural points (on the structural surface) including the effect that each point has on all other points of the surface. The DAA2c on the other hand is an approximation of this and only completely accounts for interaction and the effect of this interaction between points on the surface close to the individual point where the fluid-structure interaction is being solved. Although some reference has been made to the fact that this technique should be effective for systems operating at high frequencies, the author has not come across any specific examples of this in the literature for radiating structures. Indeed it has previously been suggested to the author that such an approximate technique would not be capable of accounting for the rapid and complex near-field pressure variations that are of interest here.

For all three Gaussian source models with different *ka* values the DAA2c model showed excellent agreement with analytical predictions. For the other two source

types the *ka* ~ 15.8 model showed some inconsistencies very close to the source although overall agreement was reasonable. For both the *ka* ~ 34 and ~ 54 models the results for the ½ cosine model were very good but for the plane piston case they were again much less accurate close to the source, although the minima and maxima were accounted for in the correct position on-axis. These results are interesting for a number of reasons. Firstly the accuracy of the DAA2c would appear to be confirmed for increasing *ka* size. Secondly the general inaccuracy of the plane piston models is likely to be a result of the inconsistency at the edge of the source for these models, where the deformation effectively goes from zero to a maximum over a very short distance. It would seem reasonable to conclude that the approximate fluid loading is not accurately accounting for the effect of this discontinuity. In fact the consideration of the ½ cosine and Gaussian models was to some extent considered to investigate this very feature of the DAA2c. It was recognised that although the DAA2c could not handle a plane piston source accurately the discontinuity at the source edge was clearly an unrealistic feature and so other models without this feature, and therefore presumably more consistent with realistic source behaviour, were considered.

The results of these 'idealised' sources were further confirmed when the physiotherapy transducer-fluid model was considered. The WEE and DAA2c models showed excellent agreement whereas the CHIEF model was less consistent. On the basis of all of these results subsequent modelling used the DAA2c option, although regular comparison against WEE models was used to ensure that the DAA2c model was operating consistently. It is the use of the DAA2c that has made the results generated here possible and enabled the analysis of model parameters and their effects on the field. It has also been seen that DAA2c is capable of accurately modelling systems with much larger *ka* values, making the modelling and analysis of other realistic medical ultrasound systems feasible. However it is also interesting to note that the use of WEEs helped to identify a bug in the BE implementation.

7.2.4 Accurate, repeatable experimental results for model evaluation

The generation of accurate, repeatable experimental measurements on a real device is a fundamental requirement if the corresponding model is to be tested and evaluated to a satisfactory level. The experimental measurements made here consist of measurements made on the basis of the IEC standard for the safe and effective use of physiotherapy devices, and additional measurements designed to more comprehensively investigate the variation in the near-field of the device. The IEC measurements showed the device used here to be typical, effective and safe. Model-experimental comparison of several IEC standard parameters – the effective radiating area A_{ER}, the beam cross-sectional area in four different planes A_{BCS}, and the beam type – are in very good agreement. Although all of these results are extremely encouraging the problem with them is that they are inherently designed to be robust with respect to the detailed variation in the near-field. There is one IEC near-field parameter for which model-experimental agreement is very poor, the beam non-uniformity ratio R_{BN}. In contrast the problem with the R_{BN} is that it is not robust at all, being essentially the ratio of the maximum pressure value in the field to an average value. The accurate measurement of this parameter therefore requires the accurate measurement of the maximum value in the near-field. For the model this is easy to establish as it lies on the acoustic axis – the true acoustic axis due to a truly circularly symmetric (modelled) device, however for the real device this is not such an easy measurement to make and accurate model-experimental comparison is therefore very difficult.

The experimental maximum field value was also measured on the axis, although some search close to the axis was undertaken to ensure that the true maximum was found. However there are several problems with this measurement. Firstly the acoustic axis of the device was established using an alignment procedure in the far-field. This is less than ideal and indeed model results have been generated showing that a misalignment of 1 mm at the face of the device, compared to the closest alignment position of 120 mm, would essentially account for the model-experimental

disagreement observed in Chapter 5 for the R_{BN}. Secondly is the fact that the real device will not be truly circularly symmetric. This means that there isn't a definitive acoustic axis, making a measurement of a specific point on it problematic. Furthermore the asymmetry is likely to have some effect on the maximum value in the field, although this is something that cannot be accounted for in the current model. Thirdly there is the difficulty of accurately finding and measuring the maximum value. The measuring hydrophone is of finite dimension and the maximum is likely to be very close to the face of the device - less than 3 wavelengths away from the face of the transducer for the experimental measurement. Also the area covered by the maxima may be very small - the *modelled* peak measured less than a wavelength in dimension in both the axial and radial directions. All of which makes it very difficult to get an accurate, non-averaged maximum value, assuming it can be located in the first place. Fourthly there is the frequency dependence of the real device which has been shown to generate different axial outputs when operating at frequencies only a couple of kHz away from the resonant frequency. The maximum field value has been shown to shift somewhat with frequency in the model, again making model-experimental comparison difficult when experimentally the value has been measured at only one frequency. And finally there is the possibility that inaccuracies in model parameters, specifically piezoelectric and matching layer material properties, could account for axial discrepancies close to the source. This was discussed earlier when it was observed that the analysis of piezoelectric and matching layer parameters suggests that the model is sensitive enough and variable enough to these parameters, that parameter values might be established that would significantly improve model-experimental axial comparisons near to the source.

All of these factors highlight the difficulty in making a specific comparison of a value in the very near-field, between the model and the measured data. The above comments have been made with respect to the measurement of the maximum value in the field. In addition to the IEC measurements a series of additional near-field measurements were made and many of the points raised above can be applied to the model-experimental comparison for these results. Essentially a number of cross-axial

scans were made close to the face of the device (including some at different frequencies), as well as a number of repeat axial scans, axial scans at different frequencies and scans along lines parallel to the axis. All of the measurements were made because it was realised that model-experimental comparison close to the device, where pressure variation is extreme and rapid, would be difficult. For example, consider a model-experimental comparison of a cross-axial measurement at 5 mm from the device. Firstly to make an effective comparison at exactly 5 mm from the source the hydrophone has to be aligned and positioned. In addition the sensitivity of the model to a number of parameters and the fact that the model is an approximation, will all make it difficult to make comparisons at exactly 5 mm.

So a series of additional near-field measurements were made. Cross-axial scans were made at 4 mm, 4.5 mm, 5 mm, 5.5 mm and 6 mm from the source and at 9 mm, 10 mm and 11 mm. At 9 mm, 10 mm and 11 mm the measurements were made at 1.031 MHz in addition to the measurement at 1.027 MHz. These measurements were intended to give a much more detailed picture of the variation in the very near-field, and therefore some insight into how reliable model-experimental comparability in this region could be. Also the axial alignment of the transducer was repeated a number of times and three sets of results generated at 1.027 MHz. This was designed to see how robust the axial alignment process was and how reliable model-experimental axial comparison would be. Also a series of axial scans at frequencies around resonance were taken. As for the previous cross-axial scans at 1.031 MHz these measurements were intended to give some idea of exactly how sensitive the near-field is to small frequency variations. Finally some measurements parallel to the axis were made. These were made with the intention of again establishing how variable the real near-field was close to the axis, as well as how reliable the alignment process was.

The over-riding conclusions of these measurements are two-fold. Firstly, overall model-experimental comparability was shown to be very good where the experimental measurements were repeatable or where a comprehensive picture of the

near-field variation had been established. And secondly, the complexity of the near-field along with the sensitivity of the modelled device to frequency and a number of model parameters makes model-experimental comparisons of specific pressure measurements very difficult. Consider the fact that the last axial maxima was consistently measured over three experimental scans, but consistent axial variation closer to the device could not be achieved. This is very significant in terms of making model-experimental axial comparisons here. Specifically this suggests that for repeatable axial near-field measurements the acoustic axis should be established using an alignment process in the very near-field of the device. This is as opposed to establishing the axis in the region of the last maximum, as for the case of making IEC measurements. The significance of this for the measurement of R_{BN} follows.

The cross-axial measurement close to the device showed the near-field to be highly variable as expected, but by comparing, say, model output at 5 mm with the experimental results between 4 - 6 mm it is clear that the model is accurately predicting the complex behaviour here - both quantitatively and qualitatively. Again this is very encouraging but highlights the need for detailed and comprehensive measurements here. The variation with frequency was obvious from experimental axial scans over a range of frequencies, when again it was established to a certain extent that only the last axial maxima could be classed as consistent. Axial variation with frequency close to the device is highly variable. Furthermore the cross-axial scans made at different frequencies also showed the effect of frequency on the near-field results and only served to highlight the complexity of making model-experimental comparisons in this area. Finally the parallel-axial scans show that the model predicts the variation of the device as you move away from the axis very well, but again highlights the sharp variation in the near-field region over distances comparable to a wavelength.

7.3 Conclusions

To summarise, FEM and BEM have been used to predict the near-field of a physiotherapy transducer operating close to 1 MHz with some accuracy. The field due to such a device has been shown to be highly complex, with extreme variations occurring on scales comparable to a wavelength, and is very different to the field due to an idealised plane piston source. Overall predictions of the near-field are reasonably accurate, both qualitatively and quantitatively. The IEC standard measurement of the effective radiating area A_{ER} has been shown to be robust and effective in accurately determining the nature of the beam due to a therapy device. By contrast the IEC beam non-uniformity ratio R_{BN} parameter has been shown to be sensitive to misalignment, experimental error and variations in a number of device components and parameters. Some further consideration of the definition and importance of R_{BN} is therefore recommended.

The vibrational behaviour of the modelled device has also been seen to be highly irregular. An analysis of device parameters suggests that the gross behaviour of the device and subsequent field are determined by its basic design features – an air-backed piezoelectric disc deforming to some degree in its thickness dimension and supported at its edges. The vibration of the device is fairly insensitive to variations in the mounting but the specific features of the source response are highly sensitive to all piezoelectric and matching layer parameters. Some of the model-experimental discrepancies that have been observed may be accounted for by the inaccurate specification of these parameters in the model. Both the experimental results and response of the modelled system also indicate that the device is sensitive to variation with operating frequency, even within 10 kHz of the established working frequency.

The simulation of an unbounded fluid medium has been considered in some detail for a large *ka* system. The use of acoustic elements and WEEs surrounding a structure has been shown to be a highly effective option and some detailed consideration has been given to using these elements effectively for the type of problem considered

here. It has been found that for large *ka* systems, such as the one considered here, the use of WEEs with radial orders of at least 9 is likely to be a requirement. However the large number of parameters required to define such a system accurately, the excessive number of nodes required and associated run times and memory requirements all make this option impractical for any substantial analysis. The fact that the accuracy of this option can be tested easily makes it an ideal source for model-to-model evaluation. The CHIEF BEM has been shown to be inaccurate for large *ka* systems. The approximate DAA2c BEM has, by contrast, been shown to generally be both accurate and substantially more practical to use than the WEE option. The run times for such a model make the consideration of the response of the device to frequency and the running of a large number of models approachable. The only high frequency source for which this option has been shown to be inaccurate is the plane piston case containing an unrealistic discontinuity at its edge.

Overall, then, this work has established that the simulation of realistic medical ultrasound systems is complicated by large numbers of model parameters, inaccurate material property specifications, the sensitivity of the system to many parameters and operating frequency, long run times, and difficulties in making definitive experimental measurements for model evaluation. Nevertheless it has been shown that FEM and BEM can be used to effectively simulate the realistic behaviour of a medical ultrasound device and its generated near-field, both of which have been shown to be highly irregular here. Furthermore it has been established that the use of the DAA2c option for modelling the surrounding fluid region enables some substantial analysis of the sensitivity of the modelled system to design variations, component parameters including a large number of material properties, and operating frequency.

7.4 Further work

In many respects the work presented has only been a starting point for the analysis and use of FEM and BEM for the modelling of medical ultrasound devices and fields.

The ability of these techniques to simulate the complex behaviour and field variations of a real device offers the potential for modelling transducers and fields for a wide range of devices as well as the opportunity to investigate the effects of design variations without the need for prototyping. On the other hand the work presented here has also sought to highlight the many problems and difficulties involved in such modelling and analysis, and in doing so stress that there is still some considerable way to go with respect to refining and improving the processes and techniques employed here. What will follow is a summary of some of the areas that the author feels are worthy of further investigation.

With respect to the IEC standards on physiotherapy devices considered here it would certainly seem necessary to give some more detailed consideration to the measurement of the R_{BN} and establishing the acoustic axis experimentally. The results of the model calculation of the R_{BN} suggest that the small area of the (modelled) hot spot may make it harmless, nevertheless this requires further investigation. Some consideration of establishing the acoustic axis specifically with the R_{BN} measurement in mind would be a starting point along with a more detailed look at the effect of the finite hydrophone on the measurement of the maximum field value when it is very close to the source.

The results of the analysis of model parameters here, and specifically the sensitivity of the model with respect to piezoelectric and matching layer material properties, would suggest that some further investigation with respect to the sensitivity analysis/ optimisation of the modelled device is necessary. Whilst a comprehensive optimisation towards experimental measurements is probably both unnecessary and unfeasible at this time, certainly a more comprehensive look at the parameters space of properties would be useful. In practical terms this would require looking at the post-processing of PAFEC data in order to extract information to determine the search direction. The very action of establishing an optimal function for model-experimental comparison will in itself offer a considerable insight into the significant features of the field, the behaviour of the device and how these are important.

Consideration would have to be given to which field and electrical measurements should be compared and the effect of frequency. The author would certainly emphasise that disc and transducer *deformation* data would be invaluable for the more accurate modelling of devices and fields.

In addition to the previous points there is undoubtedly a need for the model-experimental comparison of other physiotherapy devices to ensure that the techniques used here and the issues considered are applicable to other physiotherapy devices and fields. Such work would offer considerable insight into the behaviour and near-fields of such devices and their design requirements. Not only could such information be used to pro-actively effect the behaviour of the device and field response, but also this should allow more insight into the general characteristics of the field when it comes to establishing and investigating international standards for physiotherapy devices.

Leading on from all of these points is the consideration and simulation of other types of real medical ultrasound systems - including backed transducers driven in pulse-wave mode. A model of the physiotherapy device used here has already been run with a backing layer. Although such devices will undoubtedly require longer run times due to the additional d.o.f.s, the problem of high sensitivity to frequency variation should not be such an issue. Of course such devices are likely to be pulsed and therefore require analysis over a large range of frequencies - unless a transient response is considered - which will undoubtedly be time consuming. Nevertheless this approach has been adopted elsewhere for models operating at lower frequencies and is certainly something that could be approached. In reality devices are not limited to being circularly symmetric and a whole range of geometries and arrays of active elements are used in many devices. The fully 3-D simulation of such devices would undoubtedly be very time consuming if not unfeasible, however the use of symmetry along with ever improving computing power should make such analysis more approachable in the near future.

One of the most powerful uses of a modelling approach such as that adopted here is in terms of its use for investigating the design of transducers in general and the effect on the field with the intention of design improvement. Consideration here, for example, could be given to an analysis of the true optimal design of a matching or backing layer, as opposed to the 1-D theoretical prediction. Some analysis of how energy is dissipated throughout the device, possibly including the effect of heating on the device, could be approached and the effect of this on the behaviour of the device and its efficiency analysed. Source data from FE models might be used for propagation in non-linear models to consider the effect of realistic vibrational behaviour on finite amplitude propagation. Variations in design could be approached such as holes in the piezoelectric component, the optimal excitation and lay-out of arrays of active elements, multiple matching layers, and angled matching and backing layers. Furthermore novel design features could be considered such as original geometries of components and the use of restraints at the edges of the device to effect the field.

Further to the previous point is the potential for considering the use of ultrasound devices for original medical applications. With an effective model of realistic devices the potential for design variation with the intention of generating specific field characteristics with applications for other types of treatment and/or diagnostic purposes would not appear to be unrealistic.

Overall the potential for the use of FEM and BEM as modelling tools for the simulation of real medical ultrasound devices and fields is wide and varied. Undoubtedly the techniques offer the potential for a considerable amount of additional work on the performance and response of real devices.

References

Allik, H. & Hughes, T.J.R. (1970). Finite element method for piezoelectric vibration. Int. J. Numer. Meth. Engng., **2**, pp. 151-157.

Astley, R.J. & Eversman, W. (1981). A note on the utility of a wave envelope approach in finite element duct transmission studies. J. Sound Vibrat., **76**(4), pp. 595-601.

Astley, R.J. & Eversman, W. (1983). Finite element formulations for acoustical radiation. J. Sound Vibrat., **88**(1), pp. 47-64.

Astley, R.J. (1983) Wave envelope and infinite elements for acoustical radiation. Int. J. Numer. Meth. Fluids, **3**, pp. 507-526.

Astley, R.J., Macaulay, G.J. & Coyette, J.P. (1994). Mapped wave envelope elements for acoustical radiation and scattering. J. Sound Vibrat., **170**(1), pp. 97-118.

Astley, R.J. (1996). Transient wave envelope elements for wave problems. J. Sound Vibrat., **192**(1), pp. 245-261.

Astley, R.J., Macaulay, G.J., Coyette, J.P. & Cremers, L. (1998). Three-dimensional wave envelope elements of variable order for acoustic radiation and scattering. Part I. Formulation in the frequency domain. J. Acoust. Soc. Amer., **103**(1), pp. 49-63.

Astley, R.J. (1998). Mapped spheroidal wave-envelope elements for unbounded wave problems. Int. J. Numer. Meth. Engng., **41**, pp. 1235-15454.

Astley, R.J. & Hamilton, J.A. (2000). Numerical studies of conjugated infinite elements for acoustical radiation. J. Comp. Acoust., **8**(1), pp. 1-24.

Baker. B.B. & Copson, E.T. (1950). The mathematical theory of Huygens principle. 2nd ed. Oxford: Clarendon Press

Bettess, P. (1977). Infinite elements. Int. J. Numer. Meth. Engng., **11**, pp. 53-64.

Bettess, P. & Zienkiewicz, O. (1977). Diffraction and refraction of surface waves using finite and infinite elements. Int. J. Numer. Meth. Engng., **11**, pp. 1271-1290.

Bettess, P. (1980). More on infinite elements. Int. J. Numer. Meth. Engng., **15**, pp. 1613-1626.

Bettess, P. (1987). A simple wave envelope element example. Commun. Appl. Numer. Meth., **3**, pp. 77-80.

Brebbia, C.A. & Dominguez, J. (1989). Boundary elements: An introductory course. Bath, UK: Computational Mechanics Publications, McGraw-Hill Book Co.

Burnett, D.S. (1994). A three-dimensional acoustic infinite element based on a prolate spheroidal multipole expansion. J. Acoust. Soc. Amer., **96**(5), pp. 2798-2815.

Capineri, L., Masotti, L., Rinieri, M. & Rocchi, S. (1993). Ultrasonic transducer as a black box: Equivalent circuit synthesis and matching network design. IEEE Trans. Ultrason., Ferroelect., Freq. Cont., **40**(6), pp.694-702.

Chen, L.H. & Schweikert, D.G. (1963). Sound radiation from an arbitrary body. J. Acoust. Soc. Amer., **35**(10), pp. 1626-1632.

Chertock, G. (1964). Sound radiation from vibrating surfaces. J. Acoust. Soc. Amer., **36**(7), pp. 1305-1313.

CIBA-GEIGY. (1982). Araldite Electronics Resins: Araldite CY 1301 GB/Hardener HY 1300 GB Instruction sheet No. C.110a.

Ciskowski, R.D. & Brebbia, C.A. eds. (1991). Boundary element methods in acoustics. Bath, UK: Elsevier Science Publishers Ltd.

Cook, R.D. (1995). Finite element modelling for stress analysis. New York: John Wiley & Sons, Inc.

Copley, L.G. (1966). Integral equation method for radiation from vibrating bodies. J. Acoust. Soc. Amer., **41**(4), pp. 807-816.

Copley, L.G. (1967). Fundamental results concerning integral representations in acoustic radiation. J. Acoust. Soc. Amer., **44**(1), pp. 28-32.

Cremers, L., Fyfe, K.R. & Coyette, J.P. (1994). A variable order infinite acoustic wave envelope element. J. Sound Vibrat., **171**(4), pp. 483-508.

Cremers, L. & Fyfe, K.R. (1995). On the use of variable order infinite wave envelope elements for acoustic radiation and scattering. J. Acoust. Soc. Amer., **97**(4), pp. 2028-2040.

Desai, C.S. (1979). Elementary finite element method. New Jersey: Prentice-Hall, Inc.

Duck, F.A., Baker, A.C. & Starritt, H.C. eds. (1998). Ultrasound in medicine. Bristol, England: Institute of Physics Publishing.

Eaton, J.A. & Regan, B.A. (1996). Application of the finite element method to acoustic scattering problems. AIAA Journal, **34**(1), pp. 29-34.

Ellis, N.S. (1994). Course notes: Numerical solutions of P.D.E.s – finite element methods. Manchester: The Manchester Metropolitan University.

Emerson & Cuming, (1999). Eccobond 24 A/B technical data sheet. Ref 1755-24/12-99.

Ensminger, D. (1988). Ultrasonics: Fundamentals, technology, applications. New York: Marcel Dekker, Inc.

Ergin, A. (1997). The response behaviour of a submerged cylindrical shell using the doubly asymptotic approximation method (DAA). Computers & Structures, **62**(6), pp.1025-1034.

Everstine, G.C. (1997). Finite element formulations of structural acoustic problems. Computers & Structures, **65**(3), pp.307-321.

Felippa, C.A. (1980). Top-down derivation of doubly asymptotic approximations for structure-fluid interaction analysis. Proc. of 2nd Symp. on Innovative Numerical analysis for engineering sciences, Montreal, pp. 79-88.

Felippa, C.A. (1980). A family of early-time approximations for fluid-structure interaction. J. Appl. Mech., **47**, pp. 703-708.

Ferroperm Piezoceramics. (1995). Piezoelectric ceramic data sheet.

Francis, D.T.I. (1993). A gradient formulation of the Helmholtz integral equation for acoustic radiation and scattering. J. Acoust. Soc. Amer., **93**(4), pp. 1700-1709.

Gallaher, A., Macey, P. & Hardie, D. (1999) Optimising active sonar arrays using finite element and boundary element methods. Proc. of the IOA Sonar Trnasducers '99, pp. 186-193.

Geers, T.L. (1978). Doubly asymptotic approximations for transient motions of submerged structures. J. Acoust. Soc. Amer., **64**(5), pp. 1500-1508.

Geers, T.L. & Felippa, C.A. (1983). Doubly asymptotic approximations for vibration analysis of submerged structures. J. Acoust. Soc. Amer., **73**(4), pp. 1152-1159.

Ginsberg, J.H. (2000). Wave-number-based assessment of the doubly asymptotic approximation. I. Frequency domain wet surface impedance. J. Acoust. Soc. Amer., **107**(4), pp. 1898-1905.

Guo, N., Cawley, P. & Hitchings, D. (1992). The finite element analysis of the vibration characteristics of piezoelectric discs. J. Sound Vibrat., **159**(1), pp. 115-138.

Hamilton, M.F. & Blackstock, D.T. eds. (1998). Nonlinear acoustics. London: Academic Press.

Han, K. & Roh, Y. (1998). A study on the design of a shear wave ultrasonic transducer considering the effect of the side layer. Sensors and Actuators, **A 71**, pp. 127-132.

Hansen, H.H. (1997). Optimal design of an ultrasonic transducer. Structural Optimization, **14**, pp. 150-157.

Hedrick, W.R., Hykes, D.L. & Starchman, D.E. (1995). Ultrasound physics and instrumentation. St. Louis, Missouri: Mosby-Year Book, Inc.

Hekkenberg, R.T., Reibold, R. & Zeqiri, B. (1994). Development of standard measurement methods for essential properties of ultrasound therapy equipment. Ultrasound Med. Biol., **20**(1), pp. 83-98.

Hekkenberg, R.T. (1998). Characterising ultrasonic physiotherapy systems by performance and safety now internationally agreed. Ultrasonics, **36**, pp. 713-720.

Hill, C.R. ed. (1986). Physical principles of medical ultrasonics. Chichester, England: Ellis Horwood Ltd.

Huang, H. & Wang, Y.F. (1985). Asymptotic fluid-structure interaction theories for acoustic radiation prediction. J. Acoust. Soc. Amer., **77**(4), pp.1389-1394.

Hunt, J.T., Knittel, M.R. & Barach, D. (1974). Finite element approach to acoustic radiation from elastic structures. J. Acoust. Soc. Amer., **55**(2), pp.269-280.

Ihlenburg, F. (1998). Finite element analysis of acoustic scattering. New York: Springer-Verlag.

Ikegami, S., Ueda, I. & Kobayashi, S. (1974). Frequency spectra of resonant vibration in disk plates of $PbTiO_3$ piezoelectric ceramics. J. Acoust. Soc. Amer., **55**(2), pp.339-344.

Kagawa, Y. & Yamabuchi, T. (1976). Finite element approach for a piezoelectric circular rod. IEEE Trans. Sonics & Ultrason., **SU-23**(6), pp.379-385.

Kaye, G. W. C. & Laby, T. H. (1992). Tables of physical and chemical constants 15 th ed. New York: Longman Scientific & Technical.

Kinsler, L.E., Frey, A.R., Coppens, A.B., and Sanders, J.V. (1982) Fundamentals of Acoustics 3rd ed. New York: John Wiley & Sons, Inc.

Kochbach, J., Lunde, P. & Vestrheim, M. (1999). FE simulations of piezoelectric disks with a front layer of varying thickness. Proc. of the IEEE Ultrasonics Symposium, pp. 1113-1117.

Kochbach, J., Lunde, P. & Vestrheim, M. (2000). Finite element modeling of piezoceramic disks including radiation into a fluid medium. Presentation held at 23rd Scandinavian Symposium on Physical Acoustics, Ustaoset, 2000.

Lamberti, N., Caliano, G., Iula, A. & Pappalardo, M. (1997). A new approach for the design of ultrasono-therapy transducers. IEEE Trans. Ultrason., Ferroelect., Freq. Cont., **44**(1), pp.77-84.

Lancaster, M.J. (1983). The finite amplitude field of a circular piston. Ph.D thesis, The University of Bath.

Locke, S., Kunkel, H.A. & Pikeroen, B. (1987). Finite element modelling of piezoelectric ceramic disks. Proc. of the IEEE Ultrasonics Symposium, pp. 701-706.

Macey, P.C. (1987). Acoustic and structure interaction problems using finite and boundary elements. Ph.D Thesis, The University of Nottingham.

Macey, P.C. (1996). Analysis of linear arrays of ring transducers using wave envelope elements. Proc. of the Institute of Acoustics, **18**(5), pp. 169-175.

Macey, P.C. (1996). Finite element/boundary element modelling techniques applied to ring transducers with viscoelastic coating. Ferroelectrics, **187**, pp. 201-211.

Madrid*. (1999). Piezoelectric characterization sheet. REF:TX/RX No. 4978.

Matthews, I.C. (1986). Numerical techniques for three-dimensional steady-state fluid-structure interaction. J. Acoust. Soc. Amer., 79(5), pp.1317-1325.

Meire, H.B. & Farrant, P. (1995). Basic ultrasound. Chichester, England: John Wiley & Sons, Ltd.

Morand, H. J.-P. & Ohayon, R. (1995). Fluid structure interaction: Applied numerical methods. Paris, France: John Wiley & Sons, Ltd.

Morgan, S., Oswin, J., Hardie, D.J.W. & Macey, P.C. (1999) FE/BE modelling of transducer interaction. Proc. of the IOA Sonar Trnasducers '99, pp. 194-201.

Morgan, S., Hardie, D.J.W & Macey, P.C. (2000). Robustness of boundary element and wave emvelope element formulations applied to exterior coupled acoustic problems. Proc. of the 7th International Congress on Sound and Vibration, pp. 1967-1974.

Nicolas-Vullierme, B. (1991). A contribution to doubly asymptotic approximations: An operator top-down derivation. J. Vib. And Acoust., **113**, pp. 409-415.

Ostergaard, D.F. & Pawlak, T.P. (1986). Three-dimensional finite elements for analyzing piezoelectric structures. Proc. of the IEEE Ultrasonics Symposium, pp. 639-644.

PAFEC Ltd. (1984). PAFEC Theory.

PAFEC. (1995). PAFEC-FE Level 8 Data preparation manual part 3. PAFEC Ltd: Nottingham, UK.

Piranda, B., Steichen, W. & Ballandras, S. (1998). Comparison between different finite element/boundary formulations for modeling acoustic radiation in fluids. Proc. of the IEEE Ultrasonics Symposium, pp. 1073-1076.

Preston, R.C. ed. (1991). Output measurements for medical ultrasound. Berlin, Germany: Ellis Springer-Verlag.

RS Components, (1999). Acrylonitrile Butadiene Styrene (ABS) data sheet. Ref. TX/RX No. 4961, p.2.

Schenck, H.A. (1968). Improved integral formulation for acoustic radiation problems. J. Acoust. Soc. Amer., **44**(1), pp.41-58.

Seybert, A.F. & Rengarajan, T.K. (1987). The use of CHIEF to obtain unique solutions for acoustic radiation using boundary integral equations. J. Acoust. Soc. Amer., **81**(5), pp.1299-1306.

Seybert, A.F., Charan, A. & Herrin, D.W. (2000). Survey of numerical methods for sound radiation. Proc. of the 7th International Congress on Sound and Vibration, pp. 1887-1894.

Smith, R.R., Hunt, J.T. & Barach, D. (1973). Finite element analysis of acoustically radiating structures with applications to sonar transducers. J. Acoust. Soc. Amer., **54**(5), pp.1277-1288.

Turo, A., Salazar, J., Chavez, J.A., Ortega, J.A. & Garcia, M.J. (1999). Performance improvement of ultrasonic therapy equipment by modifying the classical transducer design. IEEE Proc. Sci., Meas., Technol., **146**(2), pp.107-112.

Van Randeraat, J. & Setterington, R.E. eds. (1974). Piezoelectric ceramics. London: Mullard Limited.

Verma, P.K. (1995). Experimental and theoretical determination of non-linear pressure fields in biological fluids. Ph.D thesis, The University of Bath.

Vernitron Ltd. (1976). Piezoelectric ceramic data Bulletin 66011/F.

Wood, W.L. (1976). On the finite element solution of an exterior boundary value problem. Int. J. Numer. Meth. Engng., **10**, pp. 885-891.

Wu, L. & Chen, Y-C. (1999). PSPICE approach for designing the ultrasonic piezoelectric transducer for medical diagnostic applications. Sensors and Actuators, **75**, pp. 186-198.

Zagzebski, J.A. (1996). Essentials of ultrasound physics. St.Louis; London: Mosby.

Zemanek, J. (1970). Beam behaviour within the nearfield of a vibrating piston. J. Acoust. Soc. Amer., **49**(1) part 2, pp.181-191.

Zienkiewicz, O.C., Emson, C. & Bettess, P. (1983). A novel boundary infinite element. Int. J. Numer. Meth. Engng., **19**, pp. 393-404.

Zienkiewicz, O.C. & Taylor, R.L. (1989). The finite element method 4th ed. Vol 1:Basic formulation and linear problems. Maidenhead, England: McGraw-Hill.

Appendix 1

This appendix presents a more detailed account of the examples used in Chapter 2 to demonstrate how an FE problem is approached and tackled. The examples begin in Chapter 2, page 23, section 2.2.2 "Interpolating Polynomial":

A1.2.2 Interpolating polynomial

Having made an initial discretisation of the system to be modelled, consideration is given to how the *system* is expected to respond to applied conditions. The response of the system can be considered in terms of how a particular sub-domain of the system, or element, is likely to respond. A feature of FEM is that the solution is generated initially only at nodal points – although subsequently interpolation may be used to generate values elsewhere within an element. In accordance with this, the analyst seeks to express the variation of the unknown, $h(Q)$, at a point Q in the solution domain of the element, *in terms of the unknown only at nodal points*. For the 2-D element shown in Figure A1.1a where the length of the element in the x direction is α and in the y direction is β, and the mid point is (x_{mid}, y_{mid}), this can be expressed as (Ellis, 1994)

$$h(x,y) = \underline{N}(x,y)\underline{h}. \qquad \text{(A1.1)}$$

Here $\underline{h}$ is a 4-term column vector containing the values of the unknown h at the 4 nodes. $\underline{N}$ is a 4-term row vector termed the vector of shapes functions or *basis* vector which relates the values of the unknown anywhere in the solution domain of the element, $h(x,y)$ to the value of the nodal unknowns. $\underline{N}$ can be expressed as $\underline{N}(x,y) = [N_1, N_2, N_3, N_4]$.

A common approach to establishing such a relationship is to seek the unique polynomial that fits the nodes of an individual element. Lagrange interpolation

techniques are frequently used to find a unique n^{th} order polynomial that passes through a set of data points (x_i, h_i), i=0, 1, 2, …, n. In 1-D this can take the form

$$h = \sum_{i=0}^{n} L_i(x) h_i, \qquad \text{(A1.2)}$$

where

$$L_i(x) = \frac{(x-x_0)(x-x_1).....(x-x_n)}{(x_i-x_0)(x_i-x_1).....(x_i-x_n)}. \qquad \text{(A1.3)}$$

Here the $(x-x_i)$ term is omitted from the numerator and (x_i-x_i) from the denominator. In 2-D this polynomial takes the form

$$h = \sum_{i=0}^{n} L_j(x).L_k(y) h_i. \qquad \text{(A1.4)}$$

Here j=0, 1, 2, …, n and k=0, 1, 2, …, m. Also n is the number of points in the x direction and m the number of points in the y direction. Comparing Equations A1.1 and A1.4 it can be seen that $N_i(x,y) = L_j(x).L_k(y)$. Considering node 2 in Figure A1.1a, where n=m=2, and j=2, k=1:

$$L_2(x) = \frac{(x-(x_{mid}-\alpha/2))}{((x_{mid}+\alpha/2)-(x_{mid}-\alpha/2))} \quad \text{and} \quad L_1(y) = \frac{(y-(y_{mid}+\beta/2))}{((y_{mid}-\beta/2)-(y_{mid}+\beta/2))}.$$

Substituting into Equation A1.4 this gives

$$N_2(x,y) = -\frac{(x-(x_{mid}-\alpha/2))(y-(y_{mid}+\beta/2))}{\alpha\beta}. \qquad \text{(A1.5b)}$$

Similar calculations lead to:

$$N_1(x,y) = \frac{(x-(x_{mid}+\alpha/2))(y-(y_{mid}+\beta/2))}{\alpha\beta}, \qquad \text{(A1.5a)}$$

$$N_3(x,y) = -\frac{(x-(x_{mid}+\alpha/2))(y-(y_{mid}-\beta/2))}{\alpha\beta} \qquad \text{(A1.5c)}$$

$$\text{and } N_4(x,y) = \frac{(x-(x_{mid}-\alpha/2))(y-(y_{mid}-\beta/2))}{\alpha\beta}. \qquad \text{(A1.5d)}$$

So the unknown at any point (x,y) in the element, (Figure A1.1a), can now be expressed in terms of the unknowns at the element nodal points

$$h(x,y) = \begin{pmatrix} N_1 & N_2 & N_3 & N_4 \end{pmatrix} \begin{pmatrix} h_1 \\ h_2 \\ h_3 \\ h_4 \end{pmatrix}. \qquad \text{(A1.6)}$$

The vector of shape functions, $\underline{N}$, is clearly dependent on both the geometry of the element under consideration and the number of nodes defining that element. The same principles applied here can be used to generate the shape functions for any FE.

A1.2.3 Local co-ordinates

A relationship between the unknowns at any position within the element and the unknowns at the nodal points has now been established, however this particular formulation for $\underline{N}$ is dependent on the position of the element. It is desirable to have a formulation for $\underline{N}$ that is not position dependent, in this example one that is appropriate for a generic linear 4-node quadrilateral element. Such a basis vector can be generated through the use of a local co-ordinate system. One such co-ordinate system uses a parent element defined in local co-ordinates ζ and ξ

over the domains [-1,1] and [-1,1], as shown in Figure A1.1b. It will be seen that the integration of functions of the basis vector is a common part of a finite element analysis. Not only does the local co-ordinate system allow for the determination of a generic element basis vector, but the numerical integration of such functions is also made simpler by the definition of an element over the domain shown in Figure A1.1b.

A *linear* transformation in both co-ordinate directions for Figure A1.1 can be given as

$$\zeta = \frac{2}{\alpha}(x - x_{mid}) \qquad \text{(A1.7a)}$$

$$\text{and } \xi = \frac{2}{\beta}(y - y_{mid}). \qquad \text{(A1.7b)}$$

Using the same Lagrange interpolation technique, as outlined in section A1.2.2, this leads to the following terms in the basis vector expressed in local co-ordinates

$$N^L{}_1 = \tfrac{1}{4}(1-\zeta)(1-\xi), \qquad \text{(A1.8a)}$$

$$N^L{}_2 = \tfrac{1}{4}(1+\zeta)(1-\xi), \qquad \text{(A1.8b)}$$

$$N^L{}_3 = \tfrac{1}{4}(1-\zeta)(1+\xi) \qquad \text{(A1.8c)}$$

$$\text{and } N^L{}_4 = \tfrac{1}{4}(1+\zeta)(1+\xi). \qquad \text{(A1.8d)}$$

So there is a new relationship in terms of local co-ordinate basis functions

$$h(\zeta,\xi) = \begin{pmatrix} N^L{}_1 & N^L{}_2 & N^L{}_3 & N^L{}_4 \end{pmatrix} \begin{pmatrix} h_1 \\ h_2 \\ h_3 \\ h_4 \end{pmatrix}. \qquad \text{(A1.9)}$$

Any integration over the domain of the element can therefore be performed in local co-ordinates. It will be seen in section A1.2.5 how the transformation from global to local co-ordinates is applied in practice

A1.2.4 Governing equations

The response of the unknown within an element with respect to the unknown nodal values has been considered. Now the fundamental equations that actually govern the behaviour of the element must be determined. Clearly the types of element that are used is problem dependent and numerous types of element have been developed to simulate the behaviour of various systems. For example 2D 'plate' elements allowing in-plane x and y direction displacement as well as xy shear displacement, and acoustic elements with a single pressure d.o.f. per node.

Fundamental relationships defining the behaviour of the system over a given domain are employed to generate the equations governing the behaviour of an element. Consider the problem of generating an acoustic element. The Helmholtz wave equation governing acoustic propagation in 3-D space for the steady-state case where the system responds harmonically, was introduced in Chapter 1, Equation 1.3:

$$\nabla^2 p + k^2 p = 0 . \qquad \text{(A1.10)}$$

Generally the 'fundamental' equations are arranged in such a way as to be expressed in terms of the primary unknown in the analysis. Here this is already the case as the primary unknown is pressure.

A1.2.5 Element equations

Having established the equation(s) that define the behaviour of a specific part of the system under analysis, there are primarily two techniques that are used to

generate the equations that govern the response of an element. These are variational methods and residual methods. As previously mentioned the detailed consideration of such techniques is beyond the scope of this work. However, continuing with the example of the generation of an acoustic element, the Galerkin weighted residual method will be included here to indicate how element equations can be formulated.

Equation A1.10 defines the response of the primary unknown, pressure, within an acoustic element, for which an approximate solution is required. The residual technique now proceeds as follows:

- A trial function, p', is proposed as an approximation to the exact solution p.
- Expressions for the differences between the equations defining the behaviour of the pressure in the exact and trial cases are generated. This difference is the residual. Here this is simply the difference between p and p' for the single Equation A1.10.
- Residuals are now minimised. This minimisation process "forces" the residual to be zero thus making the trial solution p' equal to the exact solution p. It is this minimisation process that generates the equations defining the behaviour of an element which are subsequently solved for the primary unknown(s).

It will now be reiterated that when solving a problem by the FEM the whole system is solved simultaneously. The response of the single acoustic element considered here is governed only by the Helmholtz wave equation. When this element is part of a system there will be other equations governing the behaviour of other elements, as well as a number of boundary conditions. The boundary conditions both restrict the response of the system to specific conditions and also express 'natural' conditions across elements. All of these features combined govern the response of the system leading to a number of equations for which the residual method would be applied. The minimisation of all of these equations

simultaneously generates a system of equations that can be solved to approximate the response of the entire system. Here, however the residual technique will be applied only to a single element, governed by Equation A1.10.

Of primary importance for the residual technique is the choice of trial function p'. In the Galerkin method it is proposed to be of the form

$$p' = \sum_{i=1}^{n} q_i N_i . \qquad \text{(A1.11)}$$

Here N_i are the *known* functions, q_i are *unknown* coefficients and i=0, 1, 2, ..., n. Comparing Equations A1.11 with A1.1 it can be seen that taking the N_i as elements of the known basis vector $\underline{N}$, the values of the n nodal unknowns are given by q_i.

An expression for the residual R for Equation A1.10 is

$$R = \nabla^2 p' + k^2 p' = 0 . \qquad \text{(A1.12)}$$

Minimisation can be expressed as (Desai, 1979)

$$\int_D R(\psi).W_i(\psi) dD = 0 ,$$

where D is the domain of the system under consideration and the W_i are weighting functions, i=0, 1, 2, ..., n. For a 3-D problem this gives a system of n equations defined over the domain of the element, V:

$$\left(\nabla^2 p' + k^2 p'\right) W_i dV = 0 \qquad , \qquad i=0, 1, 2, \ldots, n . \qquad \text{(A1.13)}$$

Applying the divergence theorem to the first term in the integral to reduce the system to first order (Eaton & Regan, 1996; Astley et. al., 1998):

$$k^2 \iiint_V p' W_i dV - \iiint_V (\nabla p' \cdot \nabla W_i) dV + \iint_S W_i \left(\frac{\partial p'}{\partial n} \right) dS = 0. \quad \text{(A1.14)}$$

The third term in this equation is a surface integral representing the boundary conditions over the surface of the system under consideration, in this case the surface of the element with domain V. Here n is a normal co-ordinate. Re-writing Equation A1.14

$$\iiint_V (\nabla p' \cdot \nabla W_i) dV - k^2 \iiint_V p' W_i dV = \iint_S W_i \left(\frac{\partial p'}{\partial n} \right) dS .$$

The element equations can be written as

$$[\Delta \mathbf{K} - \omega^2 \Delta \mathbf{M}] q = \Delta f(\omega). \qquad \text{(A1.15a)}$$

Here $\Delta \mathbf{K}$ and $\Delta \mathbf{M}$ can be described as (frequency independent) *element* matrices, q is a vector of the primary unknowns at the elemental nodal points – in this case pressure, and $\Delta f(\omega)$ is the (frequency dependent) element load vector. It is standard practice with the Galerkin technique to make the weighting functions, W_i, equal to the basis functions N_i. The elements of the matrices are then given by

$$\Delta \mathbf{K}_{ij} = \iiint_V (\nabla N_i \cdot \nabla N_j) dV \qquad \text{(A1.15b)}$$

$$\text{and } \Delta \mathbf{M}_{ij} = (1/c^2) \iiint_V N_i N_j dV . \qquad \text{(A1.15c)}$$

The element load vector, $\Delta f(\omega)$, is used to apply a forcing function (boundary condition) to the element. Typically this might involve the stipulation of the outward normal velocity, v_n, or acceleration, a_n at specific nodes. The relationships relating normal pressure to normal velocity and amplitude can be described as (Cremers et. al., 1994; Astley et. al., 1998),

$$\frac{\partial p}{\partial n} = -i\omega\rho v_n \qquad \text{(A1.16a)}$$

$$\text{and } \frac{\partial p}{\partial n} = \rho a_n . \qquad \text{(A1.16b)}$$

The terms in $\Delta f(\omega)$ are then given by

$$\Delta f_i = -i\omega \iint_S \rho N_i v_n dS \qquad \text{(A1.16c)}$$

$$\text{and } \Delta f_i = \iint_S \rho N_i a_n dS . \qquad \text{(A1.16d)}$$

A1.2.6 Formulation of element matrices

To outline how such a system of equations would be formulated and solved in practice, consider now a simple example based on the use of 2-D 4-noded quadrilateral elements as shown in Figure A1.1. The element matrices $\Delta\mathbf{K}$ and $\Delta\mathbf{M}$ are of the form

$$\Delta\,\mathbf{K}_{ij} = \iint_{yx} (\nabla N_i \cdot \nabla N_j) dxdy$$

$$\text{and } \Delta\mathbf{M}_{ij} = (1/c^2) \iint_{yx} N_i N_j dxdy .$$

It is generally required that the system be expressed in a local co-ordinate system, such as in Figure A1.1b. Here the terms in the local vector of shape functions, $\underline{N}^L$, are given by Equations A1.8. The derivatives of these shape functions with respect to ζ and ξ can easily be calculated:

$$\frac{\partial N^L{}_1}{\partial \zeta} = -\frac{1}{4}(1-\xi) \quad \text{and} \quad \frac{\partial N^L{}_1}{\partial \xi} = -\frac{1}{4}(1-\zeta), \tag{A1.17a}$$

$$\frac{\partial N^L{}_2}{\partial \zeta} = \frac{1}{4}(1-\xi) \quad \text{and} \quad \frac{\partial N^L{}_2}{\partial \xi} = -\frac{1}{4}(1+\zeta), \tag{A1.17b}$$

$$\frac{\partial N^L{}_3}{\partial \zeta} = -\frac{1}{4}(1+\xi) \quad \text{and} \quad \frac{\partial N^L{}_3}{\partial \xi} = \frac{1}{4}(1-\zeta), \tag{A1.17c}$$

$$\text{and} \quad \frac{\partial N^L{}_4}{\partial \zeta} = \frac{1}{4}(1+\xi) \quad \text{and} \quad \frac{\partial N^L{}_4}{\partial \xi} = \frac{1}{4}(1+\zeta). \tag{A1.17d}$$

Derivatives of Equations A1.7 with respect to x and y are given by

$$\frac{\partial \zeta}{\partial x} = \frac{2}{\alpha}, \qquad \frac{\partial \xi}{\partial y} = \frac{2}{\beta} \qquad \text{and} \qquad \frac{\partial \zeta}{\partial y} = \frac{\partial \xi}{\partial x} = 0.$$

Applying the chain rule, the $\nabla N_i(x,y)$ terms in the matrices can then be expressed in terms of local co-ordinates ζ and ξ:

$$\Delta \mathbf{K}_{ij} = \int_{-1}^{1}\int_{-1}^{1} \left[\left(\frac{4}{\alpha^2}\right) \frac{\partial N^L{}_i}{\partial \zeta} \frac{\partial N^L{}_j}{\partial \zeta} + \left(\frac{4}{\beta^2}\right) \frac{\partial N^L{}_i}{\partial \xi} \frac{\partial N^L{}_j}{\partial \xi} \right] \left(\frac{\partial(x,y)}{\partial(\zeta,\xi)} \right) d\zeta d\xi . \tag{A1.18a}$$

$$\text{and} \quad \Delta \mathbf{M}_{ij} = \left(\frac{1}{c^2}\right) \int_{-1}^{1}\int_{-1}^{1} N^L{}_i N^L{}_j \left(\frac{\partial(x,y)}{\partial(\zeta,\xi)} \right) d\zeta d\xi . \tag{A1.18b}$$

Here $\left(\frac{\partial(x,y)}{\partial(\zeta,\xi)}\right)$ is the Jacobian of the transformation from global to local co-ordinates. This enables the integrals to be calculated over the domain of the local co-ordinates. Here $\left(\frac{\partial(x,y)}{\partial(\zeta,\xi)}\right)=\frac{\alpha\beta}{4}$. These terms are expressed in a manner ideal for numerical integration by a technique such as Gaussian Quadrature. In 2-D this takes the form (Ellis, 1994):

$$\int_{-1}^{1}\int_{-1}^{1} f(\zeta,\xi)d\zeta d\xi = \sum_{i=1}^{n}\sum_{j=1}^{n} w_k w_l f(t_k,t_l)\,. \qquad \text{(A1.19)}$$

Here w_k are weighting factors in the range 0 to 1, and t_k are quadrature points in the range –1 to 1. For four point quadrature, as here, n=2 and these values are given as

$$t_k=\pm 1/\sqrt{3}$$

and $w_k=1$.

So for example, the term i=1, j=2 in the element stiffness matrix $\Delta\mathbf{K}$ would be evaluated as follows

$$\Delta\mathbf{K}_{12}=\int_{-1}^{1}\int_{-1}^{1}\left[\left(\frac{4}{\alpha^2}\right)\left(-\frac{1}{4}(1-\xi)\right)\left(\frac{1}{4}(1-\xi)\right)+\left(\frac{4}{\beta^2}\right)\left(-\frac{1}{4}(1-\zeta)\right)\left(-\frac{1}{4}(1+\zeta)\right)\right]\frac{\alpha\beta}{4}d\zeta d\xi\,. \qquad \text{(A1.20)}$$

For the very simple case where the element is a square of side unity, i.e. $\alpha=\beta=1$, Equation A1.20 becomes

$$\Delta \mathbf{K}_{12} = \frac{1}{16} \int_{-1}^{1}\int_{-1}^{1} \left(\left(1-\zeta^2\right) - \left(1-\xi\right)^2 \right) d\zeta d\xi \,.$$

Applying four-point quadrature:

$$\Delta \mathbf{K}_{12} = \frac{1}{16}\left(\left(1-\left(\frac{1}{\sqrt{3}}\right)^2 \right) - \left(1-\frac{1}{\sqrt{3}} \right)^2 + \left(1-\left(\frac{1}{\sqrt{3}}\right)^2 \right) - \left(1+\frac{1}{\sqrt{3}} \right)^2 \right) +$$

$$\frac{1}{16}\left(\left(1-\left(-\frac{1}{\sqrt{3}}\right)^2 \right) - \left(1-\frac{1}{\sqrt{3}} \right)^2 + \left(1-\left(-\frac{1}{\sqrt{3}}\right)^2 \right) - \left(1+\frac{1}{\sqrt{3}} \right)^2 \right) = -\frac{1}{6}\,.$$

This agrees with the *exact* integral value, as the four-point scheme in 2-D integrates up to the third power of the independent variable in each co-ordinate direction (Ellis, 1994). The element stiffness and mass matrices are calculated either directly or by quadrature, giving

$$\Delta \mathbf{K} = \begin{bmatrix} \frac{4}{6} & -\frac{1}{6} & -\frac{1}{6} & -\frac{2}{6} \\ -\frac{1}{6} & \frac{4}{6} & -\frac{2}{6} & -\frac{1}{6} \\ -\frac{1}{6} & -\frac{2}{6} & \frac{4}{6} & -\frac{1}{6} \\ -\frac{2}{6} & -\frac{1}{6} & -\frac{1}{6} & \frac{4}{6} \end{bmatrix} \text{ and } \Delta \mathbf{M} = \left(\frac{1}{c^2}\right) \begin{bmatrix} \frac{4}{36} & \frac{2}{36} & \frac{2}{36} & \frac{1}{36} \\ \frac{2}{36} & \frac{4}{36} & \frac{1}{36} & \frac{2}{36} \\ \frac{2}{36} & \frac{1}{36} & \frac{4}{36} & \frac{2}{36} \\ \frac{1}{36} & \frac{2}{36} & \frac{2}{36} & \frac{4}{36} \end{bmatrix}. \qquad \text{(A1.21)}$$

As expected, both matrices are symmetric, as:

$$\frac{\partial N^L{}_1}{\partial \zeta} \cdot \frac{\partial N^L{}_2}{\partial \zeta} = \frac{\partial N^L{}_2}{\partial \zeta} \cdot \frac{\partial N^L{}_1}{\partial \zeta}, \; N^L{}_1 . N^L{}_2 = N^L{}_2 . N^L{}_1, \text{ etc..}$$

A1.2.7 Formulation and solution of system matrices

Consider now Figure A1.2 showing a 2-D system of four such linear quadrilateral elements joined together. For the simple case of $\alpha = \beta = 1$, the *element* stiffness and mass matrices are as in Equation A1.21 above. Equations A1.14 and A1.15a, defining the nature of the element equation, can be assembled element by element to generate an equivalent *system* equation, with corresponding *system* stiffness and mass matrices, and forcing function vector:

$$[\mathbf{K} - \omega^2 \mathbf{M}]\, q = f(\omega). \qquad \text{(A1.22)}$$

The individual *element stiffness* matrices for the four elements, I, II, III, and IV are then:

$$\Delta \mathbf{K}^I = \begin{bmatrix} \frac{2}{3} & -\frac{1}{6} & 0 & -\frac{1}{6} & -\frac{1}{3} & 0 & 0 & 0 & 0 \\ -\frac{1}{6} & \frac{2}{3} & 0 & -\frac{1}{3} & -\frac{1}{6} & 0 & 0 & 0 & 0 \\ 0 & 0 & 0 & 0 & 0 & 0 & 0 & 0 & 0 \\ -\frac{1}{6} & -\frac{1}{3} & 0 & \frac{2}{3} & -\frac{1}{6} & 0 & 0 & 0 & 0 \\ -\frac{1}{3} & -\frac{1}{6} & 0 & -\frac{1}{6} & \frac{2}{3} & 0 & 0 & 0 & 0 \\ 0 & 0 & 0 & 0 & 0 & 0 & 0 & 0 & 0 \\ 0 & 0 & 0 & 0 & 0 & 0 & 0 & 0 & 0 \\ 0 & 0 & 0 & 0 & 0 & 0 & 0 & 0 & 0 \\ 0 & 0 & 0 & 0 & 0 & 0 & 0 & 0 & 0 \end{bmatrix},$$

$$\Delta \mathbf{K}^{II} = \begin{bmatrix} 0 & 0 & 0 & 0 & 0 & 0 & 0 & 0 & 0 \\ 0 & \frac{2}{3} & -\frac{1}{6} & 0 & -\frac{1}{6} & -\frac{1}{3} & 0 & 0 & 0 \\ 0 & -\frac{1}{6} & \frac{2}{3} & 0 & -\frac{1}{3} & -\frac{1}{6} & 0 & 0 & 0 \\ 0 & 0 & 0 & 0 & 0 & 0 & 0 & 0 & 0 \\ 0 & -\frac{1}{6} & -\frac{1}{3} & 0 & \frac{2}{3} & -\frac{1}{6} & 0 & 0 & 0 \\ 0 & -\frac{1}{3} & -\frac{1}{6} & 0 & -\frac{1}{6} & \frac{2}{3} & 0 & 0 & 0 \\ 0 & 0 & 0 & 0 & 0 & 0 & 0 & 0 & 0 \\ 0 & 0 & 0 & 0 & 0 & 0 & 0 & 0 & 0 \\ 0 & 0 & 0 & 0 & 0 & 0 & 0 & 0 & 0 \end{bmatrix},$$

$$\Delta \mathbf{K}^{III} = \begin{bmatrix} 0 & 0 & 0 & 0 & 0 & 0 & 0 & 0 & 0 \\ 0 & 0 & 0 & 0 & 0 & 0 & 0 & 0 & 0 \\ 0 & 0 & 0 & 0 & 0 & 0 & 0 & 0 & 0 \\ 0 & 0 & 0 & \frac{2}{3} & -\frac{1}{6} & 0 & -\frac{1}{6} & -\frac{1}{3} & 0 \\ 0 & 0 & 0 & -\frac{1}{6} & \frac{2}{3} & 0 & -\frac{1}{3} & -\frac{1}{6} & 0 \\ 0 & 0 & 0 & 0 & 0 & 0 & 0 & 0 & 0 \\ 0 & 0 & 0 & -\frac{1}{6} & -\frac{1}{3} & 0 & \frac{2}{3} & -\frac{1}{6} & 0 \\ 0 & 0 & 0 & -\frac{1}{3} & -\frac{1}{6} & 0 & -\frac{1}{6} & \frac{2}{3} & 0 \\ 0 & 0 & 0 & 0 & 0 & 0 & 0 & 0 & 0 \end{bmatrix}$$

and $$\Delta \mathbf{K}^{IV} = \begin{bmatrix} 0 & 0 & 0 & 0 & 0 & 0 & 0 & 0 & 0 \\ 0 & 0 & 0 & 0 & 0 & 0 & 0 & 0 & 0 \\ 0 & 0 & 0 & 0 & 0 & 0 & 0 & 0 & 0 \\ 0 & 0 & 0 & 0 & 0 & 0 & 0 & 0 & 0 \\ 0 & 0 & 0 & 0 & \frac{2}{3} & -\frac{1}{6} & 0 & -\frac{1}{6} & -\frac{1}{3} \\ 0 & 0 & 0 & 0 & -\frac{1}{6} & \frac{2}{3} & 0 & -\frac{1}{3} & -\frac{1}{6} \\ 0 & 0 & 0 & 0 & 0 & 0 & 0 & 0 & 0 \\ 0 & 0 & 0 & 0 & -\frac{1}{6} & -\frac{1}{3} & 0 & \frac{2}{3} & -\frac{1}{6} \\ 0 & 0 & 0 & 0 & -\frac{1}{3} & -\frac{1}{6} & 0 & -\frac{1}{6} & \frac{2}{3} \end{bmatrix}.$$

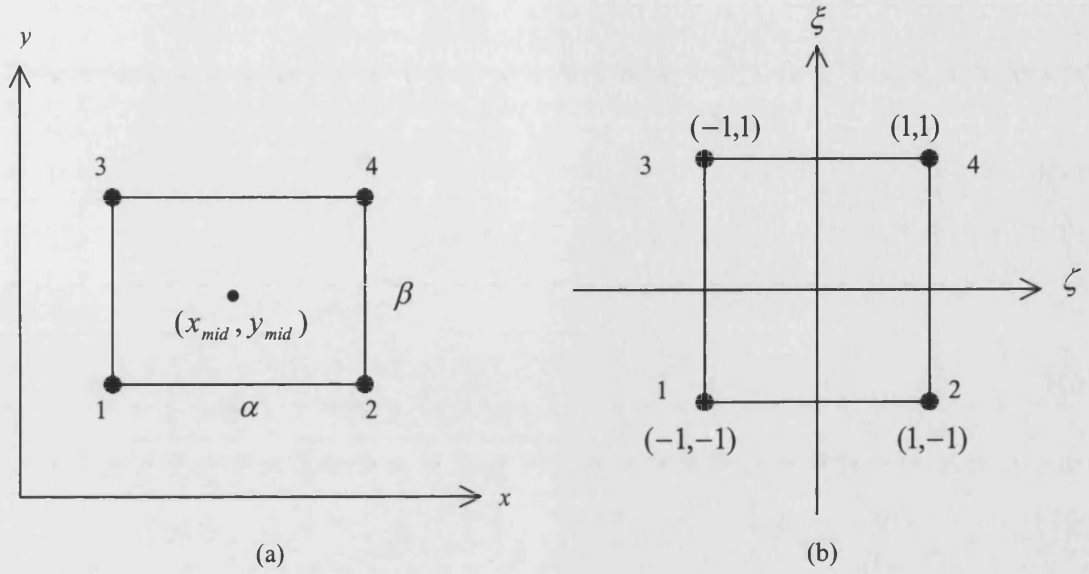

Figure A1.1 Geometry of (a) a 2-D quadrilateral element, and (b) the mapping of this 2-D quadrilateral element from global to local co-ordinates.

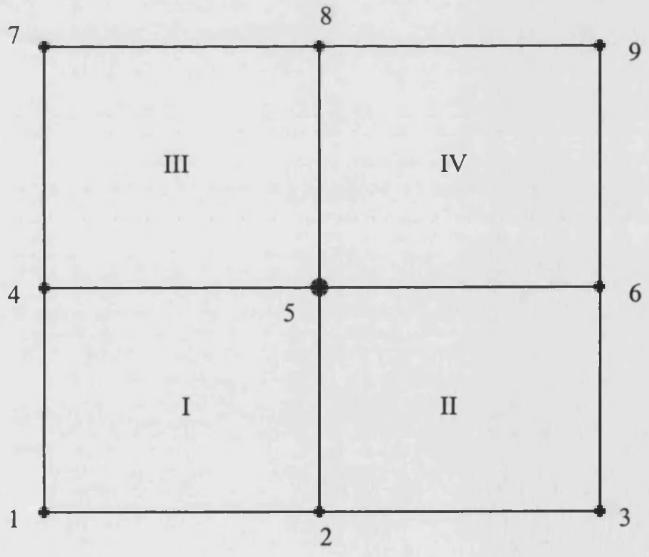

Figure A1.2 Four 2-D linear quadrilateral elements with a unit force applied at the central node, 5. Equivalent to an infinitesimally small, infinitely long cylinder.

The corresponding element mass matrices and forcing function vectors are defined in a similar manner. Adding the element matrices together at coincident nodes generates system matrices. This gives the full system matrices:

$$\left(\frac{1}{6}\right)\begin{bmatrix} 4 & -1 & 0 & -1 & -2 & 0 & 0 & 0 & 0 \\ -1 & 8 & -1 & -2 & -2 & -2 & 0 & 0 & 0 \\ 0 & -1 & 4 & 0 & -2 & -1 & 0 & 0 & 0 \\ -1 & -2 & 0 & 8 & -2 & 0 & -1 & -2 & 0 \\ -2 & -2 & -2 & -2 & 16 & -2 & -2 & -2 & -2 \\ 0 & -2 & -1 & 0 & -2 & 8 & 0 & -2 & -1 \\ 0 & 0 & 0 & -1 & -2 & 0 & 4 & -1 & 0 \\ 0 & 0 & 0 & -2 & -2 & -2 & -1 & 8 & -1 \\ 0 & 0 & 0 & 0 & -2 & -1 & 0 & -1 & 4 \end{bmatrix}\begin{bmatrix} q_1 \\ q_2 \\ q_3 \\ q_4 \\ q_5 \\ q_6 \\ q_7 \\ q_8 \\ q_9 \end{bmatrix} -$$

$$\omega^2\left(\frac{1}{c^2}\right)\left(\frac{1}{36}\right)\begin{bmatrix} 4 & 2 & 0 & 2 & 1 & 0 & 0 & 0 & 0 \\ 2 & 8 & 2 & 1 & 4 & 1 & 0 & 0 & 0 \\ 0 & 2 & 4 & 0 & 1 & 2 & 0 & 0 & 0 \\ 2 & 1 & 0 & 8 & 4 & 0 & 2 & 1 & 0 \\ 1 & 4 & 1 & 4 & 16 & 4 & 1 & 4 & 1 \\ 0 & 1 & 2 & 0 & 4 & 8 & 0 & 1 & 2 \\ 0 & 0 & 0 & 2 & 1 & 0 & 4 & 2 & 0 \\ 0 & 0 & 0 & 1 & 4 & 1 & 2 & 8 & 2 \\ 0 & 0 & 0 & 0 & 1 & 2 & 0 & 2 & 4 \end{bmatrix}\begin{bmatrix} q_1 \\ q_2 \\ q_3 \\ q_4 \\ q_5 \\ q_6 \\ q_7 \\ q_8 \\ q_9 \end{bmatrix} = \begin{bmatrix} f_1 \\ f_2 \\ f_3 \\ f_4 \\ f_5 \\ f_6 \\ f_7 \\ f_8 \\ f_9 \end{bmatrix}. \quad \text{(A1.23)}$$

This system of equations now expresses the *potential* of the system. How the system responds to given conditions is dependent on the boundary conditions applied to it, namely the forcing functions at particular nodes or the specification of pressure values at specific nodes, etc. Before solving the system for given conditions it is worth emphasising a couple of points. Firstly, the *system* matrices are themselves symmetric. This is clearly to be expected as the interaction between, say, nodes 2 and 6 is obviously the same as that between nodes 6 and 2. Secondly, there are entries in the system matrices only at positions where the row/column reference relates an interaction between nodes. If there is no direct relationship between the nodes, i.e. they do not have a common element, then there is a zero in the corresponding position. Thirdly, a number of the entries in the matrices are zero, a feature that is common to finite element problems.

Finally, the matrices are banded, that is, non-zero entries appear along the main diagonals with upper and lower 'triangles' containing zero entries only. These last two features are generally exploited for the purposes of reduction in matrix storage requirements, an issue that will not be considered further here. It is worth pointing out, however, that the numbering of the nodes in the four-element problem of Figure A1.2 is optimal for the purposes of matrix storage requirements. This can be observed by considering the case where the central node is numbered as 1 with the rest numbered in any manner. It should be clear that the central node is connected to all elements and, therefore, directly to all other nodes. There will, therefore, be non-zero entries in all positions of both row one and column one of the system matrices. This clearly removes the banded-ness of these matrices, increasing storage requirements. Most FE packages employ optimal node-numbering routines as standard to best exploit banded matrices.

Consider the solution of Equation A1.23 for the situation where a force is applied at the central node 5, only. This is equivalent to an infinitesimally small, infinitely long cylindrical source at the centre of the system and is the 2-D equivalent of a 3-D point source problem. For the case where the wave number, k=1, and the force at node 5 is defined as **four**, i.e. $[f(\omega)]^T = (0,0,0,0,4,0,0,0,0)$, Equation A1.23 can be easily solved by some Gaussian elimination technique to generate the following results for the pressure values at the 9 nodes:

$$q_1 = -1.1542,$$

$$q_2 = -1.3913,$$

$$q_3 = -1.1542,$$

$$q_4 = -1.3913,$$

$$q_5 = 0.0632,$$

$$q_6 = -1.3913,$$

$$q_7 = -1.1542,$$

$$q_8 = -1.3913$$

and $q_9 = -1.1542.$

The symmetry of the results should be noticed, with $q_1 = q_3 = q_7 = q_9$, and $q_2 = q_4 = q_6 = q_8$ as would be expected.

Dirichlet boundary conditions, such as $q_i = \psi$ can be included easily as follows. In the final system matrix, eg. Equation A1.23, the i^{th} row is set to zero except for the diagonal term, which is set to unity. The i^{th} term of the right-hand side forcing function vector, $f(\omega)$, is then set to ψ, so that the row now reads $1.q_i = \psi$. For an even simpler example of this, consider specifying zero pressure along the bottom edge of the system in Figure A1.2 so that

$$q_1 = 0,$$

$$q_2 = 0$$

and $q_3 = 0.$

There are two options here. Firstly, the previous method could be used, with $\psi = 0$ in the first 3 rows of $f(\omega)$. Alternatively, however, seeing as q_1, q_2, and q_3 will clearly play no part in the final solution, the system matrices can simply be reduced to 6 by 6 matrices, excluding rows 1-3:

$$\left(\frac{1}{6}\right)\begin{bmatrix} 8 & -2 & 0 & -1 & -2 & 0 \\ -2 & 16 & -2 & -2 & -2 & -2 \\ 0 & -2 & 8 & 0 & -2 & -1 \\ -1 & -2 & 0 & 4 & -1 & 0 \\ -2 & -2 & -2 & -1 & 8 & -1 \\ 0 & -2 & -1 & 0 & -1 & 4 \end{bmatrix}\begin{bmatrix} q_4 \\ q_5 \\ q_6 \\ q_7 \\ q_8 \\ q_9 \end{bmatrix} -$$

$$\omega^2\left(\frac{1}{c^2}\right)\left(\frac{1}{36}\right)\begin{bmatrix} 8 & 4 & 0 & 2 & 1 & 0 \\ 4 & 16 & 4 & 1 & 4 & 1 \\ 0 & 4 & 8 & 0 & 1 & 2 \\ 2 & 1 & 0 & 4 & 2 & 0 \\ 1 & 4 & 4 & 2 & 8 & 2 \\ 0 & 1 & 1 & 0 & 2 & 4 \end{bmatrix}\begin{bmatrix} q_4 \\ q_5 \\ q_6 \\ q_7 \\ q_8 \\ q_9 \end{bmatrix} = \begin{bmatrix} f_4 \\ f_5 \\ f_6 \\ f_7 \\ f_8 \\ f_9 \end{bmatrix}. \qquad \text{(A1.24)}$$

As in previous cases, Gaussian elimination can be used to solve the system.

A1.2.8 The use of symmetry

A final consideration worth mentioning here is the use of symmetry. Clearly the system shown in Figure A1.2, without a zero pressure restraint along the bottom edge, is symmetric about both the x and y (or ζ and ξ) axes. The requirement for symmetry along a specific line or plane is zero gradient, in this case $\frac{\partial p}{\partial n} = 0$. This is, in fact, the natural boundary condition for acoustic elements, so that no additional boundary conditions need to be included. Instead the problem can revert back to the format of Figures A1.1 with a forcing function term included at any node. Take, for example, $\Delta f_1 = 1$. This is the equivalent problem to the four-element case discussed in section A1.2.7. Note that in that case $\Delta f_5 = 4$, which in fact could be considered to be a result of unit contributions from each element, that is

$$\Delta f_5 = \Delta f^{I}{}_5 + \Delta f^{II}{}_5 + \Delta f^{III}{}_5 + \Delta f^{IV}{}_5 = 1+1+1+1 = 4.$$

The system can then simply be expressed as

$$\left(\frac{1}{6}\right)\begin{bmatrix} 4 & -1 & -1 & -2 \\ -1 & 4 & -2 & -1 \\ -1 & -2 & 4 & -1 \\ -2 & -1 & -1 & 4 \end{bmatrix}\begin{bmatrix} q_1 \\ q_2 \\ q_3 \\ q_4 \end{bmatrix} - \omega^2 \left(\frac{1}{c^2}\right)\left(\frac{1}{36}\right)\begin{bmatrix} 4 & 2 & 2 & 1 \\ 2 & 4 & 1 & 2 \\ 2 & 1 & 4 & 2 \\ 1 & 2 & 2 & 4 \end{bmatrix}\begin{bmatrix} q_1 \\ q_2 \\ q_3 \\ q_4 \end{bmatrix} = \begin{bmatrix} 1 \\ 0 \\ 0 \\ 0 \end{bmatrix}. \tag{A1.25}$$

This gives the same nodal pressure values for nodes in similar positions to the 9-node example in section A1.2.7, with pressure values outside the 4-node system deduced from symmetry.

This completes the summary of the finite element technique. This section has sought to explain how each part of the FE process works through the use of simple examples, and to consider how these individual parts combine for the solution of a modelled system.

Addendum

Despite generally achieving good model-experimental agreement for near-field pressure results in the work presented here, Chapters 5 and 6 (Figures 5.1, 6.15 and 6.16) have shown fairly poor model-experimental agreement for *electrical* results. Following a discussion of these results it was suggested that this might be due to the use of the DAA2c fluid-modelling option (private conversation). Because of the excessive run times of the alternative acoustic FE/WEE option, the model electrical results reported in the main thesis were only generated using the DAA2c technique. However the subsequent use of a 1 GHz PC has enabled the corresponding WEE model to be run over a range of frequencies – the model run time being around 3 hours per frequency. The WEE model was therefore run at 37 frequencies, and the resulting electrical results are shown in Figure Ad.1.

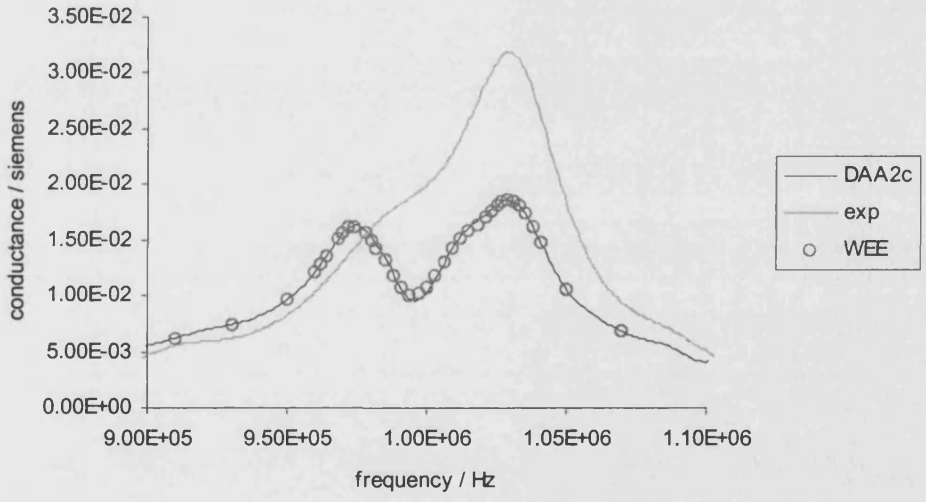

Figure Ad.1 Comparison of DAA2c-WEE-experimental electrical conductance data for the physiotherapy transducer/transducer model.

The DAA2c and WEE model results are clearly in very good agreement. This suggests that the poor model-experimental electrical agreement is *not* due to the

fluid-modelling technique used. The most likely cause of this discrepancy remains the use of inaccurate material properties in the model, and in particular inaccurate piezoelectric properties.